University of Bath

UNIVERSITY OF BATH

PHD

Control of asymmetric vortical flow over a delta wing at high angles of attack

Greenwell, D. I.

Award date:
1993

Awarding institution:
University of Bath

Link to publication

CONTROL OF ASYMMETRIC VORTICAL FLOW

OVER A DELTA WING AT HIGH ANGLES OF ATTACK

submitted by D I GREENWELL
for the degree of PhD
of the University of Bath
1993

COPYRIGHT

UMI Number: U057665

UMI

Dissertation Publishing

UMI U057665

ProQuest

ABSTRACT

Considerable operational advantages are anticipated for combat aircraft capable of manoeuvring outside the conventional angle of attack envelope. However, the development of control forces and moments presents a significant challenge, with extensive regions of asymmetric separated unsteady flow over wings, tail surfaces and fuselage resulting in loss of control power from moving control surfaces.

For delta wing planforms, the concept of Tangential Leading-Edge Blowing has previously been shown to be capable of significantly modifying the leeside vortical flow. Asymmetric blowing demonstrated the ability to generate or suppress lateral flow asymmetries and hence offered the potential for a powerful roll control system. However, at higher angles of attack a strong coupling of the vortical flowfield was evident, leading to an undesirable control moment reversal.

In this study the characteristics of symmetric and asymmetric blowing have been investigated experimentally and conceptually, with particular emphasis on the vortex coupling. The underlying flow mechanisms have been determined and a simple analysis based on the Leading-Edge Suction Analogy developed. From this analysis a number of areas requiring further experimental clarification are identified. The practical aspects of Tangential Leading-Edge Blowing as a flight vehicle control system are discussed; although a considerable potential improvement in roll authority is offered, the complex roll characteristics, uncertainties in scaling to full-size, inherently high mass-flow requirements for full-span blowing and installation difficulties render application only marginally feasible.

i

ACKNOWLEDGEMENTS

CONTENTS

Appendix A   RigTest 4.1 Configuration File Format

Appendix B   Published Papers

B1   "Determination of Vortex Burst Location from Surface Pressure Measurements", AIAA Journal, November 1992

B2   "Static Roll Moment Characteristics of Asymmetric Tangential Leading-Edge Blowing", Journal of Aircraft, to be published 1993

NOMENCLATURE

$\lvert A \rvert$	amplitude ratio
C_D	drag coefficient
C_{D0}	zero lift drag coefficient
C_l	roll moment coefficient
$C_{l\beta}$	effective dihedral, $\delta C_l / \delta \beta$ (deg^{-1})
$C_{l\psi}$	roll moment due to yaw, $\delta C_l / \delta \psi$ (deg^{-1})
$C_{l\phi}$	roll moment due to roll, $\delta C_l / \delta \phi$ (deg^{-1})
$C_{l\phi'}$	roll damping
C_L	lift coefficient
C_{LES}	leading-edge suction coefficient
C_{LVSE}	side-edge contribution to vortex lift
C_M	pitching moment coefficient
C_n	local normal force coefficient
C_N, C_Z	normal force coefficient
C_{N0}	datum normal force coefficient, sharp-edged wing
C_{NP}	potential flow component of normal force
C_{NV}	vortex flow component of normal force
C_p	static pressure coefficient
C_{pmin}	magnitude of vortex-induced suction peak
C_S	sideforce coefficient
C_μ	jet blowing momentum coefficient, mV_j/qS
C_μ^*	critical blowing level
c, c_0	root chord
D	drag
f	frequency, Hz

h	slot height
k	factor on α for underside potential lift,
	reduced frequency, $2\pi fc/U_\infty$
K	delta wing similarity parameter, $\tan\alpha/\tan\varepsilon$
K_{LE}	jet-induced leading-edge lift coefficient
K_P	potential lift coefficient, LESA
k_p	local potential lift coefficient
K_V	vortex lift coefficient, LESA
K_{VLE}	leading-edge vortex lift coefficient
K_{VSE}	side-edge vortex lift coefficient
L	rolling moment
M	pitching moment
m	jet mass flow
p	static pressure
p_{min}, p_0	static pressure at suction peak
p_∞	freestream static pressure
q	freestream dynamic pressure
q_{cl}	centreline dynamic pressure
R_e	Reynolds number based on root chord
r	leading edge radius
S	wing reference area
s	wing semispan
s'	effective semispan due to asymmetric blowing
s''	effective crossflow semispan due to sideslip
t	wing thickness,
	time
u,v,w	components of freestream velocity

u_{mean}	mean tunnel centreline velocity
u_{rms}	rms tunnel centreline velocity
U_∞, V, V_∞	freestream velocity
V_j	jet exit velocity
x	chordwise coordinate
x_V	chordwise centre of pressure of vortex lift
x_{VB}	chordwise vortex burst location
y	spanwise coordinate
y_{min}, y_0	spanwise location of suction peak
y_{ac}, y_p	spanwise centre of pressure of potential lift
y_v	spanwise location of vortex core
$y_{0.5}$	half width of suction peak
y^*	spanwise location of leading-edge separation
Z	normal force
z	height of vortex core
α, α_t	angle of attack
α_{eff}, α_s	effective angle of attack, or angle of downslip
α_s'	modified downslip angle
α_{RB}	formation of blown vortex
α_{stall}	slot stall onset
α_0	effective zero lift angle
β, β_s	angle of sideslip
β	vortex core angle of attack,
Γ	vortex strength
Γ'	vortex strength parameter, $y_{0.5}/s.x/c_0.\sqrt{-C_{pmin}}$
θ	pitch angle

θ_e, ε	wing semi-apex angle
θ_{eff}	instantaneous effective leading-edge pitch angle
θ'	pitch rate
ϕ	roll angle,
	phase lag
ψ	yaw angle
Λ, Λ_{le}	leading edge sweep
Λ_{eff}	effective leading edge sweep
λ	taper ratio, c_{tip}/c_{root}
τ	convective time, c/U_∞

Abbreviations

AD	Analogue to Digital
AR	Aspect Ratio
ASTOVL	Advanced Short Take-Off/Vertical Landing
DA	Digital to Analogue
DIO	Digital Input/Output
LDV	Laser Doppler Velocimetry
LESA	Leading-Edge Suction Analogy
TLEB	Tangential Leading-Edge Blowing

Subscripts

L	left side blowing only
R	right side blowing only
T	total (left+right) blowing

CHAPTER 1

INTRODUCTION

1.1 Background to the Research

1.1.1 The Delta Wing

The delta wing planform was originally applied to combat aircraft design in Germany in the 1940's, where its combination of high sweep for good supersonic performance and efficient structure was first recognised. Development had progressed as far as construction of a 'proof-of-concept' glider, the DM-1, when the war ended and the aircraft was captured by the Americans. Windtunnel testing at Langley[1] revealed very poor low-speed characteristics; however, it was discovered almost by accident that sharpening the leading-edges greatly improved maximum lift and handling characteristics, due to the formation of two longitudinal leading-edge vortex systems.

The sharp-edged delta wing's combination of good low and high-speed aerodynamics and efficient structure[2] led to its widespread adoption over the next two decades (Figure 1.1[3]). However, by the 1960's ever increasing requirements for large weapons loads, short field performance and manoeuvrability highlighted the pure delta planform's disadvantages: high induced-drag, loss of control effectiveness at high lift conditions, stability problems etc. Some designers, notably Dassault, returned to the swept wing while others modified the basic planform, adding a tailplane (MiG-21) or introducing compound sweep (Concorde, F-5E).

More recently, the advent of fly-by-wire (FBW) control systems incorporating artificial stability have led to a renaissance of the delta wing in the form of a canard-delta planform, typified by aircraft such as EFA and Rafale (Figure 1.2).

1

1.1.2 Combat Manoeuvrability

Current thinking on the aerodynamic design of combat aircraft is dominated by three considerations: stealth, supercruise and agility. Recent impressive flight demonstrations by Russian aircraft[4] (MiG-29, Su-27) have focused attention on agility in the low-speed flight regime(Figure 1.3[5]), where considerable tactical advantage is anticipated from an ability to manoeuvre at angles of attack beyond the stall[6]. Potential benefits include 'point-and-shoot' manoeuvres, enhanced turn performance and decoupling of trajectory from aircraft attitude.

1.1.3 Control Requirements

The good high angle of attack aerodynamic performance of the delta wing suits it to aircraft designed for 'post-stall' or 'supermanoeuvre' capability. However, at very high angles of attack the aircraft flowfield becomes increasingly complex, with extensive regions of asymmetric separated unsteady flow over wings, tail surfaces and fuselage, resulting in the onset of instabilities and nonlinearities and a loss of control power from conventional moving control surfaces[7] (Figure 1.4).

Control requirements at high angles of attack thus fall into two categories: sufficient control power (pitch, yaw and roll moments) to manoeuvre the aircraft, and sufficient control power to counteract instabilities and prevent divergence. Current combat aircraft are limited to transient excursions into the post-stall flight regime by both aerodynamics and control capacity; research aircraft such as the X-29, X-31 and F-18 HARV are demonstrating a capability to trim in pitch at high angles of attack, but are still restricted to relatively small sideslip/roll angles by the extreme nature of the lateral instabilities in this flight regime.

1.2 High Angle of Attack Control Concepts

Generation of control forces at high angles of attack has therefore been the subject of considerable work, and concepts investigated fall roughly into three categories: 'conventional' control surfaces, thrust vectoring and pneumatic (blowing or suction) schemes.

1.2.1 'Conventional' Control Surfaces

For pitch control in transient manoeuvres relatively conventional large all-moving control surfaces (tailplane or canard) have proven adequate. For lateral control, significant sideforces and yawing moments may be generated by manipulation of forebody vortices using moveable strakes or similar devices[8], though control characteristics tend to be nonlinear and asymmetric[9]. Roll control concepts have centred on modification of the wing flow[10], with leading-edge vortex flaps, apex fences, tiperons etc. In general, roll moments are modest and tend to be limited in angle of attack range.

1.2.2 Thrust Vectoring

Thrust vectoring for manoeuvre, as opposed to lift control, is currently of considerable interest, with at least three recent flight demonstrator programmes (STOL Eagle, X-31, F-18 HARV). Typically, vector angles are of the order of $\pm 10°$ which coupled with the long moment arm of a conventionally positioned propulsion nozzle appears to give adequate pitch and yaw control. Roll moment generation is feasible, but limited by practical nozzle spacings.

1.2.3 Blowing Schemes

Blowing schemes have been previously proposed to modify vortical flows on both forebodies and wings. Forebody blowing[9] has a significant capability for efficient generation of sideforce and yawing moment and is currently the subject of an

3

intensive research and development effort. For roll moment, it is again necessary to modify the wing flowfield; concepts investigated (though not necessarily ever applied as a control system) fall into four categories[11]: spanwise blowing, blowing parallel to the leading-edge, vortex core blowing and tangential leading-edge blowing (Figure 1.5). A related concept is the reaction control system (RCS), as used on the Harrier and also referred to as 'puffer jets', which uses only the momentum of the jet to generate control moments. Control power is small and severely limited by engine bleed capacity.

For spanwise blowing[12] a slot extends along each leading-edge, giving a thin jet in the spanwise direction and in the plane of the wing. A modest lift gain was achieved, at the cost of a reduction in the stall angle and a possible drag penalty. Blowing from the apex along the leading-edges[13] gave better results, with an increase in both lift and stall angle. Blowing into the vortex core[14] near the wing apex also provided some limited control of the vortex flow, but positioning of the nozzle was critical. Core suction (at the trailing edge) acts in a similar manner[15] but presents some obvious practical difficulties.

These schemes are essentially inertial and inviscid in their interactions with the wing flowfield and are thus inherently inefficient, with significant massflow requirements. In addition some advance knowledge of the vortex core or separation point is required for optimum nozzle placement. A more efficient method would be to modify the viscous flows producing the separated flow regions. A candidate technique is Coanda jet blowing, as utilised on circulation control aerofoils, where a thin tangential jet is injected into the crossflow boundary layer around the leading-edge (Figure 1.6), thus modifying the separation process generating the leading-edge vortices. The interaction is viscous in nature, with a very efficient transfer of momentum to the outer flow.

This technique is referred to as Tangential Leading-Edge Blowing (TLEB), and has demonstrated a capability to modify the vortical flow over a rounded leading-edge delta wing to the extent of suppressing the vortices completely[16]. Asymmetric TLEB has been shown to generate significant roll moments upto very high angles of attack[17], though with complex and nonlinear static and dynamic control characteristics[18], thus offering considerable potential as a flight vehicle control system.

1.3 The Research Programme

1.3.1 Motivation

Previous research indicated that the roll moment characteristics of asymmetric TLEB are highly nonlinear, with sign reversals and discontinuities, but did not offer more than a possible analogy to the effects of sideslip as an explanation. For application as a control system these characteristics were undesirable, and hence the mechanism(s) underlying roll moment generation needed to be more fully understood. Of particular concern was a strong coupling between 'blown' and 'unblown' vortices observed in the region of the stall angle.

1.3.2 Objectives

Original experimental objectives, as proposed to SERC (contract no. GR/F62995) were to:

a)   investigate the steady state characteristics of TLEB

b)   determine the sensitivity of the concept to slot geometry

c)   determine the timescales associated with the vortical flow modification

d)   demonstrate a roll control system utilising TLEB

These objectives were subsequently modified, with the development of an unsteady

blowing facility and 'free-to-roll' model support system undertaken by a visiting Fellow from Stanford University, Dr G Wong.

1.3.3 Experimental Programme

The experimental programme is summarised in Figure 1.7. Considerable experimental difficulties were encountered, resulting in delays and limited testing time.

Design and development of a model support system for high angle of attack testing diverted manufacturing resources from model construction, though some testing of an unblown wing was possible in late 1990. Initial tests on the blown wing (in an interim configuration due to a defect in the leading-edge assembly) were undertaken in mid-1991, with the majority of the static investigations (on a modified wing) at the end of 1991. Although test periods were short, the PC-based data acquisition system developed for this programme enabled the maximum use of wind tunnel time. Analysis of the data thus proved a lengthy task, occupying most of 1992 and providing a number of insights into the effects of asymmetric TLEB and into some previously unreported aspects of unblown delta wing aerodynamics.

The unsteady blowing facility and 'free-to-roll' system were commissioned at the end of 1992 and the blown wing used to demonstrate TLEB as a roll control system. Unfortunately, an unsuspected cross-coupling problem on the original sting balance was revealed, so that the remaining available tunnel time was taken up with repeat tests and no direct measurements of flowfield response to transient blowing were made.

1.3.4 Thesis Outline

The relevant aspects of high angle of attack aerodynamics of delta wings are

summarised in Chapter 2, with a review of previous work on TLEB in Chapter 3. The experimental apparatus and procedures are described in Chapter 4, with particular emphasis on the model support system and associated test facilities developed for this programme.

Experimental results for static conditions are reported in Chapter 5, for symmetric and asymmetric blowing, with a comparison with previous work. Chapter 6 presents an analysis of the results, with an assessment of the application of TLEB to a flight vehicle. Chapter 7 summarises the work and lists some recommendations for future investigation.

Appendix A lists the configuration file format for the windtunnel data acquisition program (RigTest) written in the course of this investigation, and Appendix B contains the relevant papers published by the author and his supervisor on this work.
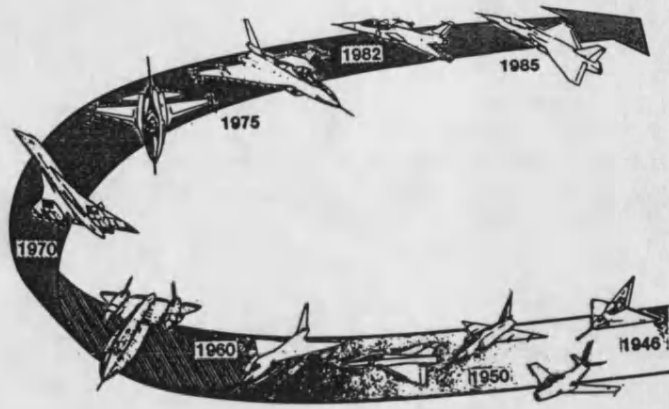
Figure 1.1 Applications of the Delta Wing Planform[3]
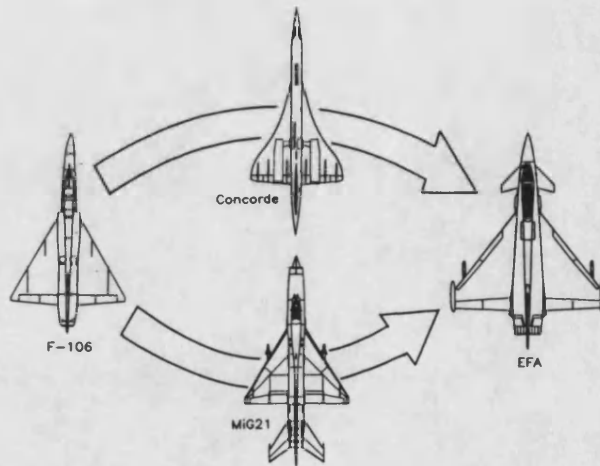
Figure 1.2 Evolution of the Delta Wing Planform
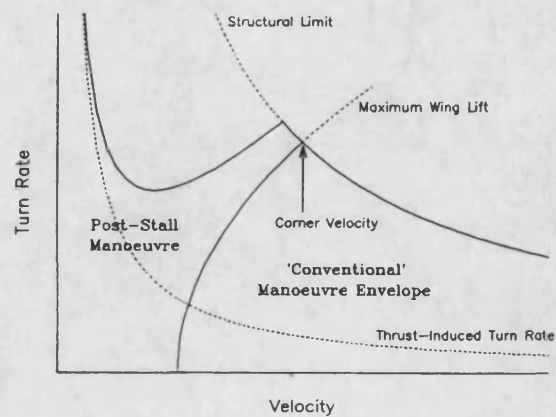
Figure 1.3 Post-Stall Manoeuvre in Relation to the Conventional Manoeuvre Envelope[5]

8
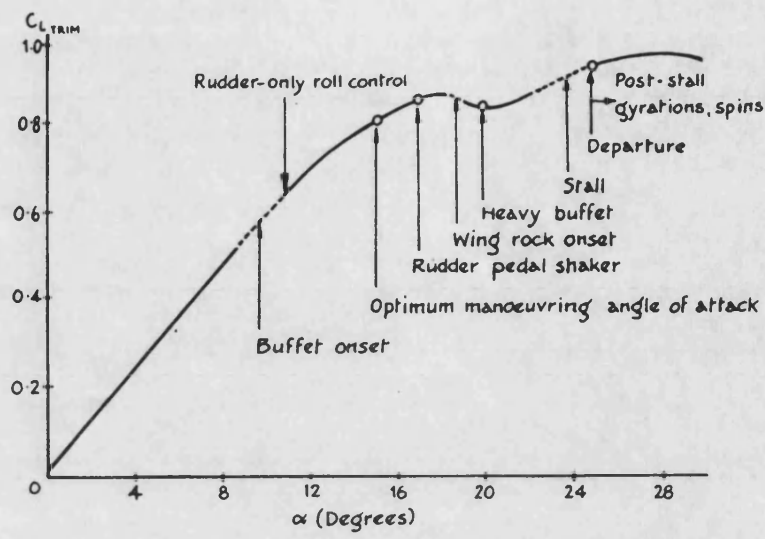
Figure 1.4 Instabilities in the High Angle of Attack Flight Regime
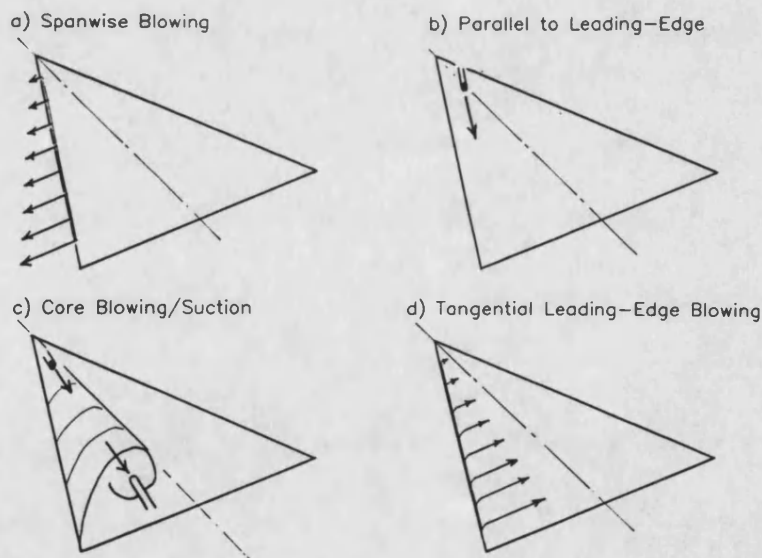
Figure 1.5 Blowing Schemes Applied to Delta Wings[11]

9

Leading edge blowing affects the
vortex equilibrium condition by control
of the location of the separation point
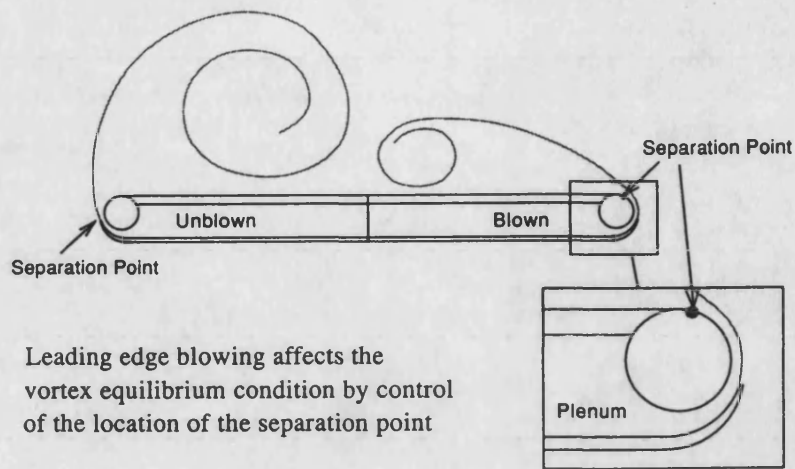
Figure 1.6 Tangential Leading-Edge Blowing
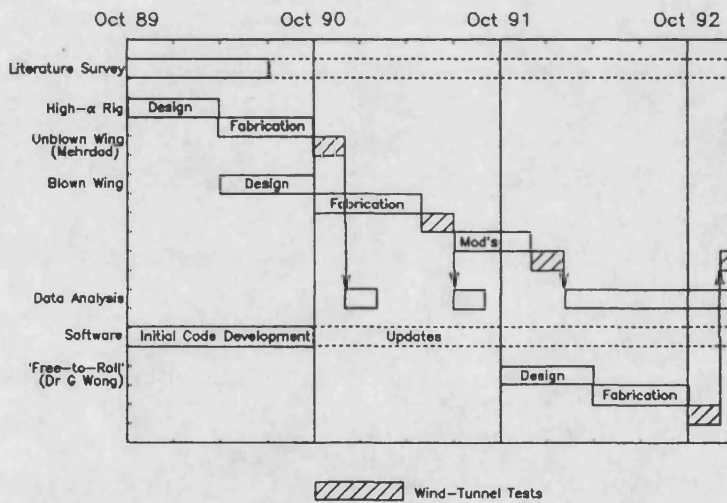
Figure 1.7 The Experimental Programme

10

CHAPTER 2

HIGH ANGLE-OF-ATTACK AERODYNAMICS OF DELTA WINGS

2.1 Introduction

Although many reviews of delta wing aerodynamics have been published, the size and complexity of this area of research is such that these reviews have necessarily tended to be limited either in scope or in depth. It was thus felt to be of use to add a further survey, concentrating on the aspects of the field most relevant to the application of Tangential Leading-Edge Blowing at high angles of attack.

In addition, a number of correlations/syntheses of published data derived during analysis of experimental blowing data are included.

2.2 General Flow Features

2.2.1 The Leading-Edge Vortex

At moderate to high angles of attack, the aerodynamics of delta wings are dominated by a longitudinal vortex system shed from the swept leading-edges. At an angle of attack dependent on the leading-edge shape, the upper and lower-surface boundary layers separate from the wing at the leading-edges to form free shear layers, which then roll up into spiral vortices lying above the wing and inboard of the leading-edges[19], as shown schematically in Figure 2.1a. On the upper surface, oil flow visualisation (Figure 2.1b) shows the primary separation at the leading-edge with a reattachment inboard of the vortex. Outboard of this line the adverse pressure gradient induced by the primary vortex results in a further separation of the flow and the formation of a secondary vortex of opposite sign to the primary. The presence of the primary vortex induces a large suction peak in the upper-surface pressure distribution.

11

2.2.2 Vortex Breakdown or 'Burst'

At a certain critical angle of attack, the leading-edge vortex flow becomes unstable, and an abrupt change in the flow structure occurs[22], characterised by the sudden deceleration of the axial flow in the vortex core, a decrease in circumferential velocity, an increase in the vortex size and a wake-type flow downstream (Figure 2.2a). This breakdown (or 'burst') initially occurs downstream of the wing, travelling upstream with increasing angle of attack until it crosses the trailing-edge. In the region of the burst the vortex-induced suction peak is reduced in magnitude and broadened, giving a nett loss in lift.

The presence of the burst phenomenon has a significant effect on the longitudinal and lateral aerodynamic characteristics of the wing[23]. Consequently, much theoretical work has been undertaken to elucidate the mechanisms underlying the breakdown. No approach has as yet proven satisfactory, but a number of parameters have emerged as critical[24]: changes in swirl, pressure gradient along the vortex core and external boundary conditions. The present unresolved theoretical background renders a more detailed description superfluous; suffice it to say that experimentally the location of the vortex burst has been shown to depend primarily on leading-edge sweep, angle of attack and sideslip[23] and to a lesser extent on leading-edge shape[25], tunnel blockage ratio[26] and downstream obstructions[20].

2.3 Steady State Aerodynamic Characteristics

2.3.1 Effect of Angle of Attack

Increasing angle of attack strengthens the leading-edge vortices, with the cores moving outboard and upward, while the primary reattachment line moves inboard. The presence of the vortex maintains an almost linear lift-curve slope upto very high

angles of attack, Figure 2.3[27]. At these angles of attack, axial forces are relatively small and the drag is almost entirely due to the streamwise component of the wing normal force (ie $C_D - C_{D0} = C_L \tan\alpha$). Further increase in angle of attack results in the occurrence of vortex breakdown on the wing, with the burst location moving up the wing with angle of attack, rapidly over the aft half and then more slowly as it approaches the apex (Figure 2.4). The onset of the burst can be clearly seen in the longitudinal characteristics of Figure 2.3, with an abrupt loss of lift and a 'nose-up' change in pitching moment. The severity of the changes are very dependent on leading-edge sweep angle.

2.3.2 Effect of Sideslip

The influence of sideslip on the delta wing flowfield is complex, with the lower-surface (attached) flow, the vortex trajectory and the vortex burst location all being affected.

The lower-surface flow changes are straightforward - the familiar stabilising 'induced dihedral' effect of wing sweep. Sideslip has relatively little effect on the strength of the unburst leading-edge vortices, but does generate an asymmetry in core height, with the windward vortex lower and vice versa, resulting in a strongly asymmetric upper-surface pressure distribution (Figure 2.5a) and hence an additional stabilising contribution.

The effect of sideslip on the vortex breakdown is equivalent to a change in leading-edge sweep angle, a reduction on the windward side and vice versa, giving an asymmetry in burst location (Figure 2.5b). Erickson[24] notes that the shift in burst location is less than might be expected from the change in geometric sweep angle due to sideslip, particularly for wings of higher aspect ratios.

13

The resultant lateral aerodynamic characteristics are complex and non-linear, and are typified by the 'effective dihedral' parameter, $C_{l\beta}$ (roll moment due to sideslip, Figure 2.6). At low angles of attack the roll moment is dominated by the stabilising contributions of the underside flow and the vortex height asymmetry. As angle of attack increases the burst comes onto the wing; the asymmetry in burst location is destabilising, giving a reversal in roll contribution. At very high angles of attack the vortex burst(s) reach the apex, the vortical flow subsides and the resulting stable roll moment is due to the underside contribution only. However, a further examination of the roll moment characteristics in the 'unstable' angle of attack region reveals that for high angles of sideslip (or roll angle) a stable trim point does exist (Figure 2.7)[30].

Effects of sideslip on longitudinal characteristics are relatively small at low angles of attack, but become more significant at higher angles of attack and sideslip[28]. At very high sideslip angles the leeward vortex moves off the wing, giving the abrupt reduction in lift evident in Figure 2.8.

2.3.3 Wing Planform Effects

An extremely comprehensive review of wing planform effects at lower angles of attack can be found in Reference 31. At high angles of attack the influence of the wing planform is seen primarily in the vortex burst phenomenon, which in turn affects the longitudinal and lateral aerodynamic characteristics.

For typical combat aircraft planforms, the important parameters are leading-edge sweep angle and wing taper ratio, of which sweep is the most critical for leading-edge vortex dominated flows.

Sweep Angle

Increasing sweep angle delays the onset of vortex bursting, and modifies the progress of the burst up the wing with increasing angle of attack (Figure 2.9)[27]. In the absence of a satisfactory theoretical technique, the effect of sweep and angle of attack on burst location must be modelled empirically in any analysis of high angle of attack delta wing aerodynamics. Reference 30 presents such a model, fitted to published data.

For very high sweep angles, the leading-edge vortices become increasingly unstable and unsteady, eventually becoming asymmetric (Figure 2.10)[32], with one vortex sitting above the other. The direction of the asymmetry is unpredictable, the phenomenon being very sensitive to apex geometry and flow angularity. It can be seen from Figure 2.10 that for sufficiently high sweep angles, asymmetry (or 'vortex contact') occurs before vortex breakdown and becomes the dominant factor in the high angle of attack aerodynamic characteristics.

The effect of sweep angle on lift coefficient is shown in Figure 2.11 (data from Reference 27, replotted in Reference 25), with the onset of vortex burst marked. For low sweep angles (55° to 70°), sweep angle has relatively little influence on 'pre-burst' lift curve slope, with onset of the vortex burst appearing to have no well-defined effect, though maximum lift appears to correlate well with the burst reaching the wing apex. For higher sweeps, increasing sweep angle reduces the low angle of attack lift curve slope, while maximum lift corresponds to the burst crossing the trailing edge. At very high angles of attack the curves converge to an approximately constant normal force coefficient, corresponding to fully separated flow. The differing effects of burst onset at low and high sweep angles are primarily due to the different onset angles of attack. For higher sweep angles the vortex lift is a greater proportion of the total and the vortex burst is delayed to a higher angle of attack where the

vortex lift is further enhanced; hence any loss of vortex lift is more apparent in the overall characteristics.

Only one systematic study of the effect of sweep on lateral characteristics appears to have been published[33], with the effective dihedral trends shown in Figure 2.12a. The delayed onset of vortex burst with increasing sweep results in a delay of the unstable roll moment break noted in Figure 2.6 and a reduction in its magnitude.

Taper Ratio

Little systematic experimental work on the effects of taper ratio appears to have been published. From an analysis in Reference 31, small taper ratios (upto 0.2) have little effect on low angle of attack longitudinal characteristics. The influence of taper ratio on burst location is, however, largely unknown.

For lateral characteristics, Figure 2.12b shows the effect of taper ratio on effective dihedral for a rounded leading-edge 53° delta[34]. Taper ratios upto 0.2 have little effect, but at 0.5 the unstable break is significantly delayed, in a similar manner to the effect of increased sweep. It is not clear as to whether this is a result of a shift in burst location or a stabilising contribution of the tip vortex.

2.3.4 Effect of Leading-Edge Shape

It is widely held that for a sharp-edged delta wing the vortical flowfield is insensitive to leading-edge shape. However, a systematic study reported in Reference 25 for a 70° delta wing showed that this is not true of the vortex burst behaviour, where increasing leading-edge 'bluntness' tends to delay the burst onset. The corresponding lift data shows no effect of leading-edge shape at low angles of attack, but significant changes in the stall region, which for this sweep angle coincides with burst onset. It

16

is also generally suggested that the effect of a rounded rather than sharp leading-edge is to delay the formation of the vortex, perhaps by upto 5°. This is not apparent in the lift data of Reference 25, but experimental data from Reference 31 does show a small reduction in vortex lift with increasing leading-edge radius, coupled with a very significant improvement in lift-dependent drag due to partial recovery of leading-edge thrust.

The available data on the effect of leading-edge radius on lateral characteristics[35,36] shows trends in effective dihedral consistent with the delay in burst onset noted above, i.e. a delay in the unstable roll moment break with increasing leading-edge radius.

2.3.5 Test Conditions

Surprisingly little work has been done on the effects of test conditions at high angles of attack (other than Reynolds Number variations) and what is available is not always consistent.

Reynolds Number

It is generally stated that for sharp-edged delta wings the (unburst) vortex characteristics are insensitive to Re[24] and this is supported by the experimental results of Reference 37 (Figure 2.13a). However, significant differences are evident in the stall region, presumably due to variations in burst trajectory. These Re effects are of a similar order to the leading-edge shape effects noted above, so that any trends in comparisons of published data tend to be masked by this and other test condition variations.

Re does significantly affect the secondary vortex formation (Figure 2.13b[21]), since this is a function of upper surface boundary layer state, but overall vortex lift seems

to be unaffected. For rounded leading-edge wings the primary vortex shear layer separation process is presumably affected by Re, in particular the delay in vortex formation noted above. However, no consistent experimental data was identified to quantify this effect.

Tunnel Interference

The effect of model size (blockage) and support interference has previously been almost completely ignored; only recently has attention been focused on this aspect of high angle of attack testing[26,38,39]. A comparison of published lift data[37] does indicate that this neglect may be justified at low 'unburst' angles of attack. However, the vortex burst phenomenon has long been known to be sensitive to downstream blockage, and the critical effects of model size and support interference on lateral characteristics were demonstrated by Johnson et. al.[39] (Figure 2.14). In general, downstream blockage[20] hastens the onset of the burst, while increasing model size delays burst onset[26]. No systematic effort to develop guidelines on maximum model size has been made, but a model-to-windtunnel area ratio of around 5% seems to be generally accepted as offering a reasonable compromise. Published test data ranges from 0.25%[119] to around 30%[25].

General Test Conditions

An indication of the level of experimental scatter due to test conditions and leading-edge shape is afforded by the results of a survey of published 60° delta wing lateral characteristics[35,36,40..44]carried out during analysis of asymmetric blowing data (Figure 2.15). The number of variables obscures most trends, though it is possible to discern a delay in the unstable roll moment break with increasing blockage. The effect of leading-edge shape noted in Section 2.3.4 can be seen in the later and less abrupt roll reversal for the rounded leading-edge wings.

2.4 Unsteady Aerodynamics

2.4.1 Longitudinal (Pitch Rate) Characteristics

Early work in unsteady aerodynamics of delta wings is reviewed in Reference 19.

Experiments had been limited to relatively low angles of attack, with the vortex burst

off the wing, and discrepancies between datasets were described as 'large'. It was

noted that the vortex core position after a transient wing motion converged to the

steady state position within one convective time.

Recent work at higher angles of attack is reviewed in Reference 45, which draws

heavily on the experimental data of Reference 46. For pitching motions in the low

angle of attack range, lift response is essentially quasi-steady, with the unburst vortex

adjusting rapidly to changes in angle of attack (Figure 2.16a). In the high angle of

attack range (Figure 2.16b) a hysteresis loop is observed, similar to the 'dynamic stall'

behaviour of 2D aerofoils, resulting from a significant lag in the response of the

vortex burst to wing motion.

Although the timescale for vortex burst reorganisation is clearly much longer than for

the unburst vortex, Reference 45 does not attempt to quantify this. Since, as will be

seen later, the characteristics of asymmetric TLEB at high angles of attack are

critically dependent on the response of the vortex burst, it was felt to be useful to

examine in more detail published data on the transient response of the vortex burst.

2.4.2 Burst Motion Timescales

A number of researchers have reported on the transient response of the vortex burst

to sinusoidal[47..50] and ramping[51..53] pitch motions and to transient blowing[11,15]. It

seems to be generally accepted that two timescales are evident in the flowfield: the

response of the unburst portion of the vortex, with a time constant of around one

convective time, and the burst response, about an order of magnitude slower. Unfortunately no quantitative rather than qualitative examination of these timescales has been identified, so a correlation of the published data was attempted, with some degree of success.

As a first approximation, the response of the burst was modelled as a linear system response with pitch angle input and burst location output.

$$\theta \rightarrow \boxed{1 - \tau_1 s} \xrightarrow{\theta_{eff}} \boxed{\dfrac{k_2}{1 + \tau_2 s}} \xrightarrow{\Gamma} \boxed{\dfrac{k_3}{1 + \tau_3 s}} \xrightarrow{x_{VB}}$$
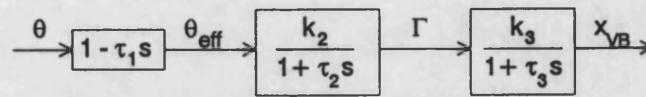
The transfer function consists of three blocks: an effective pitch angle, allowing for induced camber, the response of the vortex feeding sheet to instantaneous leading-edge angle of attack and the response of the burst.

An 'effective pitch angle' term is required, since pitch (or roll) rate induces an instantaneous camber, which has a significant effect on vortex burst trajectory[54]. Positive longitudinal camber delays burst onset and vice versa but little quantitative experimental data is available. On the basis that the wing apex region is most critical in the formation of the leading-edge vortex, the effective pitch angle was assumed to be a function of the instantaneous tip angle of attack,

$$\theta_{eff} = fn(\theta - \tfrac{1}{2}cU_\infty\theta')$$

for a wing pitching about its centroid.

20

In order to identify the system parameters (τ_1, τ_2, τ_3), the response of the burst to sinusoidal pitch inputs[47..50] was analysed using a Bode plot, with amplitude ratio and phase lag plotted as a function of reduced frequency, $2\pi fc/U_\infty$ (Figure 2.17). Although derived from a wide range of sweep angles and pitch angle ranges, the data is remarkably consistent. Unfortunately, insufficient high frequency data is available to positively identify the form of the system transfer function, but a curve fit using the model discussed above gives the system parameter values of the order of:

$$\tau_1 \approx 0.5$$
$$\tau_2 \approx 0.5$$
$$\tau_3 \approx 1.0$$

with the differing vortex response timescales evident in τ_2 and τ_3. It must be emphasised that the scatter in the data analysed and the non-linear nature of the burst phenomenon makes these values at best approximate. The effect of induced camber can be seen in the lower phase lag of the single 'plunging' motion dataset.

In order to provide some confirmation of the model, a prediction of the response to a ramp pitch motion was compared with experimental data. The ramp response of a third order system has a delay equal to the sum of the time constants, in this case approximately 2.0. Figure 2.18[51,52] shows a delay of about 2.5, satisfactorily close given the scatter in the data fitted. Figure 2.18b (from Reference 51) also shows an initial reversal in the burst motion response, consistent with the induced camber 'lead' term in the model. On cessation of the wing motion, the vortex burst continues to move towards its equilibrium position, but the application of the model in this region is complicated by the non-linear nature of the static burst trajectory. A further factor to be taking account is a small but significant difference in burst response for pitch-up

and pitch-down motions apparent in some datasets.

This semi-empirical approach to the modelling of the transient response of the vortex burst appears to be essentially new, though some investigators have come close. It would be particularly suitable for application to the well-established empirical and theoretical methods available for prediction of unsteady (but unburst) and steady leading-edge vortex flows. However, the available experimental data covers a wide range of sweep angles, pitch/roll rates and types of motion; further (parametric) investigation would be of considerable interest.

2.4.3 Lateral (Roll Rate) Characteristics

The roll characteristics at high angles of attack are of particular interest in this study. For wings of moderate sweep angle (say upto 70°) damping in roll is positive[57] and the response to a disturbance is a well-damped subsidence. The final trim roll angle depends on wing geometry, angle of attack and magnitude of the initial disturbance. The rate of subsidence is such that any lag in vortex burst location is negligible.

For higher sweep angles (typically greater than 75°) a different response occurs; a limit cycle roll oscillation (Figure 2.19a)[58] known as wing rock is exhibited. The oscillation is generally in roll about the body axis, but a combined roll-yaw motion resembling dutch roll has also been observed[59]. Amplitudes are typically around ±30° to 40° with a reduced frequency (fully developed) of about 0.3.

The underlying mechanisms of wing rock are currently the subject of some debate, but onset seems to be associated with a nonlinear roll damping characteristic (Figure 2.19b) with negative damping at small roll angles and positive (limiting) damping at higher roll angles. Previous investigations[58..62] have concluded that the primary flow

mechanism is a variation in position of the two leading-edge vortices known as 'vortex lift-off', a dynamic counterpart of the asymmetry in vortex height described in Section 2.2.3. Static asymmetry in vortex burst with roll/sideslip angle provides an additional destabilising influence, but this tends to be reduced by the lag in burst location apparent at these oscillation frequencies. Recent water tunnel flow visualisation experiments[63,64], however, reported that wing rock could occur even in the absence of asymmetric vortex lift-off, and it was suggested that the key vortex interaction takes place in the apex region of the wing. A further observation of relevance to this investigation was that rounding the leading-edges delayed the onset of wing rock.

2.5 Analytical and Empirical Methods

2.5.1 Overview

The prediction of the steady and unsteady loading on delta wings at high angles of attack has been the subject of intensive study. A number of comprehensive reviews of the field have been published[19,45,65]; this section summarises only the methods relevant to this study.

2.5.2 Linear Slender Wing Theory - Attached Flow

A special small-disturbance solution of the potential flow about a finite wing may be obtained by assuming a slender wing (AR < 1) and low angles of attack (RT Jones[66]). The resultant flowfield is conical and hence a solution in the crossflow plane (Figure 2.20) is sufficient. For a slender delta wing with straight leading-edges, normal force and sideforce coefficients are

$$C_N = \tfrac{1}{2}\pi AR\alpha$$

$$C_S = \tfrac{1}{2}\pi\alpha^2$$

23

Note that sideforce is independent of aspect ratio and that at higher angles of attack, α terms may be replaced by $\sin\alpha$. For 'not-so-slender' wings, the flow is no longer conical and a numerical panel method approach is required to account for trailing-edge effects.

2.5.3 Non-linear Separated Flow

Non-linear 3D methods range from panel methods to full Navier-Stokes solutions, but by far the most successful (and probably the simplest) is the leading-edge suction analogy due to Polhamus[32,67].

The total lift of a delta wing is assumed to consist of two components: a potential flow lift and a lift associated with the presence of the leading-edge vortices. This approach was not new, but the derivation of the two lift contributions was[67]. The analogy is usually expressed in terms of lift and drag coefficients, but a more useful form is in terms of a normal force coefficient, since axial force is predicted to be zero.

The potential flow contribution is

$$C_{NP} = K_P \sin\alpha \cos\alpha$$

where K_P is the zero-lift normal force slope, obtained from any reliable potential flow lifting surface method and the trigonometric terms account for the true boundary conditions. The vortex term is obtained by assuming that since reattachment occurs on the upper-surface, the normal force required to maintain the flow about the vortex is the same as the leading-edge suction force required to maintain the attached flow about the leading-edge in the potential flow case (Figure 2.21), giving

$$C_{NV} = K_V \sin^2\alpha$$

where K_V is a function of the leading-edge suction distribution, and as for K_p may be obtained from a suitable attached flow lifting surface method. The loss of leading-edge thrust gives

$$C_N = C_{NP} + C_{NV}$$
$$C_L = C_N \cos\alpha$$
$$C_D = C_N \sin\alpha$$

The variation of K_P and K_V with sweep angle/aspect ratio for straight-edged delta wings is shown in Figure 2.22. It can be seen that K_V is practically independent of sweep angle and has a value close to π (c.f. RT Jones sideforce), while K_P falls to zero as sweep angle approaches 90°.

Despite its simplicity, this analogy gives very good results when applied to experimental lift data, particularly at low angles of attack prior to vortex burst onset (Figures 2.3, 2.23a). Use of an appropriate compressible flow lifting surface method also enables Mach Number effects to be predicted. Significant deviations only occur when the leading-edge is not sharp, allowing some recovery of the leading-edge suction, or when vortex burst occurs over the wing. Although the analogy takes no account of the details of the vortical flow structure, a simple analysis of a slender wing flowfield (with experimentally determined vortex core location) gives an expression for lift of the same form, with very similar coefficients[68]. An experimental examination of the analogy[69] also showed that total delta wing lift could be split into potential and vortex flow components, and that these were well predicted by the analogy.

In its original form the analogy gave no information about load distribution and was restricted to sharp-edged wings. Subsequently, a number of researchers have extended the method to wings with streamwise tips[70], rounded leading-edges[71,72], the vortex burst present[73], the prediction of longitudinal[74] and lateral characteristics and to unsteady aerodynamics[75].

For trapezoidal wings typical of current fighter aircraft, the leading-edge suction analogy underestimates lift at high angles of attack[76,77] and it is necessary to take into account the separation along the side edges. An extension to the analogy was developed[70] with an additional vortex lift term, K_{VSE}. For wings of representative taper ratio this term may approach half the total vortex lift. The analogy may be extended to rounded leading-edge wings by modifying the vortex lift term. Two approaches have been used: a delayed formation of the vortex[71] or a reduction in vortex lift commensurate with the partial recovery in leading-edge thrust[72,78].

Pitch[74] and roll[73] moment prediction requires a knowledge of the load distribution on the wing, and this is generally obtained by assuming that the distribution of the potential and vortex lift components are the same as that of the leading-edge suction. This approach was verified experimentally in References 69 and 74 for aspect ratios upto 2.

The effects of vortex breakdown have been modelled by assuming a loss of vortex lift aft of the burst point[30,73]. Breakdown location is derived from a semi-empirical correlation with the leading-edge suction distribution, and vortex lift aft of this point is reduced by a further, completely empirical, factor (of the order of 0.5 depending on wing planform). A reasonable prediction of longitudinal and lateral characteristics is obtained (Figure 2.23).

A further extension to cover unsteady aerodynamics uses an empirical[46] or appropriate analytic technique[75] to derive time-dependent leading-edge suction forces, with additional allowances for the time lags of the burst and unburst vortex flow. A particularly comprehensive application of the leading-edge suction analogy (with modifications) to unsteady aerodynamics of delta wings will be found in the work of Ericsson et. al.[79,80].

2.6 Analysis of Vortex-Induced Upper-Surface Pressure Distributions

2.6.1 Background

Previous attempts have been made to correlate vortex burst with surface pressure distributions[23][81][82]. These have concentrated on the behaviour of the suction peaks induced by the leading edge vortices. In general, the variation of the magnitude of the suction peak with angle of attack for a given chordwise location is correlated with the vortex state. No consistent trends have been noted; in one case the burst is followed by a reduction in the rate of change of the peak suction with angle of attack, while in another there is a local reduction in suction underneath the breakdown point followed by a recovery as the burst moves upstream. In general, vortex burst is not associated with any consistent or well-defined change in peak suction. As a result, recent investigations of vortex breakdown have tended to disregard surface pressure variations.

However, an investigation of the variation of the shape of the vortex-induced suction peaks[83], using a form parameter derived from a simple potential flow model, has shown a much better correlation with vortex state.

2.6.2 Flow Model

Shape Parameter and Vortex Location

For a slender wing at low angles of attack the flow may be assumed to be conical, and the problem reduces to a two-dimensional flow in the cross-flow plane[84]. The simplest possible model of the vortex flow is a point vortex over an infinite plane, inducing a suction peak as shown. It can be readily shown that the halfwidth of the pressure distribution (as defined in Figure 2.24a) is directly proportional to the height of the vortex.

$$z = 1.5538 \; y_{0.5}$$

Although this model is grossly simplified, taking no account of the effects of a non-infinite surface, the feeding vortex sheet and the opposite vortex, it gives remarkably good results when applied to experimental data. Deriving a more realistic model would tend to obscure the basic physics of the flow.

Figure 2.24b shows a practical definition of halfwidth for a typical delta wing upper surface pressure distribution. Although in no way rigorous, the justification for this interpretation is that on the inner side of the suction peak, leading edge effects are small. At very high sweep angles (say > 80°), however, the vortices are close enough together for the shape of the suction peaks to deviate significantly from the simple model. Non-dimensionalising,

$$z/s \approx 1.55 \; y_{0.5}/s$$

A literature search was performed to identify published datasets containing both vortex core trajectory and upper surface pressure measurements[21,25,37,84..98]. Figure 2.25a compares the spanwise location of the vortex core and the suction peak. In general there is good agreement, though for the relatively thick biconvex wing of Reference

85 the vortex tends to be about 5% outboard of the suction peak, possibly due to the geometry. Figure 2.25b shows vortex height against suction peak halfwidth. Although there is some scatter, due in part to the small size and sometimes poor reproduction of the curves analysed, the simple flow model gives a remarkably good fit.

Vortex Strength

Returning to the simple flow model of Figure 2.24a, it can also be shown that the minimum pressure is related to vortex strength,

$$\Gamma = \pi z \sqrt{-p_{min}} / \tfrac{1}{2}\rho$$

$$= \pi V z \sqrt{-C_{pmin}}$$

$$= \pi V c_0 (1.55 \ y_{0.5}/s)(x \ \tan\varepsilon/c_0)\sqrt{-C_{pmin}}$$

For a given planform, at constant velocity, $\Gamma \propto \Gamma'$, where

$$\Gamma' = y_{0.5}/s \ x/c_0 \ \sqrt{-C_{pmin}}$$

Γ' may be thought of as a vortex strength parameter, or alternatively as a measure of the local upper surface loading (although this is a function of C_{pmin} rather than $\sqrt{C_{pmin}}$). Figure 2.26, derived from the definitive work of Hummel[28] shows this parameter increasing linearly from the wing apex, except in the vicinity of the trailing edge. Small sideslip angles have little effect on the vortex strength - which is not immediately apparent from the significantly asymmetric spanwise pressure distributions.

Rearranging the expression for vortex strength into the usual non-dimensional form

gives

$$\Gamma/Vx = 1.55 \, \pi \, \tan\varepsilon \, y_{0.5}/s \, \sqrt{-C_{pmin}}$$

Hemsch & Luckring[90] show that for delta wings,

$$\Gamma/Vl = \tan^2\varepsilon \, \cos\alpha \, g(K,M)$$

where K is the Sychev similarity parameter[97] (= $\tan\alpha/\tan\varepsilon$ for pure deltas) and $g(K,M)$ is an empirically derived function of the form $g = AK^{1.2}$. For the low-speed experimental delta wing flow field data analysed in Reference 90, A is approximately 3.5. Figure 2.27 shows vortex strengths derived from published pressure data (for unburst, approximately conical, vortex flows) plotted against Hemsch & Luckring's similarity function. The agreement is remarkably good, considering the simple nature of the flow model.

Departure From Conical Flow

The nonlinear behaviour of Γ' near the trailing edge in Figure 2.26 indicates a departure from conical flow. This can also be seen in the surface pressures; the non-dimensional spanwise pressure distribution should be constant along the wing, which is clearly not the case. This strongly non-conical loading occurs even for very slender wings[99], and is predicted by the leading-edge suction analogy[73]. A further indication that the simple flow model remains valid in non-conical flow regimes is given by the chordwise behaviour of the halfwidth parameter for the data of Figure 2.26, shown in Figure 2.28. Vortex core trajectory does not significantly deviate from conical behaviour over the wing[24], and this is reflected in the practically constant value of halfwidth along the chord. The typical upward movement of the leeward

30

vortex core is also evident.

2.6.3 Effect of Vortex Burst

In the region of the vortex breakdown the simple point vortex flow model breaks down, and the halfwidth and vortex strength parameters are no longer valid. However, in the process of analysing published pressure data, it became clear that there are consistent trends in the way that halfwidth changes as the vortex burst progresses.

Variation with Chordwise Location

Where a burst vortex is present over the wing, the simple model breaks down (Figure 2.28, for high sideslip angles). Although the core trajectory is relatively unaffected by the burst, the halfwidth exhibits a marked increase in the region of the burst, implying a change in the shape of the pressure distribution.

Variation with Angle of Attack

Figure 2.29 shows typical variations of halfwidth with angle of attack. In general, the halfwidth levels off some 10° or 20° ahead of the vortex burst, which itself is marked by a very well-defined increase in the halfwidth. If sufficient pressure data is available, the burst location may thus be determined as accurately as with flow visualisation techniques.

Erickson[24] shows that for pure delta wings the angle between the vortex core and the wing is approximately ¼ of the angle of attack, implying that vortex height varies linearly with angle of attack; this trend is evident in the 'pre-burst' portion of Figure 2.29. A prediction of the slope of this portion may thus be made:

$$\beta/2 \approx 0.25 \, \alpha/\varepsilon$$

$$\therefore \, z/s \approx 0.25 \, \alpha/\varepsilon$$

31

since z/s $\approx$ 1.554 $y_{0.5}$/s,

$$y_{0.5}/s \approx 0.16 \, \alpha/\varepsilon$$

Figure 2.29a shows that this is a good approximation for the pure delta wing datasets analysed. Strake vortices (Figure 2.29b), however, show a significantly higher slope, since the strake vortex on a double delta wing tends to be displaced upwards by the main wing vortex. Flow field measurements on the F-18[95] show a vortex trajectory considerably higher than that of a pure delta, giving

$$z/s \approx 0.36 \, \alpha/\varepsilon$$

The resultant halfwidth trend would be

$$y_{0.5}/s \approx 0.23 \, \alpha/\varepsilon$$

Figure 2.29b shows that again this is a remarkably good approximation.

A small number of delta wing datasets show an increased halfwidth relative to Figure 2.29a. These were from tests undertaken at Notre Dame University[93,96] and at the McDonnell Douglas Research Laboratories[25,37], and are characterised by very large wing/tunnel area ratios (16-30%). The high halfwidths may thus be the result of excessive blockage, an effect which would repay further investigation.

2.6.4 Correlation with Vortex Condition

The Vortex Breakdown Process

Figure 2.30 shows a schematic of the vortex breakdown process, split into four

regions[23][54]. A more complex spiral structure is sometimes observed, but this seems to be confined to very low Re flows.

A denotes the unburst vortex, where the simple model is valid and halfwidth is directly proportional to vortex height. B is a region of flow deceleration ahead of the visible burst point. In the presence of a longitudinal pressure gradient the velocity distribution through an unburst vortex (outside of the viscous sub-core) gradually changes[22][100], such that the swirl component falls off more rapidly with increasing radius.

C shows a bubble-type breakdown, with some degree of flow reversal in the core. The start of the bubble is usually defined as the burst point, since it is relatively easy to observe. The flow in this region is unsteady and difficult to model; one approach is to combine a point vortex with a source[101] to generate a semi-infinite slender body along the vortex axis aft of the breakdown point, giving a reduction in suction peak and an increase in halfwidth. The fully developed burst vortex, D, is often described as a region of large scale turbulence.

The various stages of vortex breakdown may be discerned in the halfwidth trends:

Chordwise Variation of Halfwidth

Figure 2.31a illustrates the general variation of halfwidth with chordwise location for a constant angle of attack. The difference between the unburst (A) and decelerating flow (B) regions is generally difficult to see on this plot, with halfwidth remaining essentially constant along the wing. Some datasets do show a gradual reduction in halfwidth from the apex, until the burst point is reached. The burst point, as determined visually, is always in the region of the first kink in the curve. Aft of the

burst the halfwidth increases linearly, as the bubble develops (C), until a plateau is reached when the burst is fully developed (D). This final value is typically of the order of twice the unburst halfwidth.

Halfwidth Variation with Angle of Attack

Figure 2.31b shows the variation of halfwidth with angle of attack for a given chordwise location. The initially unburst vortex (A) shows a linear increase in height with angle of attack which then levels off. This seems to correspond to the flow deceleration region (B), with a reduced halfwidth relative to the unburst vortex trend. The experimentally determined burst point is always in the region of the abrupt increase in halfwidth at the end of this almost level portion of the curve. The halfwidth now increases rapidly as the breakdown progresses (C), until the burst is fully developed (D) and the curve approaches a straight line of approximately double the slope of the initial unburst vortex.

2.6.5 Summary of Vortex Shape Parameter Analysis

For an unburst leading edge vortex, a simple model based on a point vortex above an infinite plane gives the result that vortex height is directly proportional to the halfwidth of the induced pressure distribution on the surface, while vortex strength is a function both of the halfwidth and the peak suction value. A surprisingly good match to experimental data was found.

For angles of attack where the vortex burst phenomenon is present over the wing, the burst location is marked by an abrupt change in the halfwidth of the pressure distributions. There appears to be a good correlation between the various stages of vortex breakdown and the behaviour of the halfwidth parameter.

This observation offers the ability to determine vortex condition and burst location from surface pressure measurements alone. Limitations include the need for extensive pressure tappings and the lack of data on vortex bursts off the wing (ie low angle of attack or high sideslip). Conversely, the usual experimental techniques also present considerable practical difficulties, combined with the need for an 'eyeball' judgement of burst location.
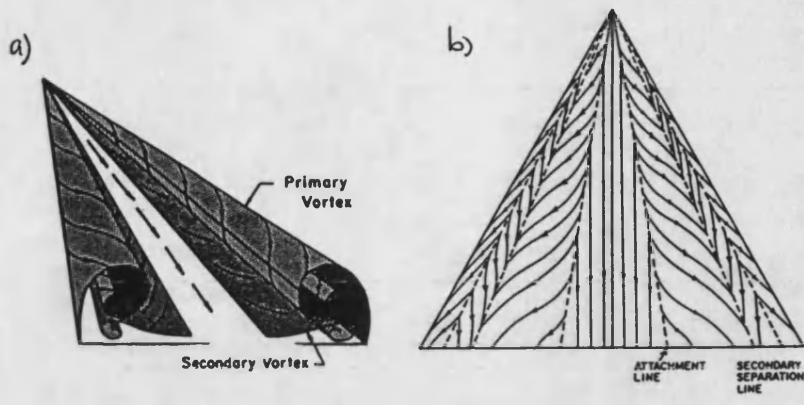
Figure 2.1 Leading-Edge Vortices over a Delta Wing
a) Schematic of Flowfield
b) Typical Upper-Surface Flow Pattern
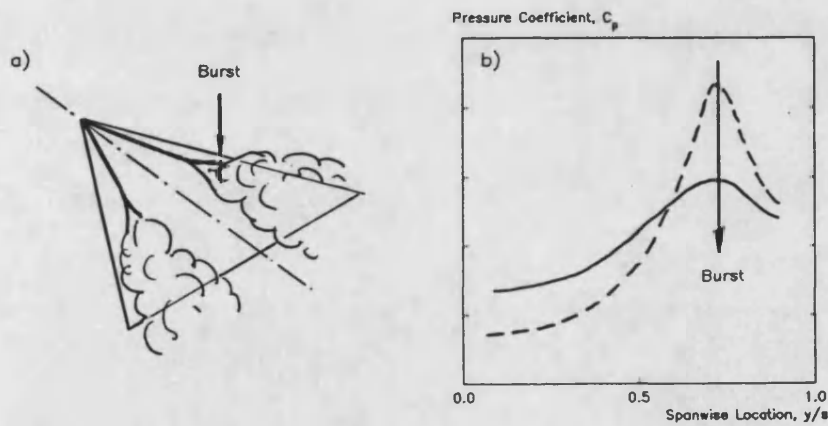
Figure 2.2 Vortex Burst or Breakdown
a) Effect on Wing Flowfield
b) Effect on Upper-Surface Pressure Distribution
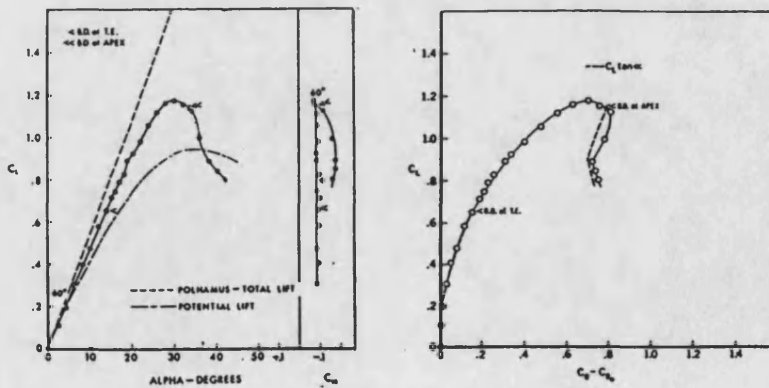
Figure 2.3 Typical Longitudinal Aerodynamic Characteristics of a Sharp-Edged Delta Wing[27]

36
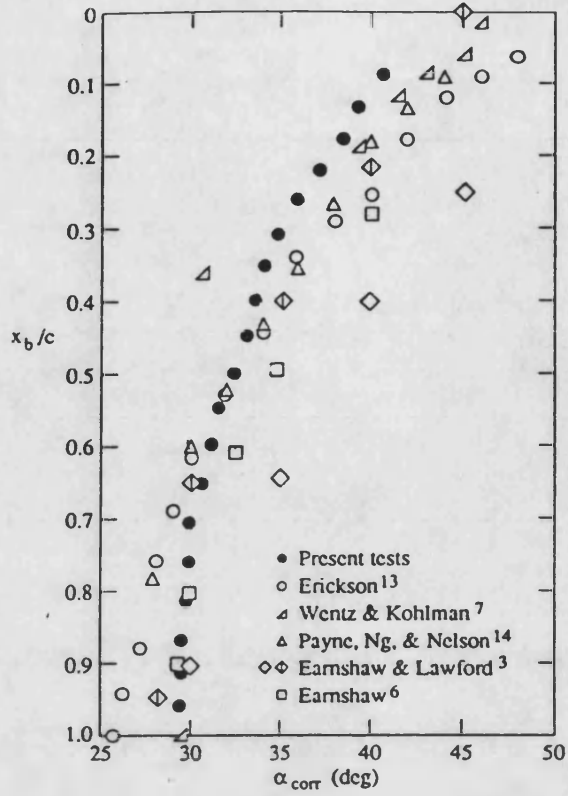
Figure 2.4 Typical Variation of Vortex Burst Location with Angle of Attack[37]
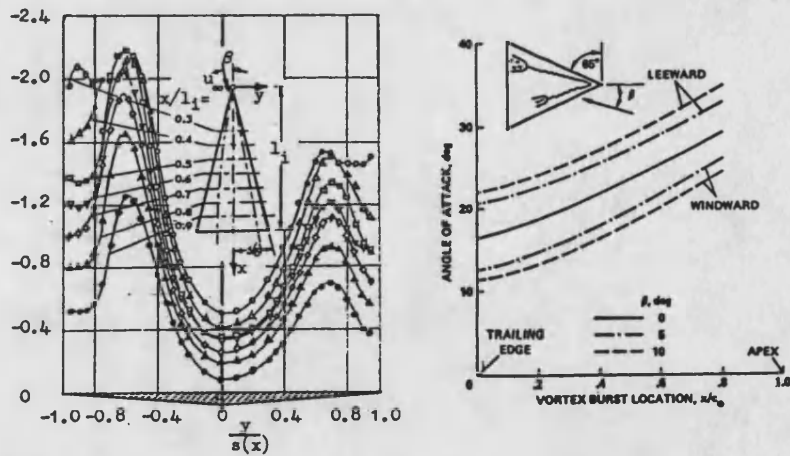
Figure 2.5 Effect of Sideslip on the Vortical Flowfield
a) Upper-Surface Pressure Distribution[28]
b) Vortex Burst Trajectory[21]

37
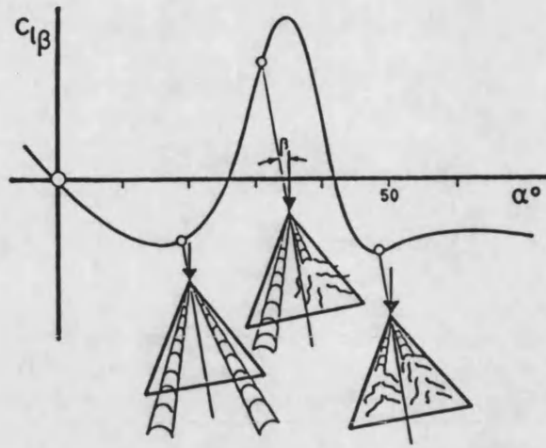
Figure 2.6 Typical 'Effective Dihedral' Characteristics of a Delta Wing[29]
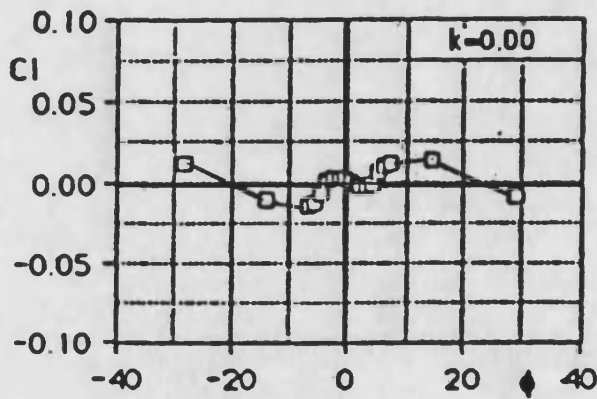
Figure 2.7 Effect of Roll Angle on Roll Moment in the 'Unstable' Angle of Attack Region[30]
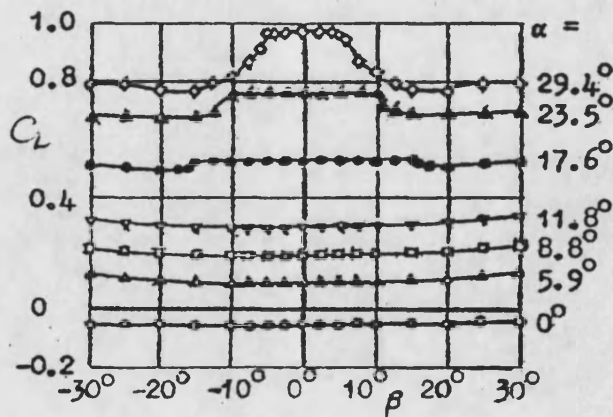
Figure 2.8 Typical Effect of Sideslip and Angle of Attack on Delta Wing Lift[28]
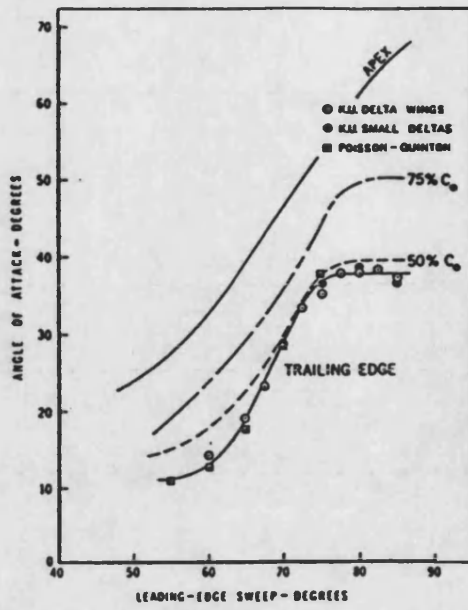
Figure 2.9 Effect of Leading-Edge Sweep Angle on Vortex Burst Trajectory[27]
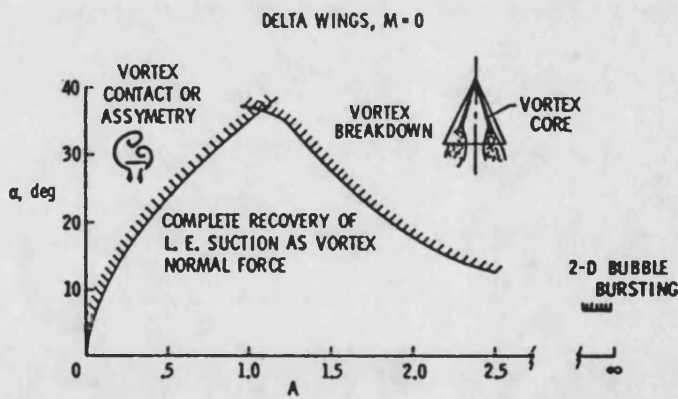
Figure 2.10 Stability Boundaries for Leading-Edge Vortex Flows[32]
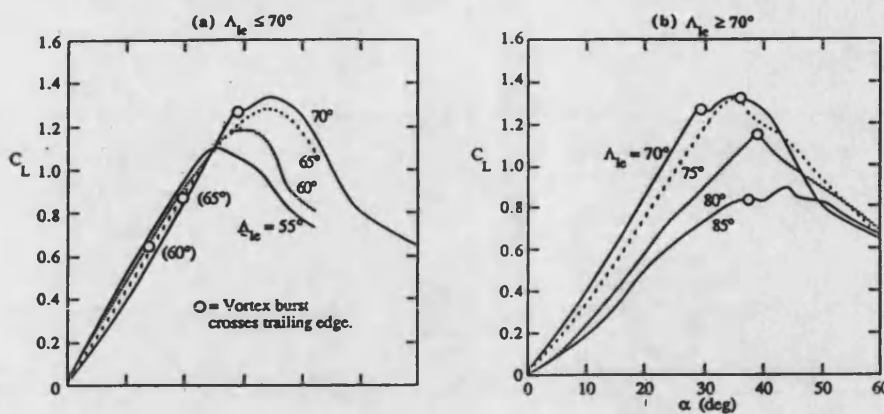
Figure 2.11 Effect of Leading-Edge Sweep Angle on Delta Wing Lift[25,27]
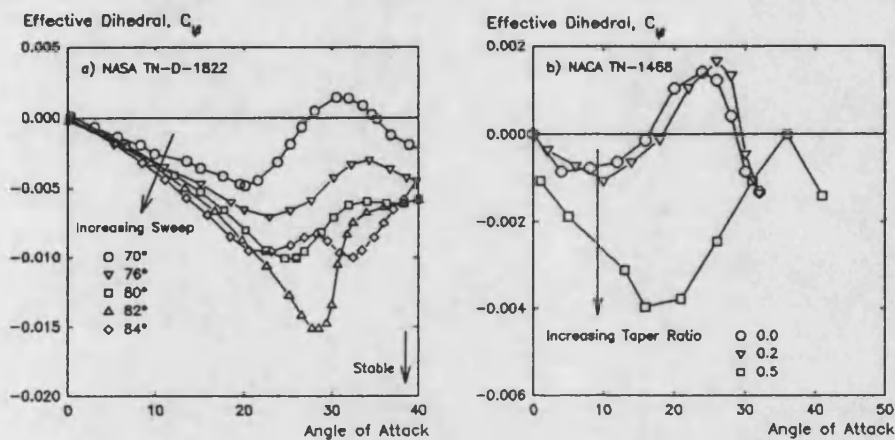
Figure 2.12 Effect of Wing Planform on 'Effective Dihedral'
a) Leading-Edge Sweep Angle[33]
b) Taper Ratio[34]
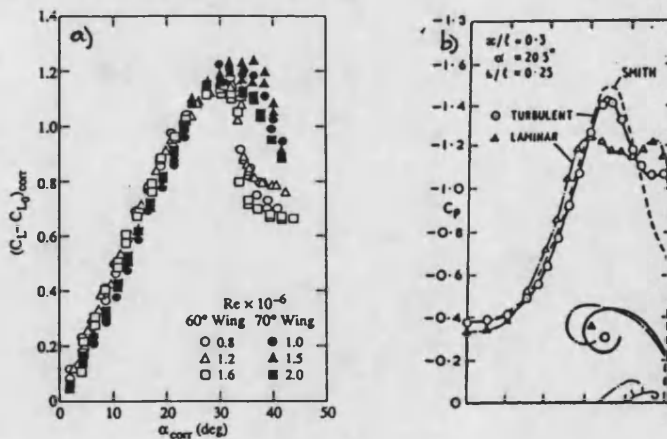
Figure 2.13 Effect of Reynolds Number on Delta Wing Flowfield
a) Lift Curve Slope[37]
b) Upper-Surface Pressure Distribution[21]

40
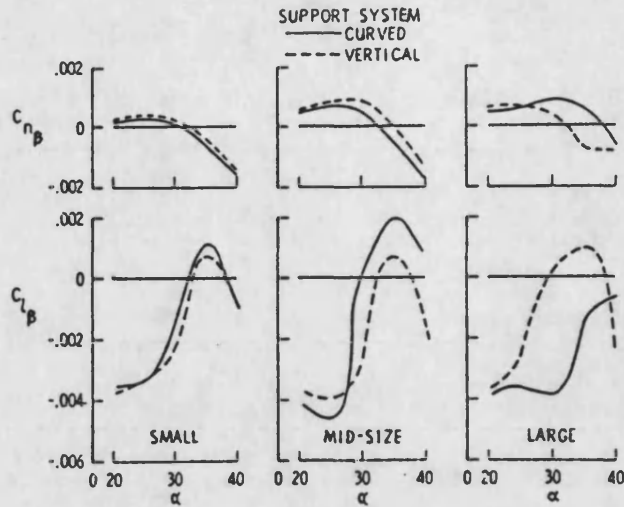
Figure 2.14 Effect of Model Size and Support Interference on Delta Wing Lateral Characteristics[39]
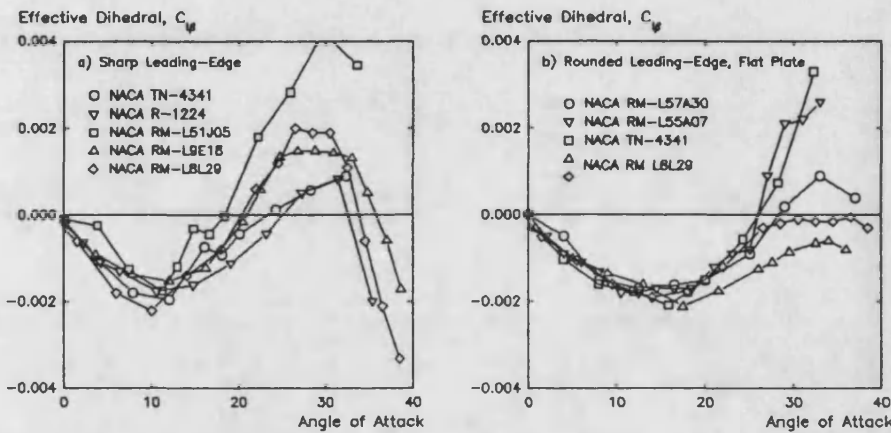
Figure 2.15 Comparison of Published 'Effective Dihedral' Characteristics for 60° Delta Wings
  a) Sharp-Edged Wings
  b) Rounded Leading-Edge, Flat Plate Wings
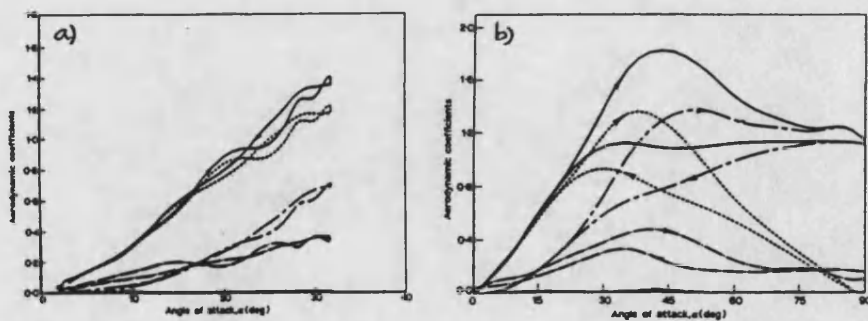
Figure 2.16 Normal Force Response of a 76° Delta Wing to Sinusoidal Pitch Motion, for 0-30° and 0-90° Pitch Angle[45]

41
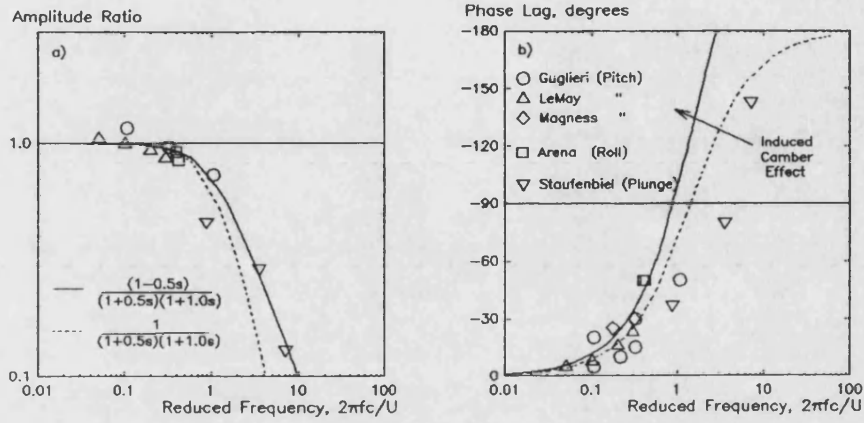
Figure 2.17 Bode Plot Representation of Published Vortex Burst Response to Sinusoidal Wing Motion Data
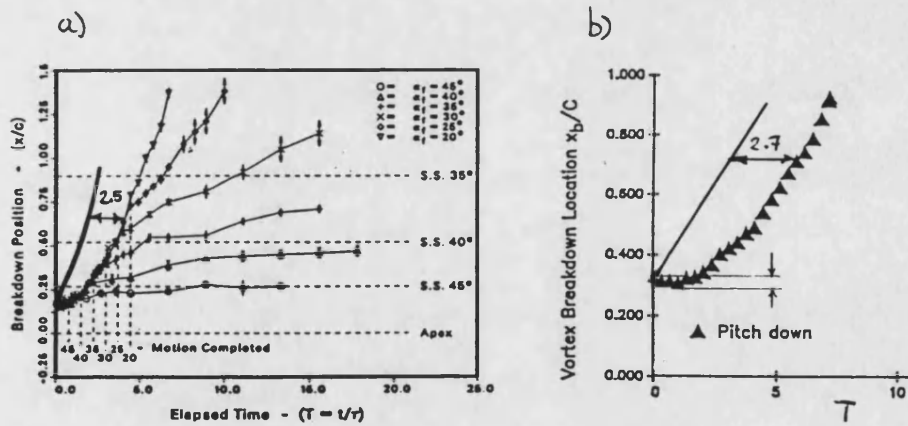
Figure 2.18 Vortex Burst Response to a Ramp Pitch Motion[52,51]

42
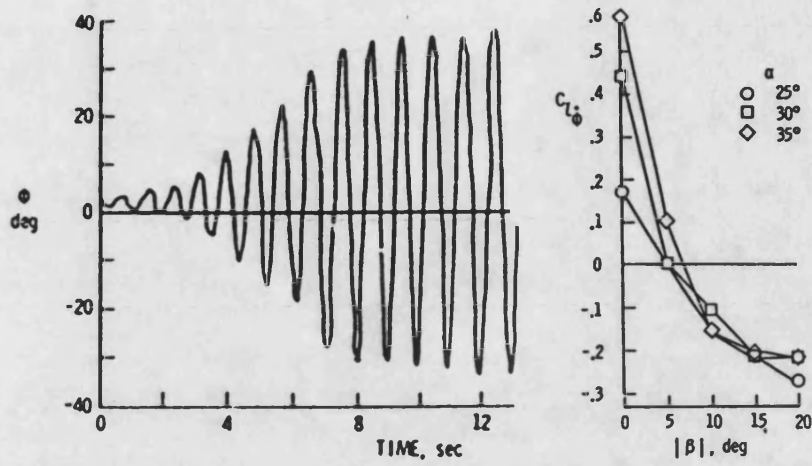
Figure 2.19 Typical Wing Rock Response of an 80° Delta Wing[58]
      a) Roll Time History
      b) Nonlinear Roll Damping Characteristic
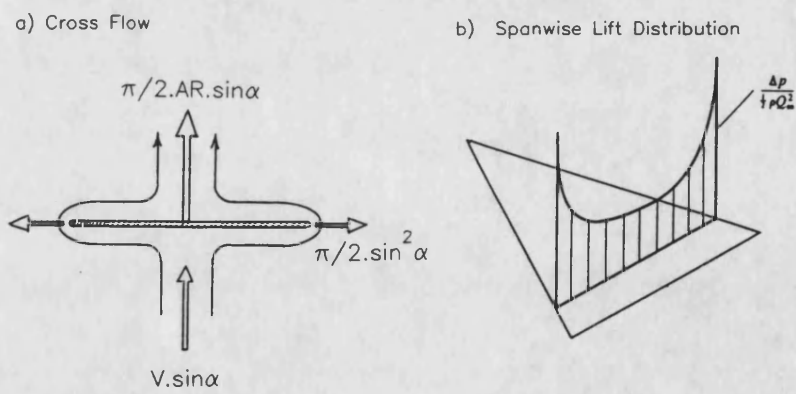
Figure 2.20 'RT Jones' Slender Wing Analysis[66]

43
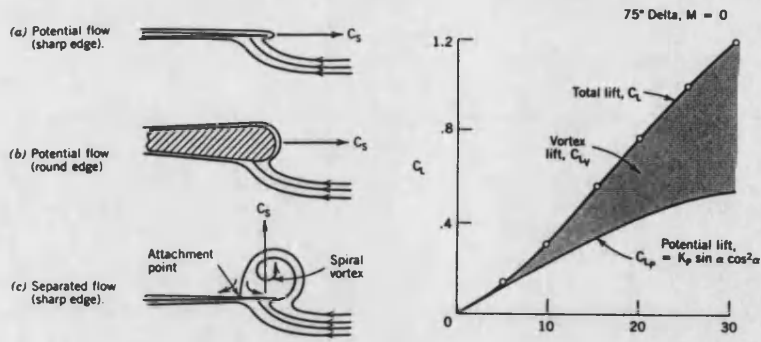
Figure 2.21 The Leading-Edge Suction Analogy[67]
a) Leading-Edge Conditions
b) Contributions to Total Delta Wing Lift
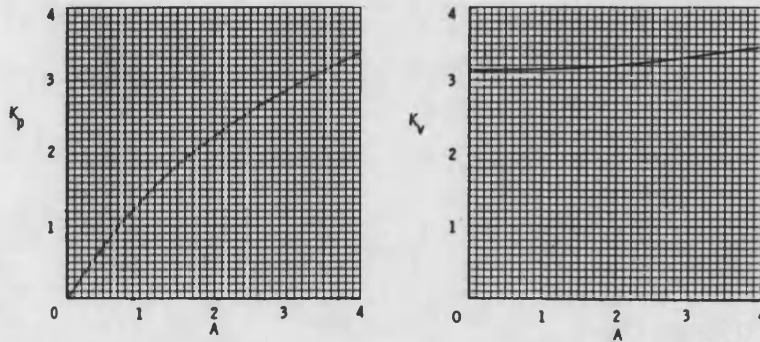
Figure 2.22 Variation of K_p and K_v with Aspect Ratio[32]
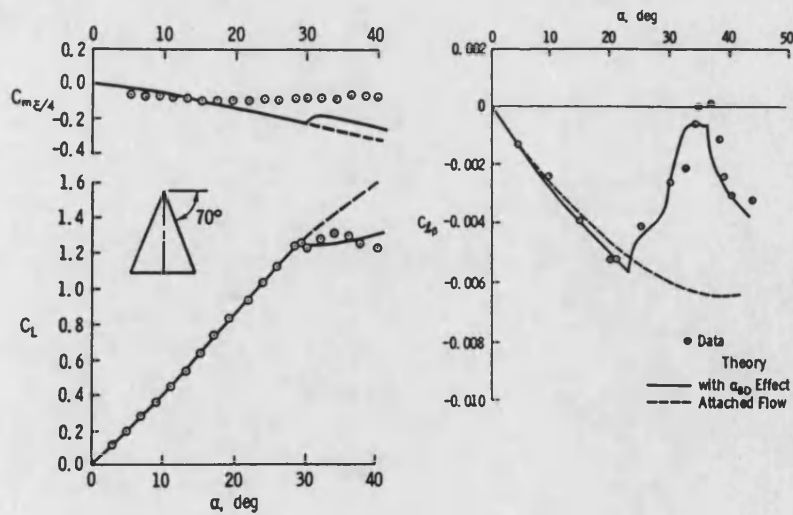
Figure 2.23 Prediction of Effect of Vortex Breakdown on Longitudinal and Lateral Characteristics of a 70° Delta Wing[73]

44
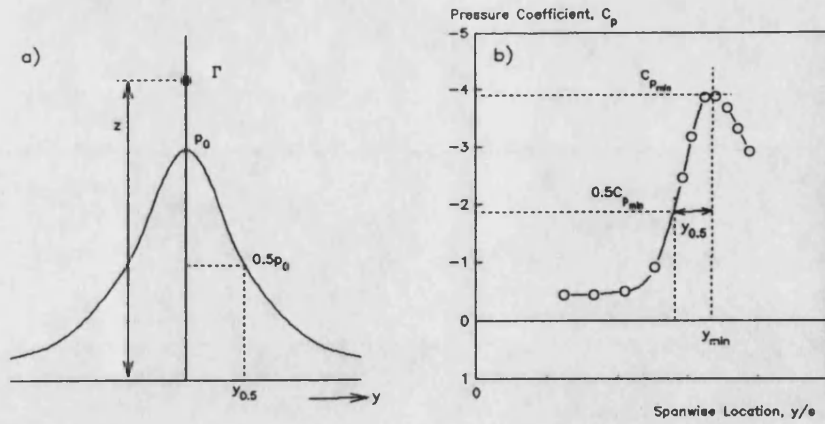
Figure 2.24 Definition of Magnitude and Halfwidth for a Vortex-Induced Suction Peak
   a) Point Vortex over Infinite Plane
   b) Typical Delta Wing Pressure Distribution
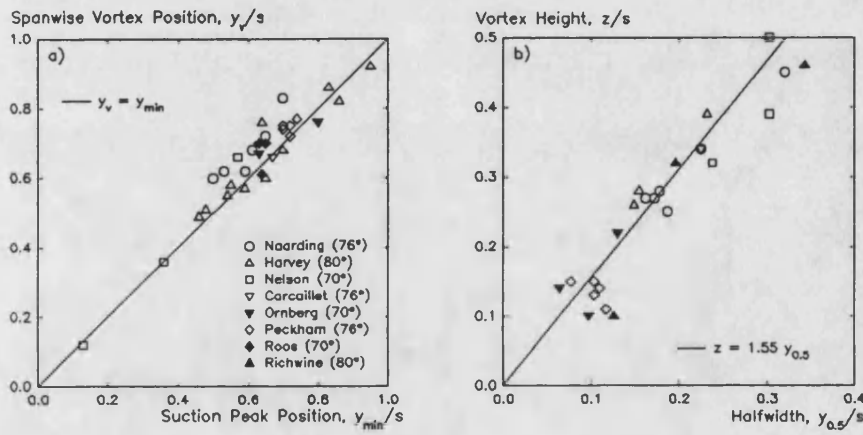
Figure 2.25 Comparison of Experimental Vortex Core Trajectory with Simple Flow Model
   a) Spanwise Location
   b) Core Height
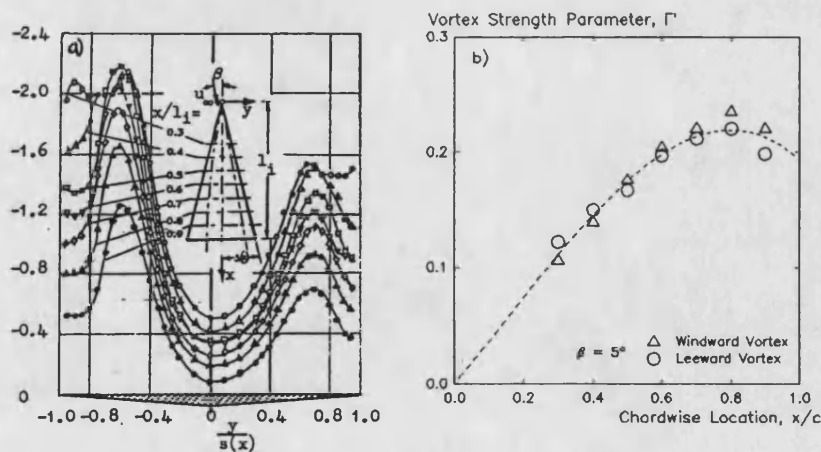
Figure 2.26 Vortex Strength Parameter Applied to Experimental Pressure Distribution Data[28]

45
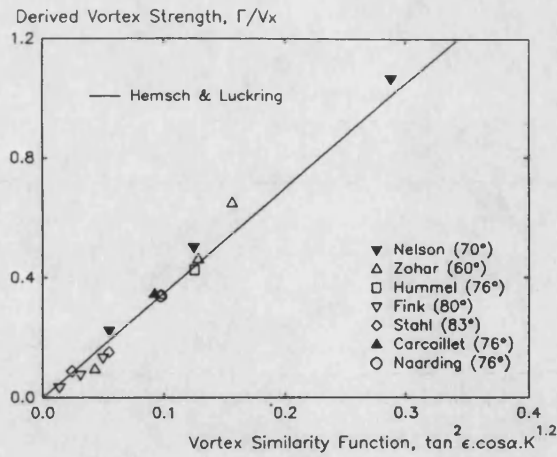
Figure 2.27 Vortex Strength Derived from Experimental Pressure Data Compared with Hemsch & Luckring's Vortex Similarity Parameter
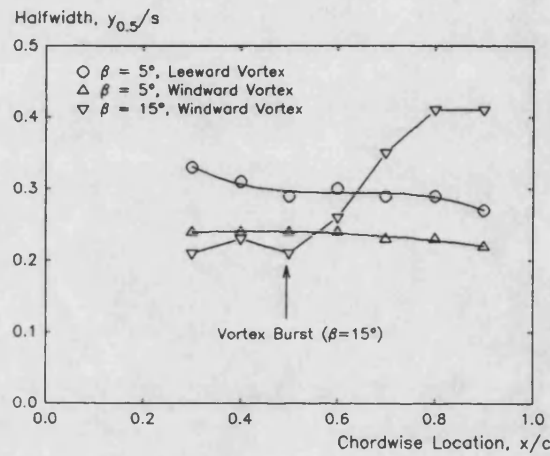
Figure 2.28 Chordwise Variation of Halfwidth Parameter[28]
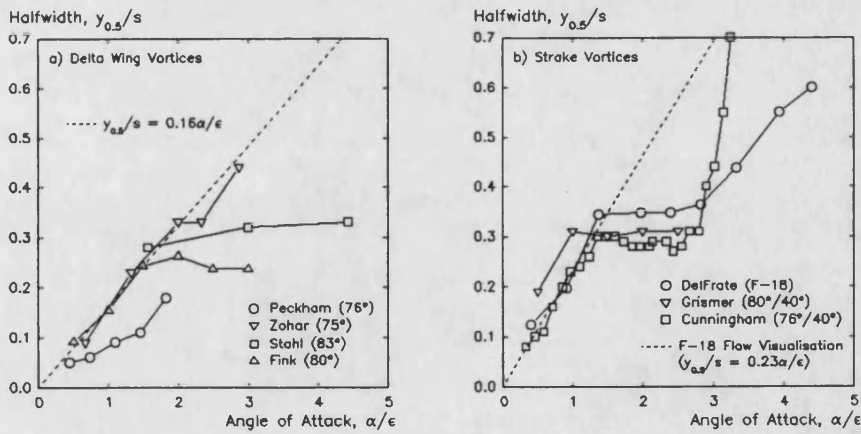
Figure 2.29 Variation of Halfwidth with Angle of Attack
a) Delta Wing Vortices
b) Strake Vortices

46
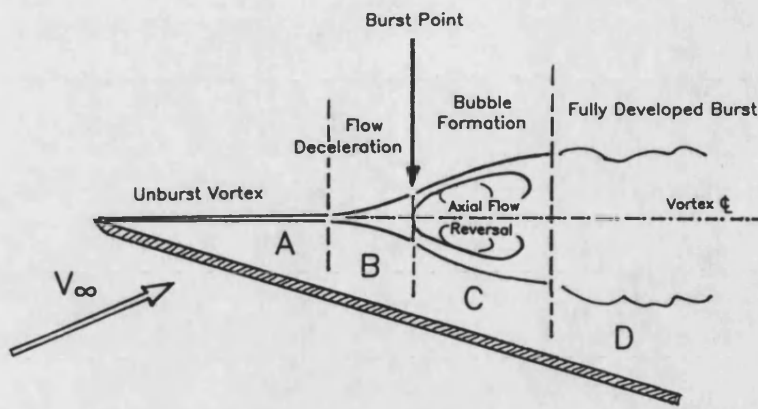
Figure 2.30 Schematic of Vortex Breakdown Process at 'High' Reynolds Number
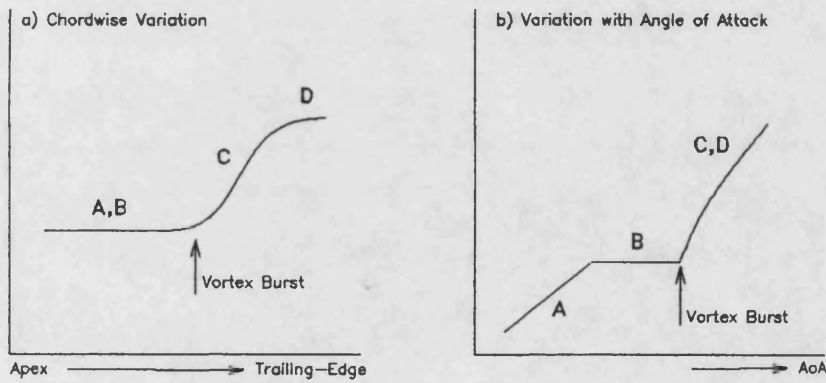
Figure 2.31 Typical Halfwidth Characteristics Related to the Vortex Breakdown Process
a) Chordwise Variation
b) Variation with Angle of Attack

47

CHAPTER 3

TANGENTIAL LEADING-EDGE BLOWING

3.1 Description of the Concept

3.1.1 Influence of Shear Layer Separation Location

For a thin sharp-edged delta wing, the location of the crossflow separation is fixed at the leading-edge, and the strength of the shed vortex is a function of sweep angle and angle of attack[90]. For a rounded leading-edge, however, the separation location is no longer fixed; this provides an additional parameter governing vortex strength, since the shed vorticity is a function (to a first approximation) of the local velocity at separation[102].

The effects of leading-edge roundness and separation location on the vortical flowfield are indicated by the results of Reference 103, a theoretical investigation of the potential flow with separation over a slender wing of elliptical cross-section. Since the original figures were of very poor quality, the relevant results have been replotted in Figure 3.1. These curves are for a non-dimensional angle of attack (α/ε) of 1.5, and are plotted relative to the well-known 'sharp leading-edge' computations of Reference 104. The independent variables were wing thickness/span ratio and spanwise separation location.

Figure 3.1a shows a loss of normal force both with increasing thickness (or leading edge radius) and movement of the separation location away from the tip, due to a reduction in vortex strength. Figure 3.1b indicates an inboard and downward motion of the vortex core as the separation location is moved inboard. Although for an ideal flow case, these computations demonstrate that a relatively small shift of the leading-

edge separation location (3% of the semi-span in this case) can have an extremely significant effect on the vortical flowfield over a delta wing.

3.1.2 Control of Leading-Edge Separation

It is clear that control of the separation location offers considerable aerodynamic 'leverage', if the adverse crossflow pressure gradient around the leading-edge can be modified efficiently. An appropriate technique is the application of Coanda jet blowing, as used on circulation control aerofoils[105]. This entails injecting a thin tangential jet into the crossflow boundary layer on the leading-edge, as illustrated in Figure 3.2a.

The convex surface stimulates strong attachment (the Coanda effect) and enhances the mixing rate of the jet with the crossflow, giving a very efficient transfer of momentum to the boundary layer. The end result is an inboard shift of the separation location, with consequent effects on the vortical flowfield very similar to the ideal flow case discussed in the previous section; that is, a reduction in vortex strength and an inboard and downward movement of the vortex core[106]. The concept of 'crossflow equilibrium' has been used to describe this outcome, where the vortex core and feeding sheet develop forces which are balanced by the pressure field due to the leading-edge separation.

This technique is referred to as Tangential Leading-Edge Blowing (TLEB), and the general effects on the vortical flowfield at low angles of attack are depicted in Figure 3.2b. At high angles of attack, the presence of the vortex burst phenomenon over the wing complicates the response; burst location is also affected by blowing, and a strong coupling between the vortices becomes apparent when blowing is applied asymmetrically.

49

3.1.3 Characteristics of TLEB

TLEB is a very efficient technique for modifying the vortical flow over a delta wing, and as such offers considerable potential for application to aircraft manoeuvring at high angles of attack. However, the aerodynamic characteristics of TLEB are complex and as yet not fully explored. As a starting point for the results presented in this thesis, the following sections will summarise previous published and unpublished work on the characteristics of symmetric, asymmetric and transient blowing.

3.2 Effects of Symmetric Blowing

3.2.1 General Features

Initial investigations into TLEB were undertaken at Stanford University, on half-models[11,16] of various cross-sections and sweep angles, so that blowing conditions were (effectively) symmetric. Instrumentation consisted solely of upper and lower surface pressure tappings, hence aerodynamic forces were derived from surface integration of the pressure distributions. Subsequent tests with a sting-mounted full-span model[18] confirmed the general features of the response to symmetric blowing and enabled direct force measurements to be made.

The movement of the leading-edge separation location with blowing is similar to the result of a reduction in angle of attack, and this similarity was shown to extend to the resulting vortical flowfield[11]. This is illustrated by Figure 3.3, showing the effect of (symmetric) TLEB on integrated sectional normal force, jet-induced contribution excluded. A shift to the right of the non-linear vortex lift component[67] is evident, analogous to a reduction in the 'effective angle of attack' of the vortical flow as blowing is increased.

If this analogy held at higher angles of attack, it was postulated, TLEB could also

affect the vortex burst phenomenon. This was subsequently observed experimentally[107], with increasing symmetric blowing moving the burst aft (to the extent of removing the burst from the wing altogether), thus reinforcing the 'effective vortex angle of attack' analogy. Reference 107 also introduced the concept of 'longitudinal equilibrium', which simply states that for any given angle of attack there is a unique vortex burst location for each vortex strength distribution.

The effects of symmetric TLEB were thus described in terms of changes in the 'crossflow equilibrium' (Section 3.1.2) and 'longitudinal equilibrium' conditions. The overall response of the wing flowfield was analogous to reducing the effective angle of attack of the vortex flow component.

3.2.2 Vortical Flowfield

Changes in the vortical flowfield are indicated by the response of the wing upper surface pressure distributions, in particular the vortex-induced suction peak. A typical response to symmetric blowing on a full-span wing at low and high angles of attack is shown in Figure 3.4, from Reference 18. At low angles of attack (Figure 3.4a) the vortex-induced peak subsides as vortex strength reduces with increasing blowing. At high angles of attack (Figure 3.4b) the vortex is burst and the suction peak is weak or non-existent. With increasing blowing the peak reestablishes, as the burst passes over the measurement location. It should be noted that this model had no tappings on the leading-edge, thus the large suction peak induced in this region by the jet is not seen in Figure 3.4.

An alternative representation of the response is given by Figure 3.5[18], showing the upper surface pressure response at a single tapping on or near the vortex centreline. At low angles of attack the suction falls off rapidly with increasing blowing, as seen

in Figure 3.4a. At high angles of attack the suction peak initially increases as the burst passes, then falls off in a similar manner to the low angle of attack case.

3.2.3 Aerodynamic Loading

Initial half-model tests[16] derived aerodynamic loads from pressure integration; a process which inevitably introduced uncertainties due to limited coverage (particularly near the trailing edge) and to the very high pressure gradients near the leading-edge when blowing. These uncertainties limited the usefulness of the results to a comparison of blowing on and off response. The later full-span tests used an integral sting balance to measure normal force, pitching moment and roll moment directly, although the high blockage level (≈17%) hindered comparison with published delta wing data.

For symmetric blowing, only the normal force and pitching moment responses are relevant, and these are shown in Figure 3.6, for increasing blowing at constant angle of attack[108]. It can be seen that for normal force the initial change with blowing is small, since the reduction in vortex contribution is counterbalanced by the increase in jet-induced leading-edge suction. The point at which the normal force reaches an almost constant value is also of interest. At low angles of attack this signifies that the flow has become fully attached over the upper surface, that is that the leading-edge vortex has been completely suppressed. At high, 'post-stall' angles of attack this point corresponds to a completely unburst vortex. The pitching moment data shows a similar 'plateau' effect, although with a more marked initial change with blowing.

The general effect of symmetric blowing is to reduce the lift curve slope and to increase stall angle, both direct consequences of the reduction in effective vortex angle of attack.

3.2.4 Transient Blowing

No transient force data has been published, but surface pressure response to step changes in blowing on a half-model has been extensively reported[11,18,107]. The basic experimental work was reported in Reference 11 and is summarised by Figure 3.7, in which pressure time histories are compared with a quasi-steady-state response.

For 'unburst' initial conditions (Figure 3.7a) the response is rapid, of the order of one convective length. For 'burst' initial conditions (Figure 3.7b) the overall response is slower, of the order of five to ten convective lengths, but exhibits an initial rapid change in the opposite direction to the quasi-steady trend.

The presence of two different time scales was attributed to the combination of two separate responses: the vortex strength and the burst location. The response of the vortex strength is a function of the 'crossflow equilibrium' condition, and is relatively rapid. The burst location movement is caused by a change in the 'longitudinal equilibrium' condition; the reduced longitudinal velocity (including regions of reverse flow) at high angles of attack and longer length scale give a much slower response time relative to the crossflow case. Reduced time constants for the pressure response were of the order of 0.5 (unburst) and 2-3 (burst), broadly consistent with published results from tests on pitching and rolling motions of delta wings (Section 2.4.2).

The initial reversal in response for the 'burst' case of Figure 3.7b can now be seen to be due to a rapid reduction in overall vortex strength followed by a slower increase in local strength as the burst passes the measurement location.

3.3 Effects of Asymmetric Blowing

3.3.1 General Features

The original half-model TLEB tests indicated considerable potential for roll moment generation with asymmetric (one-sided) blowing. However, the implied symmetry and relatively thick sidewall boundary layer made interpretation of the results uncertain, hence a full-span experiment was undertaken[108]. This wing had a similar planform, independent blowing control on each leading-edge, a three-component sting balance for load measurement and some limited pressure instrumentation.

Symmetric blowing results were comparable to the previous half-model tests, allowing for differing blockage and mounting arrangements; however, asymmetric (one-sided) blowing exhibited some wholly unexpected characteristics.

At low ('pre-stall') angles of attack, simple superposition of asymmetric blowing responses (forces and pressures) gives the symmetric results. At high ('post-stall') angles of attack, however, superposition is no longer valid, due to a strong coupling between the vortices when blowing asymmetrically. Previous attempts to elucidate the nature of this coupling will be described in the following sections.

3.3.2 Vortical Flowfield

The coupling between blown and unblown vortices is most evident in the response of the upper-surface pressure distributions.

For low angles of attack (Figure 3.8), blowing on one side reduces the magnitude of the adjacent vortex-induced suction peak, at almost the same rate as symmetric blowing, while the unblown suction peak is essentially unchanged. At high angles of attack, with the vortex burst on the wing, blowing on one side (Figure 3.9a) initially unbursts the opposite vortex. No change on the blown side is seen until a very high blowing level is attained, whereupon this vortex also unbursts. Figure 3.9b

demonstrates that the 'unbursting' process requires higher blowing levels than for the equivalent symmetric case.

Flow visualisation[108] indicated a shift of the flow 'centreline' on the wing away from the blown leading-edge over the complete angle of attack range investigated, and confirmed the premature unbursting of the unblown vortex.

3.3.3 Roll Moment Characteristics

The aerodynamic coupling described above is also evident in the force and moment characteristics of asymmetric blowing. The most critical, and the clearest, is the roll moment response shown in Figure 3.10.

It was clear that the roll characteristics of asymmetric TLEB display sign reversals and discontinuities undesirable for a flight vehicle control system, but the potential to generate very high roll moments at high angles of attack encouraged further investigations. The underlying mechanisms of roll moment generation were unclear, but were postulated[108] to be a balance between the 'blown side UP' jet-induced leading-edge suction, the 'blown side DOWN' reduction in blown vortex strength and an undetermined effect of the vortex coupling (probably an asymmetry in burst location).

An extension of the roll moment measurements required for assessment of TLEB as a control system was an examination of the effect of roll angle[17], giving the results shown in Figure 3.11 for low and high angles of attack. In general, the influence of increasing roll angle is to increase 'recovery' control power and to reduce 'manoeuvre' roll moments, with the consequence of a limited roll trim capability (of the order of ±7°).

3.3.4 The 'Effective Sideslip' Analogy

In an attempt to clarify the vortex coupling phenomenon, Reference 109 postulated an analogy between the effects of asymmetric blowing and of sideslip, prompted by the observed shift in the flow 'centreline' noted in Section 3.3.2 and resulting asymmetry in burst location. Prior to commencing an experimental investigation, the authors examined the 'effective sideslip' analogy from a conceptual viewpoint[109]. On the basis of the limited experimental data available, the analogy appeared to offer a good qualitative description of the coupling phenomenon. In particular, the similarity of the roll moment characteristics of sideslip and asymmetric blowing was encouraging (Figure 3.12).

The basic elements of the analogy were that the centreline shift with asymmetric blowing produces a change in effective leading-edge sweep angle (increasing sweep on the unblown side and reducing sweep on the blown side), in addition to the reduction in effective vortex angle of attack on the blown side only. The nett result is that the aft shift of the vortex burst due to blowing is counteracted by the earlier onset due to the reduced effective leading-edge sweep, while the unblown burst is delayed by the increasing effective sweep on that side.

The differing behaviour with angle of attack may be explained by noting that at low angles of attack the burst displacement due to change in sweep angle is very much smaller than that due to an angle of attack change, while at higher angles of attack the two effects are more nearly equal. Further, at low angles of attack the effect of sweep angle on the wing aerodynamic characteristics is relatively small. Figure 3.13 is an attempt to illustrate this, adapted from Reference 109.

Vortex burst location is plotted in the form of a carpet plot, as a function of angle of

attack and leading-edge sweep. The vertical scale is extrapolated forward of the wing apex; in this region the 'burst location' gives an indication of the stability of the vortical flow. Superimposed on the carpet plot is a contour plot of normal force coefficient, again as a function of leading-edge sweep and angle of attack. The assumption behind this figure is that the wing flowfield may be split into right and left halves, and that the roll moment contribution of each half may be derived from the normal force characteristics of the equivalent full-span wing. This was a gross simplification, but gave a reasonable match to sideslip-induced roll moments.

The arrows on Figure 3.13 show the postulated effect of asymmetric blowing on the blown and unblown wing halves. At low angles of attack the increase in leading-edge sweep of the unblown side has little effect on the normal force (and hence roll moment) contribution, giving the apparently uncoupled force behaviour noted in Section 3.3.1. The vortex burst is near or off the wing trailing edge, so no coupling was seen in the pressure measurements which were made nearer the apex (Figure 3.8). Although the plot indicates a loss in normal force on the blown side, this is counterbalanced by the jet-induced suction not accounted for in the analogy. The greater moment arm of the leading-edge suction gives a nett 'blown side UP' moment. At higher angles of attack on the blown side, the effect of reducing effective vortex angle of attack and leading-edge sweep cancel out, giving no change in the burst location. The forward shift in burst location on the unblown side gives an increase in normal force and hence a 'blown side DOWN' roll moment contribution, thus producing the reversal of operation seen in Figure 3.9. The overall roll moment is dominated by the unblown side, giving a reversal of sign relative to the low angle of attack case.

An application of the analogy to the effect of blowing with roll angle also gave a

57

good qualitative fit to observed characteristics; due to a lack of data on the magnitude of the jet-induced leading-edge suction contribution, no quantitative predictions were made.

3.4 CFD Investigations

3.4.1 General Survey

In conjunction with experimental work, considerable effort has been applied to computational investigations of tangential blowing at Stanford University, both on forebodies and delta wing leading-edges. These studies have taken two paths; a low-order panel method for dynamic simulation work[110] and a more complex thin-layer Navier-Stokes solution[111].

3.4.2 Panel Methods

The motivation behind the development of a panel method was to keep computation times to a minimum to facilitate incorporation in a dynamic simulation of the application of TLEB as a roll control system[110]. The code developed was similar to the vortex-lattice methods commonly used for prediction of the unsteady, separated flows over manoeuvring delta wings[112], but with the addition of leading edge blowing. Rather than simulate the jet flow directly, the local effects were modelled by modifying the Kutta condition to reduce the vortex strength shed into the wake, and at the same time duplicate the recovery of a potential flow component at the leading edge. Computed spanwise pressure distributions resembled previous experimental results, though no direct comparisons were made, and no force results published.

A dynamic simulation of the HP-115 with TLEB showed considerable capability for roll control at high angle of attack. However, the lack of experimental confirmation

58

and representation of vortex burst make this conclusion of limited value. Unpublished investigations at Bath University with this code revealed that it requires considerable 'adjustment' to give reasonable results; in particular, the initial separation angle of the leading-edge vortex sheet is critical.

3.4.3 Thin-Layer Navier-Stokes Solutions

A more rigorous solution requires a viscous method to determine the exact location of the primary separation location, since this plays a critical role in the subsequent vortex trajectory (Section 3.1.1). A solution of the thin-layer Navier-Stokes equations is reported in reference 111, for the full-span wing geometry of Reference 108.

The geometry of the wing in the region of the leading-edge slot is simplified by the use of the 'actuator plane' concept for representation of the wall jet. Despite this, run times are considerable, of the order of 90 hours on a Cray supercomputer.

Typical flow patterns with and without blowing are shown in Figure 3.14. Surface pressure and normal forces changes are not particularly well predicted, though roll moment characteristics do show a much better agreement. The occurrence of a vortex burst-like instability in the solution results in the capture of 'roll reversal' at high angles of attack (Figure 3.15). A very strong secondary separation is predicted which was not observed experimentally, suggesting a problem with the boundary layer turbulence model, and hence in turn casting some doubt on the validity of the jet modelling.

3.5 Summary

Previous experimental and computational investigation of Tangential Leading-Edge Blowing had shown a considerable potential for modification of vortical flows at high

angles of attack and hence for generation of control forces in the post-stall flight regime. However, the response of the flowfield is complex and strongly coupled, leading to sign reversals and discontinuities. The underlying mechanisms were unclear, although CFD methods did offer some hope of illumination of the complex nature of the problem. A role thus appeared to remain for a simpler, experimental, determination of the varying contributions to the flowfield response.
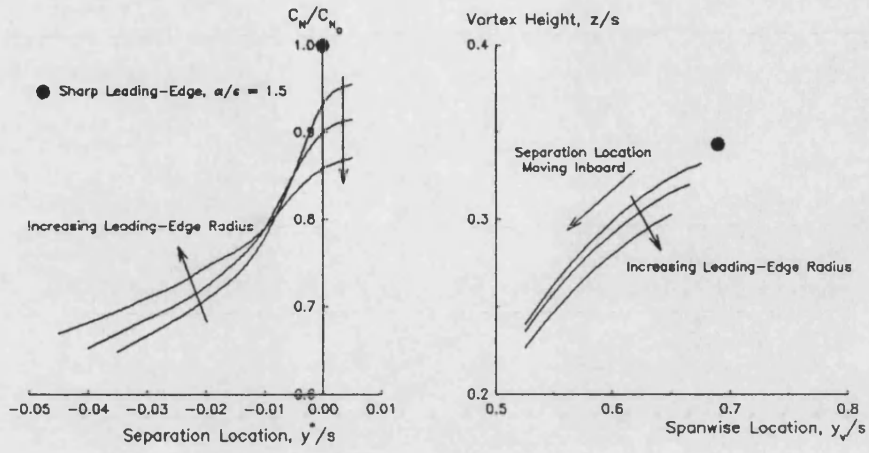
Figure 3.1 Effect of Leading-Edge Radius and Separation Location on Vortex Lift and Core Trajectory[103]
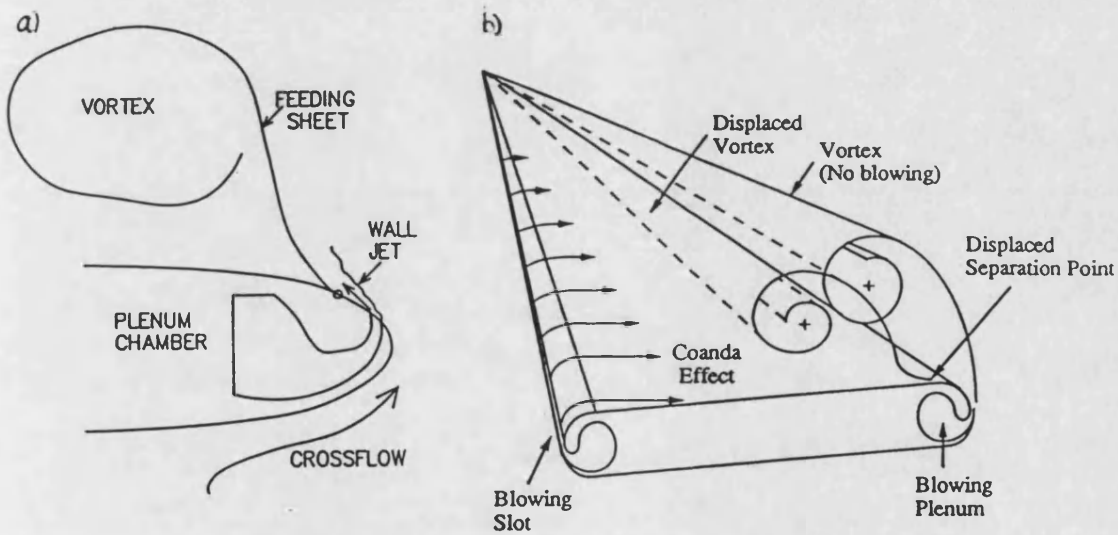
Figure 3.2 Tangential Leading-Edge Blowing

* The contribution from leading edge suction due to attached jet is excluded.
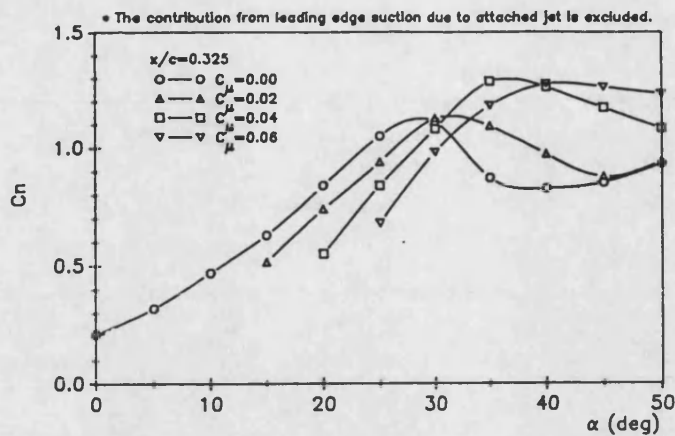
Figure 3.3 Effect of Symmetric Blowing on Pressure-Integrated Upper-Surface Normal Force[11]
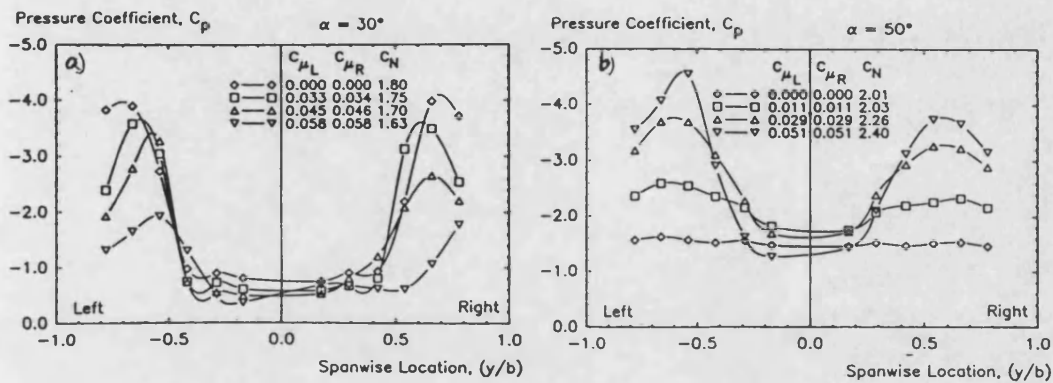
Figure 3.4   Effect of Symmetric Blowing on Inboard Upper-Surface Pressure Distributions[18]
a) 'Pre-Stall' Angle of Attack
b) 'Post-Stall' Angle of Attack
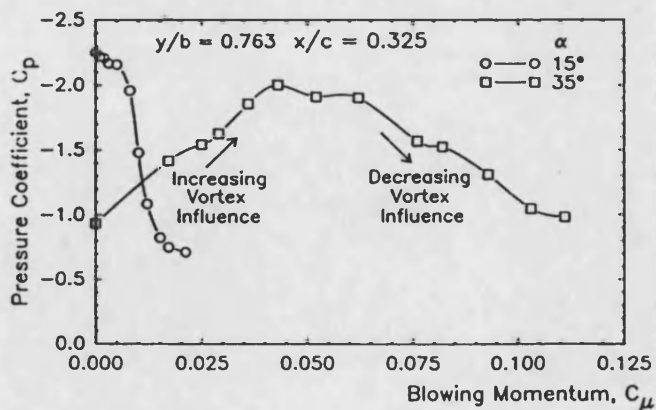
Figure 3.5   Characteristic Upper-Surface Pressure Response to Increasing Blowing, at a Fixed Location[18]

62
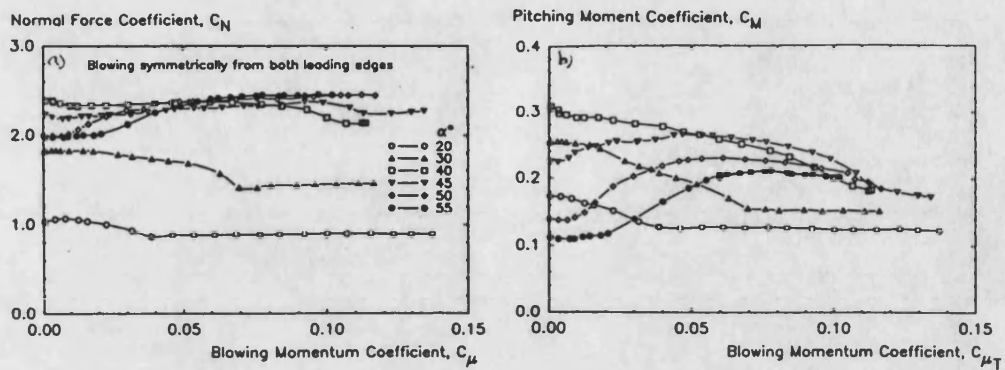
Figure 3.6 Response of Longitudinal Aerodynamic Characteristics to Increasing Symmetric Blowing at Constant Angle of Attack[108]
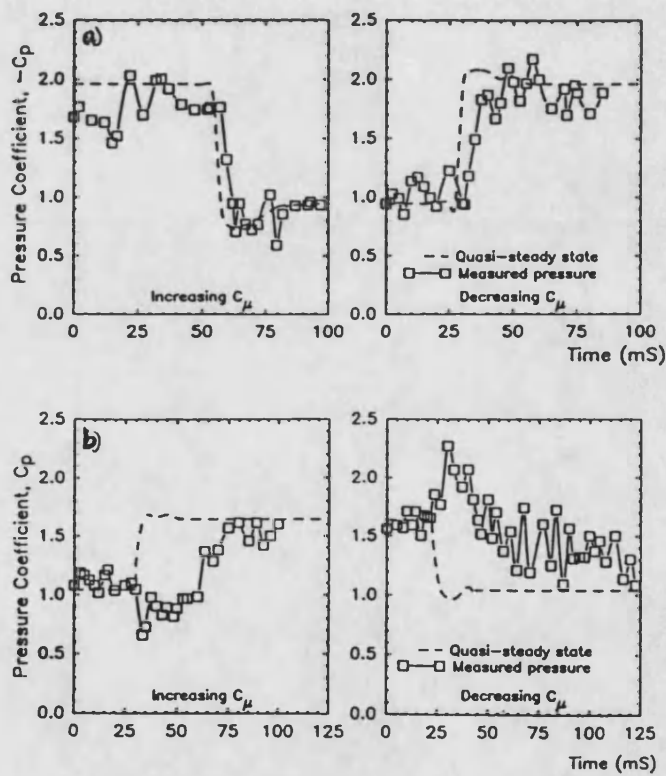
Figure 3.7 Transient Upper-Surface Pressure Response to a Step Change in Symmetric Blowing[18]
a) 'Pre-Stall'
b) 'Post-Stall'

63
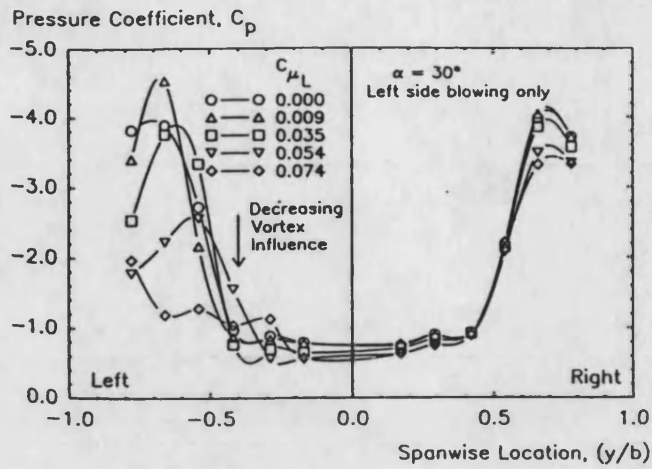
Figure 3.8 Effect of Asymmetric (Left-Side) Blowing on Upper-Surface Pressure Distribution at a 'Pre-Stall' Angle of Attack[108]
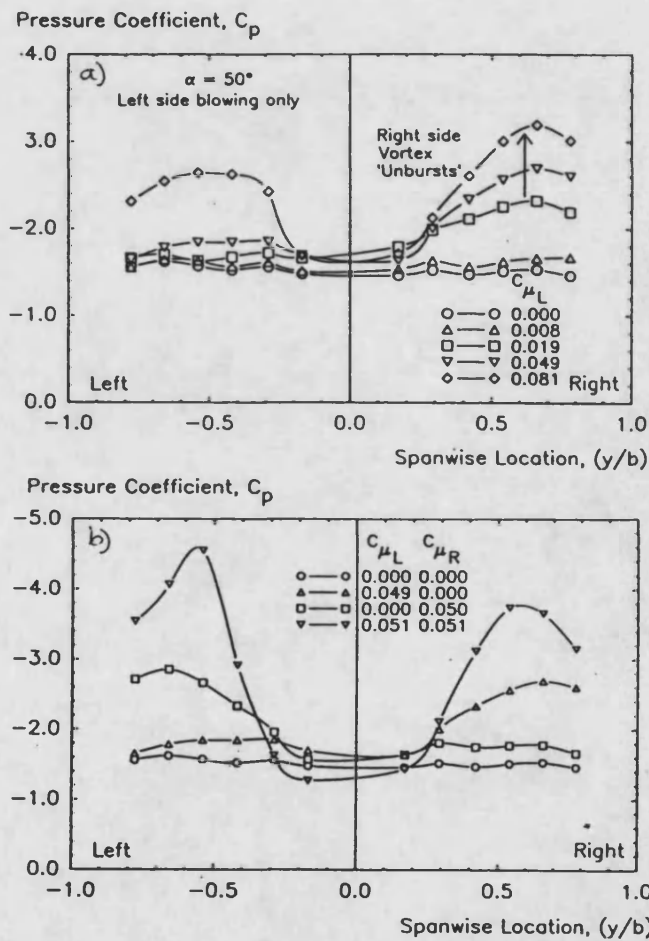
Figure 3.9 Effect of Asymmetric Blowing on Upper-Surface Pressure Distribution at a 'Post-Stall' Angle of Attack[108]
a) Left-Side Blowing
b) Left and Right-Side Blowing Compared with Symmetric Case

64
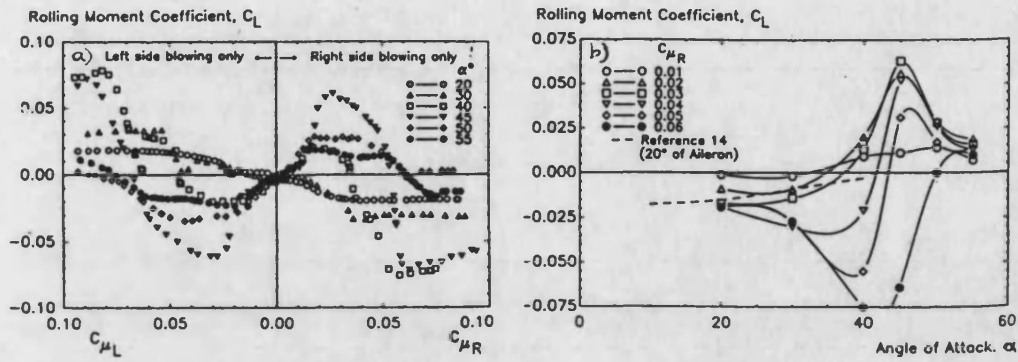
Figure 3.10 Roll Moment Characteristics of Asymmetric Blowing[108]
a) Varying Blowing, Constant Angle of Attack
b) Constant (Right-Side) Blowing, Varying Angle of Attack
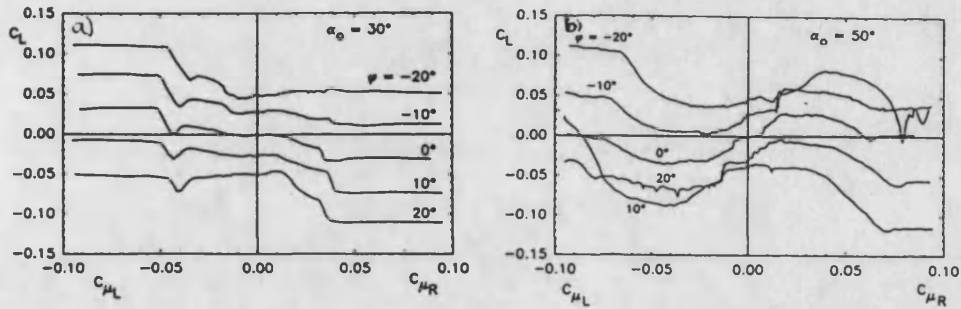
Figure 3.11 Effect of Roll Angle on Asymmetric Blowing Roll Moment Characteristics[17]
a) 'Pre-Stall' Angle of Attack
b) 'Post-Stall' Angle of Attack
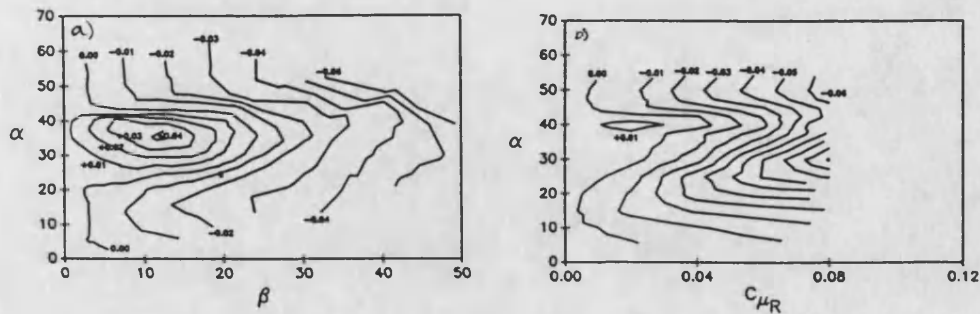
Figure 3.12   Similarity of Roll Moment Characteristics due to Sideslip and Asymmetric Blowing[109]

65
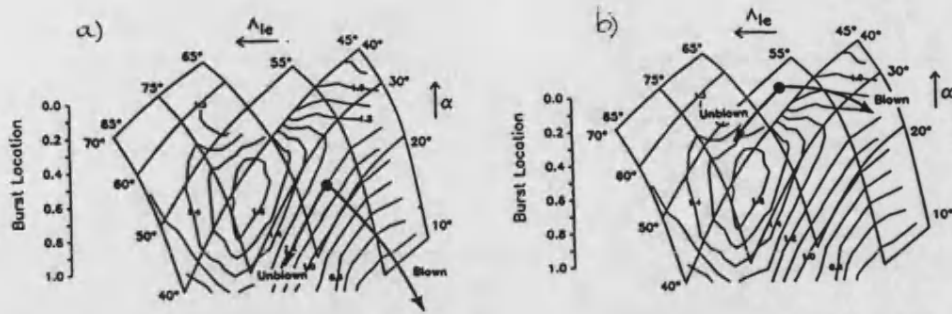
Figure 3.13 The 'Effective Sideslip' Analogy[109]
a) 'Pre-Stall' Angle of Attack
b) 'Post-Stall' Angle of Attack
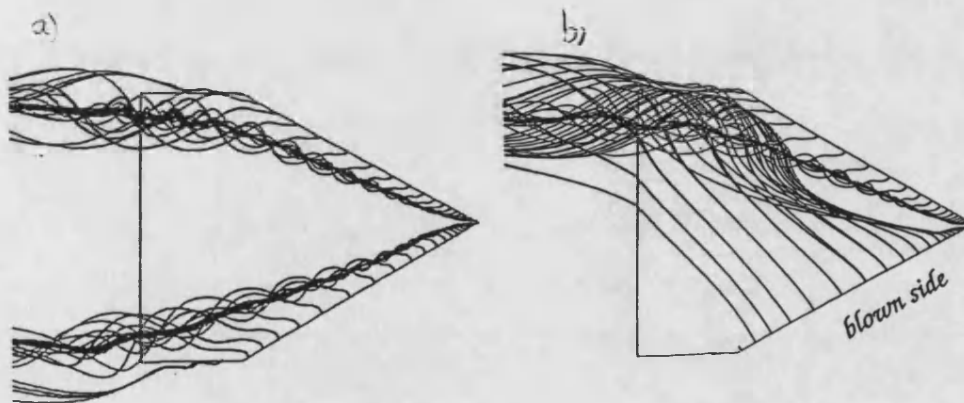
Figure 3.14 Computed Flow Patterns over a Blown Delta Wing[111]
a) Blowing Off
b) Right-Side Blowing
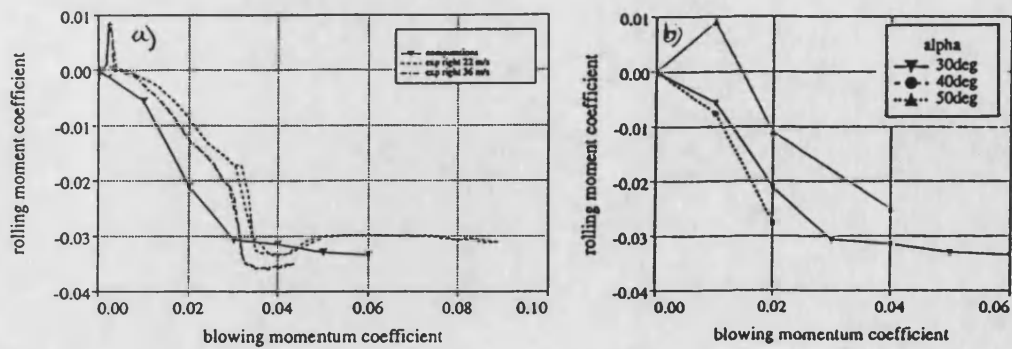
Figure 3.15 Computed and Experimental Roll Moment Characteristics of Asymmetric Blowing[111]
a) Comparison with Experiment at 30°
b) Computational Prediction of Angle of Attack Effects

CHAPTER 4

EXPERIMENTAL APPARATUS

4.1 High Angle of Attack Model Support System

4.1.1 General Description

The very high steady and unsteady loads anticipated during high angle of attack testing of delta wings[113] precluded the use of the conventional six-component balance installed in the University of Bath 2.1m x 1.5m low-speed wind-tunnel. As a result, a completely new model support system (Figure 4.1) was developed for this programme.

A novel pantograph mechanism[114] was designed, which was capable of rotating a sting-mounted model in pitch and roll about a fixed point on the wind-tunnel centreline, thus reducing asymmetric blockage and facilitating laser access for flow visualisation and LDV measurements. This rig now forms a permanent part of the University's wind-tunnel facilities, and has been used in a number of other studies[9,115] into high angle of attack flows.

4.1.2 The 2.1m x 1.5m Wind-Tunnel

The 2.1m x 1.5m wind-tunnel is a closed-return dual-purpose facility, with a 'high-speed' (45ms^{-1}) aeronautical working section and a 'low-speed' (12ms^{-1}) industrial working section. Prior to testing, the working section was calibrated[116]. A rake survey yielded the dynamic pressure variation for an empty tunnel, shown in Figure 4.2a as a ratio of the centreline value, with the dimensions of the proposed wing also indicated. In terms of wing coordinates, there is a small velocity gradient from trailing-edge to apex, but almost none from tip to tip.

Centreline turbulence intensity was measured with a hot-wire probe (Figure 4.2b). At typical test conditions turbulence intensity is of the order of 0.5%; not excessive, and unlikely to have a significant effect on the inherently unsteady flow around a delta wing at high angles of attack.

4.1.3 Support System Requirements

Basic design considerations for the model support system were that it should be capable of rigidly supporting a 60° delta wing of reasonable size and rotating it through 0° to 90° in pitch and ±30° in yaw, at tunnel speeds of upto 45ms^{-1}. In view of the sensitivity of the vortex burst to flow boundary conditions[38] it was felt to be desirable for the model to remain on or near the centreline throughout its' full range of movement, thus minimising asymmetric blockage effects, and for a minimum of support structure to impede the wing wake[39]. Subsidiary operational requirements were provision of an air supply for blowing, computer control of model attitude, and ease of removal (to maximise tunnel utilisation).

4.1.4 Rig Configuration

The required angle of attack and sideslip range may be achieved with a combination of pitch and roll, since:

$$\alpha_t = \tan^{-1}(\cos\phi.\tan\theta)$$

$$\beta_s = \sin^{-1}(\sin\phi.\sin\theta)$$

Thus 0° to 90° in pitch and ±180° in roll (about the body axis) gives a ±90° range in both angle of attack and sideslip. This is achieved with a pantograph pitch mechanism (Figure 4.3) with a model sting-mounted in roll bearings.

68

This configuration has a number of advantages. The model rotates about a fixed point on the tunnel centreline, minimising asymmetric blockage and facilitating LDV measurements. The geometry is arranged so that the centre of rotation is near the model aerodynamic centre, resulting in low actuation loads. The 'parallel arm' layout keeps angular deflections under load to a minimum, since the fore and aft members deflect equally, so that a simple static calibration of pitch angle is all that is required. A particularly desirable feature of this mechanism for high angle of attack testing is that the structure moves completely clear of the model wake with increasing pitch angles.

The pitch mechanism is mounted in the tunnel so that the model pitches in the horizontal plane, across the 'long' axis of the working section. This gives additional clearance for models with a fuselage and simplifies sting balance calibration, since for a given roll angle the gravity vector remains fixed relative to the balance, giving negligible change in wind-off tares with pitch angle.

4.1.5 Actuation and Control

Pitch actuation is provided by a 0.5m stroke electric linear actuator with a linear potentiometer mounted in parallel for position feedback. The ABSSAC actuator selected was not designed as a precision positioning device, but had the advantages of low cost and an unusual cardan ring mounting arrangement which enabled a very compact installation.

Roll actuation is provided by an 1Nm servomotor with integral brake coupled to the roll shaft through a precision 50:1 reduction gearhead. A potentiometer mounted between the roll bearings provides a roll angle feedback to the control system. This arrangement has also been used as the basis for a 'free-to-roll' experiment, with the

gearbox removed and a torsion sensor fitted to the shaft for torque feedback. The motor was then used merely to overcome bearing friction and additional stiffness due to instrumentation connections, blowing supplies etc, giving a model that was effectively completely free to roll for wing-rock and roll control investigations.

Pitch and roll actuators are operated from a control system designed and constructed by the School Instrumentation Group, enabling either manual or computer control of model attitude.

4.1.6 Tunnel Installation

Figure 4.4 shows the high angle of attack support system as installed in the 2.1m x 1.5m working section, with the various components identified.

The nominally straight members of the mechanism illustrated in Figure 4.3 have been cranked to give a more rigid geometry over the full pitch range, and to clear the tunnel building wall. An 'A-frame' layout was adopted for maximum lateral stiffness and to minimise strut interference. The rig was constructed in a modular fashion, due to size limitations of the School workshop machine tools, and for ease of modification by future users. The 'in-tunnel' components may be dismounted rapidly to clear the working section for use of the conventional tunnel balance. The components external to the tunnel are mounted on a steel structure adapted from a previous rig and are intended to be relatively permanent. The A-frames project into the working section through four slots sealed with heavy-duty foam, and a glass floor was installed to give laser access from two directions.

4.1.7 Commissioning and Operation

The support system was commissioned using a simple flat plate delta wing model,

with sealing of the A-frame wall slots presenting the only significant problem. Since the tunnel is usually operated with the high-speed vents open, the pressure differential across the seal is small so leakage was not significant; the problem lay in the mechanical behaviour, with both rubber sheet and brush seals proving unreliable. The current rubber foam seals wear rapidly, but can be readily replaced and do not tend to jam.

An initial concern was the damping of A-frame oscillations. Measurements during test assembly in the workshop indicated a first bending mode at about 8Hz, depending on pitch angle, and a torsional mode at about 20Hz. Excitation frequencies from delta wings at high angles of attack are in this region (of the order of 5Hz for typical test conditions), but such low natural frequencies were unavoidable, due to the long strut length. Contingency plans were made for increasing strut stiffness and damping, but when installed in the wind-tunnel no significant response was detected. This was probably due to a number of causes. The wall slot seals provided a high level of damping and also affected the mode shape, giving an increase in natural frequency with pitch angle. The nature of the rig structural response, with the model translating aft rather than pitching, would tend to reduce any flutter-type aerodynamic excitation.

4.1.8 Leading-Edge Blowing Air Supply

For jet momentum coefficients of around 0.1, a wing plenum pressure of about 20kPa (3psi) and a mass flow of 0.05 kgs^{-1} is required, while for good plenum flows an inlet velocity of the order of ⅓ of the jet velocity is desirable. A 1" bore for the supply hoses was found to give the best compromise between these requirements, and the availability of standard components. The necessary low pressure supply is obtained from the 80psi shop main, via a filter and regulator. Plenum pressure is adjusted manually using two restrictor valves, with pressure feedback from Kulite transducers

mounted externally to the plenums. Air is ducted to the wing using PVC hose, with sections of armoured power-cable sleeving (!) providing flexible joints where necessary.

A transient blowing supply system was developed separately[117], with valves operated by small DC servomotors (Figure 4.5) with a computer closing the pressure feedback loop, enabling the effect of various blowing schedules to be investigated.

4.2 Sting Balances

4.2.1 Balance Requirements

In conjunction with the high angle of attack model support system, a number of sting balances were developed to measure aerodynamic loads. The wing thickness necessitated positioning the balance externally to the model; the consequent very high bending loads resulted in the balance design being a compromise between the requirements for structural rigidity, reasonable sensitivity and low coupling.

Initially, a three-component balance was constructed, of a design based on previous small-scale delta wing studies. This balance measured normal force, pitching moment and roll moment. Three components were felt to be sufficient since at high angles of attack, axial force is very small compared to the other loads, while sideforce and yawing moment were felt to be of secondary importance. If necessary, the balance could be rotated through 90° to determine these components. Unfortunately, this balance proved to have a significant sideforce-on-roll coupling which could not be compensated for. This was not realised until late in the test programme, when it was observed that the sideforces generated by asymmetric blowing were much higher than anticipated. A new roll moment balance of improved design was constructed and the critical tests repeated.

4.2.2 Three-Component Balance

The general layout of the balance is shown in Figure 4.6a. This was a scaled-up version of a balance used previously, which itself was derived from an ONERA design[118]. Design loads were 500N normal force, 230Nm pitching moment and 20Nm roll moment.

This layout was sufficiently stiff, gave reasonable output levels and had relatively little coupling between the measured components. Unfortunately, the gauge layout on the cruciform roll cell, selected to reduce normal force coupling, was sensitive to sideforces. As discussed above, these sideforces proved to be much greater than anticipated, leading to significant errors in roll moment measurements. In use, the aft location of the balance relative to the wing led to significant pitching moment errors, due to the magnitude of the normal force and the close spacing of the pitch moment cells. These errors were particularly large for asymmetric loadings.

4.2.3 Roll Balance/Torque Sensor

The roll balance (Figure 4.6b) was originally designed as a torque sensor for a 'free-to-roll' experiment (Section 4.1.5), but proved to be more sensitive than the three-component balance roll cell and to have very low levels of coupling.

The configuration was based on a RAE balance on loan to the School, with strain gauge rosettes measuring torsion on a rectangular cross-section. This cross-section was sized primarily on strength requirements, but proved to be about twice as sensitive as the cruciform cross-section of the three-component balance. Accurate gauge placement was easier, while the more uniform strain gradients made symmetry of gauge location much less critical than for the original balance.

73

4.2.4 Balance Performance

In retrospect, the three-component balance was less than successful, giving reliable results only in normal force. However, the combination of normal force data from this balance and roll moments from the torque sensor enabled the critical aerodynamic characteristics to be measured. In addition, a comparison of roll data from new and old balances enabled a rough estimate of sideforce levels to be made.

4.3 Blown Wing

4.3.1 Wing Requirements and Sizing

For consistency with previous TLEB investigations at Stanford University a cropped 60° delta wing planform (Figure 4.7) was selected, with a constant thickness for ease of manufacture and two separate plenum chambers with slots extending over as much of the leading-edge as practicable. To enable an investigation of leading-edge geometry parameters, slot height and leading-edge were required to be adjustable. Instrumentation was to consist of plenum chamber pressure transducers, upper surface and leading-edge pressure tappings and pressure transducers mounted on or in the upper surface.

Blockage effects at high angles of attack have long been acknowledged to have a significant effect on vortex characteristics[26], but no reliable quantitative data (or correction method) had been identified at the time of wing design. Previous published delta wing studies show a very wide range of blockage levels, with wing/tunnel area ratios from 0.25%[119] to 30%[25]. Most work seems to have been done at area ratios of 5-10%, so a figure of 5% was taken as a design goal, giving a span of 0.5m. This compares favourably with 17% for the Stanford full-span wing[18].

Wing thickness was to a certain extent determined by available material sizes, and by

manufacturing constraints; a baseline thickness/chord ratio of 3.3% (17.6mm) was chosen, compared with about 6% for the Stanford wing.

4.3.2 Leading-Edge Geometry

For ease of manufacture a circular leading-edge profile (normal to the leading-edge) was chosen. An interchangeable leading-edge assembly gives a range of radii, while slot height adjustment is provided by a moveable mounting arrangement.

Slot and passage geometry is shown in Figure 4.8, with the critical parameters identified. For a given leading-edge radius and slot height, the geometry is fixed by a requirement for a 10° passage convergence (for good exit flow) and for the slot exit plane to be at 10° past the horizontal (at the nominal separation point). These requirements are the result of considerable experience at Stanford, and at Bath, on tangential blowing studies.

4.3.3 Wing Structure

Figure 4.9 shows an exploded view of the wing structure. Rigidity is provided by a skeleton fabricated from steel gauge plate, which also serves to separate the plenum chambers. Inlet manifolds are attached to the aft spars. The upper and lower surfaces are machined in aluminium alloy from solid, with pressure tappings inset in the upper surface. Stainless steel leading-edge assemblies are mounted on the upper surface, with the internal slot passage profile machined into the lower surface. Interchangeable leading-edge assemblies (and skeletons) provide a range of leading-edge radii (and hence wing thicknesses).

4.3.4 Instrumentation

The wing was pressure tapped by insetting stainless steel hypodermic tubing into the

75

upper surface and drilling into this at the appropriate location, giving six spanwise rows of pressure tappings on conical generators. Tappings were also drilled into the leading-edge assemblies. Pressure tapping locations are shown in Figure 4.10, and listed in the following Table.

		0.200c	0.275c	0.350c	0.425c	0.500c	0.650c
Leading-Edge	-	●		●		●	●
Upper-Surface	0.20s	●				●	
	0.40s	●				●	
	0.50s	●	●	●	●	●	●
	0.60s	●				●	
	0.65s	●	●	●	●	●	●
	0.70s	●				●	
	0.75s	●				●	
	0.80s		●	●	●	●	●
	0.85s					●	
	0.90s					●	

Steady-state pressures were measured using a five-barrel Scanivalve unit. Plenum chamber pressures are read using two Kulite 10psi transducers mounted externally and connected to tappings at the rear of the plenum. This arrangement was chosen to allow smoke injection into the plenum for flow visualisation without contamination of the transducers.

4.4 Data Acquisition and Reduction

4.4.1 Instrumentation and Signal Conditioning

A schematic of the experimental setup is shown in Figures 4.11. Data acquisition and rig control is PC-based, using a Data Translation DT2821 board in a PC-AT

compatible, with a range of software written specifically by the author. The DT2821 is a programmable analogue and digital I/O board, with upto 16 AD input channels (50kHz aggregate sample rate), 16 digital I/O lines and 2 DA analogue output channels. For analysis of flow visualisation images, a CCD video camera with a Data Translation DT2867-LC frame grabber board and associated software was available. Instrumentation amplification and filtering was provided by a rack of 16 DC amplifiers with 2-pole low-pass Butterworth filters designed and constructed in-house.

4.4.2 Data Acquisition and Test Control Software

A number of general-purpose data acquisition programs[120] were written in the course of this research programme, since it coincided with the general introduction of PC-based data acquisition systems in the School. The most significant is 'RigTest V4.1'[121], a user-friendly wind-tunnel test program which combines rig control and data acquisition functions. The majority of the experimental data in this thesis were obtained using various versions of this code.

A general flowchart of the program is shown in Figure 4.12. All experiment configuration and runtime graphics options are read from disk files, thus avoiding rewriting/recompilation of the code when the experimental setup is changed. The configuration file is generated by the user with any ASCII text editor, to a specified format (Appendix A). Display options are setup within the program, but may be saved to a file.

Examination of the configuration file format will illustrate the flexibility and capability of RigTest. The program can acquire data from (and control) Scanivalves, strain gauge balances and pressure transducers, and derive jet momentum, pressure and aerodynamic coefficients. Upto three rig angles may be controlled and the

77

corresponding aerodynamic angles derived.

RigTest is menu-driven, and relatively straightforward to use. A typical selection menu is shown in Figure 4.13a, in this case for setting-up the runtime display options. The sequence of operations for a test run is shown by the flowchart of Figure 4.12. Once the configuration files have been read, and the balance and transducer wind-off zeroes read, the model attitude may be set from a 'control panel' menu (Figure 4.13b). Either rig angles or aerodynamic angles may be specified.

Once the model position has been set, the analogue input channels may be monitored until the values read have steadied. Then the instrumentation signals are sampled, averaged and processed (including Scanivalve scans if required). Pressure data may be displayed in the form of pressure distributions for a particular data point (Figure 4.14a), followed by cumulative plots for previous data points (Figure 4.14b). The 'cumulative' display options allow any measured value to be plotted against any other.

From these displays the quality of the data just acquired may be assessed, and the data either rejected or accepted and saved. The process is repeated upto a maximum of 60 times. Processed data is saved to an ASCII text file in column format, suitable for import into a spreadsheet or graphics package.

A post-processing program, RigPlot, was also written to perform some of the more common data analysis procedures. In particular, Scanivalve data is saved by port number resulting in rather large and unwieldy data arrays when imported into a spreadsheet. RigPlot will read configuration and output files from RigTest, and generate text files corresponding to the runtime pressure distributions and cumulative displays.

The use of PC-based data acquisition has dramatically reduced wind-tunnel test and data analysis times, although at the cost of generating vastly more data requiring analysis! The particular advantages of RigTest are that it has been specifically written for wind-tunnel testing, and that the use of configuration files makes it very flexible. It has played a significant role in the increase in utilisation of the 2.1m x 1.5m tunnel in the last two years.

4.4.3 Data Reduction

Balance Calibration

The balance calibration and coupling are linear[118], enabling the calibration to be written in the form:

$$[M, L, Z]^t = \underline{A}.[V_M, V_L, V_Z]^t$$

where M, L, and Z are pitching moment, roll moment and normal force and V_M, V_L, and V_Z are the corresponding balance outputs. $\underline{A}$ is a 3x3 calibration matrix, where the leading diagonals are the principal calibrations and the off-diagonal values the cross-coupling terms.

Reference Pressure

Tunnel centreline dynamic pressure, q_{cl}, is a linear function of the tunnel reference pressure, taken from a tapping at the start of the contraction and one at the exit on the working section roof. Thus:

$$q_{cl} = k.V_{man}$$

where k is a calibration constant and V_{man} is the analogue voltage output from the

79

reference pressure digital micromanometer.

Aerodynamic Coefficients

Force, moment and pressure coefficients are defined in the conventional form:

$$C_Z = Z / q_{cl}.S$$

$$C_L = L / q_{cl}.S.b$$

$$C_p = (p - p_\infty) / q_{cl}$$

It should be noted that because of the sting balance arrangement, the experimental force data presented is in body axes rather than wind axes.

Blowing Coefficient

Blowing levels are quantified in terms of a jet momentum coefficient:

$$C_\mu = m.V_j / q_{cl}.S$$

With the assumptions of incompressible flow and jet exit static pressure equal to freestream static this becomes:

$$C_\mu = 2.(A_j/S).(V_j/V_\infty)^2$$

where

$$V_j^2 = 2.\Delta p_{plenum} / \rho$$

In terms of plenum chamber pressure coefficient ($\Delta p_{plenum} / q_{cl}$) this becomes:

$$C_\mu = 2.(A_j/S).C_{pplenum}$$

Aerodynamic Angles

The majority of experimental data is presented in terms of the conventional angles of attack (α, α_t) and sideslip (β, β_s), as defined in Figure 4.15a. In terms of the model support system pitch (θ) and roll (ϕ) angles these become:

$$\alpha_t = \tan^{-1}(\cos\phi.\tan\theta)$$

$$\beta_s = \sin^{-1}(\sin\phi.\sin\theta)$$

For high angles of attack, it is occasionally more appropriate to work in terms of angle of downslip (α_s) and effective sweep angle change (Λ'). These are defined in Figure 4.15b, and in terms of θ and ϕ are:

$$\alpha_s = \sin^{-1}(\cos\phi.\sin\theta)$$

$$\Lambda' = \tan^{-1}(\sin\phi.\tan\theta)$$
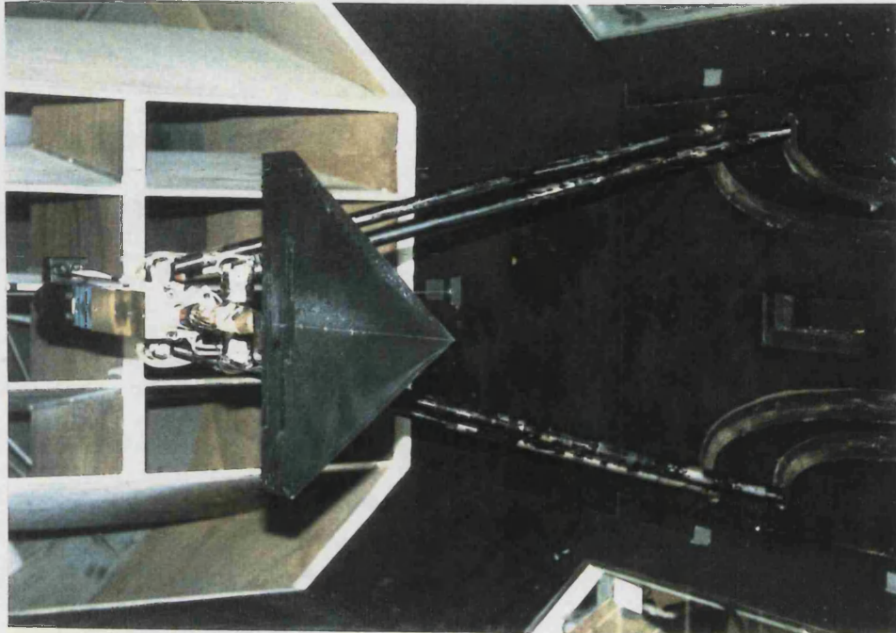
Figure 4.1 The High Angle of Attack Model Support System
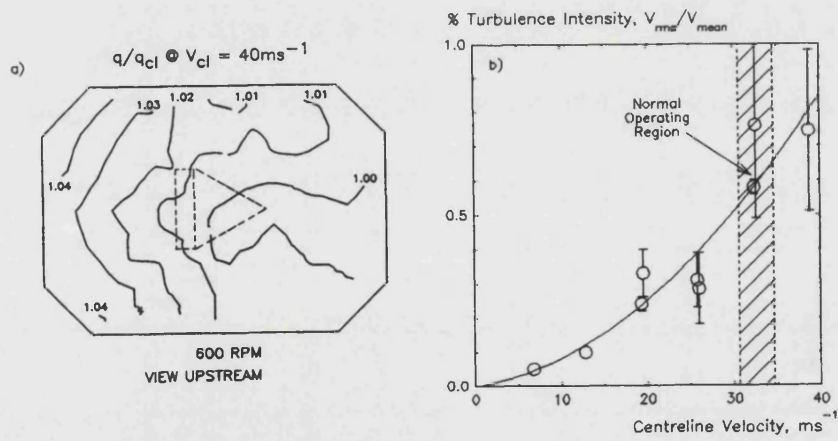
Figure 4.2 Calibration of Aerodynamic Working Section
        a) Dynamic Pressure Variation Across Working Section
        b) Centreline Turbulence Intensity

82

0–90° PITCH

+/− 180° ROLL

TUNNEL
CENTRELINE

CENTRE OF ROTATION

STRAIN GAUGE BALANCE

TUNNEL WALL

FIXED PIVOTS
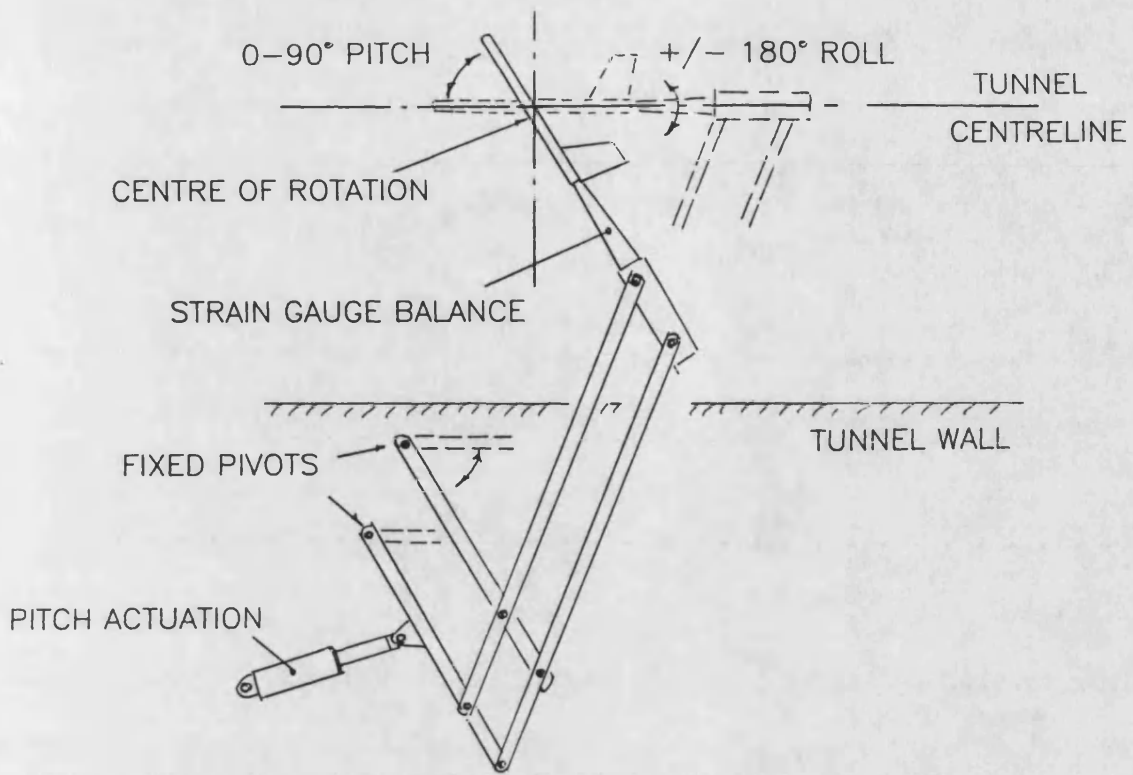
PITCH ACTUATION

Figure 4.3 Schematic of Model Support System Pitch Mechanism

83

a) Pitch Mechanism

A-FRAME

TUNNEL WALL

ELECTRIC LINEAR
ACTUATOR

MAIN FRAME

b) Roll Actuation

c) Model Support System in 7'x5' Working Section
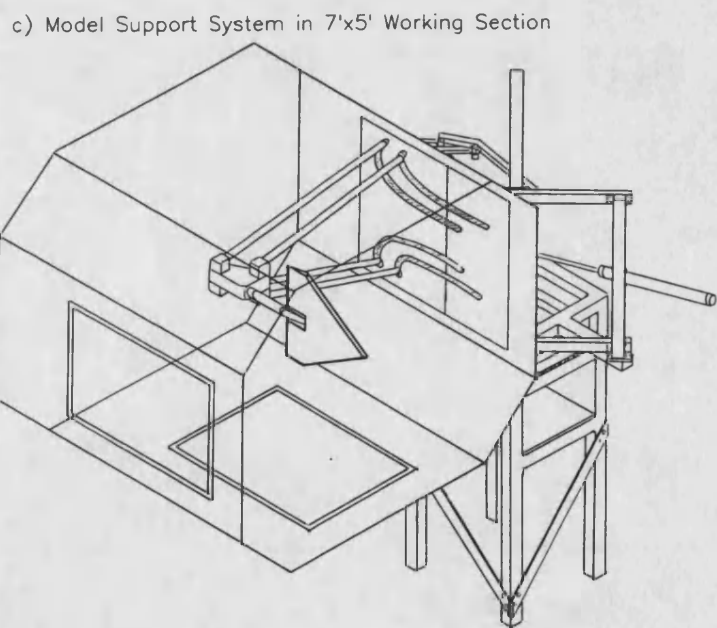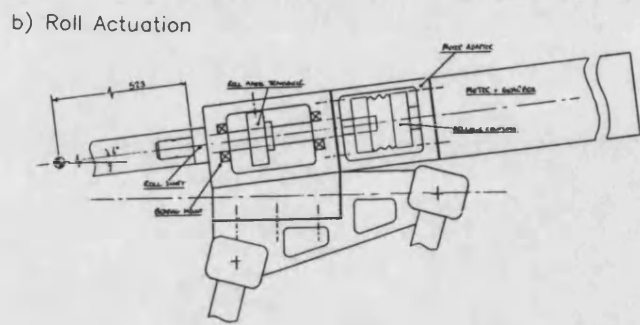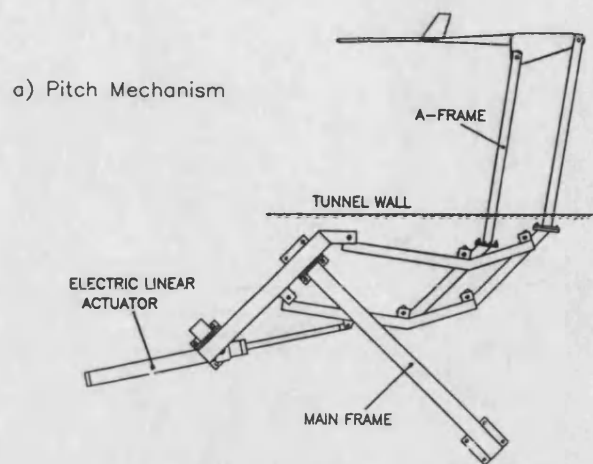
Figure 4.4 Installation of Model Support System in 7'x 5' Working Section
   a) Pitch Mechanism
   b) Roll Actuation
   c) Tunnel Installation
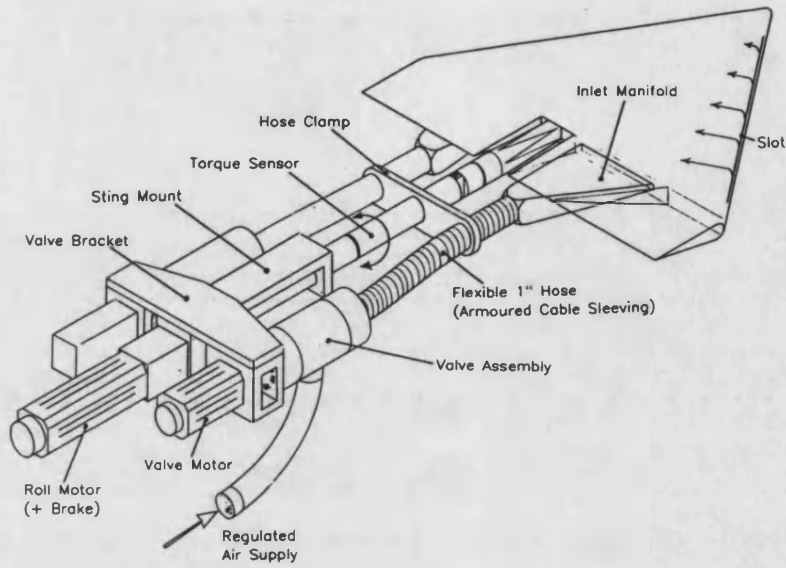
Figure 4.5 Air Supply System for Leading-Edge Blowing
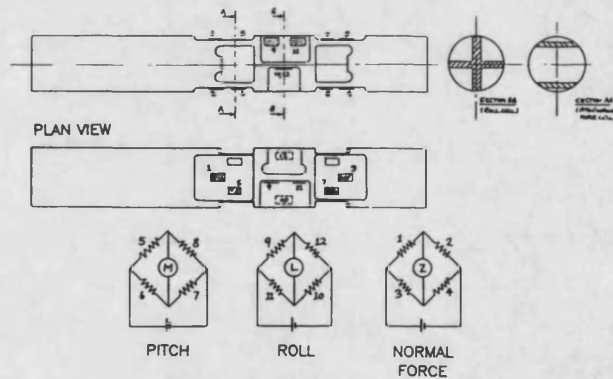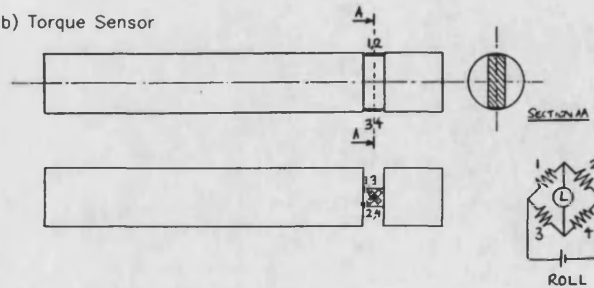
Figure 4.6 Sting Balances for the High Angle of Attack Model Support System
a) Three-Component Balance
b) Roll Balance/Torque Sensor

85

533

100

Dimensions in mm

415

500

$S = 0.158m^2$

$\Lambda = 60°$

$\lambda = 0.19$

$AR = 1.56$

$t/c = 3.3\%$

60°

17.6
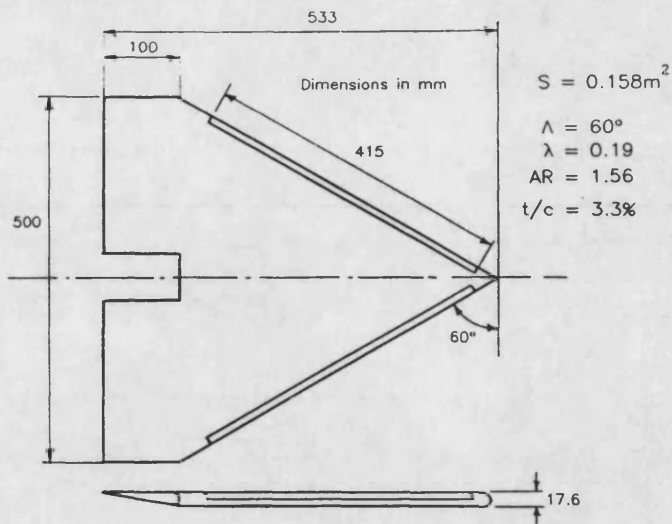
Figure 4.7 Blown Wing Planform

10°

r_{le}

h_{slot}

t

10°

LE RADIUS

INTERCHANGEABLE
SPAR & LE ASSEMBLY

SLOT HEIGHT

LOCKING SCREW

ADJUSTOR SCREW
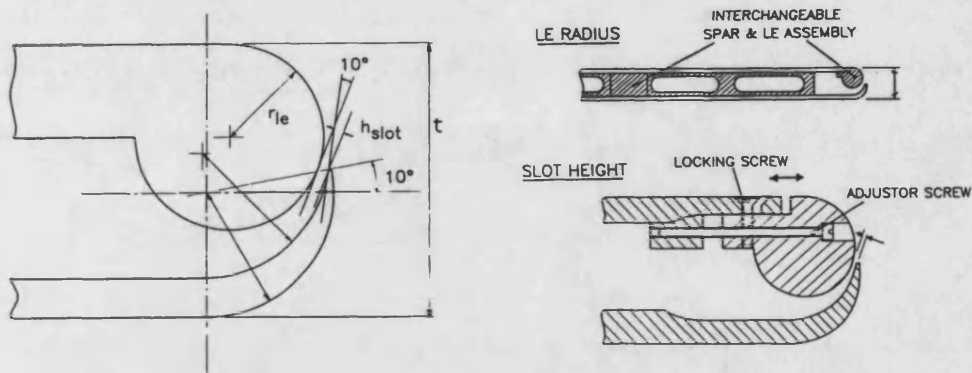
Figure 4.8 Leading-Edge Geometry
a) Critical Parameters
b) Adjustment Mechanism

UPPER SURFACE

INLET MANIFOLD

LEADING EDGE

STING ATTACHMENT
/STIFFENER

TAIL PIECE
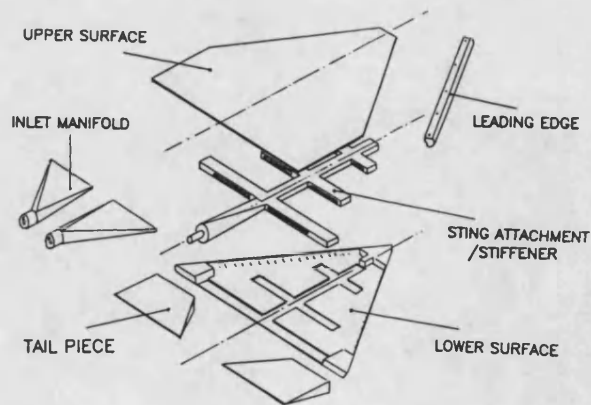
LOWER SURFACE

Figure 4.9 Exploded View of Blown Wing Structure

86
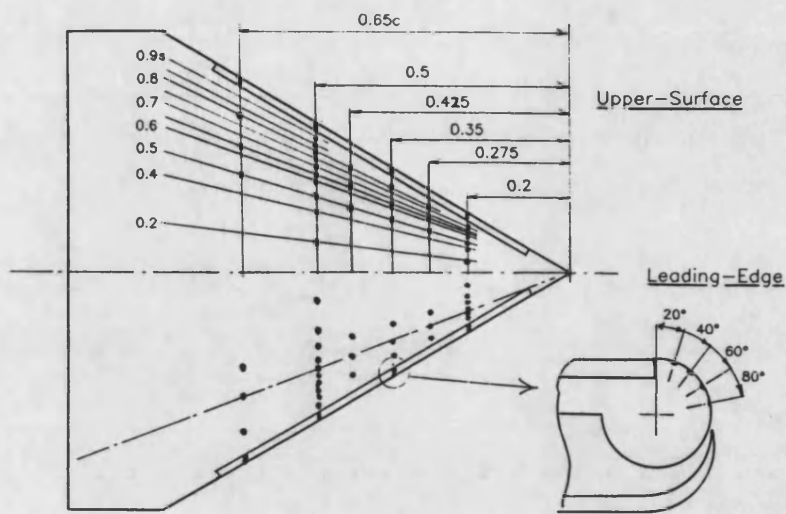
Figure 4.10 Upper-Surface and Leading-Edge Pressure Tapping Locations
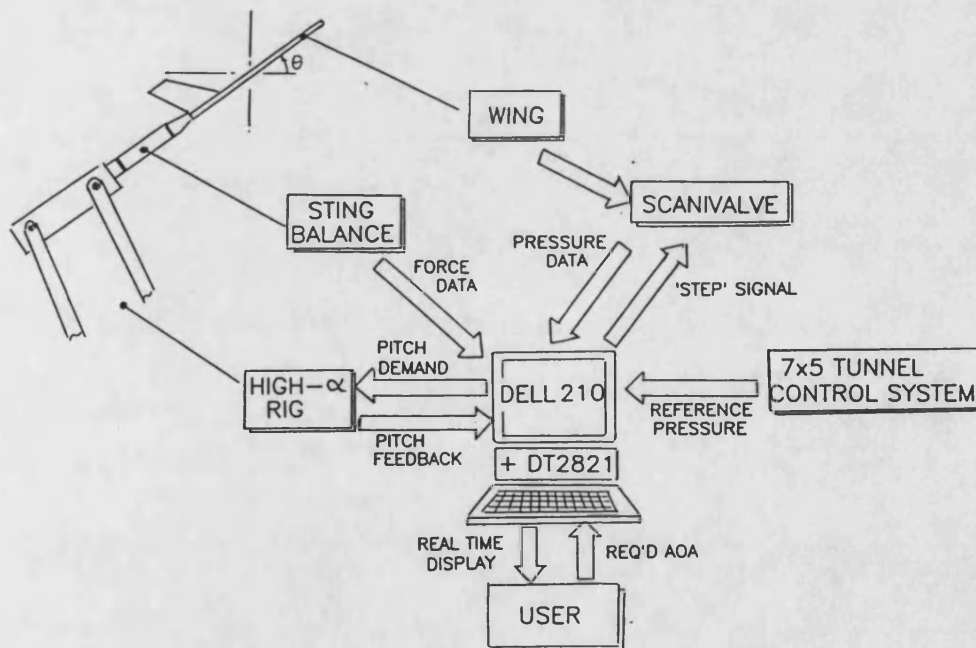
Figure 4.11 Data Acquisition And Experiment Control
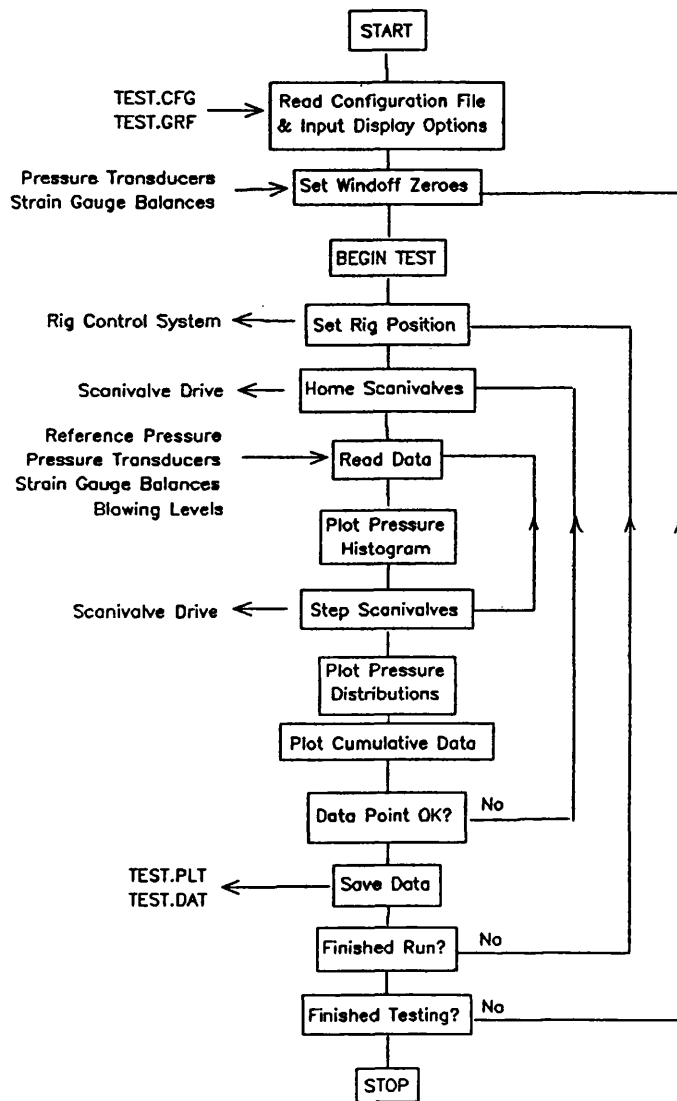
Figure 4.12 RigTest Program Flowchart

a)

```
┌─────────────────────────────────────────────────────────────────┐
│ a)      ┌──High-Incidence Rig Test Program V3.3──┐               │
│         │                                        │               │
│         │ Config File  : ubwsv.cfg               │               │
│         │    Data File : test.dat                │               │
│         │    Plot File : test.plt                │               │
│         │                                        │               │
│         │ Test Comment : sample output           │               │
│         │                                        │               │
│         │ Channel Sample Rate (Hz) : 1000.0      │               │
│         │                          : 100         │               │
│         │  ┌─────────────────────┐               │               │
│         │  │Read Display Config  │   : 0.00      │               │
│         │  │Input/Display Options│   : 0.00      │               │
│         │┌─────────────────────┐onfig            │               │
│         ││SV Barchart/Axes     │                 │               │
│         ││SV 1D Graphs         │ct Display Options│              │
│         ││SV Contour Plot      │indoff Calibration│              │
│         ││Cumulative Graphs    │ew Data/Plot File │              │
│         │└─────────────────────┘                 │               │
│         │              TAKE DATA                 │               │
│         │                                        │               │
│         └──────────────────Message───────────────┘               │
│ ‹ESC› to return to main menu                                     │
└─────────────────────────────────────────────────────────────────┘
```

b)

```
┌─────────────────────────────────────────────────────────────────┐
│ b)      ┌──High-Incidence Rig Test Program V3.3──┐               │
│         │                                        │               │
│         │ Config File  : ubwsv.cfg               │               │
│         │    Data File : test.dat                │               │
│         │    Plot File : test.plt                │               │
│         │                                        │               │
│         │ Test Comment : sample output           │               │
│         │                                        │               │
│         │ Channel Sample Rate (Hz) : 1000.0      │               │
│         │     Samples per Channel : 100          │               │
│         │                                        │               │
│         │      Rig Roll Angle : 0.00             │               │
│         │  ┌──────Set Rig Position - Point 1─────┐               │
│         │  │  RIG ANGLES    EULER ANGLES    INCIDENCE ANGLES │   │
│         │  │ ┌─────┐                                         │   │
│         │  │ │Pitch│ : 48.2   Yaw  : 0.0   AoA      : 48.2  │   │
│         │  │ └─────┘                                         │   │
│         │  │  Yaw   : 0.0   Pitch : 48.2  Sideslip  : 0.0   │   │
│         │  │                                                 │   │
│         │  │  Roll  : 0.0   Roll  : 0.0   Bank Angle : 0.0  │   │
│         │  └─────────────────Message──────────────────────┘     │
│ ‹ESC› input position,‹ENTER› confirm,^Z rezero, D change display,^Q quit │
└─────────────────────────────────────────────────────────────────┘
```

Figure 4.13 Examples of RigTest Menu-Based Input
a) Display Options Selection
b) Model Attitude Control

89
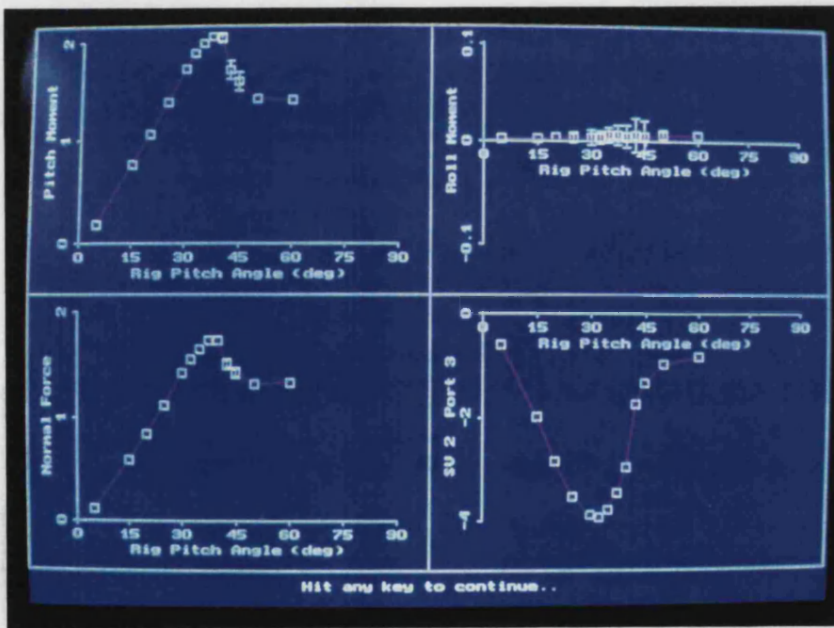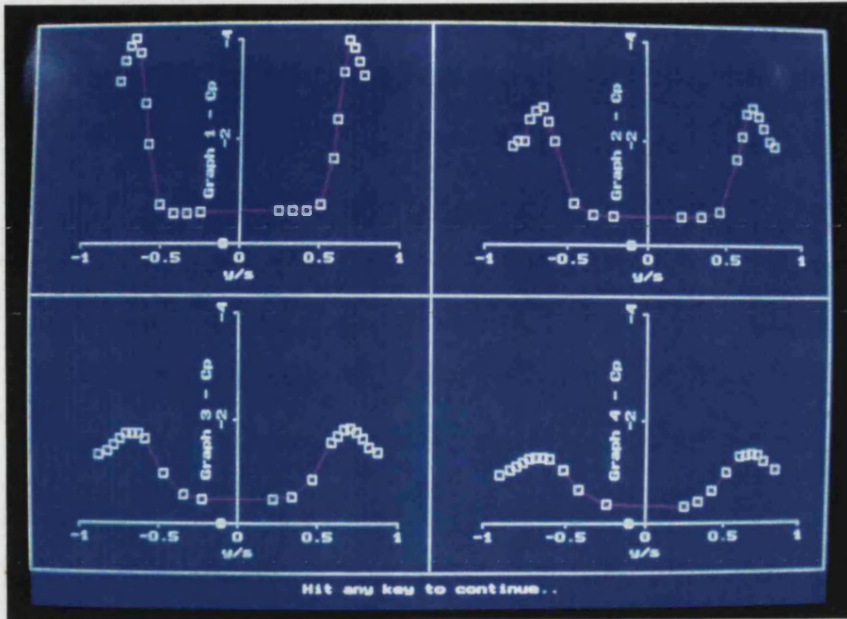
Figure 4.14 RigTest Runtime Screen Output
a) Pressure Distributions
b) Cumulative Data/Results

90

a) 'Conventional' (α_t, β_s)
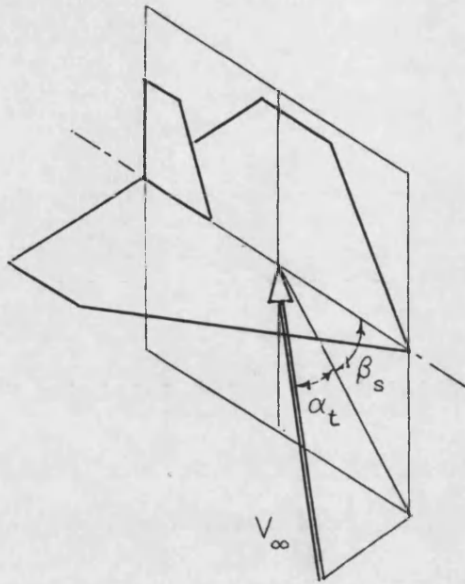
b) High Angle of Attack (α_s, β_t)
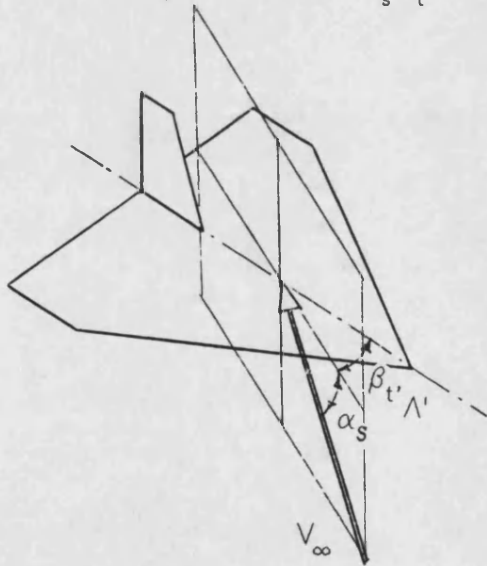
Figure 4.15 Definitions of Aerodynamic Angles

CHAPTER 5

EXPERIMENTAL RESULTS

5.1 Introduction

5.1.1 Test Schedule

The experimental programme was described and summarised in Section 1.3.3 (Figure 1.7). Initial testing of the blown wing was undertaken at the end of 1990. Unfortunately, a manufacturing defect in the leading-edge assembly limited the configuration tested to a parallel slot. A new set of leading-edges was fabricated, enabling testing of a conically tapering slot configuration in mid-1991.

In late 1992 a new roll balance was designed (Section 4.2.3) for a 'free-to-roll' experiment[117], and a comparison of roll moment measurements showed a significant discrepancy. This was at first thought to be due to a combination of a number of small changes in wing and support system configuration, but was finally traced to unexpectedly high sideforces generated by asymmetric TLEB and the poor sideforce/roll coupling characteristics of the original three-component balance. It was thus necessary to repeat critical test cases.

The consequent delays, coupled with manufacturing difficulties, meant that no investigations of leading-edge radius effects or quantitative transient blowing tests were possible in the time available.

5.1.2 Experimental Results Presented

The basic static test results are divided into four sections:

1. Baseline unblown wing characteristics

2. Effects of symmetric blowing

3. Asymmetric blowing, zero roll angle

4. Asymmetric blowing, with roll angle

Normal force and roll moment characteristics and typical surface pressure distributions are described, together with some limited flow visualisation. Upper-surface vortex-induced pressures are characterised using the halfwidth analysis derived in Section 2.6. A further analysis of the data, in particular the mechanisms underlying the generation of roll moments, will be presented in Chapter 6.

5.2 Unblown Aerodynamic Characteristics

5.2.1 Effect of Angle of Attack

Figure 5.1 shows unblown normal force characteristics for a range of Reynolds Numbers (Figure 5.1a) and compared with published data for flat-plate, rounded leading-edge wings[42,43,122..124] (Figure 5.1b). Reynolds Number effects are small, despite the rounded leading-edge, presumably due to the discontinuity at the slot lip (Figure 4.8) acting as a boundary layer trip. The curves are consistent with published data, though considerable scatter is evident at higher angles of attack, due to variations in burst trajectory.

Corresponding upper and lower-surface spanwise pressure distributions are illustrated in Figure 5.2, for x/c = 0.5. The vortex-induced suction peaks on the upper surface can be seen to increase with angle of attack, then diminish and widen as the vortex burst passes. This behaviour is illustrated in Figure 5.3, showing the variation of suction peak magnitude with angle of attack at x/c = 0.2 and 0.5, compared with published data for a sharp-edged 60° delta wing[81]. The 'break' in the curves

corresponds to onset of the burst at that chordwise location, with the abruptness of the break increasing towards the apex. The low angle of attack portions of the curves compare well, though a difference in burst onset is apparent at higher angles of attack. The reduction in suction peak magnitude from $x/c = 0.2$ to 0.5 indicates a departure from conical flow.

Figure 5.4 superimposes the corresponding halfwidth trends (Section 2.6.3), with the burst onset indicated. These curves are initially flat, with no evidence of the 'unburst' flow regime A identified in Figures 2.30 and 2.31. From vortex formation to burst onset the curves suggest a continuously decelerating 'pre-burst' flow (regime B in Figure 2.30), providing some experimental substantiation of the generally held view that a rounded leading-edge vortex is 'looser' than the corresponding sharp-edged flow. A practical consequence of this 'looseness' is considerable difficulty in obtaining good smoke flow visualisation of the vortex.

5.2.2 Effect of Sideslip Angle

As discussed in Section 3.3.4 the characteristics of asymmetric TLEB can be compared to the effects of sideslip, so the unblown lateral characteristics of this wing will be presented in some detail as a baseline for comparison.

For the initial stages of this research programme a roll actuation system was not available on the high angle of attack model support rig, limiting 'sideslip' tests to fixed roll angle pitch sweeps. Since $\beta = \sin^{-1}(\sin\phi.\sin\theta)$, this implies a continuously increasing sideslip with pitch angle. For slender aircraft at high angles of attack, roll manoeuvres tend to be about the body axis, rather than the velocity vector, so that presentation of lateral characteristics in terms of roll angle rather than sideslip is more representative and so has been retained. Some 'sideslip' curves are presented, for ease of comparison with published data.

The effect of roll angle on normal force is shown in Figure 5.5. Increasing roll angle has little effect at low angles of attack, but results in a lift loss at high angles of attack, due to vortex burst asymmetry. Similar behaviour is evident in Figure 2.8, for a 76° sharp-edged delta[28].

Corresponding roll moment behaviour is shown in Figure 5.6. At low and high angles of attack the wing is statically stable at zero roll angle, with an unstable region near the stall. In this 'unstable' region, stable roll trim points exist at roll angles of around ±20° depending on angle of attack (cf Figure 2.7[30]). The conventional roll stability parameter $C_{l\beta}$ (roll moment due to sideslip or 'effective dihedral') may be extracted from this data and is shown in Figure 5.7. A comparison with published data[36,42..44,122] for rounded leading-edge 60° delta wings shows a good match at low ('unburst') angles of attack. The onset and magnitude of the unstable region varies, due to differences in vortex burst trajectory.

Typical roll angle effects on spanwise pressure distributions are shown in Figure 5.8, for x/c = 0.5 and a roll angle of +20°. At low angles of attack the windward vortex peak is stronger than the leeward, due to asymmetry in vortex core height, giving a stabilising roll moment contribution. As angle of attack increases the windward vortex bursts ahead of the leeward, resulting in a destabilising roll moment as lift is lost on the 'down' wing side. At very high angles of attack the vortex flow has subsided and the roll moment is dominated by the asymmetric lower-surface pressure distribution. Figure 5.9 compares this behaviour with results reported in Reference 84 for a sharp-edged 60° delta wing with increasing roll angle at a fixed pitch angle.

To summarise the effects of roll angle (or sideslip) on the vortical flow, Figure 5.10 shows the resulting suction peak magnitude and halfwidth trends for x/c = 0.5 (with

similar behaviour exhibited at x/c = 0.2). The effect of changing leading-edge sweep due to sideslip on vortex burst can be seen in the shift of the breakpoints in the curves. The low angle of attack 'pre-burst' halfwidth curves show almost no change with roll; the corresponding C_{pmin} curves show an increase on the windward side and vice versa. Figure 5.11 shows sideslip effects on burst trajectory derived from this pressure data (with some flow visualisation data for comparison). Smoke injection into the vortex aft of the burst allowed the reverse flow within the burst region to define the burst extent. Sideslip is used rather than roll angle, since burst trajectory is primarily a function of leading-edge sweep angle.

Changes in burst trajectory are largest at x/c = 0.5, where the effects are broadly consistent with the changes in geometric leading-edge sweep. As the burst nears the apex the effects of roll/sideslip become smaller, particularly on the leeward side. It should be noted that for sideslip angles exceeding -20° at angles of attack above about 40°, the geometric sweep angle of the leeward leading-edge approaches 90° and the adjacent vortex becomes very close to the leading-edge and hence difficult to distinguish from pressure data.

5.3 Effects of Symmetric Blowing

Previously reported characteristics of symmetric blowing are described in Section 3.2. The behaviour of the wing tested is similar, but will be presented in a modified form, with emphasis on the analysis of pressure data. Although full-span pressure data was available at both x/c = 0.2 and 0.5, data from x/c = 0.5 is generally presented, due to better coverage near the leading-edge. Except where noted, similar behaviour was seen at x/c = 0.2.

5.3.1 Aerodynamic Characteristics

Symmetric blowing should generate no roll moment, although in practice small slot asymmetries can have a significant effect in the region of the unblown stall angle, where the flowfield is very sensitive to blowing.

A considerable effect is seen on normal force, as shown in Figure 5.12, with a comparison with previous full-span wing data[108]. Increasing symmetric blowing reduces lift-curve slope and delays the stall, which also becomes less abrupt. Figure 5.12b shows similar trends, though with much greater overall normal force levels due to high tunnel blockage (upto 17%). It can be seen from Figure 5.12a that at pre-stall angles of attack the effect of increasing blowing saturates. This is shown more clearly in Figure 5.13a for increasing blowing at a fixed angle of attack. The critical value of C_μ, or C_μ^*, is associated with the complete reattachment of the upper surface, and is plotted in Figure 5.13b. The breakpoint is not well defined, giving some difficulty in determination, but it can be seen that as angle of attack increases the level of blowing required to suppress the leading-edge vortex becomes very large.

A residual C_μ-dependent loss of normal force is evident in the supercritical (saturated blowing) characteristics. Figure 5.14a shows that the loss increases linearly with increasing blowing, above the critical value. The rate of loss is roughly half the jet momentum increase, reducing slightly with angle of attack. This phenomenon is thought to be due to the formation of a 'fountain' where the two leading-edge wall-jets meet, giving a downwards reaction. The included angle between the leading-edges results in a aft inclination of the fountain, and hence a reduction in lift loss.

5.3.2 Upper-Surface Pressures

Typical effects of symmetric blowing on upper-surface pressures are illustrated in Figure 5.15 for low (unburst), medium (burst) and high (stalled) angles of attack. At

low angles of attack the vortex-induced suction peaks subside and move inboard, mirroring the reduction in strength and relocation of the vortex core. At medium angles of attack the suction peak initially increases in strength as the burst moves aft, then diminishes once the burst has passed. At high angles of attack blowing reestablishes coherent vortical flow.

These trends are summarised in Figure 5.16, showing the effect of symmetric blowing on suction peak magnitude and halfwidth at x/c = 0.5. The general result is a shift of the curves to the right, analogous to an increase in the effective 'zero-lift' angle of the vortical flow. The halfwidth also displays an increased pre-burst level, suggesting a greater 'looseness' in the vortex structure. In addition to a shift in zero-lift angle, the angle of attack at which a suction peak is distinguishable from the jet-induced attached flow also increases. This is shown in Figure 5.17, where it can be seen that a vortex-induced suction peak forms some 5-10° after the effective zero-lift angle, with the offset increasing with blowing level.

The 'zero-lift' curve is subject to considerable uncertainty in estimation, due to the extrapolation required. Neither the zero-lift or vortex formation angles match the critical C_μ^* derived from normal force data; the reason for this lies in the relative lift contributions of the vortex and the jet-induced leading-edge suction, shown in Figure 5.18 and derived from integrations of the upper-surface pressures at x/c = 0.5. To differentiate between leading-edge and vortex forces, a fairly arbitrary spanwise position of y/s = 0.9 was taken as a dividing line.

Figure 5.18a shows the inboard contribution, assumed to be primarily the vortex contribution. At low angles of attack/high blowing rates the curves collapse, exhibiting a lift-curve slope typical of the potential flow ($\sin\alpha.\cos\alpha$) component of the

LESA. The formation of the vortex as angle of attack increases is marked by an abrupt increase in inboard lift. At the leading-edge (Figure 5.18b) the low angle of attack/high blowing curves show a $\sin^2\alpha$ trend similar to the leading-edge suction developed in potential flow, with an offset due to the jet momentum. This jet momentum contribution is not seen in the overall normal force characteristics, since it is counteracted by the reaction at the slot exit and by the formation of a centreline 'fountain' where the two leading-edge jets meet. The formation of the vortex has a pronounced effect, with a rapid loss in lift as the separation point moves to the vicinity of the leading-edge. As the vortex forms the increased vortex lift is initially balanced by the lift loss from the leading-edge, but as angle of attack is increased, the leading-edge lift stabilises while the vortex lift continues to increase. The nett result is a delay in the breakpoint in the normal force characteristics relative to the formation of the vortex.

Vortex burst trajectories derived from the pressure data are shown in Figure 5.19. The effect of blowing is to delay the onset of breakdown, appearing to approach a maximum at a blowing level above 0.12. Burst delay at x/c = 0.5 follows the shift in vortex reestablishment angle fairly well, but at x/c = 0.2 the delay is more consistent with the shift in effective zero-lift angle. This loss of effectiveness in terms of burst control may possibly be due to the blowing slot not extending to the wing apex, with the unblown apex region becoming more significant at high angles of attack.

5.3.3 Leading-Edge Geometry Effects

Some early tests were performed with a parallel rather than conical slot. This geometry has previously been shown to be less efficient[16], but was necessitated by a manufacturing defect in the leading-edge assembly. These initial tests were

undertaken with the primary aims of commissioning the blowing apparatus and development of the data acquisition software, and hence were of limited scope.

Normal force characteristics for the parallel slot are shown in Figure 5.20a. Overall trends are similar to the conical slot, in particular the saturated normal force levels; however, the critical blowing levels appear to be of the order of twice those for a conical slot. The parallel slot is 'overblowing' towards the wing apex with a consequent loss of efficiency.

The effect of slot length was also investigated, with the slot covered in stages from the rear forwards. A general loss of efficiency was observed; typical effects on normal force are illustrated in Figure 5.20b, for a half-length slot (ie ¼ of the slot area). Again, trends are similar to the baseline slot, but with saturation occurring at a much lower critical blowing level. Saturated normal forces are significantly higher, indicating a smaller effect on the vortex lift component. In effect a second leading-edge vortex is shed aft of the slot, which is relatively unaffected by blowing upstream. Unpublished data from Stanford University[125] from a half-span model with segmented and part-span slots also showed a significant loss of efficiency with limited span blowing.

5.4 Asymmetric Blowing at Zero Roll Angle

5.4.1 Aerodynamic Characteristics

The normal force characteristics of asymmetric blowing are generally similar to the symmetric case. Roll moment behaviour is more complex and will be presented in greater detail.

Asymmetric blowing schemes may be divided into two categories: one-sided and

100

mixed. One-sided blowing is simpler, but gives rise to dead-bands and large roll reversals undesirable for a flight vehicle control system. A mixture of symmetric and asymmetric blowing linearises the characteristics, but tends to obscure the underlying mechanisms of roll moment generation. The majority of experimental results presented will be for one-sided blowing, with some 'mixed' data for comparison.

One-Sided Blowing

Figure 5.21 shows the roll moment due to constant right-side blowing as angle of attack is increased. In general, moments are 'blown-side up', with two regions of sign reversal apparent. At low angles of attack a $\sin^2\alpha$ characteristic is displayed, with an abrupt break into the first sign reversal region. The break angle is a function of blowing level, and corresponds to the formation of the leading-edge vortex on the blown side. Also evident at low angles of attack is a dead-band in the roll response. A further discontinuity occurs at an angle of attack of around 65°, where flow control is completely lost. This break is almost independent of blowing level. Overall, a number of mechanisms contribute to this complex behaviour, and these will be considered in more detail in Chapter 6.

Figure 5.22 compares roll characteristics with published data, from Reference 108. The curves are very similar, though the Stanford data (Figure 5.22b) shows higher roll moments and a 5° delay of the first roll reversal region. This is consistent with the normal force data for the same wing (Figure 5.13b), which shows a comparable shift in stall angle and increase in overall force levels attributed to a very high level of tunnel blockage. The mounting arrangement for this wing did not permit testing at angles of attack high enough to observe the second roll reversal and final loss of control power.

Figure 5.23a presents roll characteristics of asymmetric TLEB in a different form, for varying blowing level at a fixed angle of attack. At low angles of attack a critical blowing level for roll moment saturation is evident, in a similar manner to the response of the normal force to symmetric blowing (Figure 5.14), but much more well defined. Figure 5.23b shows this critical level as a function of angle of attack. It should be noted that as angle of attack approaches 35°, the breakpoint becomes less well defined; this is more apparent in Figure 5.21. C_μ^* derived from the roll moment break is comparable with the 'normal force' values of Figure 5.14 and it seems reasonable to attribute it to the same phenomenon: the formation of the blown vortex. This is confirmed by an examination of the upper-surface pressure data (Section 5.4.2).

In a similar manner to the normal force characteristics of symmetric blowing, a residual C_μ-dependent variation in roll moment is seen in the supercritical blowing region (Figure 5.15b). The trend is 'blown-side-up', and increases with angle of attack upto a level equivalent to the jet momentum acting at the leading-edge. For one-sided blowing, the leading-edge jet interacts with the unblown vortex flow (primary reattachment, secondary separation) and separates on the unblown side of the wing, giving a downwards reaction and hence a 'blown-side-up' roll moment. The precise nature of the interaction was not investigated; however, the C_μ-dependent moments are small compared with the total roll capability of asymmetric blowing.

The loss of control power at high angles of attack is an occurrence that has not been previously reported for TLEB, though a similar phenomenon has been observed on circulation control aerofoils[105]. In initial tests this loss was accompanied by a high level of lateral vibration and a hysteresis loop of around 15° extent. Figure 5.24 shows the hysteresis loop, using roll data from the original three-component balance.

An examination of pressure data from the leading-edge region showed that the loss of roll power was accompanied by a sudden reduction in leading-edge suction, leaving only the small contribution of the Coanda jet itself. The conclusion reached was that the 'unblown' leading-edge separation point had reached the slot lip (ie the outer cross-flow was separating ahead of the slot) in advance of the 'blown' separation point, as sketched in Figure 5.25. The hysteresis loop is generated by the bistable separation point at high angles of attack.

On this assumption, the extent of the hysteresis loop should be reduced by delaying the separation of the outer flow, and this was achieved with a lower-surface boundary layer trip. Figure 5.24 shows the effect of a range of trip configurations, all using a 1mm wire stuck to the lower-surface and running the full length of the slot. A trip on a conical generator at $y/s = 0.5$ had no effect whatsoever, whereas trips 1,2 and 3 running parallel and successively closer to the leading-edge reduced and finally suppressed the hysteresis loop. The final configuration, trip 3, placed the trip wire at the start of the leading-edge curvature. No further attempt was made to identify an optimum trip height, since all the configurations tested had negligible effect on the pre-separation characteristics. The maximum angle of attack for flow control (or 'slot stall' angle) was also unaffected by the trip configuration, providing some confirmation that this is where the 'blown' separation reaches the slot exit. The 'slot stall' angle is almost independent of blowing level.

Mixed Blowing

The dead-bands and roll reversals of the one-sided blowing characteristics of Figure 5.21 are undesirable for a flight vehicle control system, but may be alleviated by mixing symmetric and asymmetric blowing. A number of schemes were investigated, and a 'constant total blowing' arrangement found to give the best results. This is

illustrated by Figure 5.26, for a constant $C_{\mu T}$ of 0.08 with increasing right-side/decreasing left-side blowing. The dead-band at low angles of attack and the sign reversals at higher angles have been almost completely suppressed. At low angles of attack the roll response becomes very sensitive, as illustrated by the (nominally) symmetric blowing curve: at around 60°, the left slot 'stalls' a few degrees ahead of the right, giving a sharp reversal then stall.

A comparison of one-sided and mixed blowing (Figure 5.27) shows the suppression of the dead-band at lower angles of attack and the alleviation of the roll reversal at higher angles.

5.4.2 Upper-Surface Pressures

The high angle of attack vortex coupling previously reported (Section 3.3) is apparent in the effect of one-sided asymmetric blowing on the upper-surface pressures (Figure 5.28). For unburst vortices at low angles of attack the flow appears uncoupled, with the blown vortex suction peak subsiding and the unblown peak unaffected. As angle of attack is increased past burst onset, the coupling becomes apparent, with both blown and unblown vortices unbursting. Once unburst, the behaviour resembles the low angle of attack case, with the blown vortex subsiding and the unblown vortex unaffected. At very high angles of attack the vortices have subsided. Asymmetric blowing reestablishes coherent vortex flow, on both blown and unblown sides. Close examination of Figure 5.28c shows that the unblown vortex appears to reestablish ahead of the blown vortex.

The nature of the coupling can be seen more clearly in Figure 5.29, showing the effect of asymmetric blowing on magnitude and halfwidth of the vortex-induced suction peaks (the corresponding symmetric blowing characteristics are shown in Figure 5.16).

On the blown side (Figure 5.29a) the behaviour is essentially similar to the symmetric case, with a shift in effective zero-lift angle of the vortex flow with adjacent blowing. The corresponding delay in burst onset is reduced relative to the symmetric case, giving a reduction in the maximum suction peak magnitudes achieved. On the unblown side, the effect of increasing opposite blowing is solely to delay the vortex burst. The strength and magnitude of the unburst vortex peak is unchanged, with the nett result being a significant increase in the maximum vortex lift on the unblown side.

The vortex coupling is evident in the variation of the burst location on the unblown side, and is confined to a modification of the stability of both vortices. The reduction in strength and aft burst motion of the blown vortex presumably reduces the adverse pressure gradient on the unblown side and hence affects the burst location. The converse is true, in that if the 'unblown' vortex is now manipulated (in this case by blowing) a change in the (original) blown vortex burst occurs. This is illustrated by Figure 5.30, for a constant right-side blowing level of 0.04 and left-side blowing varying from 0 to 0.08. Similar behaviour to the 'unblown' vortex of Figure 5.29 is displayed.

Effective zero-lift and vortex reestablishment angles of attack were determined from the pressure data and compared with critical blowing levels determined from the roll moment data (Figure 5.31). Clearly, the breaks in the roll characteristics correspond very closely to the formation of the vortex on the blown side, and the agreement is better than the corresponding symmetric blowing/normal force plot (Figure 5.17). The reason for this can be seen in the pressure integrated normal force data of Figure 5.18 (for symmetric blowing, but the asymmetric data is practically identical in the region of interest). Although the initial changes in leading-edge and inboard normal force

105

are of a similar order, the moment arms are significantly different. Thus, as the vortex forms, the overall normal force initially remains constant, but the moment arm reduces from y/s = 1.0 to around 0.65, giving a immediate change in roll moment and a well-defined break in the roll characteristics.

The zero-lift and vortex reestablishment curves of Figure 5.31b are very close to the symmetric curves of 5.17b, certainly within the experimental scatter of the data. This is consistent with the behaviour shown in Figure 5.30 for mixed blowing, where opposite blowing has no significant effect on the low angle of attack, unburst portion of the curves.

Burst trajectories derived from pressure data are shown in Figure 5.32. For the blown side (Figure 5.32a), the burst delay trends are similar to the symmetric case (Figure 5.19), allowing for the difference in vortex formation angles of attack. On the unblown side the coupling is manifested in a delay in burst onset, with a similar offset at both x/c = 0.5 and 0.2. The curve for x/c = 0.2 is almost identical to the blown side, implying that both unblown and blown vortex bursts reach the wing apex at the same time, independent of blowing level. This may be a further consequence of the unblown section of leading-edge towards the wing apex.

Figure 5.33 compares symmetric and asymmetric (blown side) burst trajectories as a function of blowing level, confirming the reduced effect on blown burst location of one-sided blowing indicated in Figure 5.30.

5.4.3 Flow Visualisation

The closed-return layout of the 7'x 5' wind-tunnel made smoke visualisation of the vortex flow difficult. No images of sufficient quality for presentation were obtained,

though the general trends deduced by the pressure data were confirmed. However, surface flow visualisation using mini-tufts was more successful. The images presented were digitised from a video film made during exploratory tests of transient blowing; this was a first attempt at this technique, hence the less than perfect quality. The limited frequency range of the blowing valves necessitated operation at low tunnel speeds, so no reliable absolute value of jet momentum coefficient could be measured (Section 5.4.4), but the general trends are clear.

Figure 5.34 shows the effect of right-side blowing at an angle of attack of 25°. Similar trends were reported on a half-model[16], with a complex movement of the primary separation line despite a conical blowing distribution. Of particular interest is the tip flow on the blown side. A region of reverse flow aft of the slot is apparent; the video film reveals this to be essentially fully separated and very unsteady, even at relatively low angles of attack with attached flow in the unblown tip region. This reverse flow region is evident even at very low angles of attack, and increases in extent as angle of attack is increased (Figure 5.35). No pressure data was available in this region but it is clear that a significant asymmetric loss of lift and hence roll moment must result.

5.4.4 Reynolds Number Effects

Previously, Reynolds Number effects have been reported to be negligible[108], on the basis of constant angle of attack/increasing blowing tests at different freestream velocities. However, pitch sweeps at fixed blowing levels (Figure 5.36) show a significant effect, particularly on the first break point in the roll characteristic (ie C_μ^*). Increasing RPM (and hence velocity and Reynolds Number, with 500RPM $\approx$ 1.1×10^6 Re) at a fixed C_μ increased the break angle upto a maximum of around 35°. Given the presence of a lower-surface boundary layer trip, this seemed too large an

effect to be due to Reynolds Number alone, and a reexamination of Figure 5.36b revealed a very strong resemblance to the effects of increasing blowing level. For a given roll breakpoint the 'post-break' roll characteristics seemed very similar, and this is borne out by Figure 5.37, for three combinations of blowing level and RPM giving a break at around 25°. The only velocity effect is a reduction in the final 'slot stall' angle with increasing RPM. This would appear to be a true Reynolds Number effect, since it has been previously noted that at a fixed RPM/Re slot stall is almost independent of blowing level.

Two conclusions may be drawn from these results.

Firstly, the roll characteristics of asymmetric blowing are essentially a function of the angle of attack at which the blown vortex reestablishes, which in turn is governed by the ability of tangential blowing to modify the leading-edge separation. A consequence is that leading-edge geometry (for a given planform) will not affect the form of the roll moment characteristics, but only the blowing levels required.

Secondly, that C_μ does not seem to collapse the roll characteristics satisfactorily. The non-dimensional form of jet momentum coefficient has been widely used (and validated) in the field of circulation control aerofoils, where only the trailing-edge separation is modified. For leading-edge blowing on a delta wing, the separation location is governed by the equilibrium between the cross-flow around the leading-edge and the vortex feeding sheet. The additional factor of the presence of the vortex may explain the failure of C_μ to collapse the data.

Working from the available experimental results, Figure 5.38a shows the vortex re-establishment angle as a function of jet momentum and RPM, with a second order

polynomial fitted through the data. It can be seen that the effect of varying RPM/velocity at a fixed C_μ becomes relatively small at higher speeds, accounting for the apparently negligible influence of Re previously reported[108].

Cross-plotting gives Figure 5.38b, showing the jet momentum required for a given break angle as a function of RPM. From these curves

$$C_\mu = k(\alpha_{RB}).RPM^{-0.5}$$

Since for the 2.1m x 1.5m tunnel, centreline velocity is directly proportional to RPM, this implies that in order to collapse the data the V_∞^2 term in the jet momentum coefficient should be replaced by $V_\infty^{1.5}$. Unfortunately, this problem was not apparent until after completion of the experimental programme, so insufficient data is available to clarify the situation. Recent studies on F-18 forebody blowing[125] have cast doubt on C_μ as a scaling parameter for vortex control using TLEB; current investigations at the University of Bath into forebody blowing[9] will examine this question in more detail.

5.4.5 Slot Geometry Effects

As described in Section 5.3.3, some initial tests were undertaken with a parallel slot geometry, and roll moment characteristics are compared with the baseline configuration in Figure 5.39. Note that this data was measured with the original three-component balance, and is incorrect at high angles of attack, due to side-force coupling. In this case it is the relative behaviour that is important, and it can be seen that both display the same form of roll characteristic, although with the parallel slot requiring significantly higher blowing for a given roll moment. Similar increased blowing levels were observed for symmetric blowing (Figure 5.20a). The

109

correspondence of the shape of the roll characteristics provides some confirmation of the earlier discussion in Section 5.4.4 on possible leading-edge geometry effects, with the parallel slot less efficient as a consequence of excess blowing towards the apex.

The effect of shortened slots on roll characteristics is shown in Figure 5.40, for ¾ and ½ length slots. The reduced effect on the vortical flow discussed in Section 5.3.3 for symmetric blowing is evident in the lower levels of roll moment, though the form of the characteristics is similar to the full-length slot. The most significant effect is the delay of the 'slot stall' angle of attack to past 80°. It was observed from pressure data for full-length slots that the stall tended to start at the rear, perhaps due to the reduced local leading-edge radius/span ratio, progressing rapidly forward with increasing angle of attack (typically 1-2° from onset to complete stall). Shortening the slot from the rear has a much greater effect than might be expected from this, with a delay of onset of more than 15°. Presumably, the initial occurrence of slot stall at the rear of the full-length slot destabilises the crossflow and precipitates premature separation further forward.

5.5 Asymmetric Blowing with Roll Angle

5.5.1 Aerodynamic Characteristics

The general effects of roll (or sideslip) angle on the roll moment characteristics of asymmetric blowing are illustrated by Figure 5.41, for a fixed roll angle of +20°. A comparison with Figure 5.21 shows an increase in recovery ('out-of-roll') control power and a reduction in manoeuvre ('into-roll') moments. Manoeuvre capability is further limited by an accelerated onset of slot stall on the left ('up') side. The effects of varying roll angle are shown in Figure 5.42, for increasing right-side blowing at fixed pitch angles. At 30° and 40° pitch the loss of manoeuvre power with increasing roll is evident, with a maximum trim roll angle of around 20°. At higher pitch angles,

all 'into-roll' capability is lost, though this tends to be masked by the accelerated onset of slot stall on the 'up' side and the consequent hysteresis loops.

In a similar manner to blowing at zero roll angle, mixed blowing can to some extent linearise the roll characteristics (Figure 5.43), though limited by onset of slot stall.

The shift in onset of slot stall with roll angle is shown in Figure 5.44, with reducing effective leading-edge sweep delaying onset and vice-versa. This is probably a result of the change in effective leading-edge shape, with the windward side approaching a circular profile and the leeward side becoming more elliptical.

5.5.2 Upper-Surface Pressures

The effects of roll angle on upper-surface pressure distributions with blowing are identical in form to the unblown data shown in Figure 5.11. Discussion will therefore be limited to some results derived from the pressure data.

Figure 5.45 shows the effect of roll angle on vortex burst onset at $x/c = 0.2$ for a 'one-sided' blowing level of 0.04. On the blown side, the shift in burst onset follows the 'no blowing' curve, with some increase in blowing effectiveness as the blown leading-edge sweep reduces. On the opposite unblown side the corresponding increase in sweep angle has a very similar effect to the 'no blowing' case, with negligible change in the offset due to opposite blowing. If the sense of the roll angle is such that the unblown leading-edge sweep reduces (ie blown leading-edge sweep increases), the offset in burst onset due to opposite blowing falls off very rapidly. In other words, for high roll angles with blowing on the 'up' side the vortex burst coupling is reduced but for blowing on the 'down' side is unchanged.

111

To illustrate the effect of roll angle on the effectiveness of leading-edge blowing Figure 5.46 shows pressure-integrated local normal force at x/c = 0.5 from the right-side only, with the split between inboard and leading-edge contributions as defined in Section 5.3.2. Figure 5.46 presents data for symmetric blowing, but asymmetric blowing shows almost identical behaviour on the blown side. For a fixed blowing level, reducing effective leading-edge sweep increases right-side normal force (and hence roll moment contribution) from both the inboard and leading-edge regions, over the entire angle of attack range tested. The converse is true for increasing effective leading-edge sweep. A significant feature is that roll angle has almost no effect on the angle of attack at which the blown vortex forms.

Roll angle effects on critical asymmetric blowing characteristics are summarised in the table below:

Relative to Zero Roll Angle	DOWN Side Blowing		UP Side Blowing	
	BLOWN Side	UNBLOWN Side	BLOWN Side	UNBLOWN Side
Vortex Formation	Unchanged	-	Unchanged	-
Slot Stall	Later	-	Earlier	-
Burst Offset	Increased	Unchanged	Unchanged	Reduced
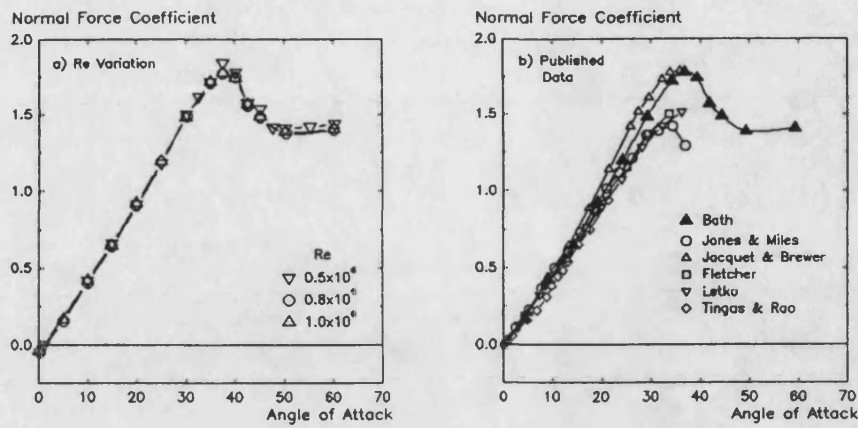
Figure 5.1 Unblown Normal Force Characteristics
a) Reynolds Number Effects
b) Comparison with Published Data[42,43,122..124]
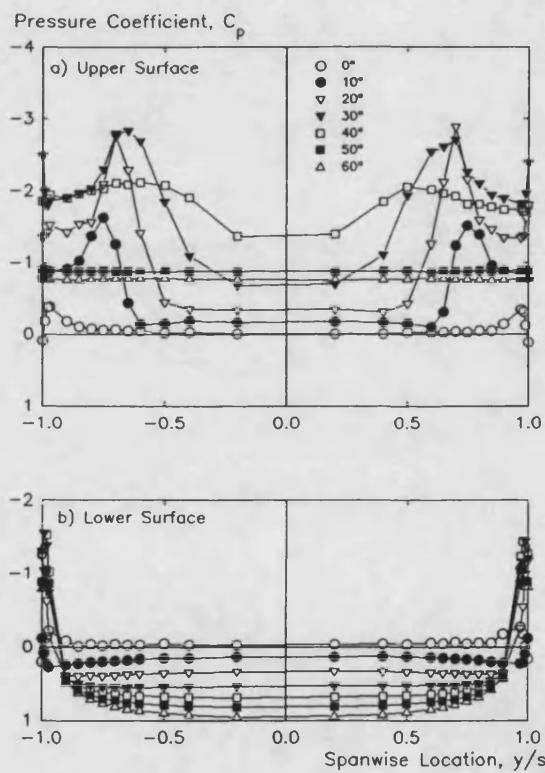
Figure 5.2 Effect of Angle of Attack on Upper and Lower-Surface Spanwise Pressure Distributions (x/c = 0.5)

113
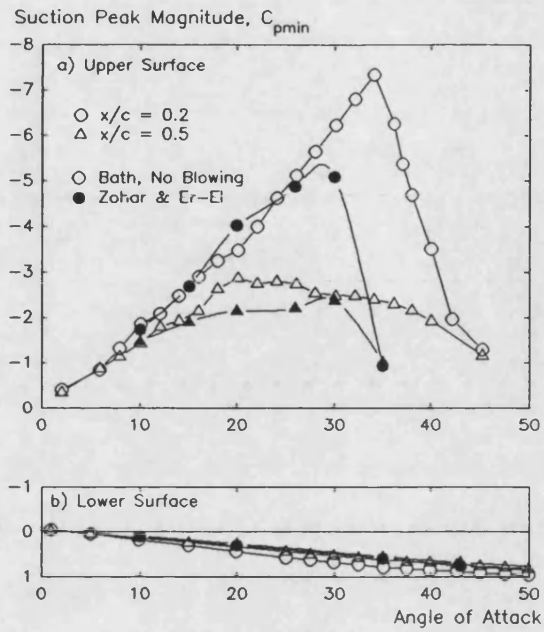
Figure 5.3 Comparison of Vortex-Induced Suction Peak Magnitude with Published 60° Delta Wing Data[81]
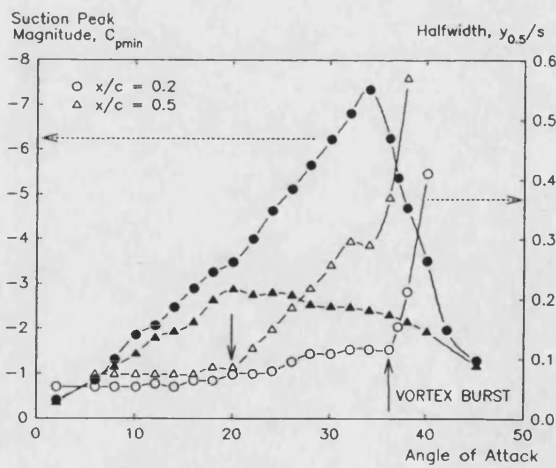
Figure 5.4 Variation of Unblown Vortex-Induced Suction Peak Magnitude and Halfwidth with Angle of Attack (x/c = 0.2, 0.5)

114
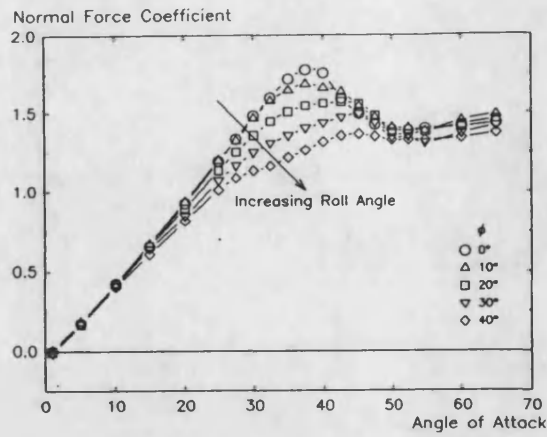
Figure 5.5 Effect of Roll Angle on Unblown Normal Force Characteristics
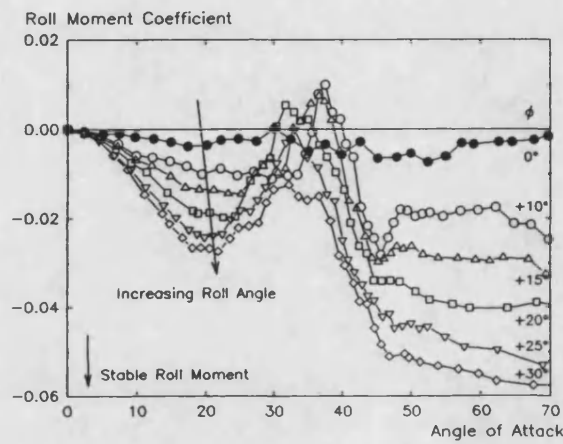
Figure 5.6 Effect of Roll Angle on Unblown Roll Moment Characteristics
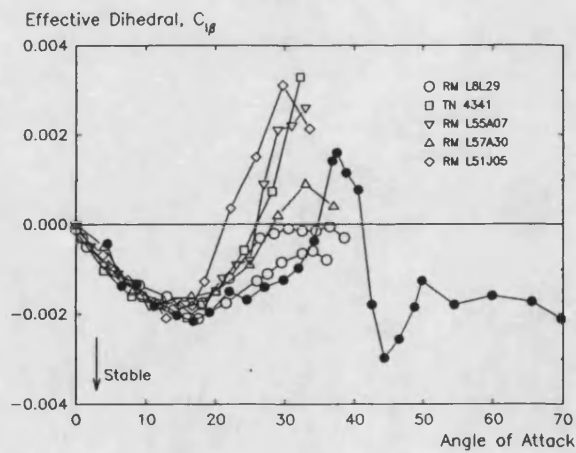
Figure 5.7   Comparison of 'Effective Dihedral' with Published Rounded Leading-Edge 60° Delta Wing Data[36,42-44,122]

115

Pressure Coefficient, C_p

a) Upper Surface

b) Lower Surface

Windward ('down')
Leading-Edge

Spanwise Location, y/s
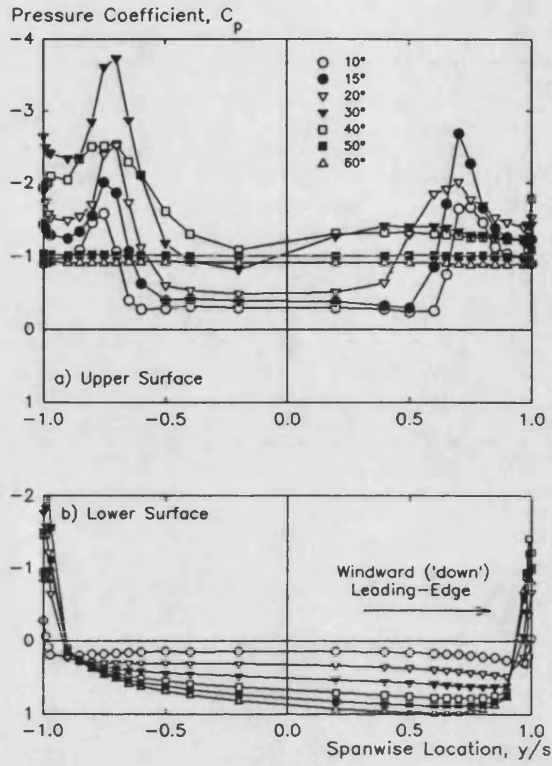
Figure 5.8 Effect of Angle of Attack on Upper and Lower-Surface Spanwise Pressure Distributions with +20° Roll Angle (x/c = 0.5)

Suction Peak Magnitude, C_{pmin}

25° Pitch Angle

15° Pitch Angle

○ Blown Wing, x/c = 0.5
● Er-El et al, x/c = 0.4

Windward
Leading-Edge
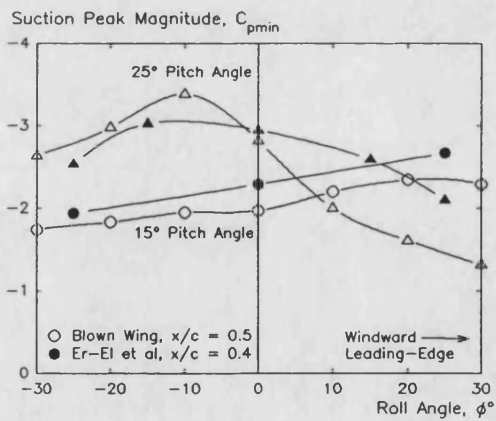
Roll Angle, $\phi°$

Figure 5.9 Comparison of Roll Angle Effects on Vortex-Induced Suction Peak Magnitude with Published Data[84]

116
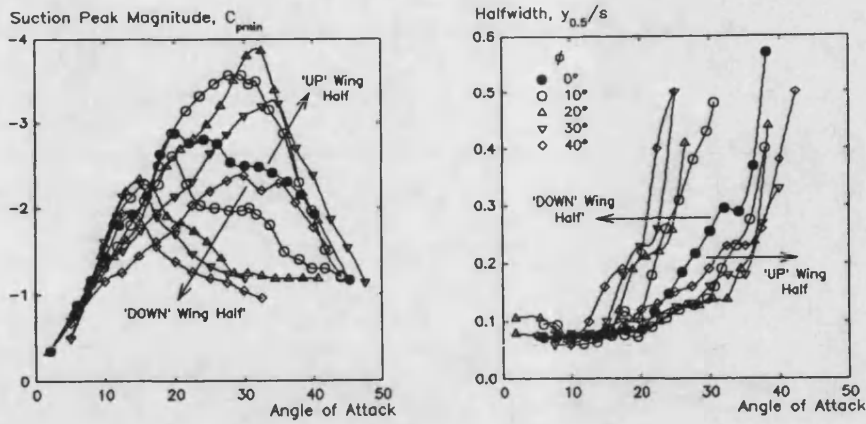
Figure 5.10 Effect of Roll Angle and Angle of Attack on Magnitude and Halfwidth of Vortex-Induced Suction Peak (x/c = 0.5)
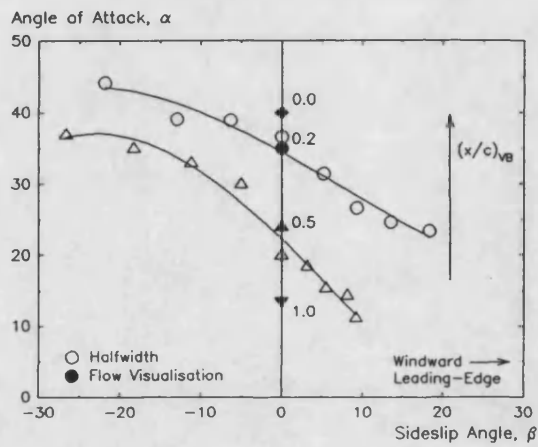
Figure 5.11 Effect of Roll/Sideslip Angle on Vortex Burst Trajectory
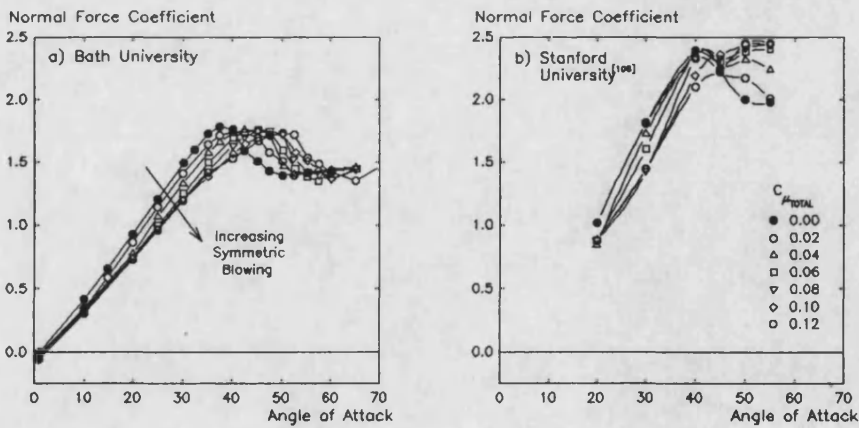
Figure 5.12 Effect of Symmetric TLEB on Full-Span Wing Normal Force Characteristics
a) Bath University
b) Stanford University[108]

117
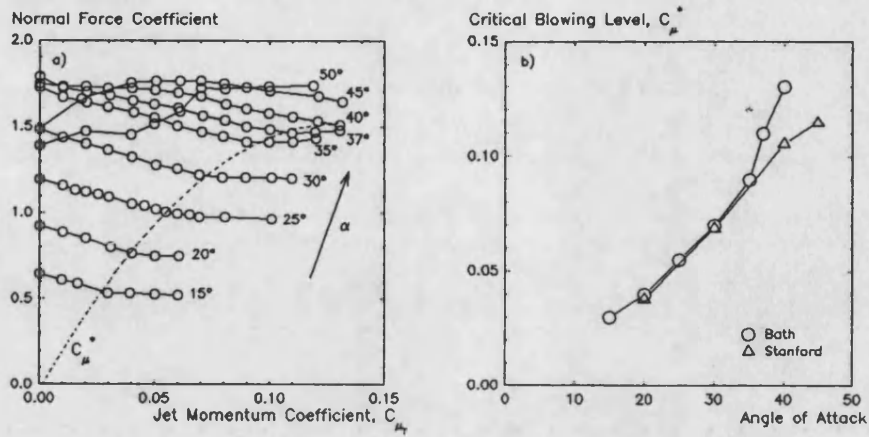
Figure 5.13 Effect of Increasing Symmetric Blowing at Constant Angle of Attack
　　　　a) Normal Force Characteristics
　　　　b) 'Critical' Blowing Level
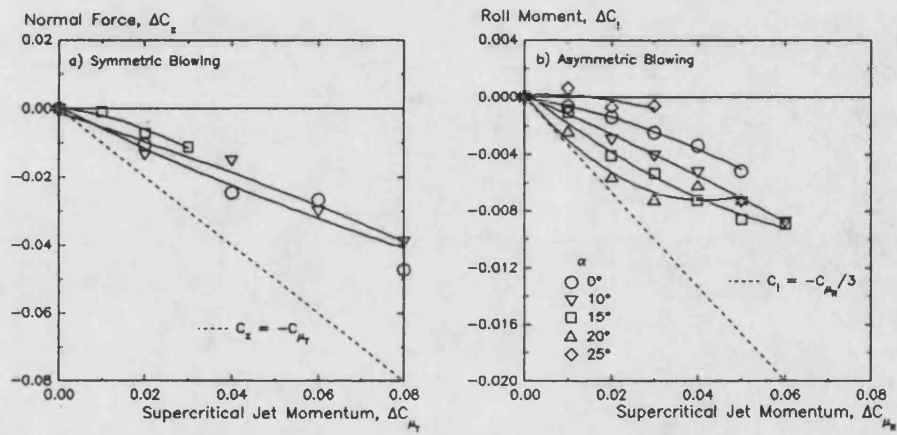
Figure 5.14 Residual C_μ-dependent Characteristics of Supercritical TLEB
　　　　a) Normal Force due to Symmetric Blowing
　　　　b) Roll Moment due to Asymmetric Blowing

118
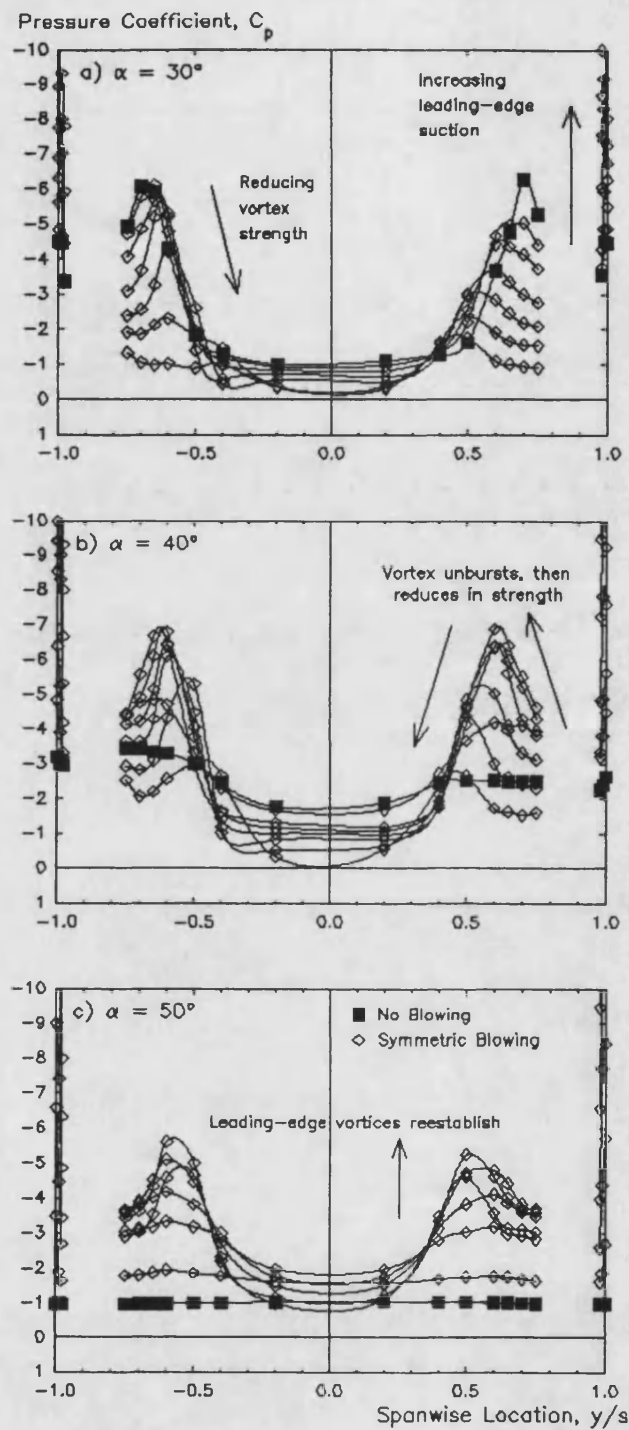
Figure 5.15 Effect of Increasing Symmetric Blowing on Spanwise Upper-Surface Pressure Distributions (x/c = 0.2)

119
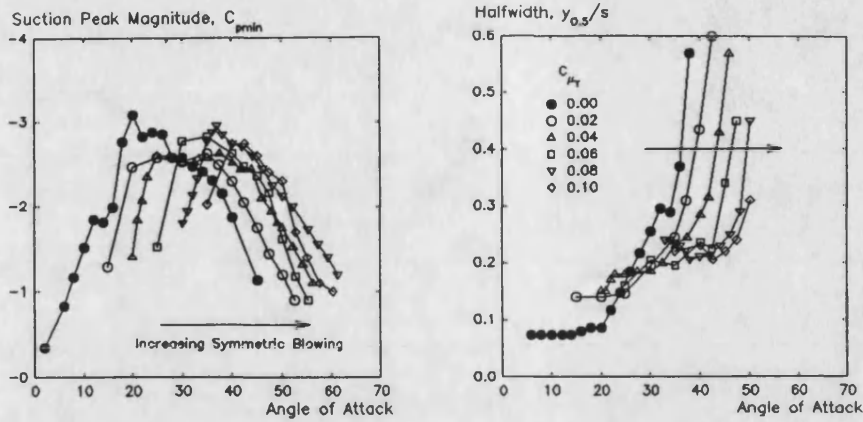
Figure 5.16 Effect of Increasing Symmetric Blowing on Magnitude and Halfwidth of Vortex-Induced Suction Peak (x/c = 0.5)
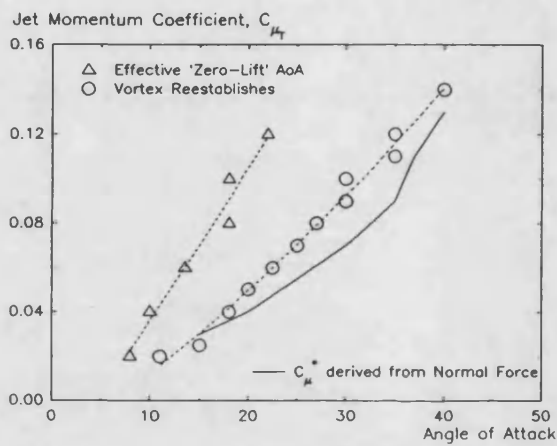
Figure 5.17 Effect of Increasing Symmetric Blowing on Vortex 'Zero-Lift' and Reestablishment Angles of Attack
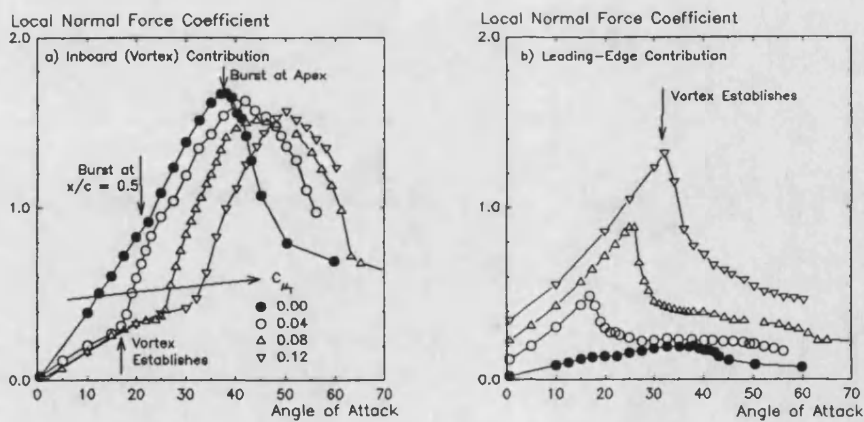
Figure 5.18 Effect of Increasing Symmetric Blowing on Pressure-Integrated Upper-Surface Contributions to Local Normal Force at x/c = 0.5

120
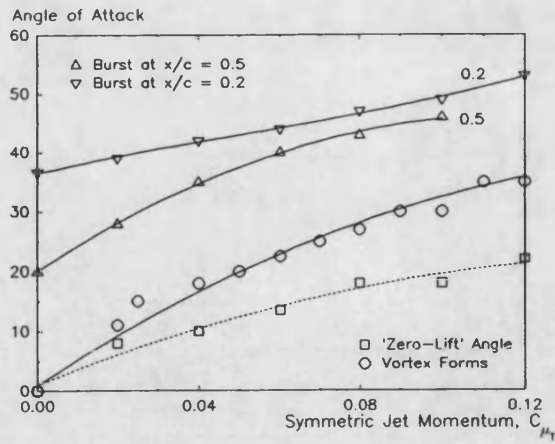
Figure 5.19 Effect of Symmetric Blowing on Vortex Burst Trajectory
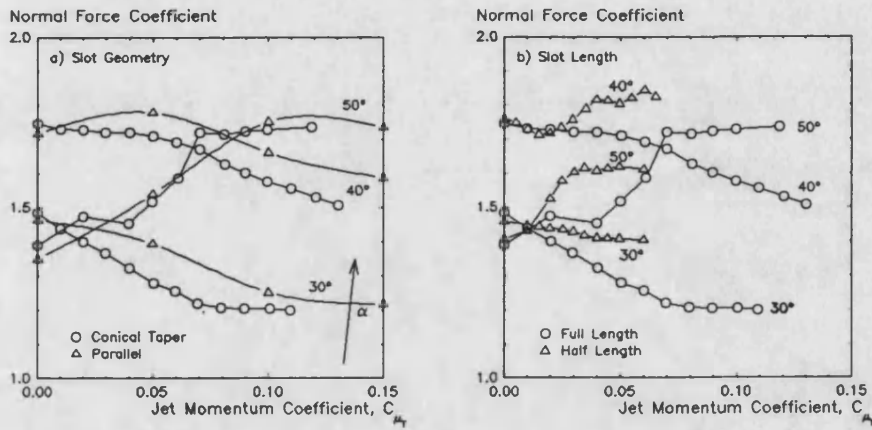
Figure 5.20 Effect of Slot Geometry on Normal Force due to Symmetric Blowing
a) Parallel vs Conical Slot
b) Slot Length
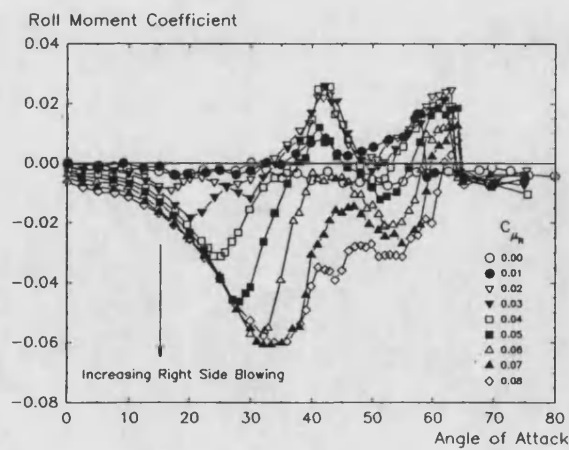
Figure 5.21 Roll Moment Characteristics of Asymmetric (Right-Side) TLEB, for Increasing Angle of Attack at Constant Blowing Level

121
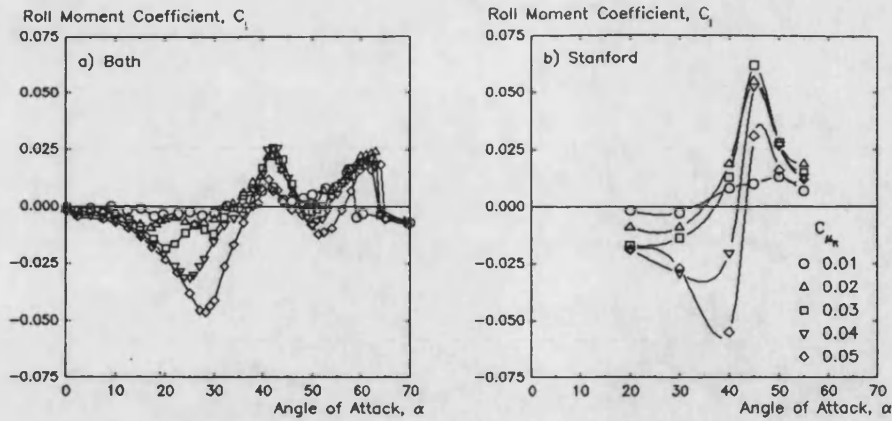
Figure 5.22 Comparison of Roll Moment Characteristics of Asymmetric Blowing with Previous Work at Stanford University[108]
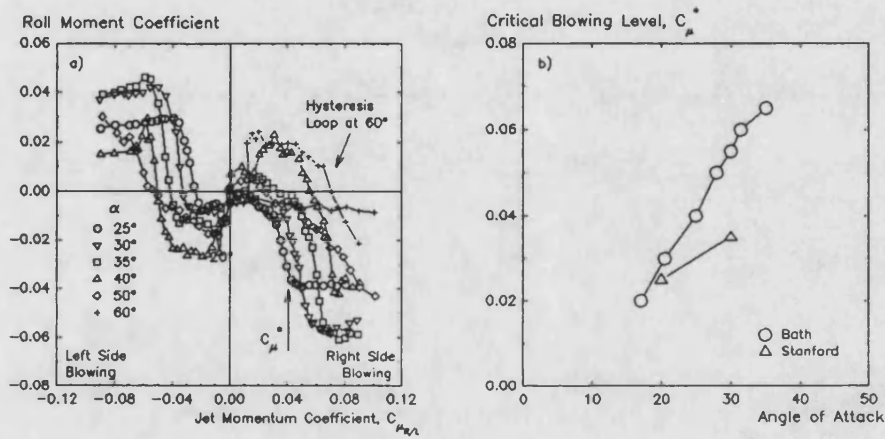
Figure 5.23 Effect of Increasing Asymmetric Blowing at Constant Angle of Attack
   a) Roll Moment Characteristics
   b) 'Critical' Blowing Level
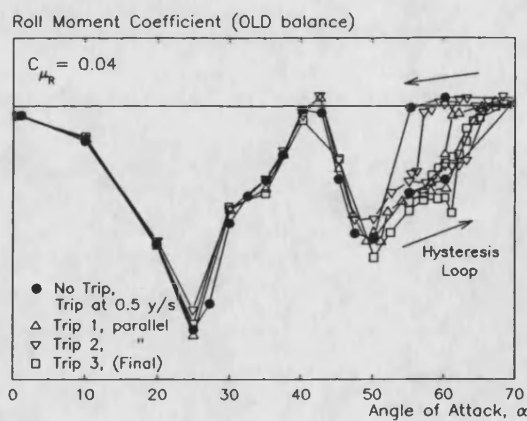
Figure 5.24 Effect of Lower-Surface Boundary Trip on 'Slot Stall' Hysteresis

122

a) Low Angle of Attack

i) Unblown — Separation Point

ii) Blown — Coanda Jet

b) High Angle of Attack

i) Fully Stalled (or Unblown) — Separation Ahead of Slot

ii) Blown, Unstalled — Jet Maintains Attached Flow
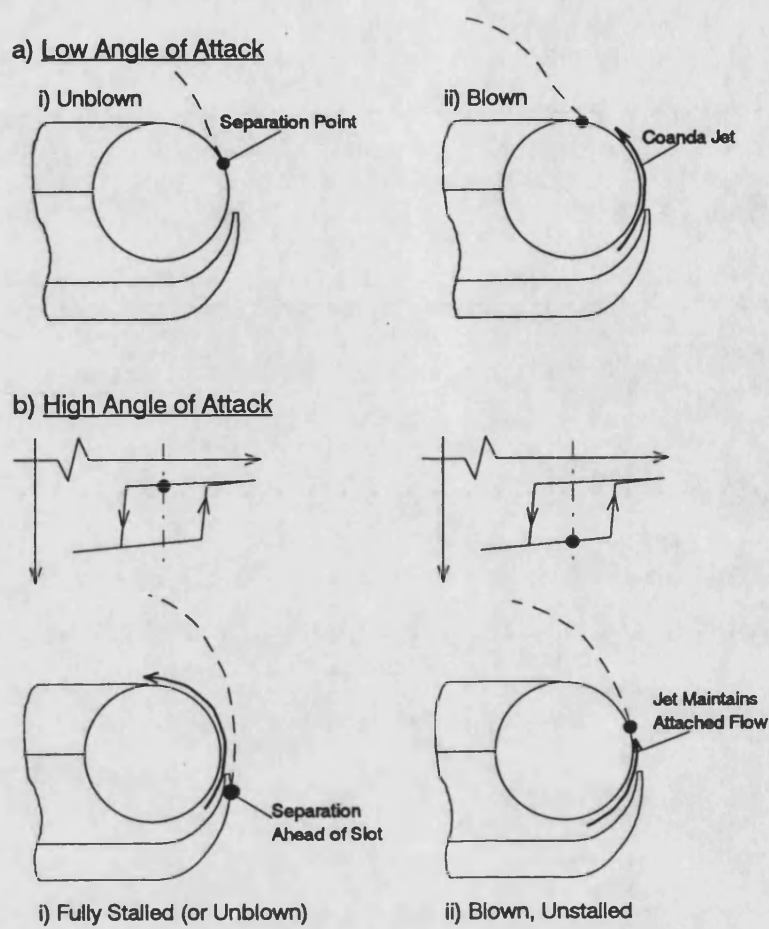
Figure 5.25 'Slot Stall' Hysteresis

Roll Moment Coefficient

$C_{\mu_{TOTAL}} = 0.08$, increasing RIGHT side blowing

C_μ(left/right)
● 0.04/0.04
□ 0.03/0.05
△ 0.02/0.06
▽ 0.01/0.07
◇ 0.00/0.08
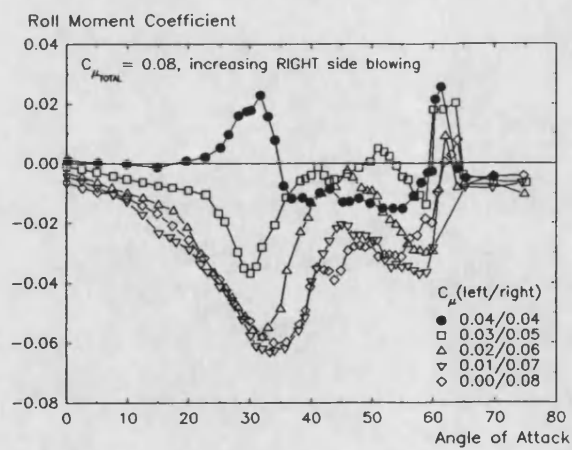
Angle of Attack

Figure 5.26 Roll Moment Characteristics of 'Mixed' Asymmetric Blowing (Constant Total Blowing Level, $C_{\mu T} = 0.08$)

123
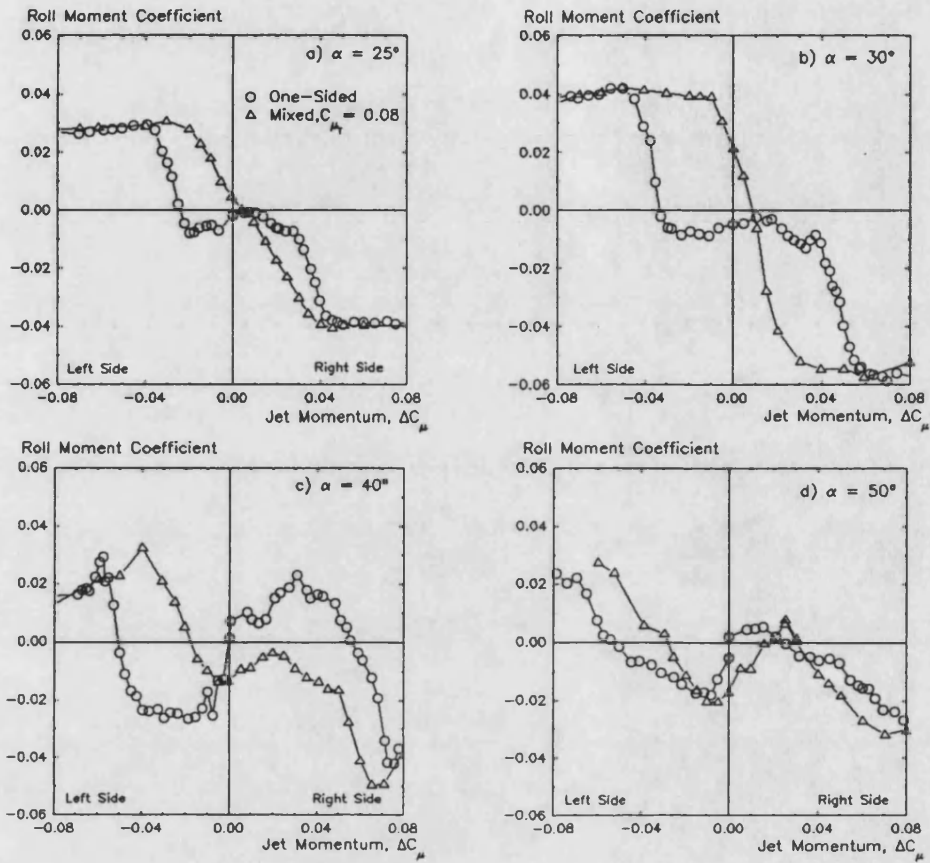
Figure 5.27 Comparison of 'One-Sided' and 'Mixed' Asymmetric Blowing at Constant Angle of Attack ($\alpha = 25°$, $30°$, $40°$, $50°$)
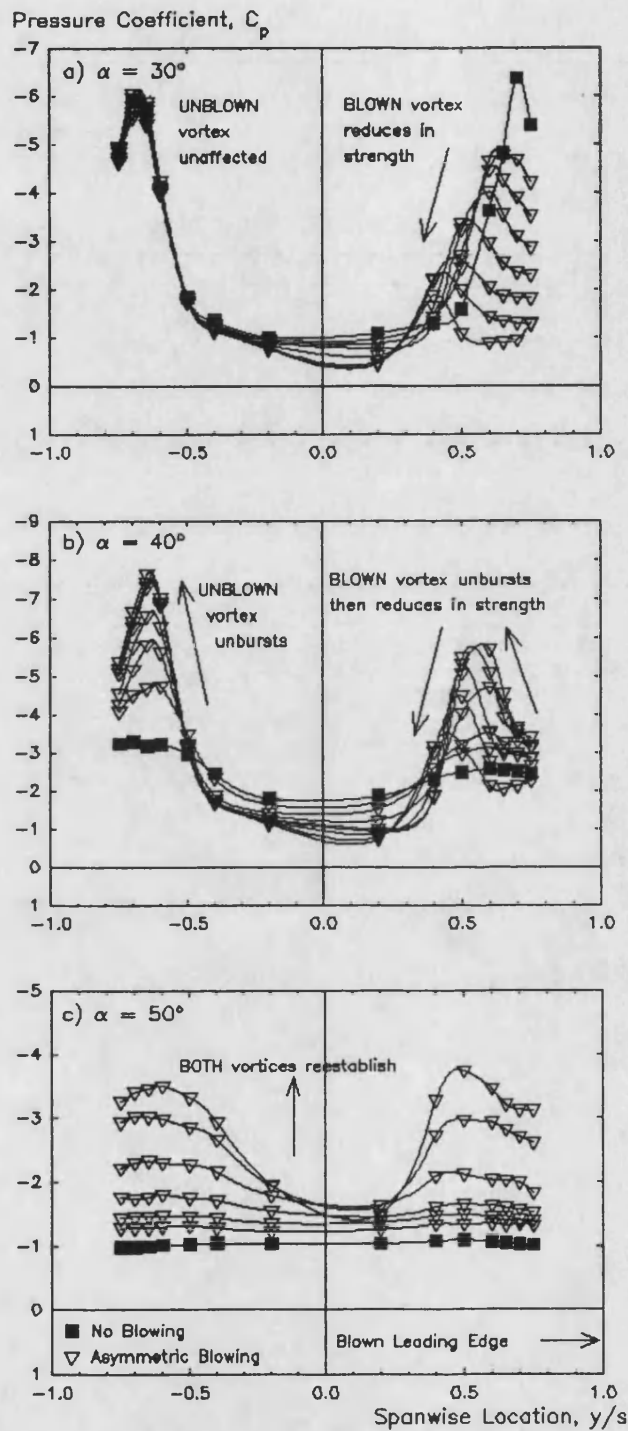
Figure 5.28 Effect of Increasing Asymmetric (Right-Side) Blowing on Spanwise Upper-Surface Pressure Distributions (x/c = 0.2)
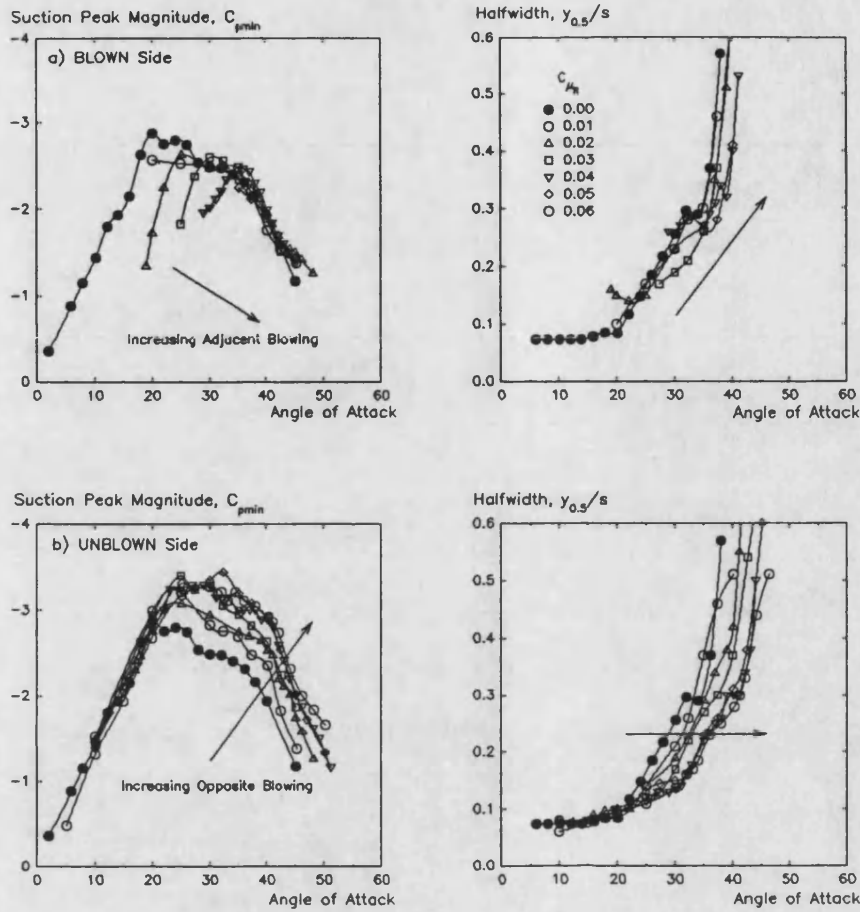
Figure 5.29 Effect of Increasing Asymmetric Blowing on Magnitude and Halfwidth of Vortex-Induced Suction Peak (x/c = 0.5)
a) Blown Vortex
b) Unblown Vortex
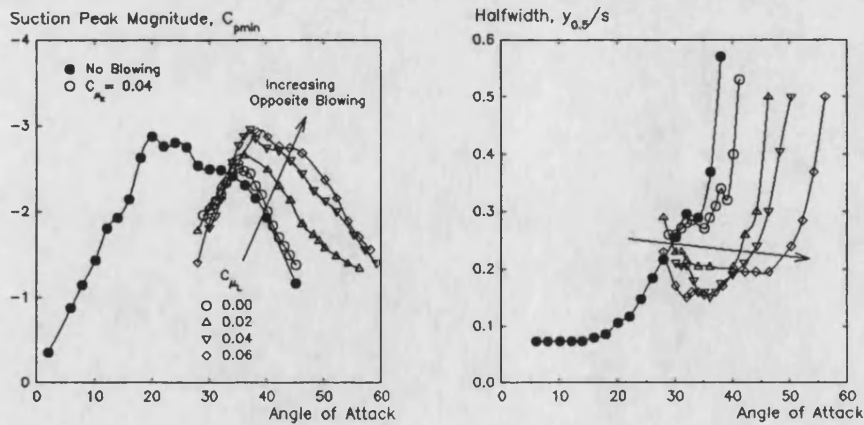
Figure 5.30 Effect of 'Mixed' Asymmetric Blowing on Magnitude and Halfwidth of Right-Side Vortex-Induced Suction Peak (Constant Right-Side Blowing, $C_{\mu R}$ = 0.04, Increasing Left-Side Blowing, $C_{\mu L}$ = 0.00 to 0.06, x/c = 0.5)

126
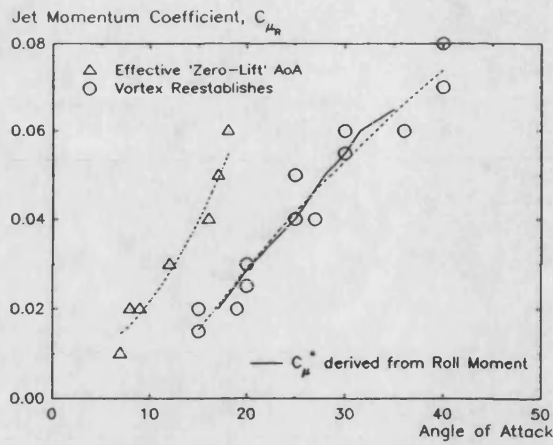
Figure 5.31   Effect of Increasing Asymmetric Blowing on Vortex 'Zero-Lift' and Reestablishment Angles of Attack
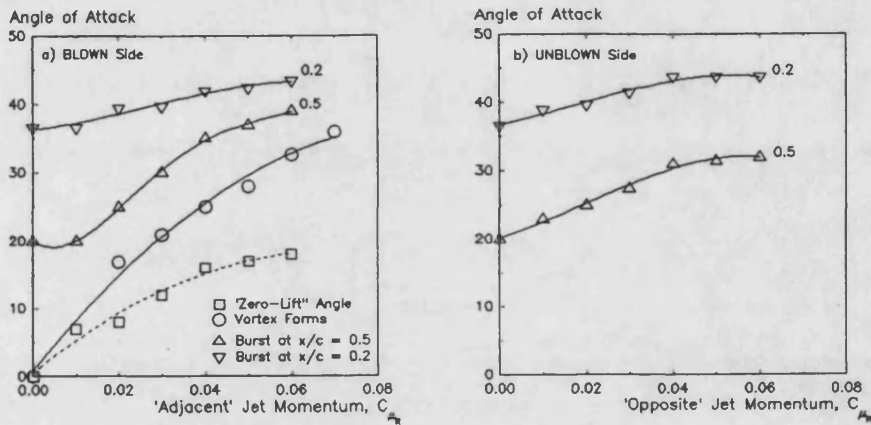
Figure 5.32 Effect of Asymmetric Blowing on Vortex Burst Trajectory
a) Blown Vortex
b) Unblown Vortex
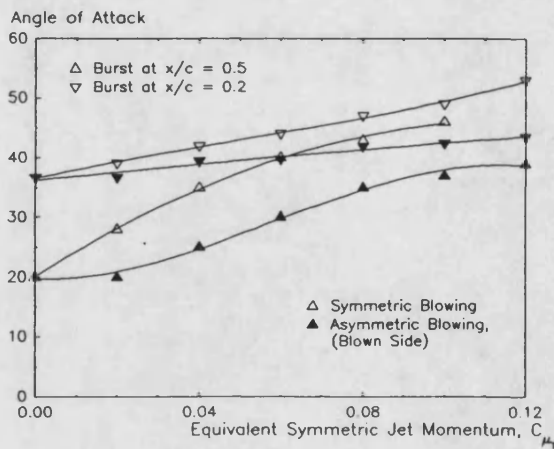
Figure 5.33   Comparison of Blown Vortex Burst Shift due to Symmetric and Asymmetric Blowing

127
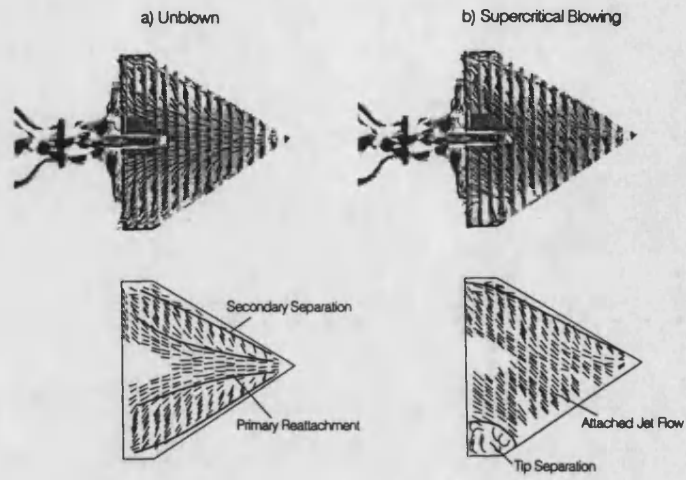
Figure 5.34 Wool Tuft Flow Visualisation (Right-Side Blowing, $\alpha = 25°$)
a) Blowing Off
b) Supercritical Blowing
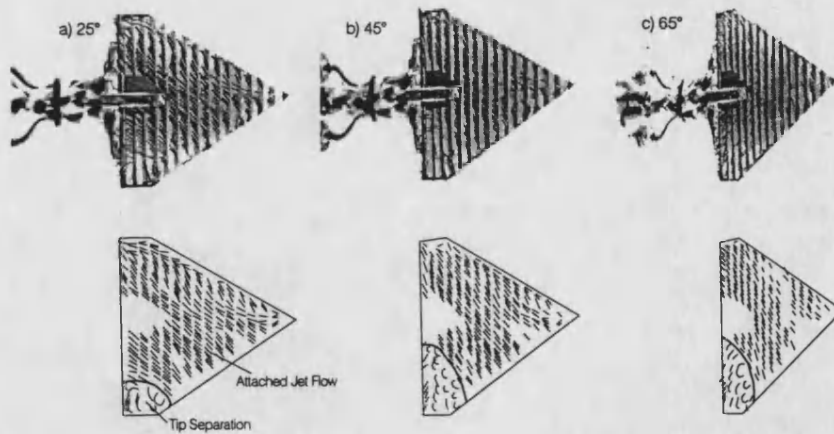
Figure 5.35 Effect of Increasing Angle of Attack on Tip Separation Region due to Right-Side Blowing

128
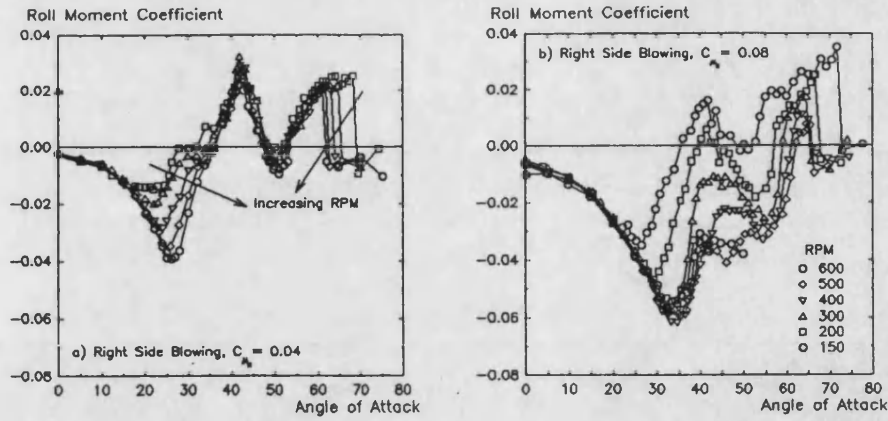
Figure 5.36 Effect of Varying Reynolds Number/Tunnel Speed on Roll Moment Characteristics of Asymmetric Blowing
a) $C_{\mu R} = 0.04$
b) $C_{\mu R} = 0.08$
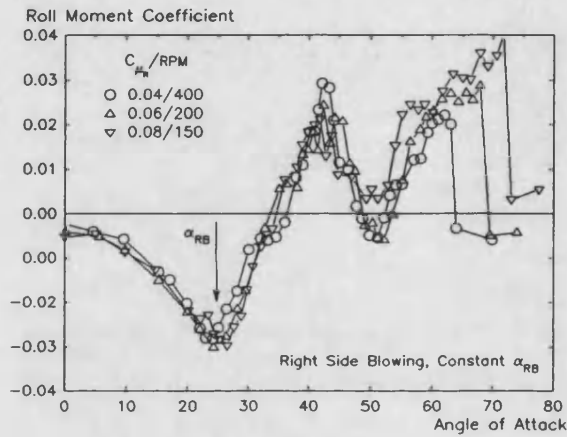
Figure 5.37 Dependence of Roll Moment Characteristics on Blown Vortex Formation Angle, α_{RB}
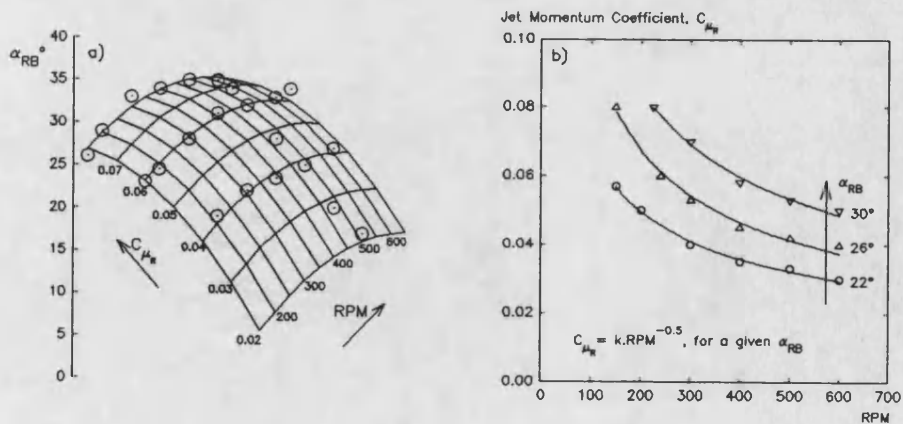
Figure 5.38 Effect of Blowing Level and Tunnel Speed on Blown Vortex Formation

129
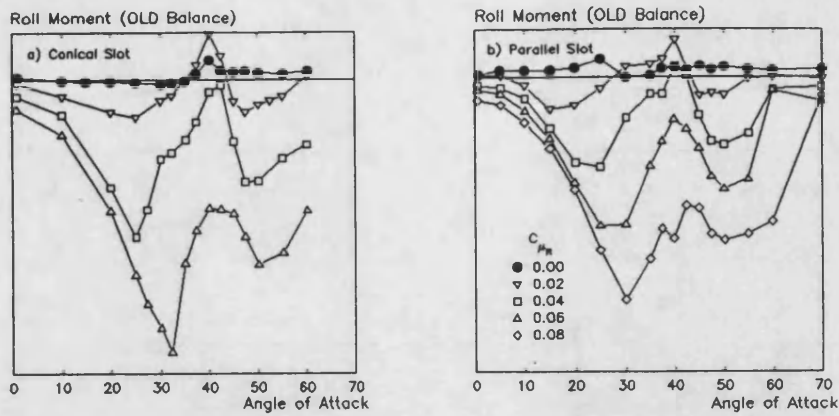
Figure 5.39 Effect of Slot Area Distribution on Roll Moment Characteristics of Asymmetric Blowing (Original Three-Component Balance Data)
a) Conical Slot
b) Parallel Slot
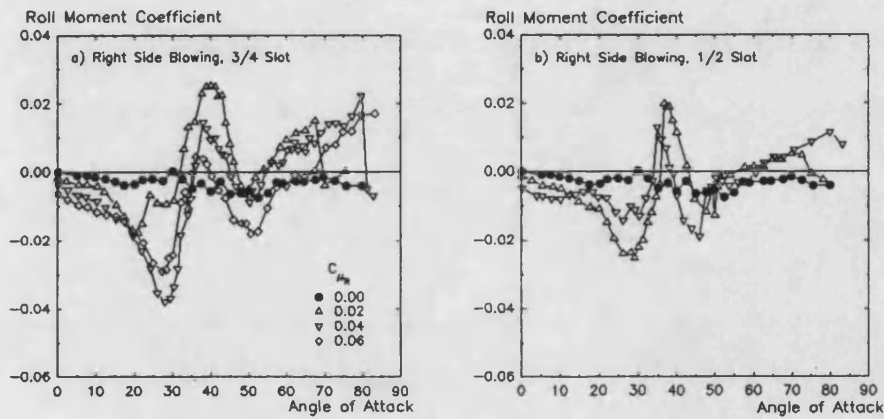
Figure 5.40 Effect of Slot Length on Roll Moment Characteristics of Asymmetric Blowing
a) ¾ Slot
b) ½ Slot
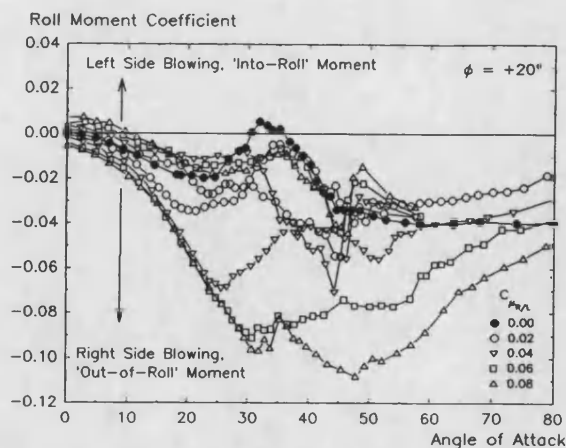
Figure 5.41 Effect of Roll Angle on Roll Moment Characteristics of 'One-Sided' Asymmetric Blowing (φ = +20°)

130
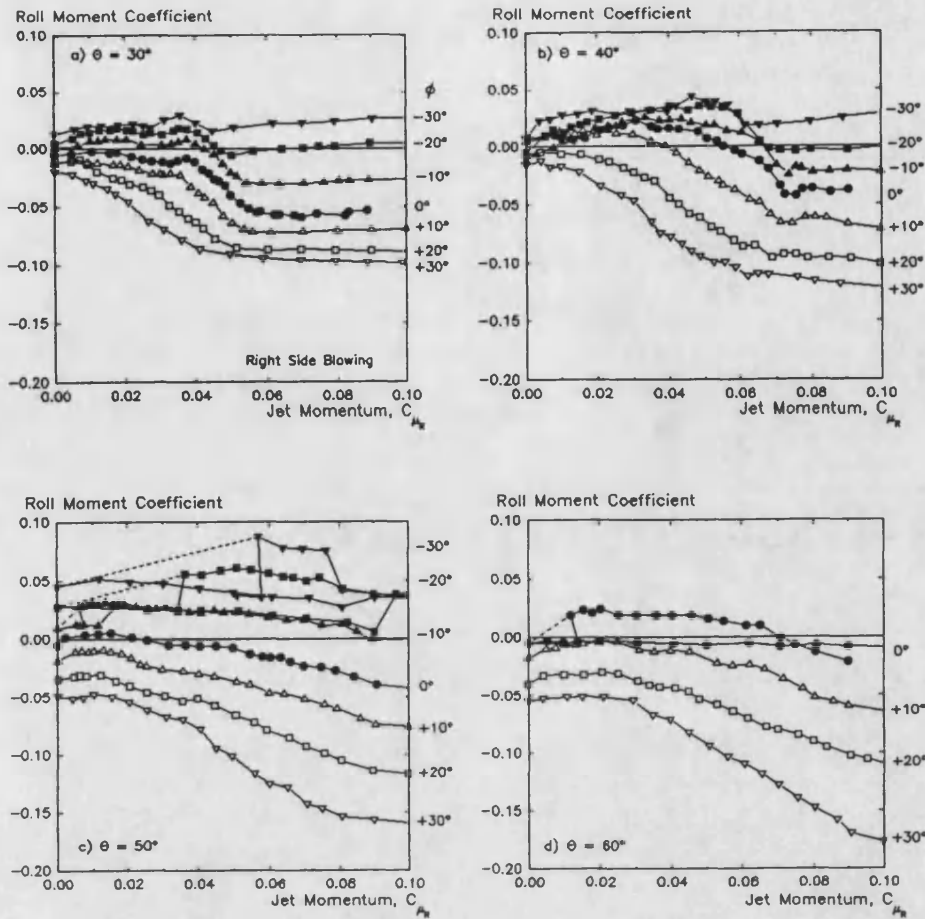
Figure 5.42 Effect of Varying Roll Angle on Roll Moment due to Increasing Right-Side Blowing at Constant Angle of Attack ($\theta = 30°, 40°, 50°, 60°$)
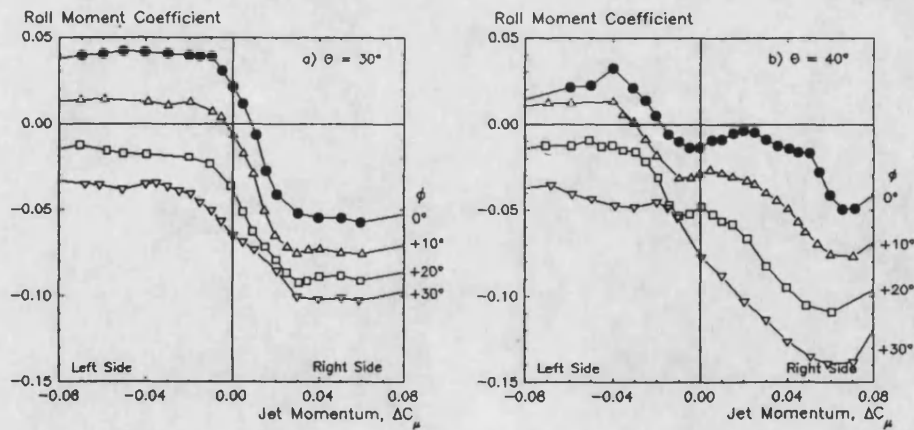
Figure 5.43 Linearisation of Roll Moment Characteristics with Varying Roll Angle Using 'Mixed' Asymmetric Blowing ($C_{\mu T} = 0.08$)

131
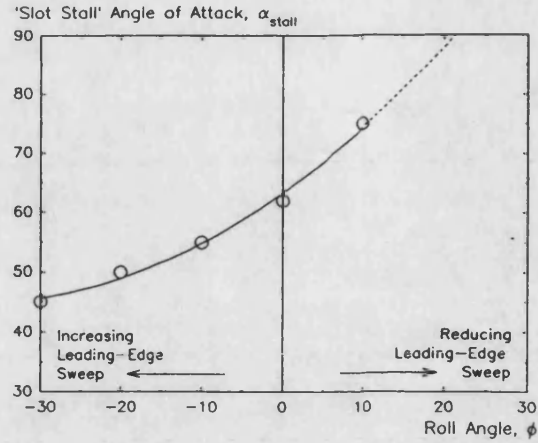
Figure 5.44 Effect of Roll Angle on 'Slot Stall' Onset
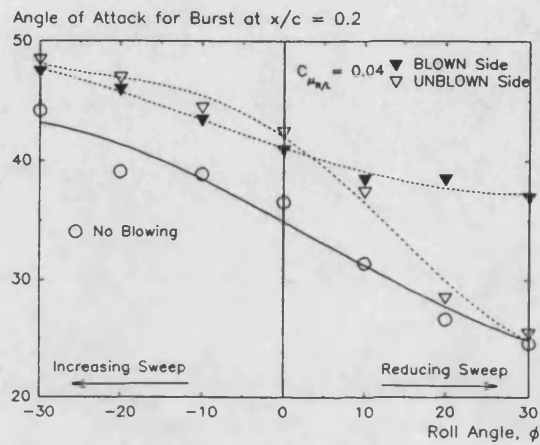
Figure 5.45   Effect of Roll Angle on Blown and Unblown Vortex Burst Shift due to Asymmetric Blowing
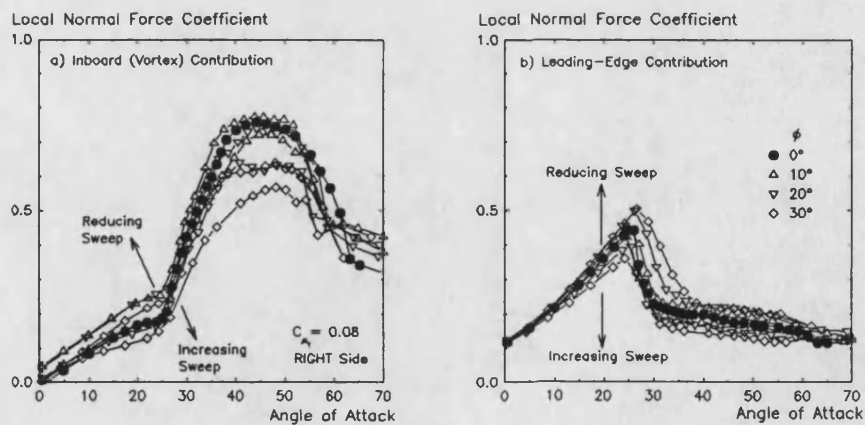
Figure 5.46   Effect of Roll Angle on Pressure-Integrated Contributions to Local Normal Force at x/c = 0.5 (Right-Side Only, $C_{\mu T}$ = 0.08)

132

CHAPTER 6

GENERATION OF LATERAL CONTROL FORCES

6.1 Introduction

The experimental results presented in Chapter 5 show that asymmetric TLEB has the capability to generate roll moments upto very high angles of attack. However, the application of the concept as a flight vehicle control system will require an understanding of the mechanisms underlying the complex characteristics typified by Figure 5.21.

The roll moments due to asymmetric blowing have been previously postulated[109] to be a complex balance between contributions from the jet-induced leading-edge suction and the leading-edge vortex, with the vortex component complicated by the strong coupling of blown and unblown burst trajectories. This chapter presents an evaluation of the nature and relative magnitudes of these contributions, based on an analysis of experimental data. From the analysis, a simple flow model derived from the Leading-Edge Suction Analogy is developed and some predictions of wing planform effects made. Finally, the application to full-scale aircraft is discussed.

6.2 Analysis of Roll Moment Generation

6.2.1 General Roll Characteristics

Figure 6.1 shows a typical roll moment curve for 'one-sided' asymmetric blowing ($C_{\mu R}$ = 0.04), with a number of well-defined regions evident. In particular, two 'roll reversal' regions are apparent. The primary data source for analysis of these roll characteristics is the spanwise upper-surface pressure distributions; as a justification of this approach, Figure 6.2 shows the roll moment curve of Figure 6.1 compared with

local roll moment coefficients derived from upper-surface pressure integrations at x/c = 0.2 and 0.5.

At low to medium angles of attack the measured roll moment follows the pressure data, particularly the x/c = 0.5 curve (suggesting that the roll characteristics are dominated by the aft portion of the wing, as one might expect from the greater moment arm). The pressure data did show a significant zero offset corresponding to the jet momentum flux at the leading-edge - from consideration of internal and external flow paths it was clear that this must be largely counterbalanced by an internal reaction in the slot passage so for purposes of comparison the zero offset was removed. A small residual C_μ-dependent roll moment does in fact remain (Figure 5.14b), but this is probably due to the jet separation from the upper-surface.

The curves diverge at higher angles of attack, with the pressure-integrated data showing no evidence of the second roll reversal region. The accuracy of the balance data was confirmed by unlocking the roll clamp on the sting mount and observing the direction of motion of the wing. It was postulated that an event at the rear of the wing (where no pressure data was available) was responsible, and this was confirmed by flow visualisation (Section 5.4.3). An extensive region of very unsteady separated reverse flow was observed at the tip on the blown side (Figure 5.34), which increased in extent with angle of attack (Figure 5.35). A simple estimate verified that the associated probable lift loss was sufficient to generate the second roll reversal.

The close correspondence of the pressure-integrated and measured roll moments trends in Figure 6.2 (excepting the contribution of the tip separation) confirmed that an examination of the pressure data would enable the various contributions to the roll characteristics to be identified with confidence.

6.2.2 Contributions to Roll Moment

'Low' Angles of Attack

For purposes of this discussion, a 'low' angle of attack is one at which the leading-edge vortices are either fully suppressed by blowing or present but unburst, corresponding to regions I and II in Figure 6.1.

The first break in the roll characteristics (the boundary between regions I and II) was identified in Section 5.4.2 as the formation of the vortex on the blown side of the wing. Region I thus corresponds to attached flow on the blown side and an essentially unaffected (unburst) leading-edge vortex on the unblown side. The contribution of the unblown vortex flow is thus relatively straightforward. In order to quantify the contribution of the blown side it was useful to first examine the symmetric blowing case.

Figure 6.3 shows the pressure-integrated local total (upper and lower-surface) normal force curves at x/c = 0.2 and 0.5 for supercritical (ie leading-edge vortices suppressed) symmetric blowing. It can be seen that they correspond closely to the behaviour predicted by RT Jones' slender wing theory predictions for fully attached flow[66] (Figure 2.20), and show little sign of the rapid reduction in loading towards the trailing-edge predicted by lifting-surface theory for finite wings. For supercritical blowing, the blown flowfield thus corresponds closely to a fully attached, conical slender wing flow. The effect of the finite leading-edge radius can be seen in the spanwise lift distribution (Figure 6.4), with the leading-edge suction peak reduced in magnitude and shifted inboard compared with the theoretical sharp-edged wing prediction.

Overall then, supercritical symmetric blowing gives a resultant total normal force that

varies approximately with $\sin\alpha$. However, for asymmetric blowing region I exhibits a roll moment curve more akin to a $\sin^2\alpha$ trend. The reason for this becomes clear if the pressure-integrated roll moment of Figure 6.2 is split into leading-edge and inboard contributions, as shown in Figure 6.5. It can be seen that on the blown side the $\sin\alpha$ normal force curve splits into a (roughly) $\sin\alpha.\cos\alpha$ inboard and a $\sin^2\alpha$ leading-edge contribution, with the leading-edge component dominating in roll due to the greater moment arm. The small 'dead-band' apparent for increasing blowing at constant angle of attack in this region is perhaps due to the gradual formation of the tip separation region. On the unblown side the combined inboard and leading-edge roll moment contributions are almost unaffected by opposite blowing.

In region II the blown vortex forms, while at the same time the leading-edge suction falls off as the separation point moves rapidly to the vicinity of the leading-edge. The redistribution of lift from the leading-edge to the inboard region results in a rapid loss of roll moment, though the overall normal force remains almost unchanged. As angle of attack is increased, the loss of leading-edge suction levels off and one would expect the roll moment curve to follow suit, with the unblown and blown vortex contributions increasing at about the same rate. However, two factors prevent this: first, the tip separation region gives an increasing roll moment loss and second, the vortex burst now comes onto the wing, first on the unblown then on the blown side. The asymmetry in burst trajectory and differing 'post-burst' characteristics gives the first roll reversal region (III).

'High' Angles of Attack

Within region II, the interaction of the vortex bursts occurs in the sub-region III, extending from burst onset on the unblown side to both bursts reaching the apex. The flowfield retains a vortical nature upto around 50°, where the vortex-induced upper-

136

surface suction peaks have completely subsided and the flow is essentially fully separated (Region IV). This area of the roll characteristic is terminated by the onset of slot stall (Section 5.3.2) above 60°.

The onset of burst on the unblown side has relatively little effect on roll moment contribution from the vortex, displaying only a modest reduction in slope. The roll moment contribution continues to increase with angle of attack, reaching a maximum as the burst reaches the wing apex. This is consistent with the general normal force characteristics for wings of this sweep angle (Section 2.3.3). The implication is that the lift loss due to the burst onset is gradual, and is initially offset by the increasing angle of attack. Once the burst reaches the apex, the vortical flow then subsides rapidly to a fully separated state at around 50°. On the blown side, however, the onset of burst is marked by a much more abrupt loss of roll moment, so that by the time the burst has reached the apex (around 45°) the vortical lift component has almost vanished.

Thus the initial roll moment loss in region II is due to the formation of the blown vortex, with a consequent reduction in leading-edge suction and roll moment arm. Burst onset on the unblown side coupled with a levelling-off of the leading-edge suction gives a small recovery, but this is overcome by the abrupt burst onset on the blown side to give the first roll reversal region. The reversal peaks when the unblown vortex burst reaches the apex. By around 50° the vortical flow has subsided (region IV) and the total roll moment is a product of a blown-side-up contribution from the jet-induced attached flow around the blown leading-edge and across the wing counterbalanced by a blown-side-down contribution from the tip separation region. The increasing extent of this separated flow region with angle of attack results in the second roll reversal.

6.2.3 Effect of Roll Angle - No Blowing

Before analysis of the effect of roll angle on asymmetric blowing characteristics it is necessary to consider the 'no blowing' case. In a similar manner to Figure 6.1 for asymmetric blowing, Figure 6.6 compares measured roll moment as a function of angle of attack for a roll angle of +20° with local values derived from pressure-integration on the upper-surface only. Again, the pressure data at x/c = 0.5 follows the measured total roll moment, although it is clear that an additional stabilising influence is present. This is provided by the asymmetric lower-surface pressure distribution (Figure 5.9). The contributions to the local roll moment are shown in Figure 6.7, which splits the pressure-integrated moment into left (leeward) side, right (windward) side and lower-surface components.

The lower-surface contribution is stabilising, increasing with angle of attack upto around 35°, then remaining approximately constant. On the upper-surface, before the onset of the vortex burst, roll angle has very little effect on lift/roll moment levels. At higher angles of attack the reduced effective leading-edge sweep angle on the right (down, or windward) side results in an earlier onset of burst, while on the opposite side the increased effective sweep angle delays the burst and also significantly affects the 'post-burst' behaviour. An explanation for the rapid loss of lift after the burst is suggested by Figure 5.12, which shows that the delay in burst onset due to sideslip/roll is greatest nearer the trailing-edge. For non-zero roll angle the burst will thus move more rapidly over the forward half of the wing, giving an accelerated lift loss aft of the burst.

Relating the trends of Figure 6.7 to the roll moment data of Figure 6.6, at low angles of attack the wing is stable in roll, due a combination the lower-surface asymmetry, and a small reduction in vortex lift on the leeward side as the vortex is displaced

upwards. Burst onset on the windward side is marked by the destabilising roll reversal, with the relatively gentle loss of lift post-burst evident in the gradual nature of the reversal. The trend is then reversed by burst onset on the leeward side, with the upper-surface contribution falling to zero by 50° as the vortical flow subsides. At higher angles of attack the roll moment is entirely due to the lower-surface, with the upper-surface exhibiting a completely separated, flat pressure distribution (Figure 5.9).

Coupled with Section 6.2.2, this analysis has some significance for the 'effective sideslip' analogy to asymmetric blowing developed in Section 3.3.4. This analogy was prompted by the similarity between the roll moment reversals due to sideslip and asymmetric blowing[109]. However, it can be seen from the above discussions that the reversals are a result of two different mechanisms. For sideslip, roll reversal is initiated by a gradual burst onset on the windward wing half, and is terminated by the abrupt lift loss due to a later burst onset on the leeward wing half. According to the analogy, for asymmetric blowing the blown side is equivalent to the windward wing half and the unblown side the leeward half. Although the unblown (=leeward) burst is delayed by opposite blowing, the blown (=windward) burst is delayed still further, due to a reduction in effective angle of attack. The roll reversal is initiated by the formation of the blown vortex, accelerated by burst onset on the blown side and terminated by the unblown burst reaching the wing apex.

Fortunately, although the original stimulus has been found to be incorrect, the 'effective sideslip' analogy still appears to hold for the burst trajectory coupling effect of asymmetric blowing, when the reduction in effective angle of attack of the blown vortex is taken into account.

6.2.4 Effect of Roll Angle on Asymmetric Blowing

The general characteristics of asymmetric blowing with non-zero roll angle were described in Section 5.5, with increasing roll increasing 'out-of-roll' recovery control power but reducing 'into-roll' manoeuvre capability. This is shown in Figure 6.8a for ϕ = +20° and right/left blowing levels of 0.04, with a comparison with pressure-integrated local roll moments at x/c = 0.5 in Figure 6.8b. The general trends are apparent in the pressure data, though the loss of manoeuvre power is not so marked.

The individual contributions to the roll characteristics are identified in Figures 6.9 (right/down side blowing) and 6.10 (left/up side blowing). Two primary factors can be seen to contribute to the trends identified above: an increase in the jet-induced attached flow contribution for blowing on the down side (and vice versa) and the effect on the unblown burst trajectory. The attached flow variation can be seen more clearly in Figure 5.46; for constant blowing the lift/roll contribution increases with reducing effective leading-edge sweep (or increasing effective aspect ratio). The effect of roll on burst trajectory coupling is shown in Figure 5.45, where blowing on the windward/down side has relatively little effect on the unblown burst (Figure 6.9). In contrast, blowing on the leeward/up side (Figure 6.10) has a considerable effect on the unblown burst, with the increased delay resulting in a further reduction in control power.

6.3 Analysis of Sideforce Generation

6.3.1 Sideforce Characteristics

During the later stages of the test programme it became clear from observation of model behaviour and from coupling effects on the original three-component sting balance that asymmetric blowing was generating a significant sideforce. Unfortunately this could not be measured directly, but an estimate of the magnitude was made from integration of the upper-surface (upright wing) and lower-surface (inverted wing)

leading-edge pressure data, as shown in Figure 6.11 for symmetric blowing; asymmetric blowing gave almost identical results on the blown side. Note that, because of the orientation of the tappings, this figure shows the sideforce perpendicular to the leading-edge. The local sideforce curves resemble the leading-edge contribution to normal force/roll moment (Figures 5.18b, 5.46b) for supercritical blowing, with an initial $\sin^2\alpha$ trend and an abrupt reduction as the blown vortex forms.

These sideforce characteristics have two important consequences. For symmetric blowing, the axial component corresponds to a recovery of leading-edge thrust and thus a reduction in lift-dependent drag[127]. For roll recovery using asymmetric blowing (ie blowing on the down side) the effect is adverse, with the sideforce directed towards the down wing half and thus tending to accelerate the resultant sideslip motion.

6.3.2 Comparison with Theory

RT Jones' slender wing theory predicts a constant local sideforce coefficient of $\frac{1}{2}\pi.\sin^2\alpha$ from each leading-edge for attached flow, while lifting surface methods for finite wings give a reduction towards the trailing-edge. The chordwise variation of sideforce coefficient derived from the 'supercritical' region of the pressure data of Figure 6.11 is shown in Figure 6.12 and compared with the RT Jones and lifting surface longitudinal distributions (divided by $\sin\Lambda$ to give the component perpendicular to the leading-edge, Figure 6.13). Clearly, the experimental data follows neither trend, though approaching the theoretical maximum towards the apex. Previous analysis of the pressure-integrated normal force data (Figure 6.3) showed an almost conical behaviour for supercritical blowing. It seemed unlikely therefore that this was a planform effect.

A more probable cause was thought to be the reduction in local leading-edge radius/span ratio towards the trailing-edge, with increasing (effective) sharpness limiting the recovery of leading-edge suction. An analogy was seen to the behaviour of 2-D aerofoils, where theoretical leading-edge thrust levels are not attained in practice. A semi-empirical correlation for attainable leading-edge thrust as a function of leading-edge radius, chord, Reynolds Number and Mach Number was developed by Carlson & Mack[78]. For a given Re and M, attainable leading-edge thrust is directly proportional to a thrust factor parameter, of the form

$$C_{LES}(\text{attained}) = k(Re,M).(t/c)^{0.6}.(r/c)^{0.24}.C_{LES}(\text{theoretical})$$

upto the maximum theoretical value of $2\pi.\sin^2\alpha$ (for a 2-D aerofoil).

On the assumption that the attached crossflow around the leading-edges of a slender wing resembles the (potential) leading-edge flow around a lifting aerofoil at 90° incidence (Figure 6.14), this correlation was applied to the sideforce characteristics, with chord replaced by the semispan and the freestream velocity replaced with the component normal to the wing.

The results are shown in Figure 6.15, giving sideforce as a function of thrust factor for the blown wing and for the limited published data[124,128,129] compared with the correlation of Carlson & Mack. The agreement is remarkable, with the exception of the results of Bartlett & Vidal[129] which display the same general trend, but with higher overall sideforce levels. The wing tested was a rounded leading-edge flat plate of very high thickness (t/c = 10%), giving a higher maximum sideforce, while the sideforce was derived from integration of pressure data read-off from graphs, a possible source of error. The other references quote sideforce directly, and these

142

datasets are very close to the correlation.

From Figure 6.15 it is clear that wings of a realistic profile, with a thrust factor typically in the region of 0.05, will show much lower levels of adverse sideforce when blown asymmetrically. Unfortunately, drag improvements with symmetric blowing will also be reduced.

6.3.3 Effect of Roll Angle on Sideforce

The effect of roll angle on the pressure-integrated sideforce at $x/c = 0.5$ (perpendicular to the leading-edge) is shown in Figure 6.16a. Increasing geometric leading-edge sweep appears to reduce sideforce, and vice versa. However, if the sideforce is resolved into the true crossflow component, allowing for the changing effective leading-edge sweep with angle of attack (at a constant roll angle), the curves collapse.

6.4 A 'Simple' Model of the Effects of Asymmetric Blowing

6.4.1 Background

As discussed in Section 2.5.3, the Leading-Edge Suction Analogy (LESA) has been shown to give a simple and accurate prediction of longitudinal and lateral characteristics of delta wings. The analogy equates the vortex lift to the (undeveloped) leading-edge sideforce in potential flow. The effect of separation is to rotate the sideforce vector through 90° and move it inboard. TLEB can be seen to resemble the reverse of this process, suggesting that the LESA may be used as a basis for a simple model of the effects of both symmetric and asymmetric blowing.

6.4.2 Extension of the LESA to High Angles of Attack

Before adapting the LESA to model TLEB effects, it was first necessary to clarify the effects of vortex burst on unblown longitudinal and lateral characteristics. Previous

studies[30,73] have had some success, but have not considered the very high angle of attack case where the burst approaches the apex and the vortical flow subsides.

For the cropped delta planform the vortex (K_{VLE}) and potential (K_P) LESA coefficients are 2.3 and 2.2 respectively. Allowing for the side-edge vortex lift contribution[76] gives an additional vortex lift coefficient (K_{VSE}) of 0.6, so that normal force becomes:

$$C_N = 2.2 \sin\alpha\cos\alpha + 2.9 \sin^2\alpha$$

Comparing this with the experimental data (Figure 6.17a) shows that the lift curve slope at low angles of attack is well matched, providing some confirmation of the values of K_V and K_P. The effect of burst onset can be seen in the relatively gentle departure from the theoretical curve at about 12° angle of attack. At around 36° the bursts reach the wing apex and the vortical flow starts to subside, giving the gentle stall typical of the lower sweep angles. By about 50° the upper surface flow is fully separated; the normal force in this region is considerably higher than the 'potential flow' term from the above equation. Clearly, at high angles of attack both the vortex and potential lift terms in the LESA require some modification. First, the potential lift term was considered.

Potential Lift

The magnitude of the 'potential' lift may be determined experimentally by measuring the lower surface normal force contribution[68]. Although insufficient pressure data was available on the blown wing to achieve this, the chordwise variation of the centreline pressures (in conjunction with full-span pressure integrations at $x/c = 0.2$ and 0.5) gave an indication of the potential lift distribution. The assumption made was that the local normal force at a given chordwise location is proportional to the

centreline pressure; this was verified at x/c = 0.2 and 0.5. Figure 6.18a shows the variation of mean centreline pressure with angle of attack and chordwise location. The 'zero lift' slope reduces towards the trailing-edge (Figure 6.18b), in a similar manner to the longitudinal loading distribution predicted by lifting surface methods[68] and hence inherent in the LESA. However, what is also evident from Figure 6.18a is that as angle of attack increases the lower surface normal force does not follow the $\sin\alpha\cos\alpha$ behaviour of the LESA, and in fact deviates further from this trend as the trailing-edge is approached.

To account for this variation, the local potential flow was modelled as

$$C_{np} = k_p(x).\sin\alpha.\cos(k(x)\alpha)$$

where both k_p and k are functions of chordwise location, x/c. The longitudinal distribution of k_p (Figure 6.18b) is that given by the LESA, hence the potential lift curve slope at low angles of attack is preserved. The longitudinal distribution of k, as derived from a curve fit to the centreline pressures of Figure 6.18a, is shown in Figure 6.19a. k extrapolates to 1.0 at the wing apex, and falls off rapidly to zero as the trailing-edge is approached; the local variation of potential lift thus goes from the LESA form ($\sin\alpha\cos\alpha$) at the apex to a $\sin\alpha$ curve at the trailing-edge. Figure 6.19b is a confirmation of the initial assumption that local normal force is proportional to centreline pressure, with normal force derived from the previous equation compared with full span integrations at x/c = 0.2 and 0.5.

Integrating the chordwise variation of local normal force, the overall potential lift component may be represented by an equation of the form:

$$K_P \sin(\alpha)\cos(0.4\alpha)$$

A very similar potential lift curve was obtained in Reference 68, although the longitudinal loading distribution was not reported.

At very high angles of attack, the vortex flow subsides and the upper surface flow is essentially fully separated, though the lower surface remains attached. The upper surface pressure distribution becomes flat, approaching a constant value of -0.65 as angle of attack increases towards 90°. In this flow regime, the 'potential' lift term becomes:

$$K_P/2 \, \sin(\alpha)\cos(0.4\alpha) + 0.65 \, \sin^2\alpha$$

This does not fully agree with the observed upper-surface pressures at high angles of attack (Figure 5.2), which reduce with angle of attack (presumably due to the separated flow remaining vortical in nature), but appears to give a good match to the measured normal force data.

Vortex Lift

Two factors govern the effect of vortex burst: the position of the burst, and the associated lift loss.

The burst trajectory was derived from Figure 5.11, in conjunction with published data (Figure 2.9, Reference 30). For the purposes of an initial analysis, burst trajectory was modeled by a straight line variation of x_{VB} with angle of attack (Figure 6.20a).

Very little quantitative information is available on the lift loss due to vortex

breakdown, but an examination of published lift data indicates that with the burst at the apex the vortex lift is roughly ⅓ to ½ of the corresponding unburst value. Lan and Hsu[73] assumed a simple reduction of lift aft of the burst, as sketched in Figure 6.20b. The lift loss factor was derived by fitting this model to the lift data of Wentz[27]; this factor is a function of wing planform, but is of the order of 0.5 for a 60° delta.

To evaluate this model, an estimate of the effective local vortex lift coefficient at x/c = 0.5 was made by subtracting the potential lift from the pressure-integrated upper-surface normal force. The results are plotted in Figure 6.21a, showing that from burst onset to 'burst at apex', Lan and Hsu's lift loss factor of 0.5 matches the experimental data well. However, it can also be seen that the lift loss begins gradually 10° ahead of burst onset, levelling out at burst onset, then increasing rapidly when the burst reaches the apex. The model of Lan and Hsu thus tends to give a too abrupt lift loss with burst onset, but was retained for this initial analysis because of its simplicity.

The simple model sketched in Figure 6.20b shows a conical lift distribution, whereas the real lift distribution shows a reduction towards the trailing-edge. However, an investigation of the effects of lift distribution (Figure 6.21b) showed that the total lift loss due to burst is relatively insensitive to the assumptions made. The two hypothetical burst trajectories shown are typical of 60° and 75° delta wings respectively, and also demonstrate the reason for the differing stall characteristics of low and high-sweep delta wings (Section 2.3.3, Figure 2.11).

The effect of incorporating these modified potential and vortex lift models in the LESA is shown in Figure 6.17b. The lift characteristics are matched very well, considering the simplicity of the assumptions made. As implemented, the vortex lift was assumed to fall to zero when the burst reached the apex, giving the discontinuity

147

seen; however, the stall region shows clearly the gradual loss of lift evident in Figure 6.21a.

6.4.3 Roll Angle Effects

In view of the similarity of asymmetric blowing and sideslip, the next step in extending the LESA was to look at the effect of roll (or sideslip) angle for no blowing, first on normal force and then on roll moment characteristics.

Normal Force

The usual methodology for extending the LESA to account for sideslip effects (at low angles of attack and sideslip) is to consider the changes in effective sweep angle of the windward and leeward leading-edges[79]. Figure 2.22a shows that the vortex lift is almost independent of sweep angle, whereas for the wing tested the variation of potential lift with sweep is practically linear, so that the increase of lift on the windward side is matched by the reduction on the leeward side. In terms of total lift, sideslip should thus have little effect. The experimental data of Figure 5.5 shows that this is true at low angles of attack and sideslip, but that as angle of attack increases, sideslip results in a significant loss of lift.

Examination of the pressure data showed that this lift loss was primarily due to a reduction in the potential lift component (Figure 6.22a). Initially, it was thought that the reduction in lift was due to the definition of angle of attack used to plot the data. Referring to Figure 4.16, the usual 'angle of attack' parameter is a projection of the true angle of attack (or angle of downslip) onto the model plane of symmetry. Using the downslip angle gives the true crossflow velocity component for large pitch and roll angles (Figure 6.23). Unfortunately, this parameter did not completely collapse the underside lift data; empirically, a further $\cos\phi$ term was found to be necessary, giving

a modified downslip angle as shown in Figure 6.22b. The physical significance of this is not clear, but may be related to the shift of the underside stagnation point with roll angle sketched in Figure 6.23.

Using the downslip angle for the vortex lift and the modified downslip angle for the potential lift, and allowing for the asymmetric burst onset (Figure 5.11) enables the normal force variation with increasing angle of attack at a fixed roll angle to be predicted. An additional assumption was that the vortical flow did not subside until both bursts reached the apex, as indicated by the pressure-integrated data of Figure 6.7. Figure 6.24 shows that the effects of roll angle are modelled remarkably well, except at very high angles of attack and sideslip. It should be noted that in this region the sweep angle of the leeward leading-edge exceeds 90° and the simple model breaks down.

Roll Moment

Ericsson & Reding[79] estimate the roll moment due to sideslip using the LESA, considering the potential and vortex flow contributions separately. Their analysis gives the roll moment about the velocity vector; modifying it to give the moment about the wing centreline reduces the vortex component to almost zero. The potential component is estimated on the basis of an increased effective aspect ratio on the windward wing half (and vice versa) and the assumption that the spanwise load distribution remains constant with sideslip.

Two factors cause the failure of this methodology at higher angles of attack: a significant variation in spanwise potential load distribution with sideslip, and the asymmetric onset of vortex breakdown.

Considering the potential load distribution, it is clear from Figures 5.2 and 5.8 that the spanwise distribution changes significantly, both with angle of attack and roll angle. Two further points of note from Figure 5.8 are that the upper-surface pressures (away from the vortex-induced suction peaks) do not show the considerable asymmetry of the lower-surface pressures, and that the lower-surface stagnation point moves towards the windward leading-edge (as sketched in Figure 6.23).

The magnitude of the potential lift component with roll angle has already been considered; to determine the roll moment contribution the overall moment arm is required. This was derived from a spanwise integration of the lower-surface pressures at x/c = 0.5 to give local normal force and roll moment. The variation of roll moment with normal force is plotted in Figure 6.25a, for constant roll angle. The curves are linear, indicating that roll angle rather than sideslip is the critical parameter, and enabling a lateral 'aerodynamic centre' to be derived. Since the wing is flat, C_{l0} is zero, so that the lateral aerodynamic centre is equivalent to a lateral centre of pressure. Very similar trends were obtained at x/c = 0.2. Plotting the lateral aerodynamic centre vs roll angle (Figure 6.25b) gives a virtually linear trend; assuming that the aerodynamic centre tends to y/b = 0.25 as roll angle approaches 90° (since the crossflow approaches that around a thin aerofoil at low angle of attack), the variation of local moment arm with roll angle was modelled as:

$$y_p/b = 0.25 \sin\phi$$

If the lateral centre of pressure (C_l/C_n) is plotted vs angle of attack, it can be seen that at low angles of attack this model tends to overestimate the local roll moment arm. This is presumably due to the change in spanwise pressure distribution with angle of attack seen in Figures 5.2 and 5.9, with maximum pressures near the leading-edge at

low angles of attack (where the Ericsson & Reding model is valid), moving towards the centreline as angle of attack increases.

The lack of any asymmetry in the 'potential' region of the upper-surface pressure distributions noted above suggests that the potential lift contribution to the unblown roll moment due to sideslip comes from the lower-surface only. Presumably, on the upper-surface the leading-edge separation inhibits the windward shift of the stagnation point seen on the lower-surface.

Combining the potential lift model derived above with the variation in lateral centre of pressure with roll angle gives the 'Underside Potential Flow' curve on Figure 6.26, for a roll angle of +20°. At low (vortices unburst) and high (fully subsided vortical flow) angles of attack, the roll moment is modelled remarkably well.

For the vortex lift component, at low angles of attack the roll contribution of the unburst vortices is stabilising, primarily due to a small loss of lift on the leeward (up) side as the vortex core is displaced upwards (Figure 6.7). At higher angles of attack the asymmetric burst onset becomes much more significant, as evident in Figure 6.26. On attempting to model the effects of vortex burst, it was found that in contrast to the normal force predictions of Figure 6.24, the roll moment is very sensitive to the assumptions made about burst trajectory and lift loss. In particular, the burst onset is critical, due to the large moment arm at the rear of the wing.

Initially, the burst lift loss model used for the normal force predictions was applied. The asymmetry of burst trajectory was initially modelled using a linear variation with roll angle. This worked well for angles of attack with the burst on the forward half of the wing, but tended to underestimate burst onset angles of attack. The effect of

151

this can be seen in Figure 6.26, with both the magnitude and onset of the unstable roll moment region being underestimated. Using burst onset angles of attack derived from experiment gave a much better match to the peak unstable roll moment, but still gave an early breakpoint. It should be noted that the magnitude of the unstable peak is also very sensitive to the relative strengths of the unburst vortices, and to the post-burst lift loss model.

Two factors were thought to contribute to the poor prediction of the unstable breakpoint: the conical longitudinal load distribution used in the model overpredicts the change in roll moment due to vortex burst in the region of the trailing-edge (Figure 6.27a), while the gradual nature of the lift loss (Figure 6.21a) tends to smooth out the roll reversal onset. To examine the possible magnitude of these effects, the vortex burst model was modified (Figure 6.27b) to simulate a less abrupt lift loss at the trailing-edge. The resultant roll characteristic can be seen in Figure 6.26, with the gradual nature of the roll reversal captured. The leeward burst onset (which reverses the destabilising trend) is relatively unaffected by the modification to the bust model, due to the very rapid progression of the burst up the aft half of the wing (Figure 5.11).

A further indication of the significance of the longitudinal loading was afforded by a prediction of the 'effective dihedral' parameter, $C_{l\beta}$. The underside potential roll contribution (for small roll angles) gave a value for the roll moment derivative $C_{l\phi}$ of approximately $0.14\sin\theta$. Since sideslip angle, β, is equal to $\sin^{-1}(\sin\phi\sin\theta)$, this gives a <u>constant</u> effective dihedral, $C_{l\beta}$, of 0.14 per radian (0.0024 per degree). Comparing this with experimental data (Figure 6.28), the high angle of attack characteristics are well modeled, while the low angle of attack roll moment is overestimated. This is due to the departure from the linear lateral centre of pressure variation discussed above. In this region the simple model of Reference 79 is valid. In the mid-angle of attack

range, Figure 6.28 compares the effects of the two burst lift loss models. The original model gives a discontinuity as the burst comes onto the wing, with a gradual return to a stable characteristic, while the modified model more closely matches the experimental data.

To summarise, the unblown normal force and roll moment characteristics at high angles of attack of the wing tested can be modelled using a suitably modified form of the LESA. However, the sensitivity of the roll moment to the assumptions made about longitudinal load distribution, burst trajectory and burst-induced lift loss indicated that insufficient experimental data had been obtained for a rigorous representation. Nevertheless, it was felt that the simple model used at least indicated the relative magnitudes of the contributions to the roll moments, and had certainly indicated the critical areas that would require further definition. On this basis, the analysis was extended to look at the effects of symmetric and asymmetric TLEB.

6.4.4 Symmetric Blowing

The simplest case for analysis is at low angles of attack with supercritical blowing, ie with the vortical flow fully suppressed. This has been previously been shown (Section 6.2.2) to give local normal force coefficients on the blown portion of the wing approaching the 'RT Jones' slender wing prediction. Analysis of local pressure-integrated normal force data (Figures 5.18 and 5.46 for example) showed that the data could be best fitted by a $\sin(\alpha)\cos(\alpha)$ contribution distributed over the full span, and a $\sin^2\alpha$ contribution concentrated at the leading-edge. The similarity to the LESA was very encouraging.

Zero Sideslip

At $x/c = 0.5$, the local pressure-integrated normal force for supercritical blowing could

be fitted by:

$$C_n = 1.1\sin(\alpha)\cos(0.4\alpha) + 1.8\sin(\alpha)\cos(\alpha) + 1.8\sin^2\alpha$$

with the upper-surface potential term not exhibiting the chordwise variation of the lower-surface (Section 6.4.2). Figure 6.29 shows that this gives a normal force curve very close to the RT Jones prediction.

The implication is that the maximum possible jet-induced normal force may have been achieved, with the 'RT Jones' curve giving a limit for the lift due to fully attached flow over a slender wing. The magnitudes of the potential flow terms are determined by the slope at zero lift, while the leading-edge $\sin^2\alpha$ contribution is limited by the maximum lift at higher angles of attack.

Allowing for the effect of the unblown aft portion of the wing,and assuming a conical lift distribution over the blown section, a close match to the supercritical blowing normal force characteristics was obtained (Figure 6.30a).

The effect of the reestablishing blown vortex is rather complex to model, with the 'effective vortex angle of attack' analogy being too simplistic. Referring to Figure 5.18, once the blown vortex forms it increases in strength much more rapidly than the equivalent unblown vortex, assuming a simple shift in zero lift angle. Further, the shape of the lift curve is different, being modified by the associated movement of the leading-edge separation point towards the slot exit. At the same time as the vortex forms, the leading-edge normal force reduces as the separation point moves onto the leading-edge. The rate of reduction initially matches the increase in vortex lift, giving a delay in lift divergence from the supercritical blowing level.

154

However, for the purposes of a preliminary analysis, the vortex angle of attack analogy was retained, with the vortex lift modelled as

$$C_{NV} = 2.3 \sin^2(\alpha-\alpha_0)$$

The vortex lift coefficient is reduced to 2.3 to account for the loss of the side-edge lift, K_{VSE}, due to the separated flow at the tip. The zero lift angle, α_0, was determined by assuming the vortex lift to be equal to the leading-edge contribution and the point of formation. This angle was considerably less than that derived by extrapolation of the suction peak magnitude trends (Figure 5.17), but gave a good fit to the experimental data. The deviation of the blown vortex lift curve slope from a $\sin^2\alpha$ form renders any physical significance of α_0 in the above equation problematic.

With the incorporation of the vortex burst lift loss model of Section 6.4.2, and burst trajectory from Figure 5.19, this model gives a reasonably good match to the normal force characteristics of symmetric blowing, as shown in Figure 6.30b.

Sideslip Effects

The effects of sideslip on symmetric blowing were not analysed in any depth, other than the variation of the supercritical blowing potential and leading-edge normal force contributions. The potential term was found to be almost unaffected by sideslip/roll angle, with no significant change in magnitude or spanwise distribution. The leading-edge normal force, however, tended to increase with reducing effective leading-edge sweep and vice versa, as shown in Figure 6.31a. There is some uncertainty in these results, since they were extracted from 'constant roll angle' tests, where sideslip angle varied with angle of attack. For symmetric blowing, the total (left+right) normal force remains roughly constant with roll/sideslip, providing some confirmation that the

155

maximum possible 'attached flow' normal force had been achieved.

The variation of the leading-edge normal force term with sideslip is similar to the variation of the local cross-flow semispan (and hence effective aspect ratio), as defined in Figure 6.32a. It has been noted[24] that the shift in flow centreline with sideslip on delta wings tends to be less than the geometric value, which is consistent with the small deviation from the 'semispan' curve seen on Figure 6.31a.

6.4.5 Asymmetric Blowing

Starting as before with the low angle of attack regime, it can be seen from Figure 6.33a that the supercritical 'one-sided' blowing roll characteristic follows a curve of the form $-0.2\sin^2\alpha$, indicating that the primary contributions are the blown leading-edge normal force and the unblown vortex.

The effect of asymmetric blowing on leading-edge normal force is shown in Figure 6.31b. The trend seems to be consistent with the effects of sideslip on symmetric blowing, with the effective centreline shifting away from the blown leading-edge as sketched in Figure 6.32b. For the leading-edge contribution then, the total normal force is $1.1\sin^2\alpha$ (from the symmetric blowing model of the previous section, with the increase due to asymmetric blowing of Figure 6.31b) conically distributed, giving a roll moment of $-0.37\sin^2\alpha$.

For the unblown vortex, a lift coefficient (K_v) of $2.9/2$, a local spanwise moment arm (y_v/s) of 0.65 (Figure 5.28) and a longitudinal centre of pressure (x_v/c) of $0.5^{[79]}$ gives a total roll moment contribution of $+0.23\sin^2\alpha$ (right side blowing). A total roll moment of $-0.14\sin^2\alpha$ results, satisfactorily close to the $-0.2\sin^2\alpha$ curve of Figure 6.33a, considering that the presence of a small C_μ-dependent component (Figure 5.14b)

156

makes the baseline supercritical roll moment difficult to determine precisely.

At higher angles of attack the individual contributions to the roll characteristics were identified qualitatively in Section 6.2.2 (Figure 6.1). For a given blowing level the shape of the characteristic is determined by the point at which the blown vortex forms (Figure 5.37) and thence by three subsequent phenomena: the leading-edge normal force being gradually redistributed inboard to the blown vortex, asymmetric vortex strength and burst onset and finally vortex subsidence. The usable portion of the roll characteristic is terminated by slot stall, a result of non-optimum slot placement and/or leading-edge profile rather than an inherent property of asymmetric TLEB.

Bearing in mind the difficulties encountered in modelling both the effects of asymmetric vortex burst with no blowing and the formation process of the blown vortex it was apparent that insufficient experimental data was available to reliably model the high angle of attack characteristics of asymmetric blowing. Nevertheless an attempt was made, in order to determine the critical areas and indicate where further investigation is required.

Applying the assumptions of the previous section, with vortex zero lift angle and burst onset modified as appropriate, the curves of Figure 6.33b were obtained. It can be seen that the transfer of loading from the blown leading-edge to the vortex is sufficient to completely reverse the (unburst) roll moment trend. The gradual nature of this transfer (Figure 6.5) was not modelled, giving a discontinuity in the predicted curve. Accounting for vortex burst gives an initial reduction in the roll reversal (unblown burst onset), followed by an increase (blown burst onset). The breakpoints in the prediction correspond reasonably well to the experimental data, and it seems likely that modelling a gradual shift from leading-edge to vortex lift on the blown side

(over say 10°) would give a better match the shape of the roll characteristic.

At very high angles of attack the vortical flow subsides, with the available pressure data indicating only a small 'blown side up' contribution from the remaining region of jet-induced flow around the leading-edge; the experimental roll moment data shows a second roll reversal occurring, indicating that the blown tip separation now becomes dominant.

The shape of the roll characteristic in this region suggests that the extent of the separated flow region increases rapidly once the vortex flow subsides, to give a peak destabilising roll moment at about 62°, just ahead of the slot stall. The limited flow visualisation (Figure 5.35) does show an increase in size of the tip separation with angle of attack, but with insufficient detail to confirm this hypothesis.

The magnitude of the roll reversal at least enables a crude estimate of the upper-surface pressure loss in the separated region to be made. From Figure 6.33a, the peak roll moment offset due to the separation is about +0.025, which with a moment arm of b/4 gives a normal force reduction on the blown side of -0.1. Assuming the flow separation to extend over the entire right-hand side of the constant-chord trailing-edge section and a constant pressure distribution gives a pressure coefficient loss of the order of 0.6. Over the forward half of the wing at 60° angle of attack the upper-surface pressure is constant at about -0.8 (Figure 5.2), giving a pressure coefficient of -0.2 in the separated region. Further experimental investigation will be required to determine the precise nature of the tip separation contribution.

6.4.6 Asymmetric Blowing with Roll Angle

Roll angle effects are in general more complex, with additional asymmetries in vortex

158

strength and burst trajectory. The exception is the low angle of attack supercritical blowing case, where asymmetric blowing displays a very similar variation in leading-edge normal force with sideslip to symmetric blowing (Figures 5.46 and 6.31a), giving the general trend of increasing 'recovery' roll authority with roll angle previously described. Any further analysis was not thought to be justifiable until the baseline asymmetric blowing case could be more satisfactorily modelled.

6.4.7 Transient Characteristics

Although no quantitative measurements of transient roll moment response were possible (due to the low natural frequency in torsion of the sting balance) the above analysis, in conjunction with the correlation of vortex burst motion of Section 2.4.2 and the transient pressure measurements of Reference 11, enables some discussion of the possible characteristics to be made.

From Section 2.4.2, the unburst vortex has a response to changes in the leading-edge conditions with a (reduced) time constant of the order of 0.5, while the burst response has a time constant of around 1.0, giving reduced natural frequencies of 2 and 1.0 respectively. Typical wing rock frequencies are of the order of 0.3, slow enough for the burst response to be significant in the stabilisation of this motion. For combat manoeuvres, roll rates are typically very high (>360°/s) and duration is short (<0.5s). For a typical combat aircraft at 0.3M, reduced time constants of 0.5 and 1 become 0.3 and 0.6 seconds for the unburst vortex and vortex burst response respectively. it can be seen that in general the burst response may be too slow to significantly affect the manoeuvre. Indeed, for very rapid manoeuvres the unburst vortex response time also becomes relatively slow, and the dominant roll moment contribution from transient blowing may be the 'potential' jet-induced leading-edge normal force.

159

The generic response of the delta wing flow field to a step right-side blowing input is sketched in Figure 6.34, for an initial state with the burst on the wing (a) and a final condition (d) with the blown vortex reduced in strength but not yet fully suppressed. When blowing is initially applied, wool tuft flow visualisation at very low speeds indicates that the Coanda jet may initially attach across the span (b), temporarily detaching the vortex. The jet almost immediately separates to form the new 'equilibrium' position for the vortex feeding sheet. The leading-edge vortex then responds to this shift (c), reducing in strength and moving inboard. Rather more slowly, the vortex bursts move to their asymmetric equilibrium positions (d).

This generic behaviour may be translated into terms of roll moment time histories, given the relative contributions of the vortical flow and the jet-induced leading-edge normal force previously described. Figure 6.35 shows the possible results of a step change in right-side blowing at low angles of attack, with no burst present over the wing. The left (unblown) vortex contribution remains essentially constant, while the right (blown) vortex reduces in strength, with a time constant of 0.5. The leading-edge normal force, however, is likely to increase relatively rapidly, giving an initial overshoot in roll moment.

At higher angles of attack, the presence of the vortex burst complicates the response, as shown in Figure 6.36. For a small change in blowing level, the left (unblown) vortex contribution increases slowly as the burst moves aft. The right (blown) vortex contribution reduces as the vortex strength reduces, then recovers as the burst moves slowly aft. The leading-edge normal force may possibly show an initial peak as the flow fully attaches, falling back rapidly to the partially attached end condition. The nett result is an initial 'blown side up' moment, gradually reversing as the vortex strengths and burst locations respond. For a final supercritical blowing level, the time

160

history resembles the low angle of attack case (Figure 6.35), with the blown vortex strength falling to zero before the vortex burst can respond.

An adequate examination of the <u>total</u> moment response to transient changes in asymmetric blowing will require a much more rigid wing mounting system in order to isolate the model response from the flowfield response. However, it does seem likely from a survey of published vortex response data and from previous transient pressure measurements that rapid application of asymmetric blowing will give a better response than indicated by a 'quasi-steady state' analysis, particularly in the first roll reversal region.

6.4.8 Summary

The use of the LESA to model the high angle of attack characteristics of delta wings appears to be feasible. Some preliminary studies have been made, which have indicated the areas which require further investigation. The calculation of roll moment has been shown to be very sensitive to the modelling of the vortex burst; in particular, the trajectory and associated lift loss in the aft region of the wing. For blowing, the supercritical case has been relatively straightforward to represent. The critical areas for further investigation are the development of the blown vortex with angle of attack and the effect of the blown tip separation region.

6.5 Wing Geometry Effects

Inconclusive as the results of the analysis of the previous section are, in conjunction with the qualitative descriptions of Section 6.3 they enable some discussion and prediction of the likely effects of wing planform and slot geometry to be made.

6.5.1 Slot Extent & Taper Ratio

For the cropped delta planform tested, the maximum possible slot extent is determined primarily by the taper ratio. The slot extent was then further reduced by the physical limitations of the wing structure (Section 4.3.3). The principal effect of the limited slot extent is to reduce the total leading-edge normal force, giving a loss of roll control power throughout the angle of attack range. A secondary effect is the creation of a separated flow region aft of the slot, as sketched in Figure 6.37a, giving a further loss of roll control power, particularly at high angles of attack. This may be alleviated by modifying the tip geometry to give a swept tip, hence generating a second leading-edge vortex shed aft of the slot (Figure 6.37b) and recovering some vortex lift. Unfortunately, the unblown vortex also increases in strength, while the slot geometry now resembles the reduced length slots described in Section 5.4.5 and shown to be less efficient[16]. This loss of efficiency was confirmed by exploratory tests with simple aluminium sheet tip extensions.

The optimum solution is to use a pure delta planform with full length slots (Figure 6.37c). The potential improvement in roll power is large, because of the balance between the unblown vortex and the jet-induced leading-edge normal force. From Section 6.4.5, for supercritical blowing, the unblown vortex gives a roll moment of $+0.23\sin^2\alpha$. Allowing for the increase in K_V with the change to a pure delta planform gives $+0.25\sin^2\alpha$. For full-length slots the blown leading-edge normal force contribution increases from -0.37 to $-0.61\sin^2\alpha$, giving an increase in total roll moment from $-0.14\sin^2\alpha$ to $-0.36\sin^2\alpha$. The slot area is increased by 30%, resulting in a 150% improvement in roll control power at supercritical blowing levels for a 30% increase in massflow. At higher angles of attack the leading-edge normal force becomes less important; however, the blown vortex (when formed) is shed from the full length of the leading-edge and hence increases in strength relative to the unblown vortex. This will tend to reduce the magnitude of the first roll reversal region. Finally, since no

tip separation will develop, the second roll reversal will not occur. The resultant changes in the roll moment characteristics with full-span blowing are sketched in Figure 6.38.

In this analysis the principal reason for the inefficiency of short slots can also be seen. The total roll moment results from a small difference between two opposing contributions and hence a small change in leading-edge normal force gives a disproportionately large change in overall roll moment/normal force.

Unfortunately, full-span blowing would be impracticable on a real combat aircraft wing, where a finite tip extent is required both for good aerodynamics and for weapons carriage. A number of other options for alleviation of the poor tip flow are possible. It seems likely that the tip separation is associated with the strong end-vortex shed from a finite slot (Figure 6.37a). Significantly, the tip separation was not evident in CFD studies of a similar wing geometry[111], where the end-vortex was not modelled. In this case, a tapering-down of the slot height towards the aft end may reduce the strength of the end vortex and hence alleviate the separation. Alternatively, it may be possible to modify the tip geometry to help maintain attached flow: Hoerner tips or winglets for example.

An aspect of slot length not yet discussed is the forward extent. Unpublished tests at Stanford University[125] on partial slots showed that in addition to a general loss of efficiency with reducing slot length, blowing on the aft of the wing alone was less effective than blowing on the forward section alone. Structural limitations on the wing tested at Bath University prevented continuation of the slot to the apex, thus some loss of efficiency may have resulted from the formation of an initial leading-edge vortex at the apex. However, for the relatively thick rounded leading-edge

section employed the vortex tends to form downstream of the apex[31], reducing the possible effect of an unblown region there. On a practical aircraft installation the presence of a fuselage will enable the slot to be readily extended to the wing apex.

6.5.2 Wing Sweep

Leading-edge sweep angle affects the individual contributions to the unblown and blown aerodynamic characteristics in a number of ways. The unburst vortex lift is relatively unaffected by sweep angle (Figure 2.22a). Burst onset angle of attack, however, increases rapidly with sweep angle (Figure 2.9) with an associated more abrupt lift loss (Figures 2.11 and 6.21b).

The potential lift (both LESA and RT Jones) varies linearly with aspect ratio (Figure 2.22b), and hence inversely with sweep angle. From the discussion of Section 6.4.4, it appears possible that the leading-edge normal force for supercritical blowing will increase with increasing RT Jones lift - i.e. increasing sweep will reduce leading-edge normal force. Unfortunately, no experimental data is available to confirm this.

Considering the behaviour of the blown leading-edge at higher angles of attack, the angle at which the blown vortex forms (for a given blowing level) is relatively unaffected by sideslip (Figure 5.46), and hence is presumably insensitive to changes in sweep angle. Slot stall onset is significantly affected by sideslip (Figure 5.44), increasing with decreasing effective sweep and vice versa. However, the slot stall is also strongly affected by the lower-surface crossflow boundary layer condition and hence by the leading-edge profile. Thus the sideslip effects are more likely to be a result of a change in effective leading-edge shape (Section 5.5.1) than of the change in leading-edge sweep angle alone.

At low angles of attack, with supercritical blowing, reducing sweep angle will probably increase maximum roll control power as the leading-edge normal force increases and the unblown vortex strength reduces. When the blown vortex forms the primary effect of sweep will be seen in the burst onset variation. Reducing sweep angle will hasten the onset of burst on both blown and unblown sides and (in conjunction with the reduction in vortex strengths) thus reduce the severity of the first roll reversal, in a similar manner to the variation of effective dihedral with sweep (Figure 2.12a). A beneficial effect on slot stall onset may also be seen. In general, a reduction in sweep angle from the 60° planform tested (to for example a more representative 50°) should improve the roll characteristics of asymmetric TLEB.

6.5.3 Leading-Edge Geometry

Blowing Efficiency

The discussion of Section 6.4.4 suggests the maximum possible leading-edge normal force with supercritical blowing is achieved with the circular profile tested. Changes in leading-edge geometry are thus unlikely to have a significant effect on magnitude, provided that control of the separation location can be maintained, but will affect the blowing levels required. In general, from experience with circulation control aerofoils[105], reducing leading-edge radius and slot height both improve the efficiency of tangential blowing. The degree of improvement and the lower limits on radius and slot height for jet attachment are unknown and will require further investigation.

Slot efficiency is also affected by the longitudinal area distribution - Figures 5.20 and 5.39 combined with experience from previous tests at Stanford University show that a conical slot is the most efficient in terms of blowing levels required for fully attached upper-surface flow.

An improvement in efficiency for supercritical blowing implies that for a given blowing level the angle of attack at which the blown vortex reestablishes is increased. As shown in Section 5.4.4, this angle of attack governs the subsequent high angle of attack behaviour. The overall shape of the roll characteristic will not be changed, but the blowing levels required reduced throughout the angle of attack range.

Slot Stall

The onset of slot stall will be particularly sensitive to leading-edge profile. Slot stall is due to the lower-surface crossflow separating ahead of the slot exit at high angles of attack (Section 5.4.1). The outboard motion of the unblown separation location with angle of attack is a function primarily of the leading-edge profile (tending to zero for a sharp-edged wing) and also of the condition of the crossflow boundary layer on the lower surface. For the wing tested a trip wire on the lower surface was required to ensure a turbulent crossflow boundary layer, given the probably laminar boundary layer maintained by the strongly favourable pressure gradient at high angles of attack (Figure 5.2b). The presence of the trip thus delayed the onset of slot stall, upto a limit imposed by the outboard motion of the blown separation point. For a given trip configuration the slot stall was relatively unaffected by blowing level, but was affected by changes in Reynolds Number, with increasing Re tending to hasten stall onset (Figure 5.37).

In general, reducing leading-edge radius will tend to give an earlier slot stall. This may be alleviated by modification of the leading-edge profile, or more effectively by optimising the slot placement. Work in progress on tangential forebody blowing at Bath University has shown that slot stall may be completely suppressed by a small movement of the slot exit around the leading-edge towards the lower-surface.

<u>Sideforce/Drag</u>

Unlike the normal force characteristics, the jet-induced sideforce is directly related to the wing aerofoil profile (Figure 6.15), with reducing thickness and leading-edge radius reducing the proportion of the theoretical leading-edge suction achieved. For wings of practical cross-section the total sideforce and thrust generated by tangential blowing will thus be negligible. For asymmetric blowing this is a beneficial effect, since for roll control the sideforce acted in an adverse direction. For symmetric blowing the axial component of the leading-edge suction offers an improvement in lift-dependent drag[127], hence a reduction of leading-edge radius is undesirable.

<u>6.5.4 Fuselage Effects</u>

No detailed experimental investigation of wing-fuselage interference effects have yet been carried out for TLEB, but the presence of vortex coupling for asymmetric blowing suggests that these may be important. Three aspects of fuselage 'interference' have been identified, and these are discussed below.

First, the presence of a fuselage will enable the leading-edge slot to be extended to the wing apex/root. This was commented upon in Section 6.5.1, and may give some improvement in slot efficiency.

Second, the vortex burst coupling phenomenon may be affected. This was the subject of some (unpublished) exploratory tests at Stanford University, using a centreline splitter plate of increasing height. It was found that a splitter plate of similar height to the wing semispan was required to significantly modify the vortex coupling, and that a fuselage was therefore likely to have little effect.

Finally, the leading-edge jet behaviour on the upper-surface will almost certainly be

significantly affected by a fuselage. Two consequences appear likely: The residual C_μ-dependent normal force/roll moment for supercritical blowing (Sections 5.3.1 and 5.4.1) is a function of the jet separation. The jet separation will tend to be fixed by the fuselage, suppressing the residual roll moment for asymmetric blowing. A more important effect could be on the increase in blown leading-edge normal force as one goes from symmetric through 'mixed' to 'one-sided' asymmetric blowing (Figure 6.31b). This was ascribed to a shift in the effective flow centreline (Figure 6.32b, Section 6.4.5) which could be reduced or

prevented by the presence of a fuselage. A similar effect may be seen in the sideslip characteristics (Figures 6.31a and 6.32a). The overall result would be to reduce the maximum (supercritical) roll moment capability. Unfortunately, the possibility of a fuselage effect of this type was not apparent until the pressure data was fully analysed, after the completion of the experimental programme. The possible loss of roll control authority makes this an important area for further investigation.

6.6 Application to Flight Vehicles

6.6.1 Comparison with Conventional Control Systems

For asymmetric TLEB to be considered as a high angle of attack roll control system it must offer an improvement in capability over current control systems. Of the control concepts discussed in Section 1.2, the conventional moving control surface appears to offer the greatest roll moment capability. Unfortunately, quantitative roll control data at high angles of attack for current aircraft is scarce, due to the sensitive nature of post-stall manoeuvre capability. Reference 130 contains wind-tunnel test data from the research programme that led to the X-31, a research aircraft specifically designed to demonstrate high angle of attack manoeuvrability. Figure 6.39 compares X-31 roll moment for 30° aileron deflection with the maximum measured roll capability of asymmetric TLEB. For comparison, F-16 capability[108] is also shown.

168

At low angles of attack the moving control surface has a higher capability, but this falls off rapidly until at high angles of attack TLEB offers a greater roll moment. With the improvements in blowing efficiency with full-span slots discussed earlier TLEB has the potential to double the roll capability of the X-31 at high angles of attack.

6.6.2 Mass Flow Requirements

The most critical problem hindering the application of TLEB to flight vehicles is the high mass flow requirements relative to typical engine bleed flow capacity. Uncertainty over scaling parameters (Section 5.4.4) and leading-edge geometry effects (Section 6.5.4) complicates the estimation of full-scale blowing requirements, but a sample calculation will illustrate the problems.

Assume an aircraft of EFA-like dimensions and performance, with a wing area of $50m^2$ and two RB199 engines of $75kgs^{-1}$ mass flow each. Scaling directly on C_μ, with a maximum total of 0.08 at a typical post-stall manoeuvre speed of 0.3M and a maximum plenum pressure ratio of 3.0 gives a mass flow of $64kgs^{-1}$ and a jet velocity of $400ms^{-1}$. A slot area of the order of $0.12m^2$ will be required, giving a mean slot height of 12mm, very large compared to the leading-edge radius and to the crossflow boundary layer depth.

Supersonic jets have been shown to be feasible on circulation control aerofoils, but the mass flow requirement amounts to 43% of engine mass flow and is clearly excessive. The RR Pegasus is the only Western engine to be routinely operated with such high bleed levels (for RCS) and typically does not exceed 10% of compressor mass flow. Project studies for the ASTOVL 'supersonic Harrier' have assumed a maximum bleed of around 20%, with higher levels tending to choke the compressor flows and

generating severe blade flutter. An additional problem is the loss of thrust associated with very high compressor bleeds. The Pegasus engine control system compensates for small RCS bleed levels by increasing fuel flow and temporarily exceeding the usual temperature limits; this is not feasible for high bleed rates.

A number of factors could help to reduce the prohibitatively high mass flow requirements: increased jet velocity, improvements in efficiency with full-span blowing and reducing leading-edge radius and the modified scaling parameter suggested in Section 5.44.

Jet velocity could be increased still further, since modern combat engines have fan pressure ratios of the order of 5, but jet Mach Number is already high at 1.35 while the jet velocity ratio (V_j/V_∞) is greater than 4. No experimental data exists on the effects of such high jet velocities. Keeping jet velocity unchanged and assuming a possible 100% improvement in blowing efficiency reduces mass flow requirements to 22%, while scaling on $V_\infty^{1.5}$ rather than V_∞^2 gives a further improvement to 12%. This would also reduce the mean slot height to around 3mm, a rather more reasonable value.

Unfortunately, mass flow still increases rapidly with flight speed, even when scaling with $V_\infty^{1.5}$. For a typical combat wing loading of 400kgm^{-2}, a maximum C_N of 1.7 at M0.3 corresponds to a normal acceleration of roughly +2g. Assuming a structural limit of +9g gives a combat 'corner speed' (Figure 1.3) of around M0.6. This in turn would require a 300% or 400% increase in mass flow for maximum roll control, depending on the scaling parameter used.

It is clear from this simple example that the practical application of asymmetric TLEB

170

as a roll control system is marginal, purely in terms of mass flow requirements. Considerable further work will be required to clarify the effects of very high jet velocities, leading-edge geometry and scaling parameters.

6.6.3 Installation Problems

The practical difficulties of incorporating a slot into the thin aerofoils typical of high-speed combat aircraft are obvious. A particular problem is the provision of a good aerodynamic shape for 'no-blowing' operation at low angles of attack/high speed. Use could be made of the technology developed for the X-wing programme, with a composite leading-edge structure enabling the slot to be closed-off when not in use. A second possibility (proposed by Dr G Wong) is the use of a variable geometry leading-edge resembling a Kreuger flap, with the slot/plenum assembly retracting when not required (Figure 6.40). This would have the additional advantage of increasing the effective leading-edge radius when blowing.
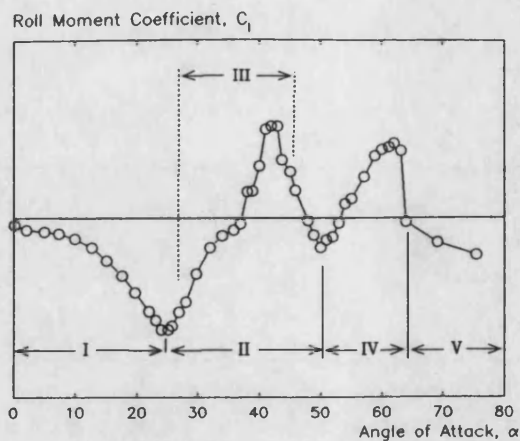
Figure 6.1 Typical Roll Moment Characteristic of 'One-Sided' Asymmetric Blowing ($C_{\mu R}$ = 0.04), with Flow Regimes Identified
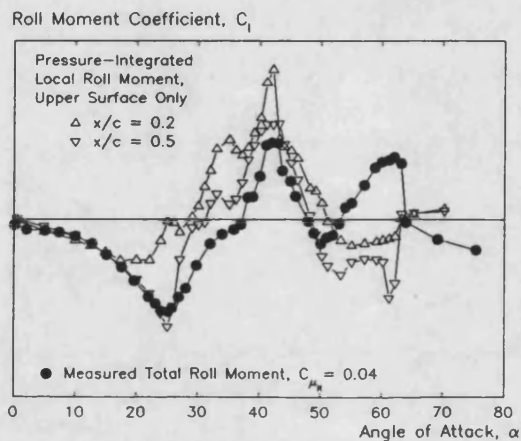
Figure 6.2 Comparison of Measured Total and Pressure-Integrated Local Roll Moments due to Asymmetric Blowing ($C_{\mu R}$ = 0.04, x/c = 0.2, 0.5)
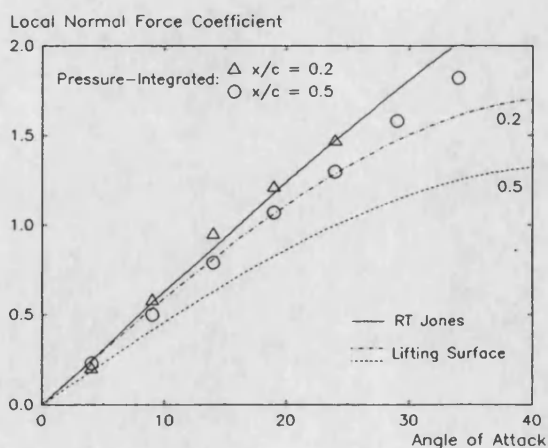
Figure 6.3 Total (Upper + Lower-Surface) Pressure-Integrated Local Normal Force for Supercritical Symmetric Blowing Compared with Potential Flow Theory

172
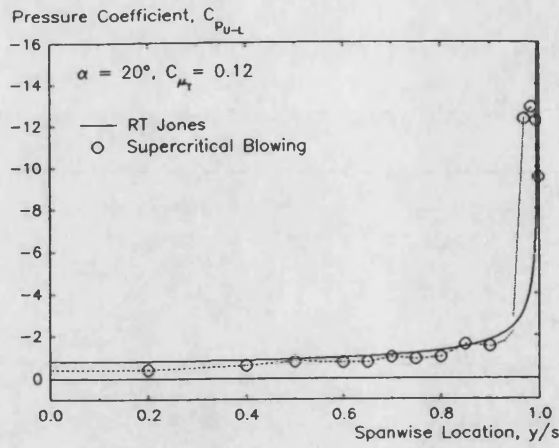
Figure 6.4 Spanwise Lift Distribution for Supercritical Blowing Compared with RT Jones Slender Wing Theory ($\alpha = 25°$, $C_{\mu T} = 0.12$, $x/c = 0.5$)
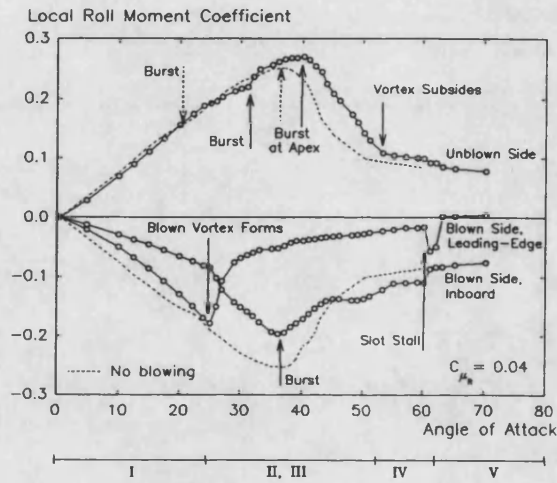
Figure 6.5 Contributions to Pressure-Integrated Local Roll Moment due to Asymmetric Blowing ($C_{\mu R} = 0.04$, $x/c = 0.5$)
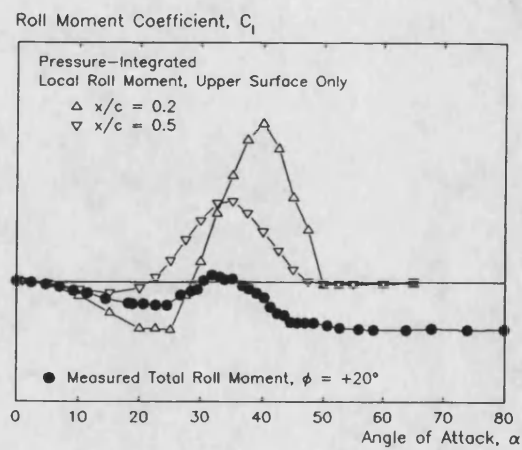
Figure 6.6 Comparison of Measured Total and Pressure-Integrated Local Roll Moments due to Roll Angle ($\phi = +20°$, $x/c = 0.2, 0.5$)

173
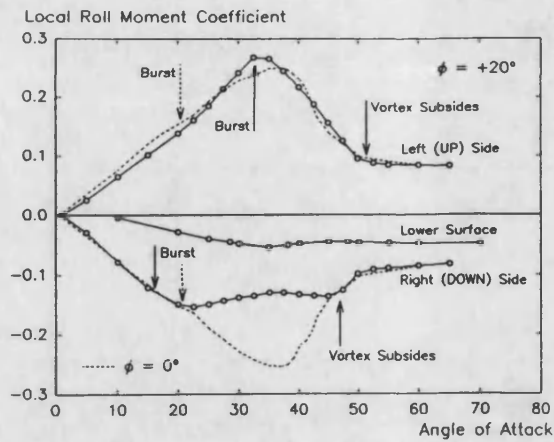
Figure 6.7   Contributions to Pressure-Integrated Local Roll Moment due to Roll Angle (ϕ = +20°, x/c = 0.5)
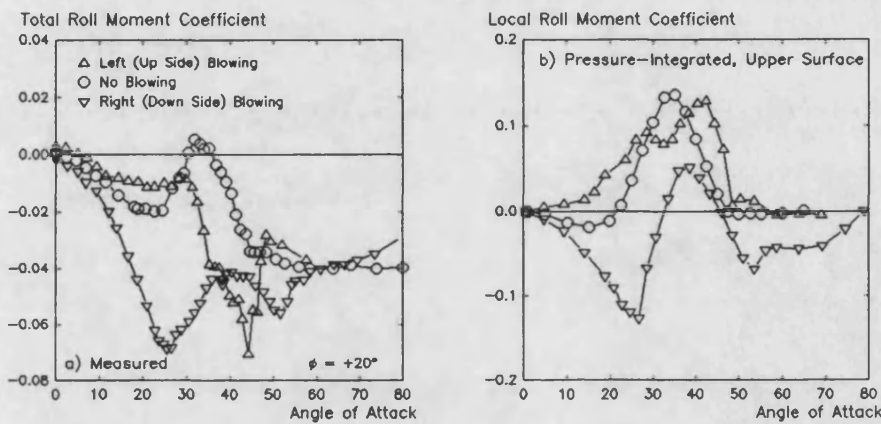
Figure 6.8   Comparison of Measured Total and Pressure-Integrated Local Roll Moments due to Asymmetric Blowing and Roll Angle (ϕ = +20°, $C_{\mu R,L}$ = 0.04)
a) Measured Roll Moment
b) Pressure-Integrated Roll Moment (x/c = 0.5)
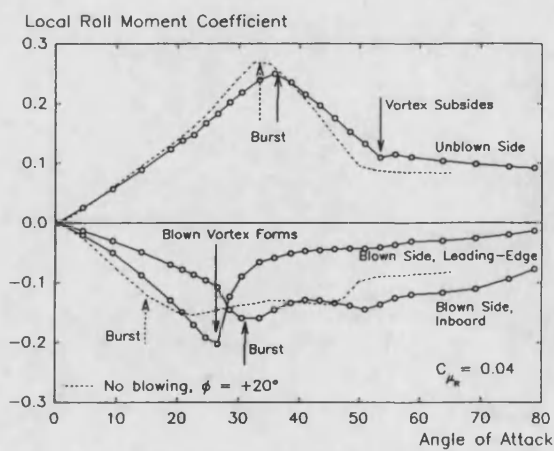
Figure 6.9   Contributions to Pressure-Integrated Local Roll Moment due to Asymmetric Blowing on 'Down' Leading-Edge (ϕ = +20°, $C_{\mu R}$ = 0.04, x/c = 0.5)

174
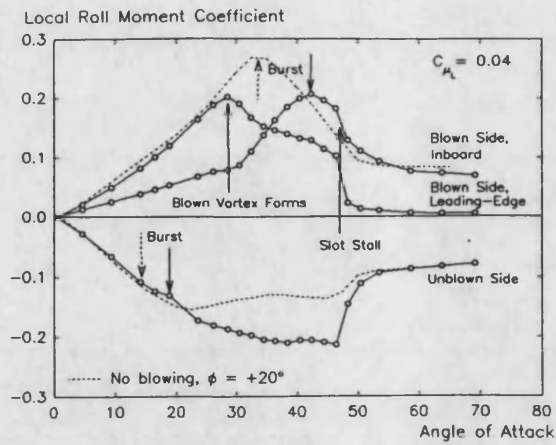
Figure 6.10 Contributions to Pressure-Integrated Local Roll Moment due to Asymmetric Blowing on 'Up' Leading-Edge ($\phi = +20°$, $C_{\mu L} = 0.04$, $x/c = 0.5$)
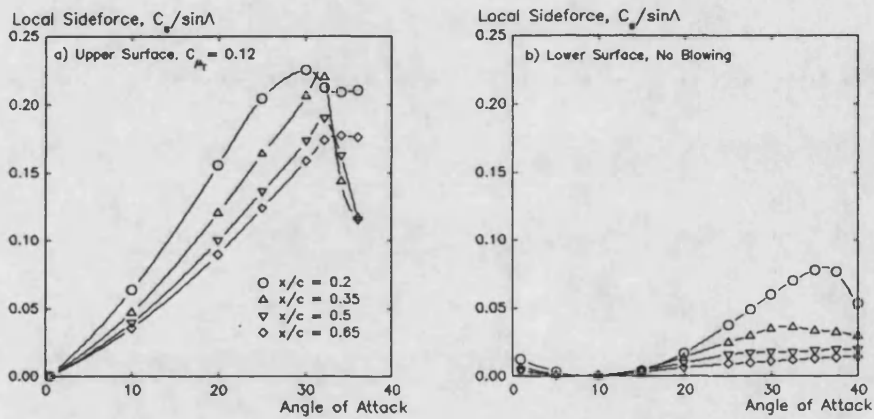
Figure 6.11 Variation of Pressure-Integrated Sideforce with Angle of Attack and Chordwise Location
a) Upper-Surface
b) Lower-Surface
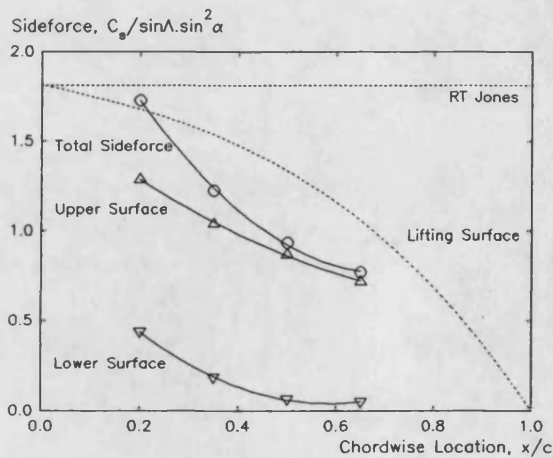
Figure 6.12 Chordwise Variation of Total Pressure-Integrated Sideforce Coefficient for Supercritical Blowing
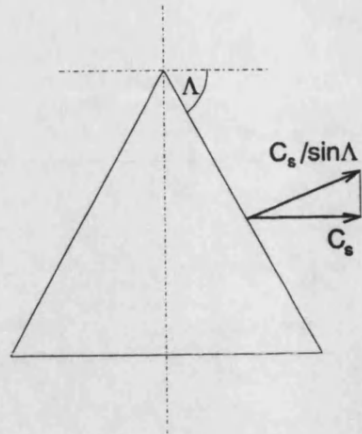
Figure 6.13   Derivation of Sideforce Coefficient from Measured Leading-Edge Suction

a) Slender Wing Cross Flow

b) Lifting Thin Aerofoil

C_S

C_{LES}

$V.\sin\alpha$

V
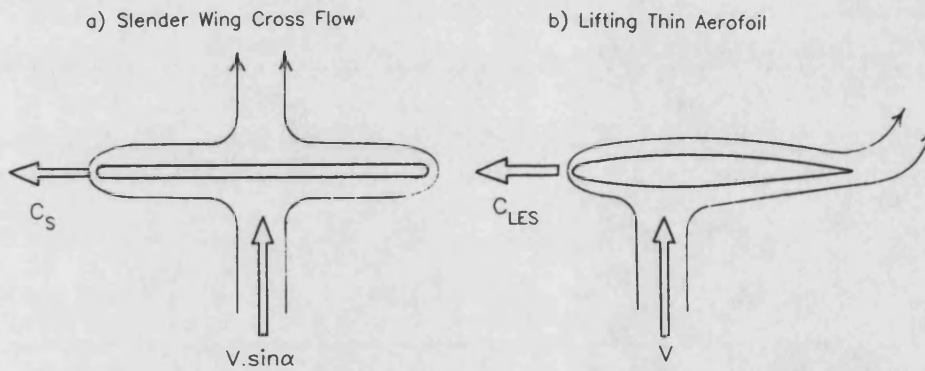
Figure 6.14   Comparison of Slender Wing Crossflow and 2-D Potential Flow Over a Lifting Aerofoil at 90° Angle of Attack

Leading Edge Side Force Coeffficient, $C_s/\sin^2\alpha$

Flat Plate — $\pi/2$

········ Slender Wing (RT Jones)
—— Carlson & Mack

● Blown Wing   (pressure)
○ Tingas & Rao   (pressure)
▽ Ridder   (force)
△ Bartlett & Vidal (pressure)

Thrust Factor Parameter, $(t/s)^{0.6}(r/s)^{0.24}$
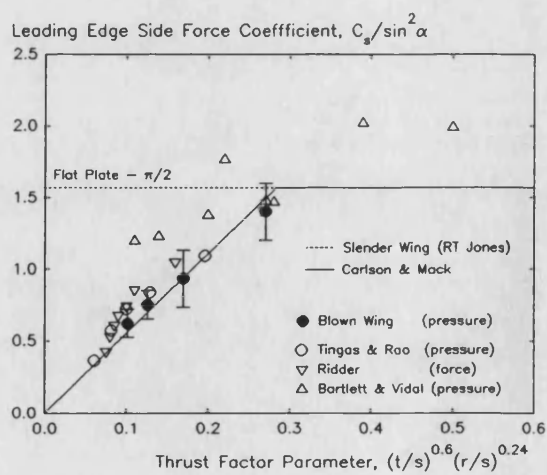
Figure 6.15 Correlation of Attained Sideforce with Local Thickness and Leading-Edge Radius

176
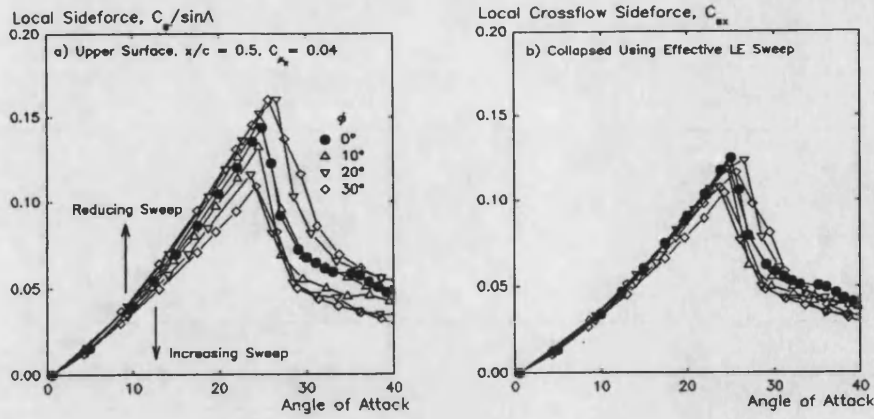
Figure 6.16 Effect of Roll Angle on Local Sideforce (ϕ = -30° to +30°, $C_{\mu R}$ = 0.04, x/c = 0.5)
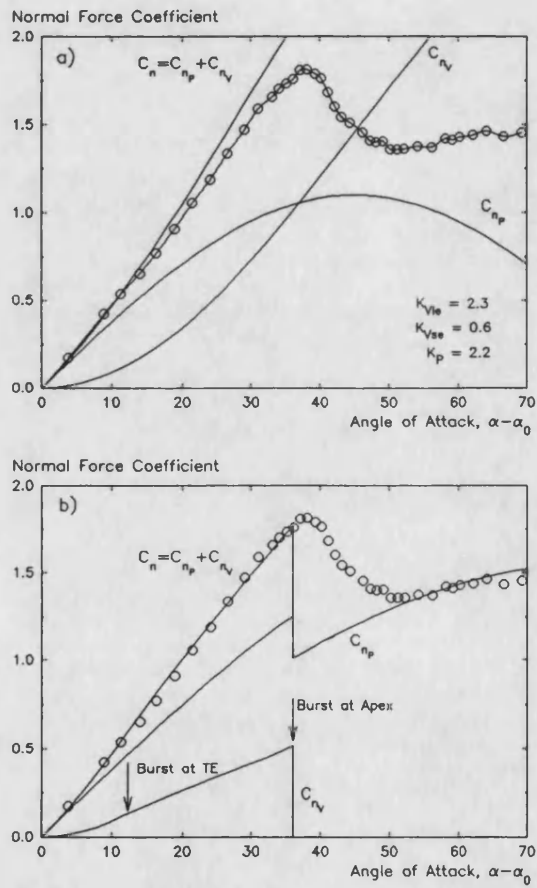
Figure 6.17 LESA Predictions of Unblown Normal Force Characteristics
　　　　a) Conventional LESA
　　　　b) Modified LESA

177
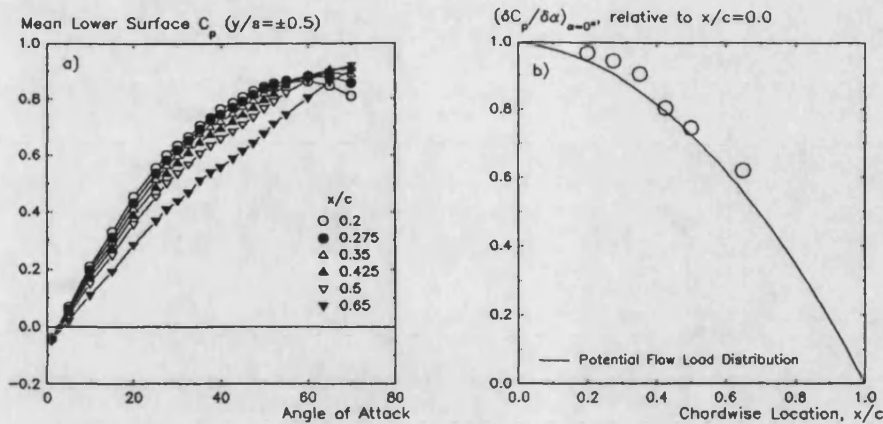
Figure 6.18 Longitudinal Potential Lift Distribution, as Indicated by Lower-Surface Centreline Pressures
a) Variation with Angle of Attack and Chordwise Location
b) Longitudinal Variation of 'Zero-Lift' Slope
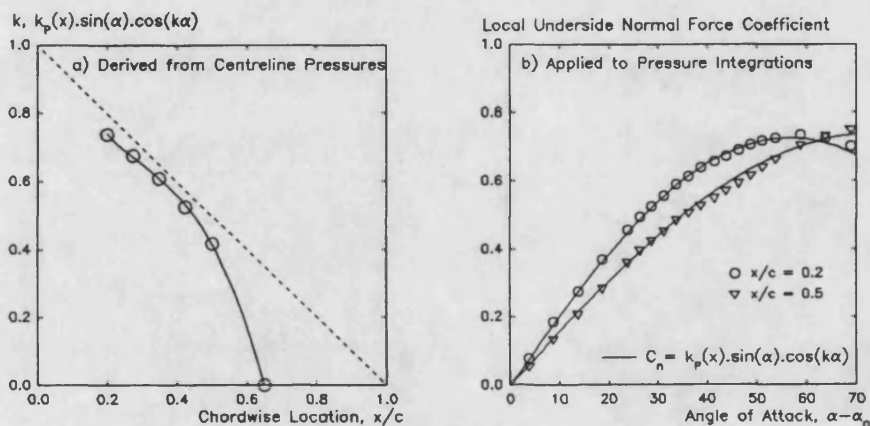
Figure 6.19 Departure of Potential Lift from LESA 'sin(α)cos(α)' Behaviour
a) sin(α)cos(kα) Model, Derived from Centreline Pressure Data
b) Centreline Pressure Trends vs Full-Span Integrations
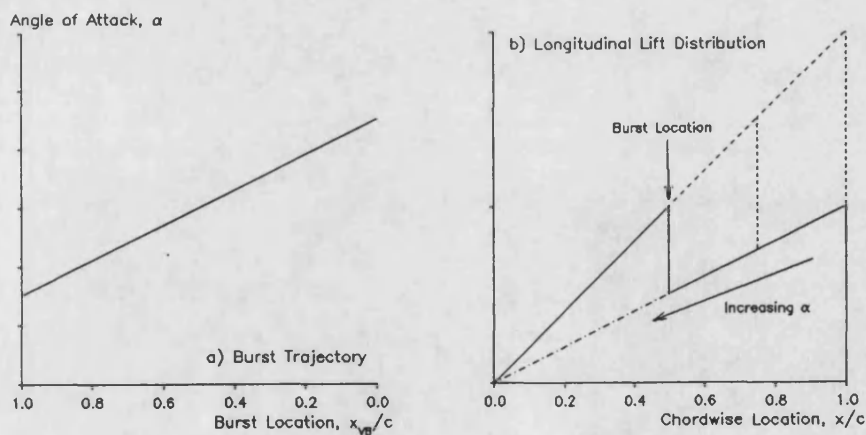
Figure 6.20 Modifications to LESA to Account for Vortex Burst
a) Simple Burst Trajectory Model
b) Burst Lift-Loss Model

178
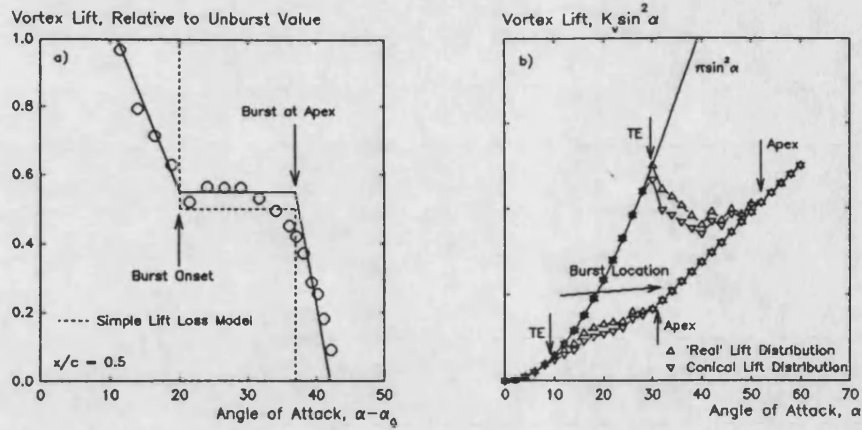
Figure 6.21 Aspects of Vortex Burst Lift-Loss Modelling
a) Local Vortex Lift-Loss (x/c = 0.5)
b) Effect of Longitudinal Lift Distribution on Total Lift-Loss
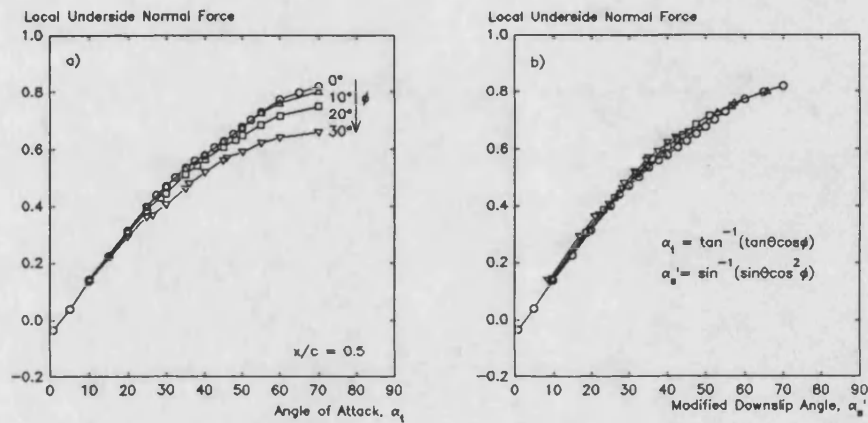
Figure 6.22 Effect of Roll Angle on Lower-Surface Normal Force, with Use of Modified Downslip Angle to Collapse Data (x/c = 0.5)
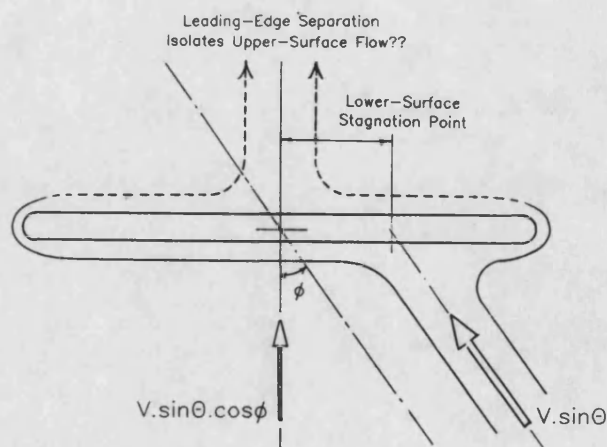
Figure 6.23 Effect of Roll Angle on 'Potential' Crossflow

179
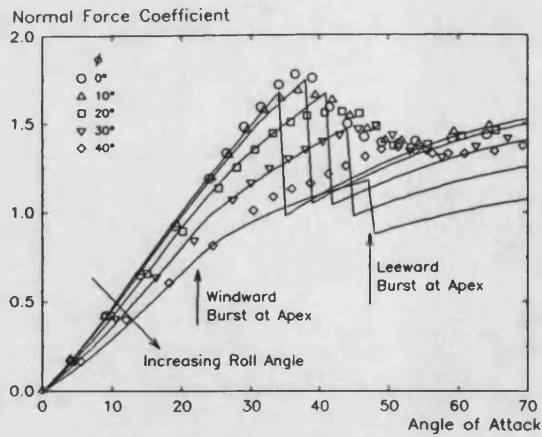
Figure 6.24 Modified LESA Predictions of Roll Angle Effects on Normal Force Characteristics
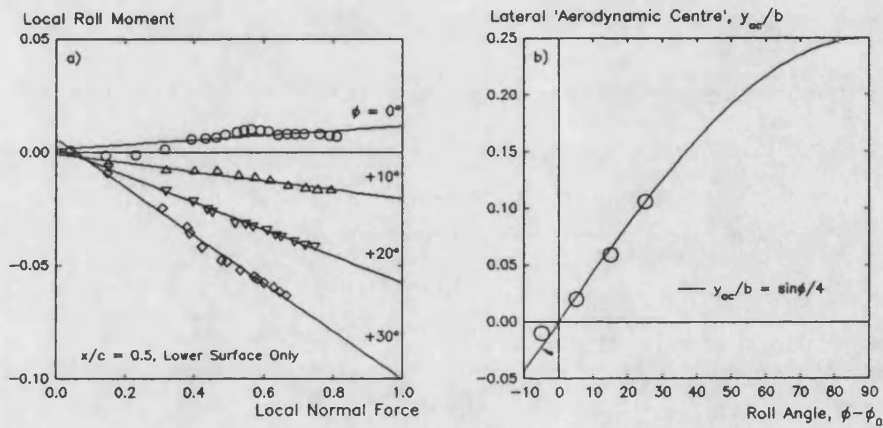
Figure 6.25 Effect of Roll Angle on Lower-Surface 'Lateral Aerodynamic Centre' (x/c = 0.5)
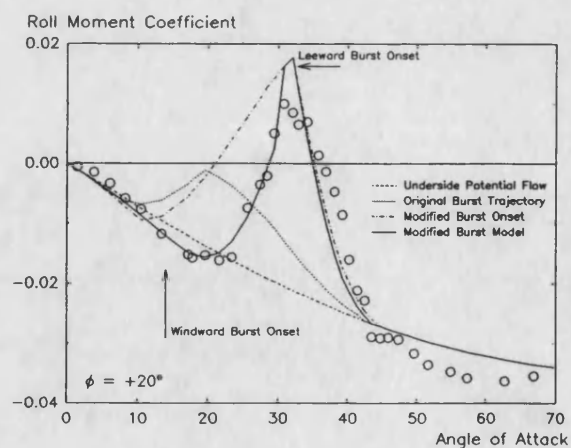
Figure 6.26 Modified LESA Predictions of Unblown Roll Moment Characteristics due to Roll Angle (ϕ = +20°)

180
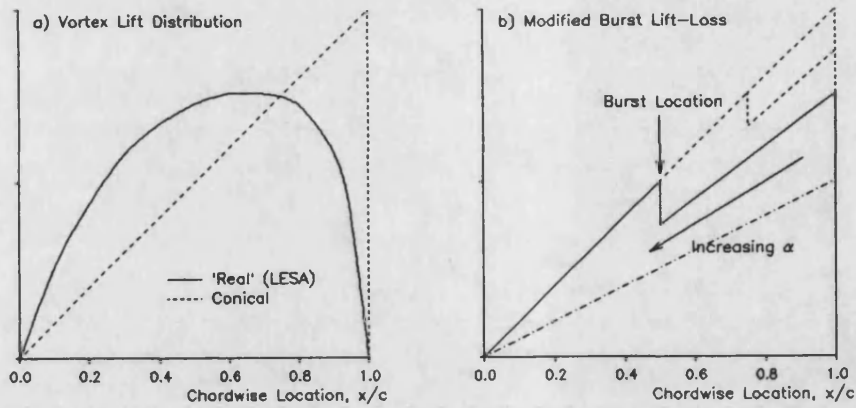
Figure 6.27 Modifications to Vortex Burst Lift-Loss Modelling
a) Real and Conical Longitudinal Vortex Lift Distributions
b) Modified Vortex Burst Lift-Loss Model
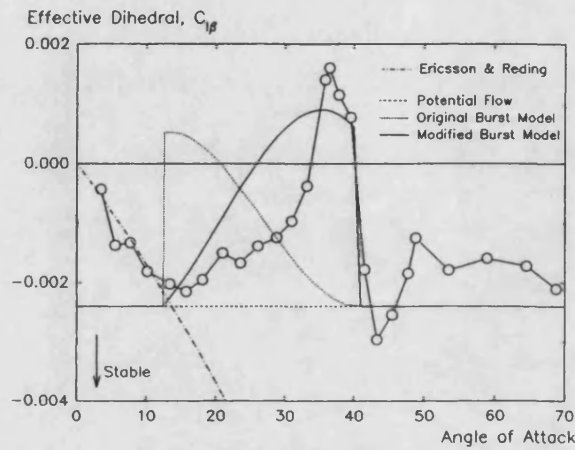
Figure 6.28 Modified LESA Predictions of Unblown 'Effective Dihedral' Characteristics
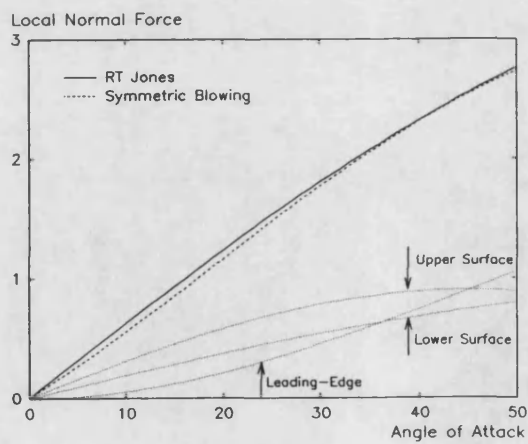
Figure 6.29 Comparison of Local Normal Force Contributions for Supercritical Blowing with 'RT Jones' Lift Curve (x/c = 0.5)

181
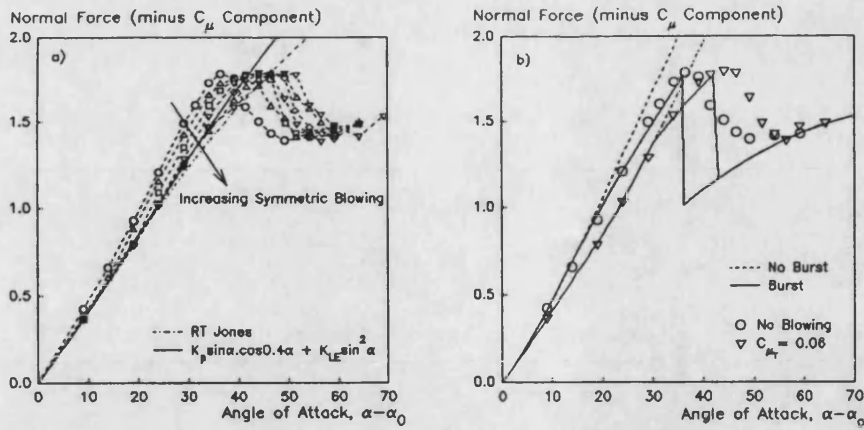
Figure 6.30 Modified LESA Predictions of Normal Force due to Symmetric Blowing
   a) Supercritical Blowing
   b) Effect of Vortex Formation and Burst
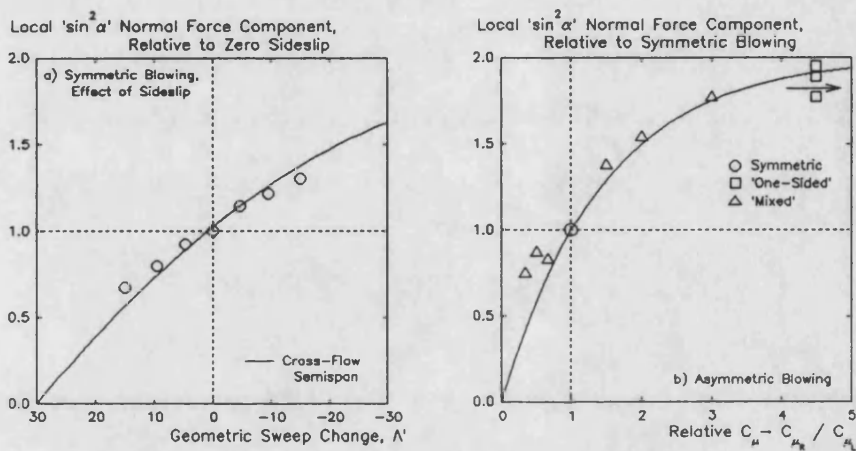
Figure 6.31 Effect of Flow Centreline Shift on Leading-Edge Normal Force for Supercritical Blowing (x/c = 0.5)
   a) Symmetric Blowing, Effect of Sideslip
   b) Asymmetric Blowing, Effect of Relative Blowing Levels
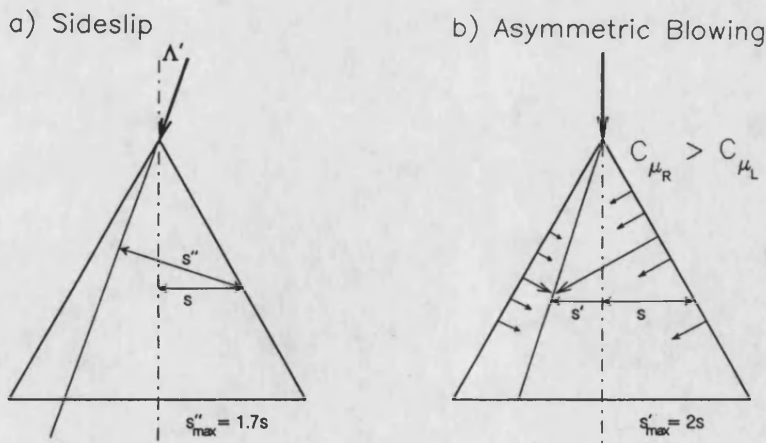
Figure 6.32 Effective Local Semispan due to Shift of Flow Centreline
   a) Symmetric Blowing, with Sideslip
   b) Asymmetric (Mixed) Blowing

182
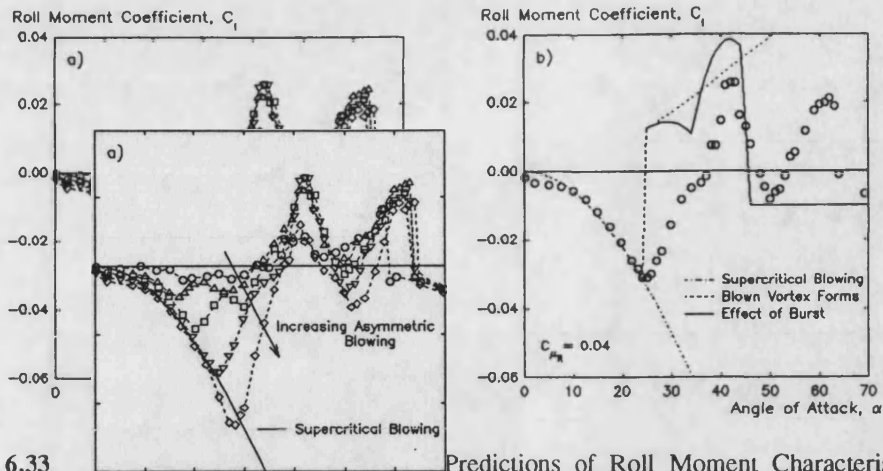
Figure 6.33 Predictions of Roll Moment Characteristics due to Asymmetric (One-Sided) Blowing
a) Supercritical Blowing
b) Effect of Vortex Formation and Burst
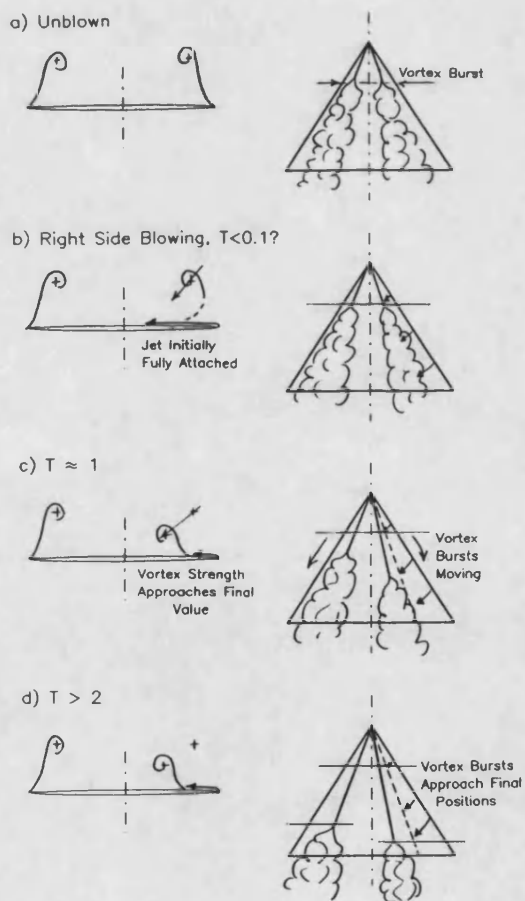
Figure 6.34 Sketch of Vortical Flowfield Response to Step Change in Right-Side Blowing Level

183
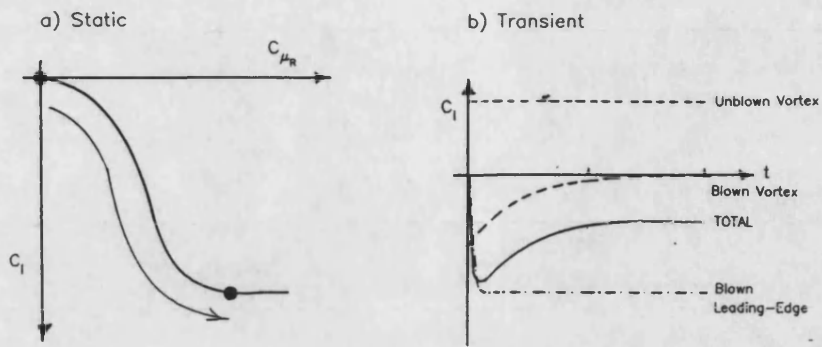
Figure 6.35   Postulated Transient Roll Moment Response to Step Change in Right-Side Blowing Level (Low α, Unburst Vortices)
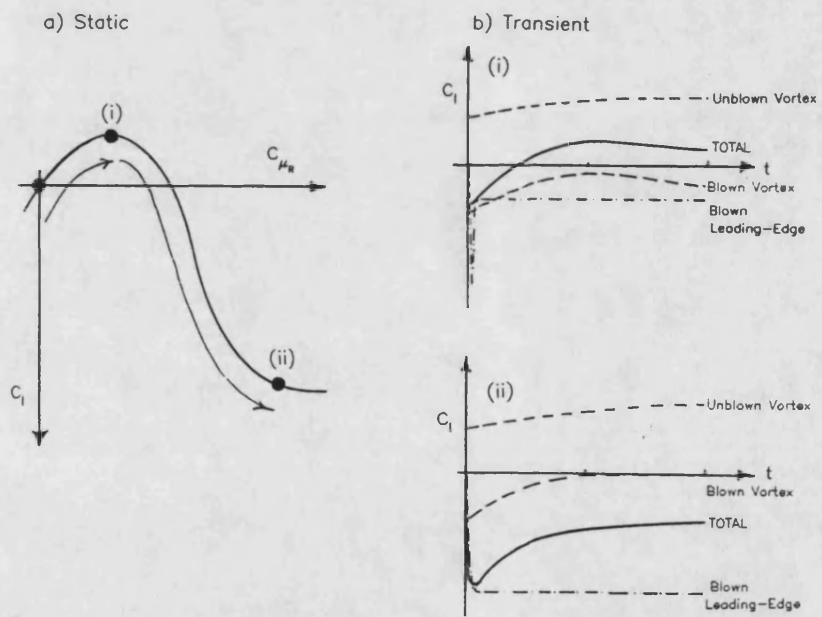
Figure 6.36   Postulated Transient Roll Moment Response to Step Change in Right-Side Blowing Level (High α, Burst Vortices)
(i) Final Blowing Level Subcritical
(ii) Final Blowing Level Supercritical

184
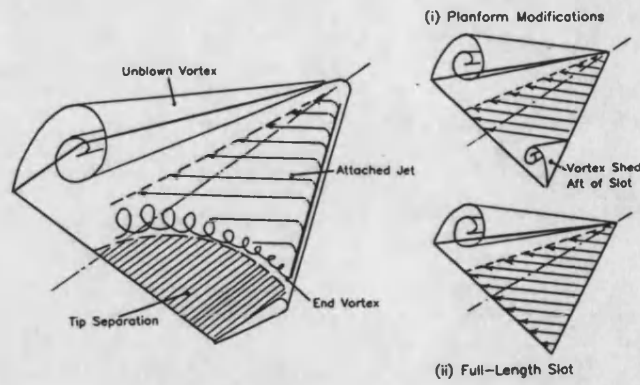
Figure 6.37   Schematic of Flowfield due to Asymmetric Blowing on Cropped Delta Planform, with Possible Effects of Changes to Wing Geometry
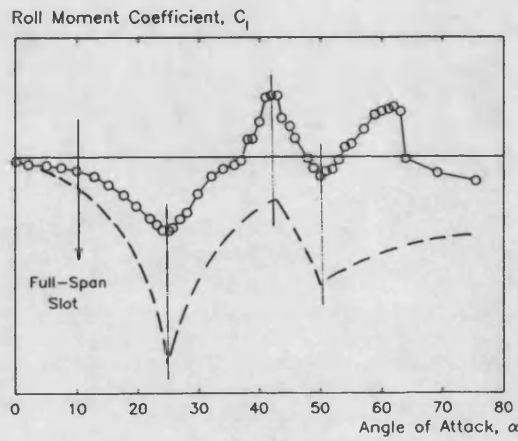
Figure 6.38   Postulated Effect of Full-Length Slots on Roll Moment Characteristics of Asymmetric Blowing
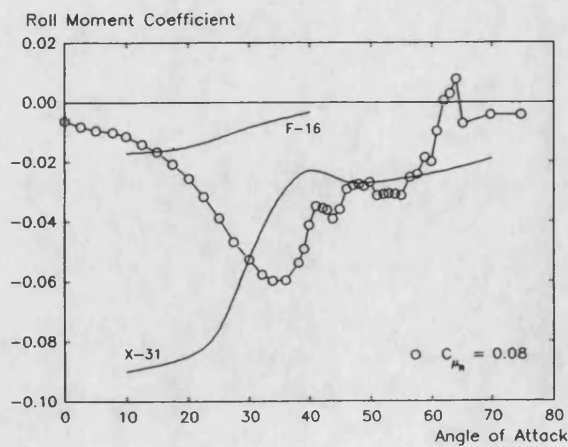
Figure 6.39   Comparison of Roll Control Capability of Asymmetric Blowing and Conventional Control Surfaces[130]

185

a) No Blowing, Flap Retracted

b) Blowing On
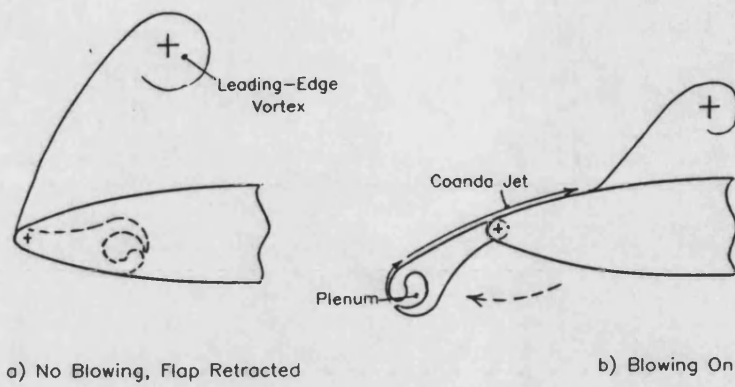
Figure 6.40 Retractable Leading-Edge Slot Assembly for Thin, High-Speed Aerofoil Sections

186

CHAPTER 7

CONCLUSIONS & RECOMMENDATIONS

7.1 Conclusions

The static behaviour of symmetric and asymmetric Tangential Leading-Edge Blowing has been investigated experimentally and conceptually. The flow mechanisms underlying the complex roll moment characteristics of asymmetric blowing have been determined and a simple model based on the Leading-Edge Suction Analogy derived. In addition, a novel analysis of experimental delta wing vortical flowfields based on a shape parameter for the vortex-induced upper-surface suction peak has been developed.

The main conclusions relating to the application of TLEB as a flight vehicle control system are as follows:

1. Asymmetric TLEB offers considerable potential for an improvement in roll control authority at post-stall angles of attack compared with conventional control systems.

2. The complex roll moment characteristics of 'one-sided' asymmetric blowing are inherent in the concept, but may be linearised by utilising a mixture of symmetric and asymmetric blowing or alleviated by reducing the wing sweep angle.

3. The 'effective vortex angle of attack' and 'effective sideslip' analogies offer a good qualitative description of the effects of symmetric and asymmetric

blowing on the vortical flowfield, but do not allow a quantitative analysis.

4. A model based on the Leading-Edge Suction Analogy has shown the potential to provide a relatively simple semi-empirical analysis of the characteristics of TLEB. Although insufficient experimental data was available to complete the analysis, an indication of the relative magnitudes of the various contributions to the roll moment and normal force characteristics was obtained, and the areas requiring further experimental definition indicated.

5. For a given wing planform, the critical parameter governing the roll moment characteristic for a given level of asymmetric blowing is the angle of attack at which the blown vortex forms/reestablishes. This does not appear to be well collapsed by the conventional jet momentum coefficient, C_μ.

6. Maximum roll moment capability requires full-span blowing. Shorter slots are less efficient, due to the reduction in 'blown' wing area and to the formation of a separated flow region aft of the slot (depending on tip geometry).

7. For thicker wings, considerable leading-edge thrust is developed. This is in an adverse direction for roll control utilising asymmetric blowing, but offers a significant reduction in lift-dependent drag for symmetric blowing.

8. Usable angle of attack range is limited by the onset of 'slot stall', where the lower-surface crossflow separates ahead of the slot. This may be delayed/prevented by optimisation of slot placement and leading-edge profile.

9. Application of TLEB as a flight vehicle control system will be hindered by

two factors: excessive mass-flow requirements and the practical difficulty of incorporating a slot in the leading-edge of a thin high-speed wing without loss of either blowing or aerodynamic efficiency.

7.2 Recommendations for Future Work

The following research areas are suggested to extend and improve the present results.

7.2.1 General Delta Wings

The review of general delta wing aerodynamics in Chapter 2 highlighted a number of areas where further research would be of interest.

1. Halfwidth - the analysis of vortex-induced suction peak shape in Section 2.6 was based entirely on published data. A more rigorous correlation between halfwidth and vortex core height, vortex strength and burst onset would require a systematic experimental investigation, with the critical variables being wing sweep/planform, leading-edge shape and tunnel blockage ratio. A combination of surface pressure measurements, off-surface velocity measurements and flow visualisation would be necessary.

2. Transient Burst Motion - the correlation presented in Section 2.4 suggested that the transient motion of the vortex burst could be represented by a simple linear transfer function approach. Unfortunately, insufficient consistent published data was available to confirm this, but the potential for application to the semi-empirical methods commonly used for high angle of attack aerodynamics prediction would encourage an experimental investigation.

3. Burst Lift-Loss - surprisingly little work has been published on this topic. The

usual approach of applying a factor to the vortex lift aft of the burst has been shown in this work to give a too abrupt lift-loss. This is particularly critical when modelling the roll moment characteristics of delta wings of lower (< 60°) sweep angle.

7.2.2 Tangential Leading-Edge Blowing

The analysis of roll moment generation in Sections 6.2 and 6.4 revealed a number of aspects of TLEB which require further experimental investigation.

1. Blown Vortex Formation - several aspects of this phenomenon need further clarification: the minimum blowing level required to suppress the blown vortex, the scaling of this critical blowing level, the movement of the leading-edge separation point with subcritical blowing and the related rate of redistribution of normal force from leading-edge to blown vortex.

2. Supercritical Leading-Edge Normal Force - the variation of the blown leading-edge normal force contribution with sideslip and relative (mixed) blowing level was not anticipated, and hence was not well defined experimentally. Further investigation will also be required on the possible effects of wing sweep and fuselage interference.

3. Slot Extent Effects - the most significant effect of slot extent was the formation of a tip separation region aft of the slot. The cause of the separation, the variation in extent with angle of attack and the associated lift/roll moment loss are unknown.

4. Mass-Flow Scaling - the conventional jet momentum coefficient, C_μ, does not

appear to collapse the roll moment characteristics well. Again, this failure was not anticipated and hence insufficient experimental data was obtained to clarify the situation. In view of the marginal nature of the mass-flow requirements of TLEB at full-scale, the proper scaling parameter becomes very important.

5. Optimisation of Leading-Edge Profile - for maximum blowing efficiency and suppression of slot stall.

6. Transient Force Measurements - the transient pressure response to TLEB has been previously investigated, but no corresponding force/roll moment measurements have been made.

7. Simple Flow Model - the simple LESA-based model developed in Section 6.4 showed promise, but was not completed due to insufficient data. The above recommendations, if undertaken, would provide the necessary information.

8. Strake Blowing - the high mass-flow requirements of TLEB stem directly from the need for full-span slots. An alternative would be to blow along the strake leading-edge on a double-delta planform, using the strake vortex as an aerodynamic lever to manipulate the main wing vortices. Much less blowing would be required, and installation would be simplified. The high sweep and small span typical of strakes may also result in the fuselage becoming effective as a 'splitter plate' and hence reducing vortex coupling with asymmetric blowing.

REFERENCES

1. Wilson, H.A. and Lovell, J.C., "Full-Scale Investigation of the Maximum-Lift Flow Characteristics of an Airplane Having an Approximately Triangular Planform", NACA RM-L6K20, November 1946

2. Whitford, R., "Design for Air Combat", Janes Publishing, 1987

3. Hitzel, S.M. and Schmidt, W., "Slender Wings with Leading-Edge Vortex Separation: A Challenge for Panel Methods and Euler Solvers", Journal of Aircraft, Vol 21 No 10, October 1984, pp751-759

4. Ericsson, L.E., "Cobra Manoeuvre Considerations", ICAS-92-4.6R, September 1992

5. Raymer, D., "Post-Stall Manoeuvre and the Classic Turn Rate Plot", AIAA-91-3170, September 1991

6. Herbst, W.B., "Dynamics of Air Combat", Journal of Aircraft, Vol 20 No 7, July 1983, pp594-598

7. Ross, A.J., "High Incidence - The Challenge to Control Systems", lecture presented to the Royal Aeronautical Society, 17 January 1990

8. Malcolm, G.N., Ng, T.T., Lewis, L.C. and Murri, D.G., "Development of Non-Conventional Control Methods for High Angle of Attack Flight Using Vortex Manipulation", AIAA-89-2192, July 1989

9.   Crowther, W.J. and Wood, N.J., "Tangential Forebody Blowing - Yaw Control at High Angles of Attack", AIAA-93-3406, August 1993

10.   Lamar, J.E., "Non-Linear Lift Control at High-Speed and High Angle of Attack Using Vortex Flow Technology", AGARD R-740

11.   Lee, K.T., "Controlled Vortical Flow on Delta Wings Through Unsteady Leading-Edge Blowing", PhD Thesis, Stanford University, August 1989

12.   Trebble, W.J.B., "Exploratory Investigation of the Effects of Blowing from the Leading-Edge of a Delta Wing", ARC R&M 3518, April 1966

13.   Bradley, R.G. and Wray, W.O., "A Conceptual Study of Leading-Edge Vortex Enhancement by Blowing", Journal of Aircraft, Vol 11 No 1, January 1974, pp33-38

14.   Malcolm, G.N. and Skow, A.M., "Flow Visualisation Study of Vortex Manipulation of Fighter Configurations at High Angles of Attack", AGARD CP-413, October 1986

15.   Parmenter, K. and Rockwell, D., "Transient Response of Leading-Edge Vortices to Localised Suction", AIAA Journal Vol 28 No 6, June 1990, pp1131-1133

16.   Wood, N.J. and Roberts, L., "Control of Vortical Lift on Delta Wings by Tangential Leading-Edge Blowing", Journal of Aircraft, Vol 23 No 3, March 1988, pp236-243

17. Wood, N.J., "Development of Lateral Control on Aircraft Operating at High Angles of Attack", ICAS-90-5.6.3, 1990

18. Roberts, L. and Wood, N.J., "Control of Vortex Aerodynamics at High Angles of Attack", AGARD CP-465

19. Parker, A.G., "Aerodynamic Characteristics of Slender Wings with Sharp Leading Edges - a Review", Journal of Aircraft, Vol 13 No 3, March 1976, pp161-168

20. Hummel, D., "On the Vortex Formation Over a Slender Wing at Large Angles of Incidence", AGARD CP-247

21. Nelson, R.C., "Unsteady Aerodynamics of Slender Wings", AGARD R-776

22. Wedemeyer, E., "Vortex Breakdown", AGARD LS-121

23. McKernan, J.F and Nelson, R.C., "An Investigation of the Breakdown of the Leading Edge Vortices on a Delta Wing at High Angles of Attack", AIAA-83-2114, August 1983

24. Erickson, G.E., "Flow Studies of Slender Wing Vortices", AIAA-80-1423, July 1983

25. Kegelman, J. and Roos, F., "Effects of Leading Edge Shape and Vortex Burst on the Flowfield of a 70° Sweep Delta Wing", AIAA-89-0086, January 1989

26. Weinberg, Z., "Effects of Tunnel Walls on Vortex Breakdown Location Over Delta Wings", AIAA Journal, Vol 30 No 6, June 1992, pp1584-1586

27. Wentz, W.H. and Kohlman, D.L., "Vortex Breakdown on Slender Sharp-Edged Wings", Journal of Aircraft, Vol 8 No 3, March 1971, pp156-161

28. Hummel, D., "Research in Vortex Breakdown on Slender Delta Wings", ARA Library Translation 12, October 1965

29. John, H. and Kraus, W., "High Angle of Attack Characteristics of Different Fighter Configurations", AGARD CP-247

30. Huang, X.Z. and Hanff, E.S., "Prediction of Leading Edge Vortex Breakdown on a Delta Wing Oscillating in Roll", AIAA-92-2677, June 1992

31. Kulfan, R.M., "Wing Geometry Effects on Leading Edge Vortices", AIAA-79-1872, August 1979

32. Polhamus, E.C., "Prediction of Vortex-Lift Characteristics by a Leading-Edge-Suction Analogy", Journal of Aircraft, Vol 8 No 4, April 1971, pp195-199

33. Shanks, R.E., "Low-Subsonic Measurements of Static and Dynamic Stability Derivatives of Six Flat-Plate Wings Having Leading-Edge Sweep Angles of 70° to 84°", NASA TN-D-1822, July 1963

34. Tosti, L.P., "Low-Speed Static Stability and Damping in Roll Characteristics of some Swept and Unswept Low Aspect Ratio Wings", NACA TN-1468,

October 1947

35. Fletcher, H.S., "Low-Speed Experimental Determination of the Effects of Leading-Edge Radius and profile Thickness on Static and Oscillatory Lateral Stability Derivatives for a Delta Wing with 60° of Leading-Edge Sweep", NACA TN-4341, July 1958

36. McLemore, H.C., "Low-Speed Investigation of the Effects of Wing Leading-Edge Modifications and Several Outboard Fin Arrangements on the Static Stability Characteristics of a Large-Scale Triangular Wing", NACA RM-L51J05, January 1952

37. Roos, F.W. and Kegelman, J.T., "An Experimental Investigation of Sweep-Angle Influence on Delta-Wing Flows", AIAA-90-0383, January 1990

38. Ericsson. L.E., "Another Look at High Angle of Attack Support Interference", AIAA-90-0188, January 1990

39. Johnson, J.L., Grafton, S.B. and Yip, L.P., "Exploratory Investigation of the Effects of Vortex Bursting on the High-Angle-of-Attack Lateral-Directional Stability Characteristics of Highly-Swept Wings", AIAA-80-0463, 1980

40. Goodman, A. and Thomas, D.F., "Effects of Wing Position and Fuselage Size on the Low-Speed Static and Rolling Stability Characteristics of a Delta Wing Model", NACA R-1224, 1955

41. Jacquet, B.M. and Brewer, J.D., "Effects of Various Outboard and Central Fins

on Low-Speed Static Stability and Rolling Characteristics of a Triangular Wing Model", NACA RM-L9E18, June 1950

42.   Jacquet, B.M. and Brewer, J.D., "Low-Speed Static Stability and Rolling Characteristics of Low-Aspect Ratio Wings of Triangular and Modified Triangular Planforms", NACA RM-L8L29, March 1949

43.   Letko, W., "Experimental Determination at Subsonic Speeds of the Oscillatory and Static Lateral Stability Derivatives of a Series of Delta Wings with Leading-Edge Sweeps from 30° to 86.5°", NACA RM-L57A30, April 1957

44.   Riley, D.R. and Bird, J.D., "Experimental Determination of the Aerodynamic Derivatives Arising from Acceleration in Sideslip far a Triangular, a Swept and an Unswept Wing", NACA RM-L55A07, March 1955

45.   Ashley, H., Katz, J., Jarrah, M.A. and Vaneck, T., "Survey of Research on Unsteady Aerodynamic Loading of Delta Wings", Journal of Fluids and Structures (1991) 5, pp363-390

46.   Jarrah. M.A., "Unsteady Aerodynamics of Delta Wings Performing Manoeuvres to High Angles of Attack", PhD Thesis, Stanford University Report SUDDAR 574, December 1988

47.   Guglieri, G. and Quagliotti, F.B., "Experimental Investigation of Vortex Dynamics on Delta Wings", AIAA-92-2731, 1992

48.   Guglieri, G., Onorato, M. and Quagliotti, F.B., "Vortex Breakdown Study on

a 65° Delta Wing Tested in Static and Dynamic Conditions", ICAS-92-4.10.2, 1992

49.   LeMay, S.P., Batill, S.M. and Nelson, R.C, "Vortex Dynamics on a Pitching Delta Wing", Journal of Aircraft, Vol 27 No 2, February 1990, pp131-138

50.   Staufenbiel, R., Steckemetz, B. and Zhu, S., "Vortical Flows Around Delta Wings in Unsteady Manoeuvres and Gusts", ICAS-88-3.11.2, 1988

51.   Magness, C., Robinson, O. and Rockwell, D., "Control of Leading-Edge Vortices on a Delta Wing", AIAA-89-0999, March 1989

52.   Reynolds, G.A. and Abtahi, A.A., "Instabilities in Leading-Edge Vortex Development", AIAA-87-2424, August 1987

53.   Thompson, S.A., Batill, S.M. and Nelson, R.C., "Separated Flowfield on a Slender Wing Undergoing Transient Pitching Motions", Journal of Aircraft, Vol 28 No 8, August 1991, pp489-495

54.   Lambourne, N.C. and Bryer, D.W., "The Bursting of Leading-Edge Vortices - some Observations and Discussion of the Phenomenon", ARC R&M 3282, April 1961

55.   Wolffelt, K.W., "Investigation on the Movement of Vortex Burst Position with Dynamically Changing Angle of Attack for a Schematic Delta Wing in a Watertunnel with Correlation to Similar Studies in a Windtunnel", AGARD CP-413

56.   Portnoy, H., "Unsteady Motion of Vortex-Breakdown Positions on Delta Wings", ICAS-88-6.8.3, 1988

57.   Boyden, R.P., "Effects of leading-Edge Vortex Flow on the Roll Damping of Slender Wings", Journal of Aircraft, Vol 8 No 7, July 1971, pp543-547

58.   Nguyen, L.E., Yip, L.P. and Chambers, J.R., "Self-Induced Wing Rock of Slender Delta Wings", AIAA-81-1883, August 1981

59.   Ross, A.J., "Lateral Stability at High Angles of Attack, Particularly Wing Rock", AGARD CP-260

60.   Levin, D. and Katz, J., "Dynamic Load Measurements with Delta Wings Undergoing Self-Induced Roll Oscillations", Journal of Aircraft, Vol 21 No 1, January 1984, pp30-36

61.   Arena, A.S. and Nelson, R.C., "The Effect of Asymmetric Vortex Wake Characteristics on a Slender Delta Wing Undergoing Wing Rock Motion", AIAA-89-3348, 1989

62.   Ericsson, L.E., "Fluid Mechanics of Slender Wing Rock", Journal of Aircraft, Vol 21 No 5, May 1984, pp322-328

63.   Ng, T.T. and Malcolm, G.N., "Effect of Leading-Edge Roundness on a Delta Wing in Wing-Rock Motion", AIAA-90-3080, 1990

64.   Ericsson, L.E., "Sources of High-Alpha Vortex Asymmetry at Zero Sideslip",

Journal of Aircraft, Vol 29 No 6, November-December 1992, pp1086-1090

65.   Hitzel, S.M. and Schmidt, W., "Slender Wings with leading-Edge Vortex
        Separation: A Challenge for Panel Methods and Euler Solvers", Journal of
        Aircraft, Vol 21 No 10, October 1984, pp751-759

66.   Jones, R.T., "Properties of Low Aspect Ratio Pointed Wings at Speeds Above
        and Below the Speed of Sound", NACA R-835, 1946

67.   Polhamus, E.C., "A Concept of the Vortex Lift of Sharp-Edge Delta Wings
        Based on a Leading-Edge-Suction Analogy", NASA TN-D-3767, December
        1966

68.   Coe, P.L., "A Vortex Entrainment Model Applied to Slender Delta Wings",
        AIAA Journal, Vol 12 No 1, January 1974, pp110-112

69.   Er-El, J. and Yitzhak, Z., "Experimental Examination of the Leading-Edge
        Suction Analogy", Journal of Aircraft, Vol 25 No 3, March 1988, pp195-199

70.   Lamar, J.E., "Extension of the Leading-Edge Suction Analogy to Wings with
        Separated Flow Around the Side Edges at Subsonic Speeds", NASA TR-R-428,
        1974

71.   Lan, C.E. and Su, I., "Effect of a Round Airfoil Nose on Leading-Edge
        Suction", Journal of Aircraft, Vol 24 No 7, July 1987, pp472-474

72.   Carlson, H.W., Mack, R.J. and Barger, R.L., "Estimation of Attainable

Leading-Edge Thrust for Wings at Subsonic and Supersonic Speeds", NASA TP-1500, October 1979

73.   Lan, C.E. and Hsu, C-H., "Effects of Vortex Breakdown on Longitudinal and Lateral-Directional Aerodynamics of Slender Wings by the Suction Analogy", AIAA-82-1385, 1982

74.   Snyder, M.H. and Lamar, J.E., "Application of the Leading-Edge Suction Analogy to Prediction of Longitudinal Load Distribution and Pitching Moments for Sharp-Edged Delta Wings", NASA TN-D-6994, October 1972

75.   Lan, C.E., "The Unsteady Suction Analogy and Applications", AIAA Journal, Vol 20 No 12, December 1982, pp1647-1656

76.   Lamar, J.E., "Prediction of Vortex Flow Characteristics of Wings at Subsonic and Supersonic Speeds", Journal of Aircraft, Vol 13 No 7, July 1976, pp490-494

77.   Lamar, J.E., "Recent Studies of Subsonic Vortex Lift Including Parameters Affecting Stable Leading-Edge Vortex Flow", Journal of Aircraft, Vol 14 No 12, December 1977, pp1205-1211

78.   Carlson, H.W. and Mack, R.J., "Studies of Leading-Edge Thrust Phenomena", Journal of Aircraft, Vol 17 No 12, December 1980, pp890-897

79.   Ericsson, L.E. and Reding, J.P., "Approximate Nonlinear Slender Wing Aerodynamics", Journal of Aircraft, Vol 14 No 12, December 1977, pp1197-

80. Ericsson, L.E. and King, H.H.C., "Rapid Prediction of High-Alpha Unsteady Aerodynamics of Slender-Wing Aircraft", Journal of Aircraft, Vol 29 No 1, January 1992, pp85-92

81. Zohar, Y. and Er-El, J., "Influence of the Aspect Ratio on the Aerodynamics of the Delta Wing at High Angle of Attack", Journal of Aircraft, Vol 25 No 3, March 1988, pp200-205

82. Kirkpatrick, D.L.I., "Analysis of the Static Pressure Distribution on a Delta Wing in Subsonic Flow", ARC R&M 3619, August 1968

83. Greenwell, D.I. and Wood, N.J., "The Determination of Vortex Burst Location on Delta Wings from Surface Pressure Measurements", AIAA Journal, November 1992

84. Er-El, J., Seter, D. and Weihs, D., "Nonlinear Aerodynamics of Delta Wing in Combined Pitch and Roll", Journal of Aircraft, Vol 26 No 3, March 1989, pp254-259

85. Naarding, S.H.J. and Verhaagen, N.G., "Experimental and Numerical Investigation of the Vortex Flow over a Sharp Edged Delta Wing With and Without Sideslip", Delft University of Technology Report LR-573, December 1988

86. Harvey, J.K., "Some Measurements on a Yawed Slender Delta Wing with

Leading Edge Separation", ARC R&M 3160, October 1958

87.   Carcaillet, R., Manie, F., Pagan, D. and Solignac, J.L., "Leading Edge Vortex
       Flow over a 75 degree Swept Delta Wing - Experimental and Computational
       Results", ICAS-86-1.5.1, 1986

88.   Ornberg, T., "A Note on the Flow Around Delta Wings", Royal Institute of
       Technology, Stockholm, Report KTH-AERO TN38, February 1950

89.   Peckham, D.H., "Low-Speed Wind-Tunnel Tests on a Series of Uncambered
       Slender Pointed Wings with Sharp Edges", ARC R&M 3186, December 1958

90.   Hemsch, M.J. and Luckring, J.M., "Connection between Leading-Edge Sweep,
       Vortex Lift and Vortex Strength for Delta Wings", Journal of Aircraft, Vol 27
       No 5, May 1990, pp473-475

91.   Stahl, W., Hartmann, K. and Schneider, W., "Force and Pressure
       Measurements on a Slender Delta Wing at Transonic Speeds and Varying
       Reynolds Numbers", AGARD CP-83

92.   Fink, P.T. and Taylor, J., "Some Early Experiments on Vortex Separation",
       ARC R&M 3489, 1967

93.   Grismer, D., Nelson, R.C. and Ely, W., "An Experimental Study of Double
       Delta Wings in Sideslip", AIAA-91-3308, September 1991

94.   Cunningham, A.J. et al, "Unsteady Low-Speed Windtunnel Tests of a Straked

Delta Wing Oscillating in Pitch", AFWAL TR-87-3098, April 1988

95. Richwine, D.M. and Fisher, D.F., "In-Flight Leading-Edge Extension Vortex Flow-Field Survey Measurements on a F-18 Aircraft at High Angle of Attack", AIAA-91-3248, September 1991

96. Payne, F.M., Ng, T.T. and Nelson, R.C., "Experimental Study of the Velocity Field on a Delta Wing", AIAA-87-1231, June 1987

97. Hemsch, M.J., "Similarity for High Angle of Attack Subsonic/Transonic Slender Body Aerodynamics", Journal of Aircraft, Vol 26 No 1, January 1989, pp56-66

98. DelFrate, J.H., Fisher, D.F. and Zuniga, F.A., "Inflight Flow Visualisation with Pressure Measurements at Low Speeds on the NASA F-18 High Alpha Research Vehicle", NASA TM-101726, October 1990

99. Polhamus, E.C., "Applying Slender Wing Benefits to Military Aircraft", Journal of Aircraft, Vol 21 No 8, August 1984, pp545-558

100. Hall, M.H., "The Structure of Concentrated Vortex Cores", Progress in Aeronautical Sciences, Vol 7, pp53-110

101. Ashenberg, J., "A Model for Vortex Breakdown on Slender Wings", AIAA Journal, Vol 25 No 12, December 1987, pp1622-1624

102. Fiddes, S., "Separated Flow About Cones at Incidence - Theory and

Experiment", RAE-TM-Aero 2055, 1985

103. Zakharov, S.B., "The Effect of Rounding the Leading Edges on the Characteristics of Separated Flow Past Delta Wings of Low Aspect Ratio", Uchenye zapiski TsAGI, Vol 13 No 4 pp1-9, 1982, also RAE Library Translation 2164, November 1990

104. Smith, J.H.B, "Improved Calculations of Leading-Edge Separation from Slender, Thin, Delta Wings", RAE TR-660070, 1966

105. Wood, N.J. and Nielsen, J.N., "Circulation Control Airfoils as Applied to Rotary Wing Aircraft", Journal of Aircraft, Vol 23 No 12, December 1986, pp865-875

106. Wong, G., "Experimental in the Control of Wing Rock at High Angle of Attack Using Tangential Leading-Edge Blowing", PhD Thesis, Stanford University, 1992

107. Wood, N.J. and Roberts, L., "The Control of Delta Wing Aerodynamics at High Angles of Attack", presented to RAeS conference "The Prediction and Exploitation of Separated Flows", April 1989

108. Wood, N.J., Roberts, L. and Celik, Z., "The Control of Asymmetric Vortical Flow over Delta Wings at High Angles of Attack", Journal of Aircraft, Vol 27 No 5, May 1990, pp429-435

109. Greenwell, D.I. and Wood, N.J., "Control of Asymmetric Vortical Flows",

AIAA-91-3272, September 1991

110. Mittelman, Z. and Kroo, I., "Unsteady Aerodynamics and Control of Delta Wings with Tangential Leading Edge Blowing", AIAA-89-3374, 1989

111. Craig, K., "Computational Study of the Aerodynamics and Control by Blowing of Asymmetric Vortical Flows over Delta Wings", AIAA-92-0410, January 1992

112. Levin, D. and Katz, J., "Vortex-Lattice Method for the Calculation of the Nonsteady Separated Flow over Delta Wings", Journal of Aircraft, Vol 18 No 12, December 1981, pp1032-1037

113. Earnshaw, P.B. and Lawford, J.A., "Low-Speed Wind Tunnel Tests on a Series of Sharp-Edged Delta Wings", ARC R&M 3424, 1964

114. Greenwell, D.I., Bean, D.E. and Wood, N.J., "Calibration of the High-Speed Working Section of the 7'x 5' Wind-Tunnel", School of Mechanical Engineering Report 49/1992, July 1992

115. Bean, D.E. and Wood, N.J., "An Experimental Investigation of Empennage Buffeting", AIAA-91-3224, September 1991

116. Greenwell, D.I., Bean, D.E. and Wood, N.J., "A High Angle of Attack Model Support System for the 7'x 5' Wind-Tunnel", School of Mechanical Engineering Report 50/1992, July 1992

117. Wong, G.S., Rock, S.M., Wood, N.J. and Roberts, L., "Active Control of Wing Rock of a Delta Wing at Post-Stall Using Tangential Leading-Edge Blowing", AIAA-93-0056, January 1993

118. Greenwell, D.I., Bean, D.E. and Wood, N.J., "The Design and Calibration of a Three-Component Strain Gauge balance", School of Mechanical Engineering Report 53/1992, July 1992

119. Wick, B.H., "Chordwise and Spanwise Loadings Measured at Low Speed on a Triangular Wing Having an Aspect Ratio of Two and a NACA 0012 Airfoil Section", NACA TN-1650, June 1948

120. Greenwell, D.I. and Wood, N.J., "Some General Purpose Data Acquisition and Reduction Programs in use in the Aerodynamics Group", School of Mechanical Engineering Report 52/1992, July 1992

121. Greenwell, D.I., "RigTest V4.1 User Guide", School of Mechanical Engineering Report 51/1992, December 1992

122. Jones, R. and Miles, C.J.W., "Tests on Three Equilateral Triangular Plates in the Compressed Air Tunnel", ARC R&M 2518, September 1946

123. Fletcher, H.S., "Low-Speed Experimental Determination of the Effects of Leading-Edge Radius and Profile Thickness on Static and Oscillatory Lateral Stability Derivatives for a Delta Wing with 60° of Leading-Edge Sweep", NACA TN4341, July 1958

124. Tingas, S.A. and Rao, D.M., "Subsonic Balance and Pressure Investigation of a 60° Delta Wing with Leading-Edge Devices", NASA CR165923, May 1982

125. Wood, N.J., Lee, K.T. and Roberts, L., "The Control of Vortical Flow on Delta Wings by Tangential Leading-Edge Blowing", unpublished JIAA report, University of Stanford, December 1987

126. Meyn, L.A., Lanser, W.R. and James, K.D., "Full-Scale High Angle-of-Attack Tests of an F/A-18", AIAA-92-2676, June 1992

127. Mabey, D.G., Private Communication, 1992

128. Ridder, S-O, "On the Induced Drag of Thin Plane Delta Wings - An Experimental Study of the Spanwise Distribution of the Leading-Edge Forces at Low Speeds", Royal Institute of Technology Report KTH-AERO-TN-57, Stockholm, Sweden, May 1971

129. Bartlett, G.E. and Vidal, R.J., "Experimental Investigation of the Influence of Edge Shape on the Aerodynamic Characteristics of Low Aspect Ratio Wings at Low Speeds", Journal of the Aeronautical Sciences, 1955, pp517-533

130. Kraus, W., "X-31, Discussion of Steady-State and Rotary Derivatives", AGARD CP-497, May 1991

APPENDIX A

RIGTEST V4.1 CONFIGURATION FILE FORMAT

A.1 Main Configuration Data


```
/* Title & Initial DT2821 Settings */

config_title        char[80]       - file title
config_date         char[10]       - date of file (dd/mm/yy)

ch_sample_rate      float          - channel sample rate (Hz)
                                     ( 1 → board limit )
ch_samples          int            - no of samples per AD channel
                                     ( 2 → 1000 )

/* Optional Sections */

no_angles           int            - no of degrees of freedom of model
                                     support system ( 0 → 3 )

        ..if no_angles > 0 → Support System Data ( Section A.2 )

no_bals             int            - no of balances ( 0 → 2 )

        ..if no_bals > 0  →  Balance Data ( Section A.3 )

no_SVs              int            - no of Scanivalves ( 0 → 6 )

        ..if no_SVs > 0  →  Scanivalve Data ( Section A.4 )

no_kulites          int            - no of pressure transducers
                                     ( 0 → 10 )

        ..if no_kulites > 0  →  Transducer Data ( Section A.5 )

no_slots            int            - no of blowing slots ( 0 → 2 )

        ..if no_slots > 0  →  Blowing Data ( Section A.6 )

/* Reference Pressure Data */

refp_title          char[40]       - title of ref pressure data
refp_flag           int            - ref pressure input flag
                                     0 → input from keyboard
                                     1 → read from micromanometer
                                     2 → read from Scanivalve port
                                     3 → read from Kulite
                                     4 → Δ between two SV ports

..if refp_flag = 1
        {
        channel     int            - AD channel for ref pressure
                                     ( 0 → 15 )
        output      double         - max transducer output
                                     ( < 10V )
        }

..if refp_flag = 2
        {
        Scanivalve  int            - Scanivalve number ( 1 → 6 )
        port        int            - port number ( 2 → 47 )
        }
```

```
..if refp_flag = 3
     {
     Kulite         int             - Kulite number ( 1 → 10 )
     }

..if refp_flag = 4
     {
     SV_total       int             - SV for 'total' pressure
     port_total     int             - port      "        "
     SV_static      int             - SV for 'static' pressure
     port_static    int             - port      "        "

     ( NB - reference pressure reading = 'total' - 'static' )
     }

refp_to_q          double          - factor on rdg to give dynamic
                                     pressure (q) in N/m2
```

A.2 Model Support System Data

```
..for each support system angle
     {
     title          char[80]        - angle title

     type_flag      int             - angle type flag
                                        0 → roll
                                        1 → pitch
                                        2 → yaw
     control_flag int              - angle control flag
                                        0 → angle input from keyboard
                                        1 → angle read on AD channel
                                        2 → angle set from DA port

     ..if control_flag = 1, 2
          {
          channel      int             - angle feedback AD channel
                                          ( 0 → 15 )
          output       double          - max feedback signal
                                          ( < 10V )
          order        int             - order of polynomial fit
                                          for angle = f(V_{angle})
                                          ( 1 → 5 )
          f[0..order]  double          - order+1 coefficients of fit

          .. if control_flag = 2
               {
               DAC          int     - DA port for angle control
                                       ( 0, 1 )
               DIO_port     int     - DIO port for enable signal
                                       ( 0, 1 )
               DIO_line     int     - DIO line for enable signal
                                       ( 0 → 7 )
               order        int     - order of polynomial fit for
                                       V_{angle} = g(angle)
                                       ( 1 → 6 )
               g[0..order]  double
               }

          max_angle    double          - upper limit on angle
                                          ( < 360° )
          min_angle    double          - lower limit on angle
                                          ( > -360° )

          }
     }
```

A.3 Balance Data

```
display_flag        int           - force/moment display switch
                                     0 → coefficients
                                     1 → SI units

..for each balance
      {
      title         char[80]      - balance title
      no_cpts       int           - no of components

      ..for each component
            {
            title         char[40]      - component title
            type          int           - type flag
                                           0 → normal force
                                           1 → axial force
                                           2 → side force
                                           3 → pitching moment
                                           4 → rolling moment
                                           5 → yawing moment

            channel       int           - AD channel ( 0 → 15 )
            output        double        - max channel output ( < 10V )

            ref_area      double        - reference area ( m2 )
            ..if type = moment ( ie 3,4,5 )
            ref_len       double        - reference length ( m )
            }

      cal_matrix    double[][]    - balance calibration matrix
                                     ( enter in usual order, row by row )
      res_matrix    double[][]    - resolution matrix
                                     → resolve 'balance' forces,
                                        moments about required point

      woff_flag     int           - wind-off zero flag
                                     0 → independent of model position
                                     1 → zero vs support system angle 1
                                     2 → zero vs support system angle 2
                                     3 → zero vs support system angle 3

      ..if woff_flag > 0
            {
            ..for each component
                  {
                  S             double        - factor on sinθ term
                  s0            double        - θ offset
                  C             double        - factor on cosθ term
                  c0            double        - θ offset
                  }
            }

      }
```

Notes - if the balance voltages are V ($= [\ cpt1,\ ..\ cpt?\ ]^t$), the calibration matrix is C and the resolution matrix is R, then the balance forces are

$$F = R.C.V$$

- if woff_flag > 0, then for each component the 'wind-off zero' is

$$S*\sin(\theta+s0) + C*\cos(\theta+c0) + A$$

where θ is the appropriate support system angle and A is the actual wind-off zero. $S, s0, C, c0$ must be determined prior to testing

A.4 Scanivalve Data

```
display_flag          int           - pressure display switch
                                       0 → pressure coefficient
                                       1 → SI units ( Pa )

..if display_flag = 0   ( ie pressure coefficients )
      {
      SV_pfs_flag  int              - P_freestream source flag
                                       0  → applied to transducer
                                       2  → from given SV port
                                       3  → from given Kulite
                                       5  → P_fs = 0.0
                                       12 → factor * SV port
                                       13 → factor * Kulite
                                       15 → factor * dynamic pressure

      ..if SV_pfs_flag > 10
            {
            factor         double       - factor on given pressure source
            }

      ..if (SV_pfs_flag-10) = 2
            {
            SV_pfs        int          - SV for P_fs ( 1 → 6 )
            port_pfs      int          - port for P_fs ( 2 → 47 )
            }

      ..if (SV_pfs_flag-10) = 3
            {
            Kulite_pfs    int          - kulite for P_fs ( 1 → 10 )
            }
      }

..for each Scanivalve
      {
      title         char[80]       - scanivalve title

      drive_flag   int            - SV drive type
                                     ( 0  for  +ve  pulse,  1  for  -ve  )
      home_port    int            - DIO port for 'home' signal
                                     ( 0, 1 )
      home_line    int            - DIO line for 'home' signal
                                     ( 0 → 7 )
      step_port    int            - DIO port for 'step' command
                                     ( 0, 1, ≠ home_port )
      step_line    int            - DIO line for 'step' command
                                     ( 0 → 7 )

      step_length  double         - length of step pulse ( s )
      read_delay   double         - delay before read     ( s )

      first_port   int            - first port to be read
                                     ( 2 → 47 )
      last_port    int            - last port to be read
                                     ( 2 → 47, >= first_port )

      coord_flag   int            - port coordinate flag
                                     0  → no coordinates
                                     1  → x only
                                     11 → x, y
                                     12 → x, θ
                                     13 → r, θ
                                     21 → x, y, z
                                     22 → x, r, θ
                                     23 → r, θ, ψ

      ..if coord_flag >= 1
      {
      x_title                      char[40]      - x title
      x[first_port..last_port]     double[]      - x coord
      }
```

```
..if coord_flag >= 11
{
y_title                       char[40]       - y title
y[first_port..last_port]      double[]       - y coord
}


..if coord_flag >= 21
{
z_title                       char[40]       - z title
z[first_port..last_port]      double[]       - z coord
}


transducer_title    char[40]        - pressure transducer
plusV_to_p          double          - +ve gain ( Pa/V )
minusV_to_p         double          - -ve gain ( Pa/V )
channel             int             - AD channel ( 0 → 15 )
output              double          - max transducer output
                                      ( < 10V )
calibration_flag    int             - transducer calibration
                                       0  → gain & zero offset
                                               read from file
                                      11 → gain read from file,
                                            transducer zeroed on
                                            port 0 ( home )
                                      12 → transducer zeroed on
                                            port 0, gain set from
                                            reference pressure
                                            applied on port 1
                                            ( dummy gains input above )
..if calibration_flag = 0
{
zero_offset         double          - 'zero' pressure rdg ( V )
}


..if calibration_flag = 12
{
cal_pressure        double          - calibration pressure on port 1 (Pa)
}
```

A.5 Pressure Transducer Data

```
display_flag          int           - pressure display switch
                                       0 → pressure coefficient
                                       1 → SI units ( Pa )

..if display_flag = 0   ( ie pressure coefficients )
      {
      kulite_pfs_flag      int     - P_freestream source flag
                                      0  → applied to transducer
                                      2  → from given SV port
                                      3  → from given Kulite
                                      5  → P_fs = 0.0
                                      12 → factor * SV port
                                      13 → factor * Kulite
                                      15 → factor * dynamic pressure

      ..if kulite_pfs_flag > 10
          {
          factor         double        - factor on given pressure source
          }


      ..if (kulite_pfs_flag-10) = 2
          {
          SV_pfs         int     - SV for P_fs ( 1 → 6 )
          port_pfs       int     - port for P_fs ( 2 → 47 )
          }


      ..if (kulite_pfs_flag-10) = 3
          {
          Kulite_pfs     int     - kulite for P_fs ( 1 → 10 )
          }
```

```
        }
..for each kulite
        {
        transducer_title      char[40]      - transducer title
        plusV_to_p            double        - +ve gain ( Pa/V )
        minusV_to_p           double        - -ve gain ( Pa/V )
        channel               int           - AD channel ( 0 → 15 )
        output                double        - max transducer output
                                              ( < 10V )
        }
```

A.6 Blowing Data

```
..for each slot
        {
        slot_title            char[40]      - slot title
        transducer_flag       int           - plenum pressure t.ransducer
                                              2 → Scanivalve
                                              3 → Kulite

        ..if transducer_flag = 2
                {
                slot_SV       int           - SV for plenum pressure
                slot_port     int           - port      "         "
                }

        ..if transducer_flag = 3
                {
                slot_kulite   int           - kulite for plenum pressure
                }

        exit_area             double        - slot exit area ( m² )
        ref_area              double        - reference area ( m² )
        }
```

Notes -   the plenum pressure transducer(s) must have been set for 'Coefficient' output (ie display_flag = 0).

-   assuming incompressible flow,

$$C_\mu = 2 * C_p * A_{exit} / A_{ref}$$

where $C_p = \Delta P_{plenum} / q$

APPENDIX B

PUBLISHED PAPERS

Journal Papers (Enclosed)

B1.   Greenwell, D.I. and Wood, N.J., "Determination of Vortex Burst Location on Delta Wings from Surface Pressure Measurements", AIAA Journal, Vol 30 No 11, November 1992, pp2736-2739

B2.   Greenwell, D.I. and Wood, N.J., "Static Roll Moment Characteristics of Asymmetric Tangential Leading-Edge Blowing on a Delta Wing at High Angles of Attack", AIAA-93-0052, accepted for Journal of Aircraft 1993

Conference Papers (Not Enclosed)

1.   Greenwell, D.I. and Wood, N.J., "Control of Asymmetric Vortical Flows", AIAA-91-3272, September 1991

2.   Bean, D.E., Greenwell, D.I. and Wood, N.J., "A Vortex Control Technique for the Attenuation of Fin Buffet", ICAS 92-4.10.3, 1992

3.   Craig, K.J., Roberts, L., Greenwell, D.I. and Wood, N.J., "Theoretical and Experimental Investigation of a Delta Wing with Turbulent Leading-Edge Jets", AGARD Conference on 'Experimental and Computational Assessment of Jets in a Cross-Flow', Winchester, UK, April 1993

Determination of Vortex Burst Location on Delta Wings from Surface Pressure Measurements

Douglas I. Greenwell* and Norman J. Wood†
University of Bath, Bath BA2 7AY, England, United Kingdom

A shape parameter for the vortex-induced upper surface pressure distribution on a delta wing has been derived from a simple two-dimensional potential flow model. For this model the half-width of the suction peak is a function solely of the vortex height above the wing surface. Published experimental data are used to show that this result holds for real delta wing flows at low angles of attack, thus allowing a good estimate of vortex trajectory and strength to be made from surface pressure measurements alone. At higher angles of attack, where the vortex burst region is over the wing, the simple model breaks down; however, the variation in half-width with both chordwise location and angle of attack appears to correlate well with the condition of the adjacent vortex. In particular, the burst point corresponds to an abrupt, well-defined change in half-width. This observation offers an alternative to flow visualization techniques for experimental determination of burst location.

Nomenclature

C_p = pressure coefficient
$C_{p_{min}}$ = pressure coefficient at suction peak
c = root chord
K = nondimensional angle of attack, $\tan \alpha / \tan \epsilon$
p_{min}, p_0 = static pressure at suction peak
s = local semispan
V = freestream velocity
x = chordwise coordinate
y = spanwise coordinate
y_{min}, y_0 = spanwise location of suction peak
y_v = spanwise location of vortex core
y_h = half-width of suction peak
z = height of vortex core
α = angle of attack
β = sideslip angle
Γ = vortex strength
Γ' = vortex strength parameter, $y_h/s \cdot x/c \cdot \sqrt{-C_{p_{min}}}$
ϵ = wing semiapex angle
Λ = leading-edge sweep
ρ = density

Introduction

AT high angles of attack, the aerodynamics of delta wings are dominated by the trajectory of the vortex burst region. This is particularly true for lateral behavior, where asymmetric bursts induce significant nonlinearities in force and moment characteristics.[1]

The measurement of burst location is thus an important part of the investigation of these flow regimes. However, conventional experimental methods are, to some extent, unsatisfactory. Visual measurements depend on observer judgment of burst location, introducing errors of the order of 5% (Ref. 2), while the tests are often carried out at very low Reynolds numbers to facilitate flow visualization. Direct flow measurements require the use of either a physical probe, which may itself affect the burst location,[3] or a sophisticated and hence expensive nonintrusive technique such as laser Doppler velocimetry. Further, the oscillatory nature of the burst location[4] may complicate the interpretation of velocity measurements.

Previous attempts have been made to correlate vortex burst with surface pressure distributions.[2,5-7] These efforts have concentrated on the behavior of the suction peaks induced by the leading-edge vortices. In general, the variation of $C_{p_{min}}$ with angle of attack for a given chordwise location is correlated with the vortex state, but no consistent trends have been noted. For example, in one case the burst is followed by a reduction in the rate of change of the peak suction with angle of attack, whereas in another there is a local reduction in suction underneath the breakdown point followed by a recovery as the burst moves upstream. The results presented in Ref. 7 suggest that this difference in behavior may be a function of chordwise location of the pressure measurements. In general, vortex burst is not associated with any abrupt or well-defined change in peak suction. As a result, recent investigations of vortex breakdown have tended to disregard surface pressure variations.

This paper presents an alternative analysis of surface static pressure data, using a shape parameter derived from a simple potential flow model. At low angles of attack this analysis enables an estimate to be made of vortex strength and core trajectory. At high angles of attack, where the vortex burst is over the wing, the position of the burst point may be determined with comparable accuracy to that of flow visualization techniques. In addition, an insight is provided into the structure of the entire burst region.

Flow Model

For a slender wing at low angles of attack the flow may be assumed to be conical, and the problem reduces to a two-dimensional flow in the crossflow plane.[8] The simplest possible model of the flow induced by a leading-edge vortex is a point vortex over an infinite plane (Fig. 1a), inducing a suction peak as shown. It can be readily shown that the half-width of the pressure distribution is directly proportional to the height of the vortex. In addition, the vortex strength is a function of the half-width and peak suction of the pressure distribution:

$$z = \sqrt{\frac{1}{\sqrt{2}-1}} \cdot y_h$$

$$\approx 1.5538 \, y_h$$

$$\Gamma = \pi \cdot z \cdot \sqrt{(-p_{min}/\tfrac{1}{2}\rho)}$$

$$\propto y_h \cdot \sqrt{(-p_{min})}$$

a) Point vortex over infinite plane

b) Typical delta wing pressure distribution
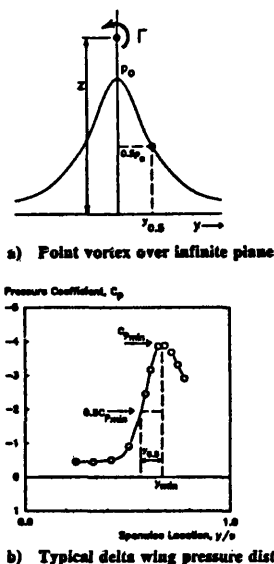
Fig. 1 Definition of half-width for vortex-induced suction peak.

a) Spanwise location of vortex relative to suction peak

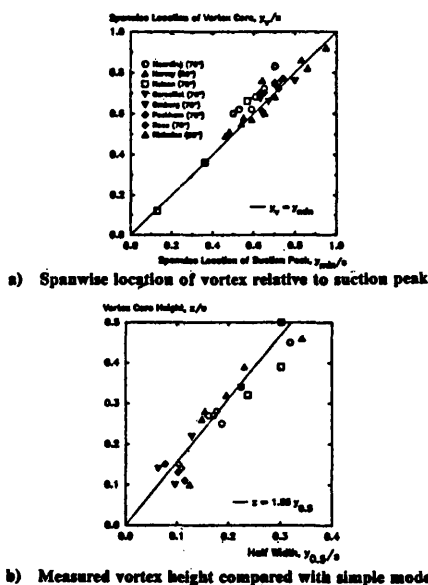b) Measured vortex height compared with simple model

Fig. 2 Application of simple model to experimental vortex trajectory data.

Clearly, a more realistic model would need to take account of the finite nature of the wing, the freestream velocity, the feeding vortex sheet, etc.[8] However, this would complicate the application of this analysis and tend to obscure the basic physics of the situation. In fact, as will be seen, the simple model gives remarkably good results when applied to experimental data.

Figure 1b shows the definition of half-width as applied to a typical delta wing upper surface pressure distribution.[7] Although the treatment is in no way rigorous, the justification for this interpretation is that the inner edge of the suction peak

most closely resembles the isolated vortex case, being relatively unaffected by the secondary separation, the leading-edge suction, and the opposite vortex. For ease of application the suction peak is measured relative to a pressure coefficient of zero, rather than the extrapolated asymptote of the pressure distribution curve. Since for low angles of attack the component of freestream velocity in the plane of the wing is close to freestream, the resultant error will be small. For this case,

$$z/s \approx 1.55\, y_H/s$$

$$\Gamma = \pi \cdot V \cdot z \cdot \sqrt{} - C_{p_{min}}$$

$$= \pi \cdot V \cdot c \cdot (1.55 y_H/s) \cdot (x \cdot \tan \epsilon/c) \cdot \sqrt{} - C_{p_{min}}$$

$$\therefore\ \Gamma/(V \cdot c \cdot \epsilon) \propto \Gamma'$$

where

$$\Gamma' = y_H/s \cdot x/c \cdot \sqrt{} - C_{p_{min}}$$

Γ' may be regarded as a vortex strength parameter, and y_H/s characterizes the shape of the vortex-induced pressure distribution.

A literature search was performed to identify published results containing both vortex core trajectory and upper surface pressure measurements.[9-18] Figure 2a compares the measured spanwise location of the vortex core and the suction peak. In general, there is good agreement, although for the relatively thick biconvex wing described in Ref. 9 the vortex tends to be around 5% outboard of the suction peak, possibly due to the high spanwise curvature of the wing. Figure 2b shows the measured vortex height plotted against the pressure distribution half-width. The simple flow model can be seen to give a good fit to the data. Figure 3 shows local nondimensional vortex strength (derived from Γ') as a function of Hemsch and Luckring's vortex similarity parameter.[19] Note
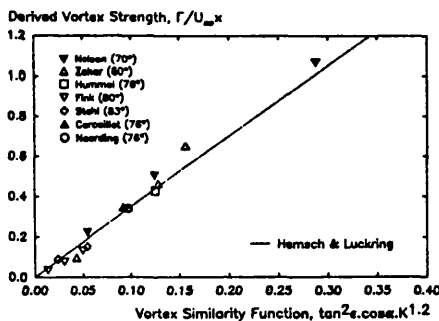

Fig. 3 Vortex strength derived from simple flow model compared with semi-empirical correlation of Ref. 19.
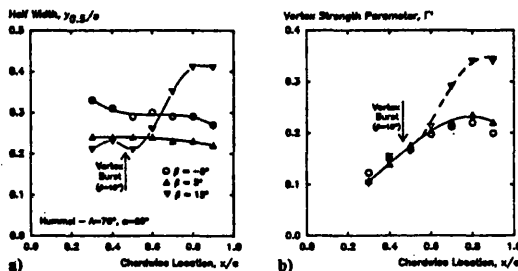

Fig. 4 Chordwise variation of half-width and vortex strength parameter (Ref. 20), showing effect of sideslip and vortex burst.

that only flows approximating to conical behavior (e.g., close to the wing apex) are shown in this figure. A semiempirical correlation from Ref. 19 is also shown.

Although there is some scatter, due in part to the small size and sometimes poor reproduction of the curves analyzed, the simple flow model gives a remarkably good fit. For very high sideslip angles the model breaks down, as the leading-edge effects become significant.

These results encouraged a closer examination of the behavior of the half-width and vortex strength parameter. Figure 4 illustrates the variation of these parameters with chordwise location for a 76-deg delta wing[20] at a constant angle of attack. From Fig. 4a it can be seen that for small sideslip angles the nondimensional half-width remains almost constant along the wing, implying a constant nondimensional vortex height, as is indeed the case. The typical upward movement of the leeward vortex with sideslip can also be seen. Similar trends are apparent in data from Refs. 8 and 14. Figure 4b shows the vortex strength parameter increasing linearly from the wing apex as in the classical conical flow assumption, except in the vicinity of the trailing edge. Small sideslip angles have little effect on the vortex strength; this is not immediately apparent from the significantly asymmetric pressure distributions.

It is clear from Fig. 4 that where a burst vortex is present over the wing the simple flow model breaks down. Although the core trajectory is relatively unaffected by the burst, the half-width exhibits a marked increase in the region of the burst, implying a change in the shape of the pressure distribution. This change can also be seen in the vortex strength parameter, which deviates from the "unburst" curve.

Effect of Vortex Burst

Thus, in contrast to the behavior of the suction peak, the half-width of the pressure distribution can change abruptly in the region of a burst vortex. This is confirmed by the analysis of published pressure data[2,5,8,14] and data from current research work at Bath. These data revealed surprisingly consistent behavior. Figure 5 shows typical variations of half-width with chordwise location and angle of attack, with the burst location marked. In general, vortex burst corresponds to a
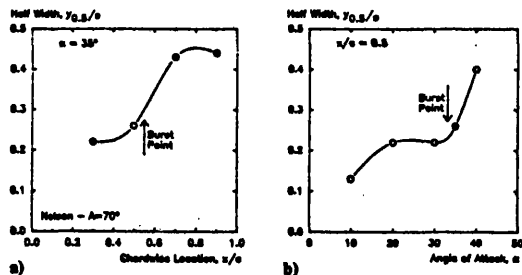
Fig. 5 Typical variation of half-width with chordwise location and angle of attack in the region of the vortex burst (Ref. 2).
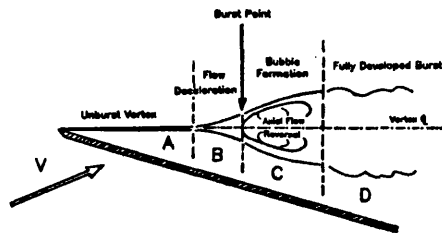
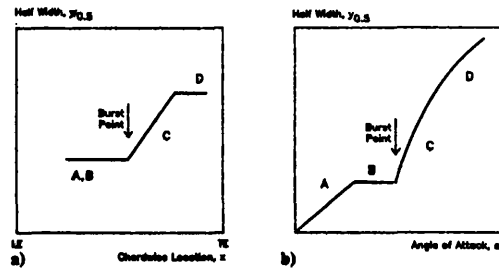Fig. 6 Schematic of the vortex burst region.

Fig. 7 General half-width trends with chordwise location and angle of attack, related to vortex condition.
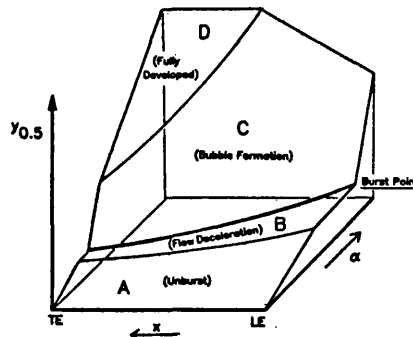
Fig. 8 Proposed interpretation of general half-width trends.

marked, well-defined change in the half-width. If sufficient pressure data are available, the burst location may thus be determined as accurately as with flow visualization techniques.

Inasmuch as half-width is a function of the pressure distribution shape (for constant vortex height), the half-width trends contain considerable information about the vortex breakdown phenomenon.

Figure 6 gives a schematic of the vortex breakdown process split into four regions.[2,21] Region A denotes the unburst vortex, where the simple model is valid and the half-width is directly proportional to vortex height. Region B indicates flow deceleration ahead of the visible burst point. In the presence of a longitudinal pressure gradient the velocity distribution through an unburst vortex (outside the viscous subcore) gradually changes,[22,23] such that the swirl component falls off more rapidly with increasing radius. The net effect should be a reduction in half-width. Region C shows a bubble-type breakdown, with some degree of flow reversal in the core. The start of the bubble is usually defined as the burst point, since it is relatively easy to observe. The flow in this region is unsteady and difficult to model; one approach has been to combine a point vortex with a source[24] to generate a semi-infinite slender body along the vortex axis aft of the breakdown point, giving a reduction in suction peak and an increase in half-width. The fully developed burst vortex, region D, is often described as a region of large-scale turbulence, although flow visualization indicates that it retains an essentially vortical character.

These stages in the vortex breakdown process may be discerned in the half-width trends typified by Fig. 5. These trends, as synthesized from a wide range of published data, are shown diagrammatically in Fig. 7.

Figure 7a illustrates the general variation of half-width with chordwise location for a constant angle of attack. The difference between the unburst (A) and decelerating flow (B) regions is generally difficult to see on this plot, with half-width remaining essentially constant. Some data sets do show a grad-

tal reduction in half-width from the apex, until the burst point is reached. The burst point, as determined visually, is always in the region of the first kink in the curve. Aft of the burst the half-width increases linearly, as the bubble develops (C), until a plateau is reached when the burst is fully developed (D). This final value is of the order of twice the unburst half-width.

Figure 7b shows the variation of half-width with angle of attack for a given chordwise location. The initially unburst vortex (A) shows a linear increase in half-width and hence height with angle of attack, consistent with observed behavior.[25] The curve then levels off, which seems to correspond to the flow deceleration region (B), with a reduced half-width relative to the unburst vortex. The burst point is always in the region of the abrupt increase in half-width at the end of this almost level portion of the curve. The half-width now increases rapidly as the breakdown progresses (C), until the burst is fully developed (D) and the curve approaches a straight line of approximately double the slope of the initial unburst vortex region.

Figure 8 is an attempt to combine the observed half-width trends with both angle of attack and chordwise location in one figure. The shape of the surface will depend on leading-edge sweep and profile.[26] The change in half-width at the burst point is most pronounced in the direction of increasing angle of attack.

Conclusions

For an unburst leading-edge vortex, a simple flow model based on a point vortex above an infinite plane gives the result that vortex height is directly proportional to the half-width of the induced pressure distribution on the surface. A surprisingly good match with experimental data is found.

For angles of attack where the vortex burst phenomenon is present over the wing, the burst location is marked by an abrupt change in the half-width of the pressure distributions. There appears to be a good correlation between the various stages of vortex breakdown and the behavior of the half-width parameter.

This observation offers the ability to determine vortex condition and burst location from surface pressure measurements alone. Limitations include the need for extensive pressure tappings and the lack of data on vortex bursts off the wing (i.e., low angle of attack or high sideslip). Conversely, the usual experimental techniques also present considerable practical difficulties, combined with the need for an "eyeball" judgment of burst location.

References

[1]Lan, C. E., and Hsu, C., "Effects of Vortex Breakdown on Longitudinal and Lateral Directional Aerodynamics of Slender Wings by the Suction Analogy," AIAA Paper 82-1385, Aug. 1982.

[2]McKernan, J. F., and Nelson, R. C., "An Investigation of the Breakdown of the Leading Edge Vortices on a Delta Wing at High Angles of Attack," AIAA Paper 83-2114, Aug. 1983.

[3]Payne, F. M., Ng, T. T., and Nelson, R. C., "Experimental Study of the Velocity Field on a Delta Wing," AIAA Paper 87-1231, June 1987.

[4]Portnoy, H., "Unsteady Motion of Vortex Breakdown Positions

on Delta Wings," International Council of the Aeronautical Sciences, ICAS-88-6.8.3, Sept. 1988.

[5]Zohar, Y., and Er-El, J., "Influence of the Aspect Ratio on the Aerodynamics of the Delta Wing at High Angle of Attack," Journal of Aircraft, Vol. 25, No. 3, March 1988, pp. 200-205.

[6]Kirkpatrick, D. L. I., "Analysis of the Static Pressure Distribution on a Delta Wing in Subsonic Flow," Aeronautical Research Council, R&M 3619, Aug. 1968.

[7]Greenwell, D. I., "Control of Delta Wing Flows at High Angles of Attack," School of Mechanical Engineering Transfer Rept., Univ. of Bath, Bath, England, May 1991.

[8]Er-El, J., Seter, D., and Weihs, D., "Nonlinear Aerodynamics of Delta Wing in Combined Pitch and Roll," Journal of Aircraft, Vol. 26, No. 3, March 1989, pp. 254-259.

[9]Naarding, S. H. J., and Verhaagen, N. G., "Experimental and Numerical Investigation of the Vortex Flow over a Sharp Edged Delta Wing With and Without Sideslip," Delft University of Technology Rept. LR-573, Delft, The Netherlands, Dec. 1988.

[10]Harvey, J. K., "Some Measurements on a Yawed Slender Delta Wing with Leading Edge Separation," Aeronautical Research Council, R&M 3160, Oct. 1958.

[11]Nelson, R. C., "Unsteady Aerodynamics of Delta Wings," AGARD R-776, April 1991.

[12]Carcaillet, R., Manie, F., Pagan, D., and Solignac, J. L., "Leading Edge Vortex Flow over a 75 degree Swept Delta Wing—Experimental and Computational Results," International Council of the Aeronautical Sciences, ICAS-86-1.5.1, Sept. 1986.

[13]Ornberg, T., "A Note on the Flow Around Delta Wings," Royal Inst. of Technology, Stockholm, Sweden, Rept. KTH-AERO TN38, Feb. 1950.

[14]Peckham, D. H., "Low-Speed Wind-Tunnel Tests on a Series of Uncambered Slender Pointed Wings with Sharp Edges," Aeronautical Research Council, R&M 3186, Dec. 1958.

[15]Roos, F. W., and Kegelman, J. T., "An Experimental Investigation of Sweep Angle Influence on Delta Wing Flows," AIAA Paper 90-0383, Jan. 1990.

[16]Richwine, D. M., and Fisher, D. F., "In-Flight Leading-Edge Extension Vortex Flow-Field Survey Measurements on a F-18 Aircraft at High Angle of Attack," AIAA Paper 91-3248, Sept. 1991.

[17]Fink, P. T., and Taylor, J., "Some Early Experiments on Vortex Separation," Aeronautical Research Council, R&M 3489, 1967.

[18]Stahl, W., Hartmann, K., and Schneider, W., "Force and Pressure Measurements on a Slender Delta Wing at Transonic Speeds and Varying Reynolds Numbers," AGARD CP-83, Paper 9, April 1971.

[19]Hemsch, M. J., and Luckring, J. M., "Connection Between Leading-Edge Sweep, Vortex Lift and Vortex Strength for Delta Wings," Journal of Aircraft, Vol. 27, No. 5, May 1990, pp. 473-475.

[20]Hummel, D., "Research on Vortex Breakdown on Slender Delta Wings," Aircraft Research Association Library Translation No. 12, Oct. 1965.

[21]Lambourne, N. C., and Bryer, D. W., "The Bursting of Leading Edge Vortices—Some Observations and Discussion of the Phenomenon," Aeronautical Research Council, R&M 3282, April 1961.

[22]Hall, M. H., "The Structure of Concentrated Vortex Cores," Progress in Aeronautical Sciences, Vol. 7, 1964, pp. 53-110.

[23]Wedemeyer, E., "Vortex Breakdown," AGARD LS-121, Dec. 1982.

[24]Ashenberg, J., "A Model for Vortex Breakdown on Slender Wings," AIAA Journal, Vol. 25, No. 12, Dec. 1987, pp. 1622-1624.

[25]Erickson, G. E., "Flow Studies of Slender Wing Vortices," AIAA Paper 80-1423, July 1980.

[26]Kegelman, J., and Roos, F., "Effects of Leading Edge Shape and Vortex Burst on the Flowfield of a 70° Sweep Delta Wing," AIAA Paper 89-0086, Jan. 1989.

AIAA 93-0052
Static Roll Moment Characteristics of Asymmetric Tangential Leading Edge Blowing on a Delta Wing at High Angles of Attack

D.I. Greenwell and N.J. Wood
University of Bath
Bath, England

31st Aerospace Sciences Meeting & Exhibit
January 11-14, 1993 / Reno, NV

STATIC ROLL MOMENT CHARACTERISTICS OF ASYMMETRIC
TANGENTIAL LEADING EDGE BLOWING ON A DELTA WING
AT HIGH ANGLES OF ATTACK

D I Greenwell[*] and Dr N J Wood[**]
University of Bath
Bath, BA2 7AY, England

ABSTRACT

The concept of asymmetric Tangential Leading Edge Blowing for the control of separated vortical flows is presented. Experimental results for the development of roll moment on a delta wing at high angles of attack and sideslip have been obtained and the underlying flow mechanisms examined. The application of the concept as an aircraft control system is discussed.

NOMENCLATURE

A_j	slot exit area
C_l	wing roll moment coefficient
C_p	pressure coefficient
C_{pmin}	minimum pressure coefficient (vortex suction peak)
C_μ	blowing moment coefficient
c	wing root chord
m	jet mass flow
q	freestream dynamic pressure
r	leading edge radius
s	wing semispan
S	wing reference area
t	wing thickness
V_j	jet exit velocity
V_∞	freestream velocity
y	spanwise coordinate
α	angle of attack
β	sideslip angle
Λ	leading edge sweep
λ	wing taper ratio
ρ	freestream density
ϕ	roll angle
θ	pitch angle
Δp	difference between plenum chamber and freestream static pressure

Subscripts

L	left side blowing only
R	right side blowing only
T	total wing blowing = L+R

INTRODUCTION

The advantages for combat aircraft of extended operation in the high angle of attack flight regime are considerable[1], with the potential for 'point and shoot' or agile 'reduced time to turn' manoeuvres. However, the development of control forces in this regime remains a significant challenge, with extensive regions of asymmetric separated unsteady flow over wing, tail and fuselage generating non-linear instabilities (wing rock, nose slice etc[2]) and at the same time reducing the effectiveness of conventional control surfaces. It is thus of interest to investigate new mechanisms for the production of pitch, yaw and roll moments such that aircraft can be trimmed or manoeuvred at extreme angles of attack and sideslip or that instabilities and non-linearities can be corrected.

Recent experimental[3][4] and numerical[5][6] investigations into the concept of tangential leading-edge blowing (TLEB) for the control of separated vortical flows on delta wings have demonstrated a capability for yaw and roll moment generation at high angles of attack. This paper will focus on the static roll moment characteristics of asymmetric TLEB, describing the results of further experimental studies and identifying the mechanisms associated with the vortical flow control. The implications for vehicle application will be discussed.

TANGENTIAL LEADING EDGE BLOWING

The concept of flow control by tangential leading-edge blowing is based on the phenomenon of Coanda jet attachment to convex surfaces[7]. The high curvature of the surface enhances the entrainment rate of the jet, induces strong suction under the jet and accelerates the transfer of momentum from the jet to the outer flow. This can be used to delay the separation of an outer flow, and in some instances produce a global modification of the flow field. Examples of the application of Coanda wall jets include circulation control aerofoils[8], control of wind tunnel boundary layers[9] and blown

---

[*]Research Officer, School of Mechanical Engineering
[**]Senior Lecturer, School of Mechanical Engineering, Member AIAA

1

trailing edge flaps[10].

Recently, wall jet blowing has been applied to the control of the crossflow separation on rounded leading-edge delta wings[11], Figure 1. The wall jet momentum now controls the strength and location of the leeside vortex pair. Previous results[12] have shown this particular application also capable of removing a vortex burst from the wing, in a process analogous to reducing the 'effective' angle of attack of the vortical flow.

EXPERIMENTAL APPARATUS

Full details of the experimental set-up are given in Reference 13. A full-span cropped 60° delta wing was sting mounted in the University of Bath 7' x 5' low-speed wind-tunnel, Figure 2. The model support rig had a pitch angle range of -5° to 85°; coupled with a roll angle capability of ±180° (about the model axis) this gave a ±90° range in both angle of attack and sideslip angle. The pantograph-type pitch mechanism maintained the wing on the tunnel centreline, thus minimising asymmetric blockage effects.

The wing was of constant thickness, approximately 3% at the root chord with a circular leading-edge profile. Maximum blockage ratio was approximately 5%, keeping interference effects to a minimum. Tangential blowing slots extended over the majority of the swept leading-edges, supplied from separate internal plenum chambers.with slot height varying conically from 0.1mm near the apex to 0.5mm at the tip. Mean slot height/radius ratio was 0.05. This slot configuration has previously been shown to give more readily interpreted results[11][12].

Normal force and roll moment data were provided by a sting balance integral with the model support system. Four rows of pressure tappings at 20%, 35%, 50% and 65% chord gave upper-surface and leading-edge pressure distributions, while blowing plenum chamber pressures were measured using two internal pressure transducers. An indication of lower-surface pressure variations was obtained by inverting the wing. No corrections were applied to the experimental data. Test Reynolds Numbers were around 1.1×10^6, based on wing root chord, corresponding to a freestream velocity of $30ms^{-1}$.

The blowing momentum coefficient, C_μ, is defined as the non-dimensional form of the jet momentum:

$$C_\mu = mV_j / qS$$

With the simplifying assumptions of incompressible flow and the local exit static pressure equal to freestream static, this becomes:

$$C_\mu = 2 (A_j/S) (V_j/V_\infty)^2$$

where

$$V_j^2 = 2 (\Delta p/\rho)$$

EFFECT OF BLOWING ON THE VORTICAL FLOWFIELD

The effects of symmetric blowing on the upper-surface pressure distribution on a delta wing have been previously described[11], and are illustrated in Figure 3. For an unburst vortex the inboard movement of the leading-edge separation point with blowing results in a reduction in vortex strength, Figure 3a. If the vortex is burst, blowing also moves the burst point aft, giving an initial increase in the suction peak at a given chordwise location as the burst moves past followed by a reduction as before, Figure 3b. At high blowing levels the leading edge vortex is completely suppressed, with the separation point displaced to the wing centreline and the pressure distribution approaching the fully attached 'RT Jones' slender wing case. The overall result of symmetric blowing is analogous to reducing the effective angle of the vortical flow[13].

With asymmetric blowing (Figure 4), a strong coupling of the vortical flow is apparent[3]. At low angles of attack (Figure 4a), with both vortices unburst, the blown vortex reduces in strength in a similar manner to the symmetric case, while the opposite unblown vortex is unaffected. At high pre-stall angles of attack, with both vortices burst but coherent vortical flow still present (Figure 4b), a reversal of operation occurs, in that blowing on one side initially unbursts the opposite vortex. This unblown vortex increases in strength with blowing up to a maximum and thereafter remains constant. The blown vortex behaviour resembles the symmetric case, with an initial increase in strength as it unbursts followed by a subsidence into fully attached flow. At post-stall angles of attack (Figure 4c), the wing flow is fully separated. Blowing on the right side results in the reestablishment of coherent vortical flow on both sides, at about the same rate.

Reference 3 notes, from flow visualisation, that the effect of asymmetric blowing is to shift the wing 'plane of symmetry' (for want of a better term) away from the blown leading edge, in a similar manner to the effect of sideslip. This resemblance is reinforced by the effect of sideslip on burst location[14], and by the similarity of blowing and sideslip induced roll moments[13], in particular the 'roll reversal' at high angles of attack as illustrated by Figure 5. This figure shows roll moment coefficient contours as a function of angle of attack and right-side blowing (Figure 5a) and sideslip angle (Figure 5b). An 'effective sideslip' analogy was expanded in Reference 13 from a conceptual viewpoint, and it was shown that the roll moment characteristics of

2

asymmetric blowing are consistent with an increase in 'effective sweep angle' on the unblown side coupled with a reduction in 'effective sweep' and vortex angle of attack on the blown side. An significant implication of this analogy is that the cross-coupling phenomenon is not merely a 'post-stall' effect, as previously suggested[3], but occurs at all angles of attack at which a burst vortex is present on the wing and has the primary effect of altering burst point position on both sides of the wing.

Examination of the chordwise behaviour of upper-surface pressure distributions supports the essential features of the analogy. However, the effects of sideslip and blowing on vortex strength are dissimilar, and this may be illustrated by the behaviour of the magnitude of the vortex-induced suction peak, C_{pmin}, as angle of attack is increased, Figure 6. Reference 15 demonstrates that vortex strength is a function of the magnitude of the suction peak and its halfwidth. For the relatively thick rounded leading-edge wing tested the halfwidth remains effectively constant with angle of attack and/or blowing up to the onset of the burst, thus the suction peak magnitude is directly related to the vortex strength. Onset of vortex burst is indicated by a break in the curve.

Figure 6a shows the effect of a non-zero roll angle on C_{pmin} on the right-side wing half as angle of attack is varied. Since the "roll angle" is about the geometric body axis, this corresponds to angle of sideslip, which increases with angle of attack (for fixed roll angle). Increasing effective-leading edge sweep ($\phi=-20°$) reduces the strength of the vortex before the burst, delays the burst and gives a more abrupt break. Reducing effective sweep increases pre-burst strength and hastens burst onset.

Figure 6b shows the effects of symmetric and asymmetric blowing on C_{pmin}, on both sides of the wing. The result of symmetric blowing is a simple shift to the right relative to the baseline 'no blowing' curve, consistent with the 'effective vortex angle of attack' analogy. For asymmetric (one-sided) blowing the results are more complex. On the blown side of the wing, the curve shifts to the right as for the symmetric case, but shows an earlier onset of vortex burst. On the unblown side pre-burst vortex strength, and the post-burst trend, are unaffected; the sole influence of blowing on one side on the flow on the other side of the wing is to delay the vortex burst.

Thus the essential difference between the effects of sideslip and asymmetric blowing (on the opposite side) on a leading-edge vortex is that sideslip results in a change in leading-edge sweep and hence a change in both vortex strength and burst location, while opposite blowing affects the burst location only.

This result in itself is possibly worthy of further investigation, since it provides evidence of a strong coupling between leading-edge vortices even at relatively low sweep angles and angles of attack. Previous studies have shown the sensitivity of the burst location to leading edge profile and downstream blockage[16], but an interaction between leading edge vortices has not been considered.

ROLL MOMENT CHARACTERISTICS

The result of this strong vortex coupling can be seen in the complex non-linear roll moment characteristics of asymmetric blowing.

Figure 7 shows the effect of increasing angle of attack at constant asymmetric blowing levels on roll moment at zero roll angle. These results may be compared with the data of Reference 3 for a similar planform tested at Stanford University, as replotted in Figure 5. Overall roll moments are similar, despite the considerably greater thickness and tunnel blockage of the Stanford wing. Significant features of the curves are the roll reversal at the stall and a complete loss of control power above 60°; these will be discussed in more detail later.

The effects of non-zero roll angle are essentially similar to the zero roll case, with an initial asymmetry in burst location and post-burst vortex characteristics due to the different effective leading edge sweep angles. The general effects may be illustrated by the examination of results for one roll angle, +20°, with right and left side asymmetric blowing, Figure 8. A significant asymmetry in control power has developed. Stabilising (negative, out of roll) moments have increased while manoeuvre (positive, into roll) moments have reduced over the whole angle of attack range. This asymmetry was also seen in Reference 4. The maximum roll angle at which the wing could be trimmed was between 10° and 15°, depending on angle of attack.

ROLL MOMENT GENERATION

To understand the underlying mechanisms for these complex roll characteristics, the individual contributions of regions of the flow field need to be isolated. For this purpose, an analysis of the pressure-integrated local roll moment at 50% chord was carried out. Total local roll moment at this location was found to correlate reasonably well with the measured total wing moments, presumably due to the very rapid motion of the burst over the aft half of the wing[17].

Zero Roll Angle

Figure 9 illustrates a representative asymmetric blowing

3

case, $C_{\mu g} = 0.04$, with the curve divided into five angle of attack regions. Corresponding local roll moment at 50% chord is shown in Figure 10, split into vortical flow and jet-induced contributions. The jet-induced contribution is primarily from the flow around the leading edge, while the vortical contribution is from the inboard portion of the wing. Note that the onset of vortex burst is not necessarily marked by an immediate change in the vortical contribution; the reduction in C_{min} shown in Figure 6 is counterbalanced by a rapid increase in halfwidth of the suction peak.

At low angles of attack (region I) the blown side vortex is completely suppressed, and the roll moment is dominated by the large contribution of the jet-induced suction, giving a 'blown wing up' moment. Significantly, this roll moment is largely independent of blowing level (Figure 7). A closer examination of the corresponding upper surface pressures show a remarkable similarity to the 'RT Jones' potential flow pressure distribution predicted by slender wing theory, with some modification due to the finite thickness of the wing. The implication is that this roll moment is a result primarily of the jet-induced displacement of the separation point, and not directly due to the suction induced by the jet itself. The impact of leading edge profile on this component of the roll moment is likely to be a second order effect; a further experimental investigation is in progress.

The overall magnitude of the roll moment is somewhat less than the levels indicated by integration of upper-surface pressures on the forward section of the wing. The most likely explanation is that on the blown side of the wing, the side-edge vortex[18] is very much reduced in strength relative to the unblown side, counteracting the leading-edge suction and giving a decrease in overall roll moment in region I. This hypothesis is supported by experimental data from Reference 18, which indicates that small changes to the tip geometry (and hence tip flowfield) of a cropped-delta wing can generate significant roll moments.

At around 25° the blown vortex reestablishes (region II), and an there is an abrupt loss of the 'RT Jones' flow component as the separation point moves rapidly from the wing centreline to near the leading edge. The overall change in normal force is small, but the reduced roll arm of the vortex-induced load results in a rapid loss of roll moment.

Within region II, a subregion III is apparent, corresponding to the presence of the vortex bursts on the wing, with the associated coupling effect. As angle of attack increases, first the unblown and then the blown vortex burst come onto the wing. The unblown burst is relatively gentle, giving a modest recovery in roll moment. However, the more abrupt lift loss shown by the blown vortex as it bursts results in a sharp further loss

of roll moment to give the 'roll reversal' phenomenon.

By around 50° the vortex bursts have reached the wing apex and the vortical flow has largely subsided (region IV). The contribution of the jet-induced flow over the forward portion of the wing is negative ('blown side up'), but is counteracted by the loss of lift at the tip noted in Region I.

At around 60° a phenomenon occurs which was not seen in earlier TLEB studies, but has been previously noted on circulation control aerofoils[6]. The flow around the blown leading edge separates before the slot lip, and there is a sudden loss of blowing effectiveness. The jet-induced component vanishes and roll moment falls to practically zero (region V), with the small suction contribution of the jet itself counterbalanced by the reaction at the slot. The onset of this 'slot stall' is a function of leading edge profile, slot position and sweep angle. In early tests a hysteresis loop was present in this region, until the lower surface boundary layer transition was fixed using a trip parallel to the leading edge.

On the basis of this analysis, the resemblance between the effects of sideslip and asymmetric blowing on overall roll moment behaviour is no more than that; a resemblance. Although both exhibit a 'roll-reversal' effect due to an asymmetry in burst location and in post-burst vortex characteristics, the details of that asymmetry are very different. Sideslip-induced roll reversal is due to the earlier vortex burst onset on the 'into wind' wing compared with the 'out of wind' wing, whereas the equivalent blown vortex burst actually occurs later than the unblown burst. The blowing-induced roll reversal phenomenon is primarily a function of the more abrupt burst behaviour of the blown vortex. It is possible, therefore, that a change in wing sweep may significantly affect this occurrence; tests on the effect of sideslip suggest that the blown post-burst loss in roll moment is considerably less violent for a lower effective leading edge sweep angle. The overall effect of a less highly swept wing (say 50° to 55°) may thus be to smooth out the roll reversal region.

The reduction in roll control power due to lift loss at the tip indicates that for maximum capability the slot should extend to the tip, and that the tip chord be kept to a minimum. Exploratory tests with a tip extension piece have shown the roll moment curve of Figure 9 to be sensitive to tip shape, particularly in region I. An application of the 'side-edge vortex' method of Reference 18 gives a crude estimate of a 10% increase in roll power in Region I for a full-length slot.

Effect of Non-Zero Roll Angle

A similar analysis may be performed for the roll moment

characteristics due to a non-zero roll angle. Figure 11 shows total wing roll moment for a representative roll angle of +20°, with blowing levels of 0.06 on the left (up, out of wind) side and 0.04 on the right (down, into wind side). The individual local roll moment contributions at 50% chord are identified in Figures 12 (left blowing) and 13 (right blowing). An additional factor is the presence of a stabilising roll contribution from the underside (potential) flow.

For left side blowing, the regions identified for the zero roll case have shifted considerably. At low angles of attack (region I), the jet-induced roll moment has reduced as effective aspect ratio of the left side has reduced with increasing leading edge sweep. On the right side, with a lower initial sweep angle, the unblown vortex bursts before the blown vortex forms, resulting in region III (burst vortices on the wing) overlapping regions I and II. The nett result is that the 'roll reversal' phenomenon occurs earlier and is less pronounced, but control power has been almost completely lost. The rapid loss in roll control power with the formation of the blown vortex (region II) occurs as for the zero roll case. However, the early onset of 'slot stall' (as a result of the high effective sweep angle of the leading edge) preempts the formation of region IV; the loss of blowing effectiveness results in the flow field returning to a fully separated flow.

For right (down) side blowing, the roll moment behaviour and contributions are essentially similar to those at zero roll angle, without the 'roll reversal'. The significant differences are that the blown vortex burst is very much gentler and slightly ahead of the unblown burst, tending to smooth out the roll reversal, and that the slot stall does not occur in the angle of attack range tested. The delay, or suppression, of slot stall is due to the lower initial effective sweep angle of the blown leading edge, and results in very high stabilising roll control power being maintained up to extremely high angles of attack (Figure 8).

The cause of the overall increase in 'stabilising' control power and reduction in 'manoeuvre' power noted above lies in the 'down' side vortex burst behaviour. The lower effective leading edge sweep gives a generally less abrupt burst process (blown and unblown), with relatively little loss of roll moment contribution.

CONSIDERATIONS FOR APPLICATION TO FLIGHT VEHICLES

Tangential Leading Edge Blowing has the potential to generate rolling moments in excess of the capabilities of conventional control surfaces at very high angles of attack[3]. Mass flow requirements are comparable to STOVL reaction control systems; for an modern combat aircraft at the low speeds typical of high angle of attack manoeuvres scaling jet mass flow directly on C_μ gives values around 20% of compressor flow. Possible increases in blowing efficiency with reduced slot height may well reduce mass flow requirements. Depending on engine rating philosophy, this level of engine bleed may not necessarily give proportional thrust losses. Interestingly, recent work on tangential forebody blowing on a full-size F18[19] suggests that a more appropriate scaling function may be mass flow ratio (ie mass flow proportional to ρV_m) rather than C_μ (proportional to ρV_m^2), significantly reducing bleed flow requirements.

For successful application a number of factors need to be resolved.

Firstly, the effect of leading edge radius. Real wings have much smaller leading-edge radii than the generic flat plate wing tests reported here. Because the contributions to roll moment identified above are all essentially responses of the outer flow to a displacement of the leading edge separation, it seems likely that the effect of further reductions in leading edge radius will be small, as long as control of the separation location can be maintained. Some confirmation of this is given by the relatively small changes in local jet-induced roll moment coefficient with chordwise location (from 20% chord to 65% chord), despite the wide variation in local leading-edge radius to span ratio (7% to 2%). In this respect, the effect of reductions in surface radius on other Coanda wall jet applications has been to improve efficiency.

The effect of wing planform on the non-linear nature of the roll moment characteristics is not known. As discussed earlier, it is possible that sweep angles of less than 60° may not exhibit the undesirable (from a flight control viewpoint) roll reversal phenomenon, due to a less abrupt vortex burst process. Encouragingly, a sweep angle of between 45° and 55° would in fact be more representative of current combat aircraft. The effect of tip geometry and blowing slot extent also need to be clarified, since these may be particularly significant.

In this test program, sideforces and yawing moments were not measured due to balance limitations. However, from visual observation of the model behaviour under test and from the leading edge pressure distributions they may be significant. Any sideforce generated by blowing will be in an adverse direction (ie towards the blown side), although a drag reduction will also result from the thrust component. Integration of leading edge pressures on the blown side at low angles of attack indicates that local sideforce coefficients fall off rapidly towards the rear of the wing as local thickness/span ratio reduces, while extrapolation forward to the wing apex gives a value very close to the sideforce predicted by slender wing theory. The implication is that for representative wing thicknesses overall sideforces will be small,

5

although limitations of model size have as yet precluded experimental confirmation.

Finally, the dynamic behaviour of transient blowing, particularly in conjunction with roll motion, requires further investigation. Initial studies of flowfield response to transient symmetric blowing (at zero roll angle)[20] have identified two time scales: a relatively fast response (of the order of one convective length) associated with the crossflow equilibrium condition and changes in vortex strength, and a slower component (five to ten convective lengths) associated with the longitudinal equilibrium of the flow and relocation of the vortex burst. At high angles of attack, where the roll moment response is a combination of jet-induced flow, asymmetric vortex strength and asymmetric burst location the resultant response to transient blowing is likely to be complex. A successful recent application of TLEB to the control of wing rock of a delta wing model[21] resolved this problem by using an initial symmetric blowing level sufficient to keep the vortex burst off the wing, and removing the second, slower, response time scale. A further complication is that roll rate can in itself generate lags in vortex position, strength and burst location[22], introducing further non-linearities.

Experimental studies into the factors discussed above, except the effect of sweep angle, are in progress at the University of Bath, and will be reported upon in due course.

CONCLUSIONS

Experimental results suggest that Tangential Leading Edge Blowing is an effective mechanism for controlling separated flows, including both burst and unburst vortices. Asymmetric blowing is capable of generating roll moments in excess of conventional moving surface controls at high angles of attack, although leading-edge geometry and wing planform effects and dynamic characteristics need further investigation prior to flight vehicle application.

The strong cross-coupling of the vortex burst phenomenon induces strongly non-linear static roll moment characteristics, which would be undesirable for a flight control system, but which may be amenable to alleviation through changes in wing planform.

The effect of asymmetric blowing on the wing flowfield is ---''tatively equivalent to an increase in sweep angle on the unblown wing side, and a reduction in both sweep angle and effective vortex angle of attack on the blown side. The overall roll moment characteristics of asymmetric blowing, although bearing a resemblance to the effects of sideslip, are in fact due to a quite different combination of vortex burst and strength asymmetries.

REFERENCES

1. Chody, J.R., "Combat Aircraft Control Requirements for Agility", Paper 4, AGARD Symposium on Aerodynamics of Combat Aircraft and of Ground Effects, AGARD CP-465, October 1990

2. Ross, A.J., "High Incidence - The Challenge to Control Systems", lecture presented to the Royal Aeronautical Society, January 1990

3. Wood, N.J., Roberts, L. and Celik, Z., "Control of Asymmetric Vortical Flows over Delta Wings at High Angles of Attack", Journal of Aircraft, Vol 27 No 5, May 1990, pp429-435

4. Wood, N.J., "Development of Lateral Control on Aircraft Operating at High Angles of Attack", ICAS-90-5.6.3, 1990

5. Yeh, D., "Numerical Simulation of the Flow Field over Delta Wings with Leading Edge Blowing", PhD Thesis, Stanford University, 1988

6. Craig, K., "Computational Study of the Aerodynamics and Control by Blowing of Asymmetric Vortical Flows over Delta Wings", AIAA-92-0410, January 1992

7. Launder, B.E. and Rodi, W., "The Turbulent Wall Jet", Progress in Aerospace Sciences, Vol 20 No 2, February 1977

8. Wood, N.J. and Nielsen, J.N., "Circulation Control Airfoils as Applied to Rotary Wing Aircraft", Journal of Aircraft, Vol 23 No 12, December 1986, pp865-875

9. Wood, N.J., Ward, S. and Roberts, L., "Wind Tunnel Boundary Layer Control by Coanda Wall Jets", AIAA-89-0149, January 1989

10. Englar, R.J., "Further Development of Pneumatic Thrust-Deflecting Powered-Lift Systems", Journal of Aircraft, Vol 25 No 4, April 1988, pp324-333

11. Wood, N.J. and Roberts, L., "Control of Vortical Lift on Delta Wings by Tangential Leading Edge Blowing", Journal of Aircraft, Vol 25 No 3, March 1988, pp236-243

12. Wood, N.J., Roberts, L. and Lee, K.T., "The Control of Vortical Flow on a Delta Wing at High Angles of Attack", AIAA-87-2278, August 1987

13. Greenwell, D.I. and Wood, N.J., "Control of Asymmetric Vortical Flows", AIAA-91-3272, September 1991

6

14. McKernan, J.F. and Nelson, R.C., "An Investigation of the Breakdown of the Leading Edge Vortices on a Delta Wing at High Angles of Attack", AIAA-83-2114, August 1983

15. Greenwell, D.I. and Wood, N.J., "The Determination of Vortex Burst Location on Delta Wings from Surface Pressure Measurements", AIAA Journal, November 1992

16. Kegelman, J. and Roos, F., "Effects of Leading Edge Shape and Vortex Burst on the Flowfield of a 70° Sweep Delta Wing", AIAA-89-0086, January 1989

17. Wentz, W.H. and Kohlman, D.L., "Vortex Breakdown on Slender Sharp-Edged Wings", Journal of Aircraft, Vol 8 No 3, March 1971, pp156-161

18. Lamar, J.E., "Prediction of Vortex Flow Characteristics of Wings at Subsonic and Supersonic Speeds", Journal of Aircraft, Vol 13 No 7, July 1976, p490-494

19. Meyn, L.A. and James, K.D., "Full-Scale High Angle of Attack Tests of an F/A-18", AIAA-92-2676, June 1992

20. Roberts, L. and Wood, N.J., "Control of Vortex Aerodynamics at High Angles of Attack", Paper 12, AGARD Symposium on Aerodynamics of Combat Aircraft and of Ground Effects, AGARD CP-465, October 1990

21. Wong, G., "Experiments in the Control of Wing Rock at High Angle of Attack Using Tangential Leading Edge Blowing", PhD Thesis, Stanford University, 1992

22. Arena, A.S. and Nelson, R.C., "The Effect of Asymmetric Vortex Wake Characteristics on a Slender Delta Wing Undergoing Wing Rock Motion", AIAA-89-3348, 1989
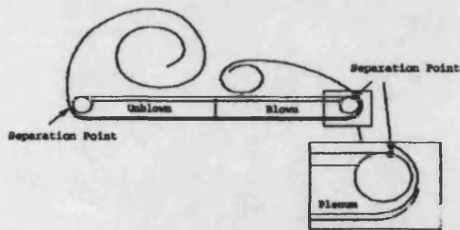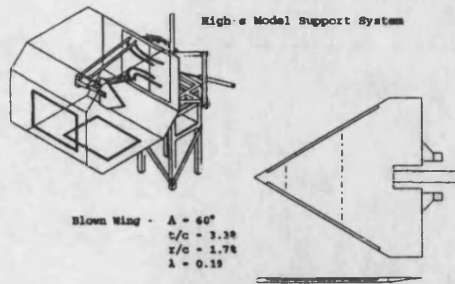
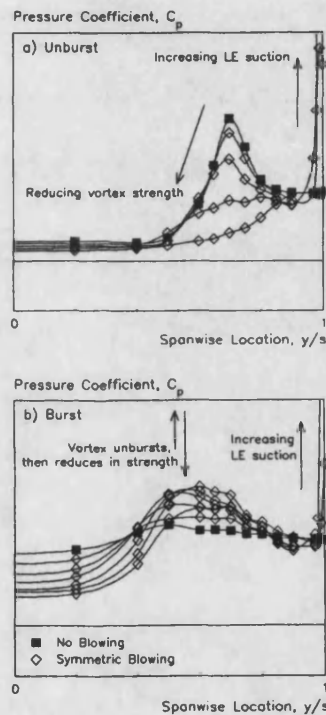Figure 2   Blown Delta Wing Model in the Bath University 7'x 5' Low-Speed Wind-Tunnel

Figure 3   Typical Effect of Symmetric Blowing on Delta Wing Upper Surface Pressures
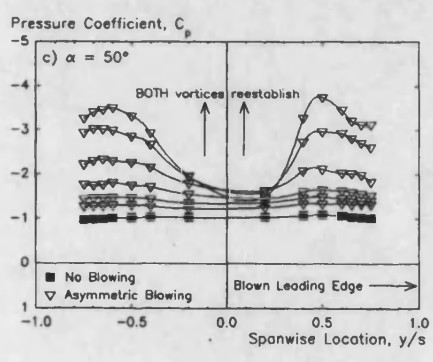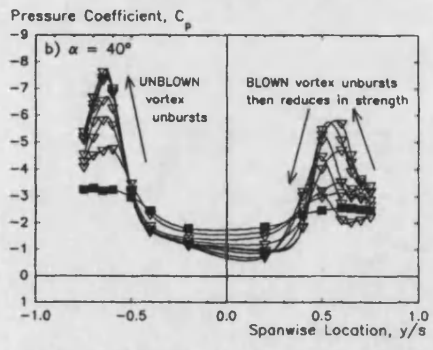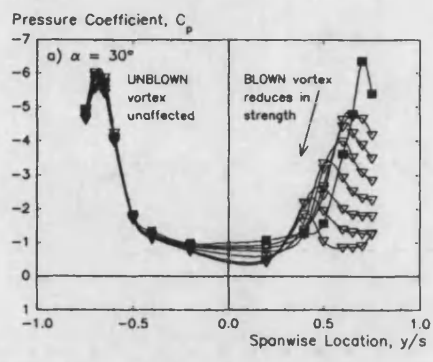a) Unburst Vortex ('Pre-Stall')
b) Burst Vortex ('Post-Stall')

Figure 1   Tangential Leading Edge Blowing Applied to a Delta Wing at High Angles of Attack

7

Pressure Coefficient, C_p

a) $\alpha = 30°$

UNBLOWN vortex unaffected

BLOWN vortex reduces in strength

Spanwise Location, y/s

Pressure Coefficient, C_p

b) $\alpha = 40°$

UNBLOWN vortex unbursts

BLOWN vortex unbursts then reduces in strength

Spanwise Location, y/s

Pressure Coefficient, C_p

c) $\alpha = 50°$

BOTH vortices reestablish

■ No Blowing
▽ Asymmetric Blowing

Blown Leading Edge ⟶

Spanwise Location, y/s

Figure 4   Effect of Increasing Asymmetric (One-Sided) Blowing on Wing Upper Surface Pressure Distribution (x/c = 0.2, α = 30°, 40°, 50°)

Angle of Attack, α

a) Asymmetric Blowing

Data from Reference 3

Blowing Momentum Coefficient, C_{μ_R}

Angle of Attack, α

b) Effect of Sideslip
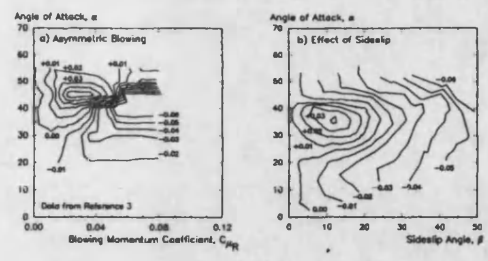
Sideslip Angle, β

**Figure 5   Roll Moment Coefficient for a 60° Delta Wing[13] vs Angle of Attack and:
a) Asymmetric (Right Side) Blowing
b) Sideslip Angle**

Minimum Pressure Coefficient, $C_{p_{min}}$

a) Effect of Roll

VORTEX BURST

INCREASING Effective Leading Edge Sweep

REDUCING Effective Leading Edge Sweep

△ $\phi = -20°$
● $\phi = 0°$
▽ $\phi = +20°$

Angle of Attack, α

Minimum Pressure Coefficient, $C_{p_{min}}$

VORTEX BURST

b) Effect of TLEB

Shift in Vortex Burst Location

Shift in Effective Vortex 'Zero Lift' Angle of Attack

Angle of Attack, α

● No Blowing
◇ Symmetric Blowing
▽ Asymmetric Blowing - BLOWN Vortex
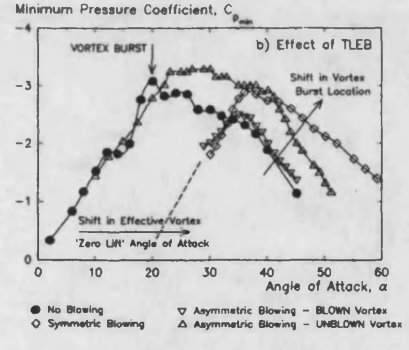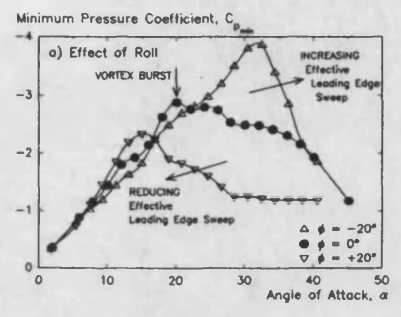△ Asymmetric Blowing - UNBLOWN Vortex

**Figure 6   Magnitude of Vortex-Induced Suction Peak at x/c = 0.5:
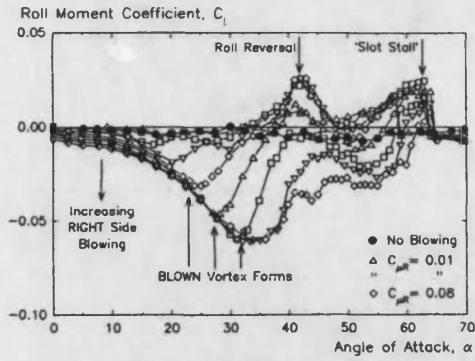a) Effect of Roll Angle
b) Effect of Blowing**

8

Figure 7   Roll Moment Characteristics due to Asymmetric (One-Sided) Blowing - Increasing Angle of Attack at Constant Right Side Blowing Levels ($C_{\mu R}$ = 0.0 to 0.08)
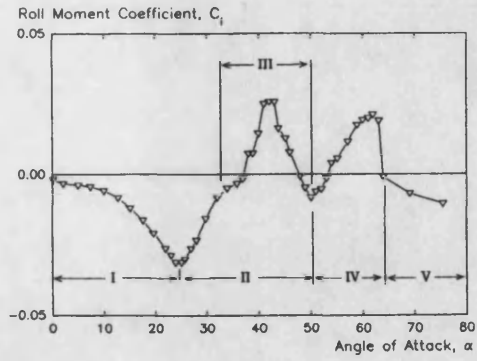

Figure 9   Roll Moment Behaviour due to Right Side Blowing at Zero Roll Angle ($C_{\mu R}$ = 0.04)
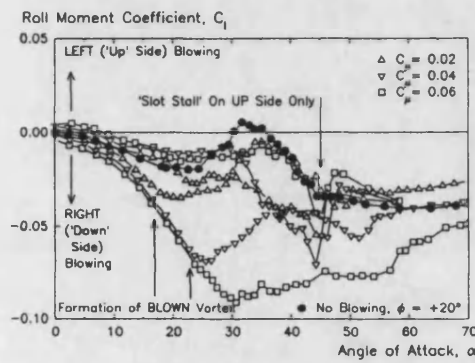

Figure 8   Roll Moment Characteristics due to Asymmetric (One-Sided) Blowing, with Non-Zero Roll Angle (ϕ = +20°, $C_{\mu L}$ = 0.0 to 0.06, $C_{\mu R}$ = 0.0 to 0.06)
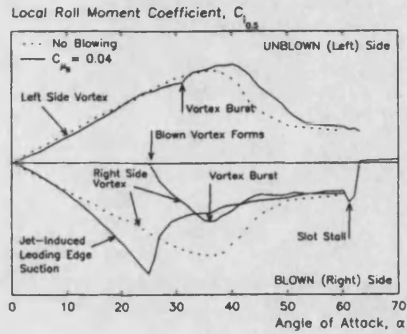

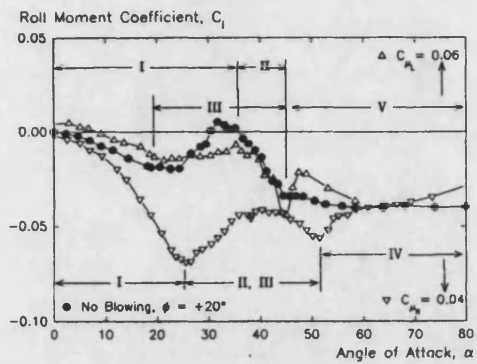Figure 10   Contributions to Roll Moment Behaviour due to Right Side Blowing (ϕ = 0°, $C_{\mu R}$ = 0.04)

9

Figure 11   Roll Moment Behaviour due to Right and Left
Side Blowing at Non-Zero Roll Angle (ϕ =
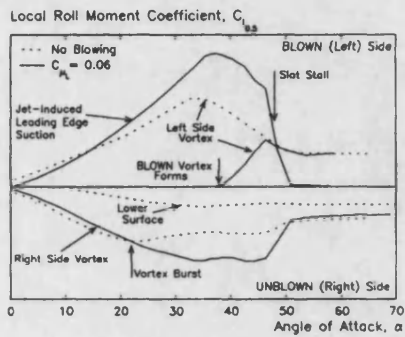+20°, $C_{\mu R}$ = 0.04, $C_{\mu L}$ = 0.06)

Figure 12   Contributions to Roll Moment Behaviour due
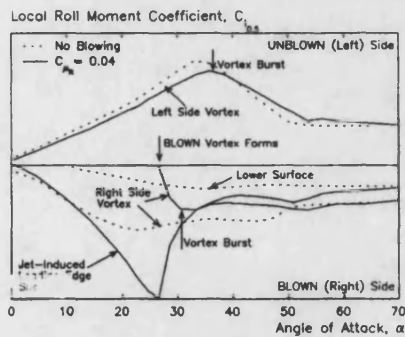to Left Side Blowing at Non-Zero Roll Angle
(ϕ = +20°, $C_{\mu L}$ = 0.06)

Figure 13   Contributions to Roll Moment Behaviour due
to Right Side Blowing at Non-Zero Roll Angle
(ϕ = +20°, $C_{\mu R}$ = 0.04)

10